FINAL REPORT

TERMINAL DESCENT SIMULATION STUDY

By Richard F. Broderick, Michael K. Mann,
Richard D. Moog, Billie W. Preston,
Parker S. Stafford, and Henry C. Von Struve

for

NATIONAL AERONAUTICS AND SPACE ADMINISTRATION

CONTENTS

LIST OF ILLUSTRATIONS

LIST OF TABLES

FINAL REPORT

TERMINAL DESCENT SIMULATION STUDY

By Richard F. Broderick, Michael K. Mann,
Richard D. Moog, Billie W. Preston
Parker S. Stafford, and Henry C. Von Struve

SUMMARY

This report documents the development of a Martian soft lander
terminal descent simulation program. This program is designed
for use relative to the parachute and terminal descent phases of
the Mars Lander (soft landing) mission; however, it can also be
used for other phases with slight modifications. The parachute-
phase simulation was developed under this contract, but the
terminal-descent-phase simulation was developed by Martin Marietta
Corporation independently. Instructions for using the program are
provided in a separate user's guide (ref. 1), which was also pre-
pared under this contract. At the same time the simulation pro-
gram was being developed, studies were conducted on several land-
ing radar mechanizations to evaluate their performance character-
istics in connection with the soft lander mission. These studies
were performed using the terminal descent program and Monte Carlo
simulations of two types, static and time-correlated.

I. INTRODUCTION

The delivery of a scientific payload to the surface of the
planet Mars, with a soft-lander capsule, is a complex mission
that includes an aerodynamic-entry phase, a parachute phase, and
a terminal-descent, retro-engine phase. The terminal descent
system must accomplish navigation, guidance, and control functions
to position the capsule just above the surface with the prescribed
velocity and vehicle attitudes. These functions must be performed
regardless of the atmospheric winds, atmospheric densities, surface
slopes, or other environmental variations encountered during the
descent.

Lander system studies have shown that multiple, differentially-
throttled, monopropellant engines are the most efficient retro-
engines and should be used for propulsion during the descent.

For effective navigation, the relative range and velocity must be measured by Lander sensors during the terminal descent. These sensors are assumed to consist of a multiple-channel Doppler velocity radar and a radar altimeter that measures the distance to the surface. But the composite effect of the multiple-stage descent, the environmental variations, and the mechanization of the terminal descent system establishes a non-analytic performance problem. This creates the need for a six-degree-of-freedom (6DOF) simulation program to be used for parametric performance investigations. Since the initial terminal descent conditions are important parameters, the 6DOF program should be capable of simulating the parachute phase as well as the terminal descent phase.

Such a program has been developed by modifying a computer program that was originally prepared for the Air Force Systems Engineering Group by Litton Systems, Inc. (ref. 2). The resulting program is a powerful tool for soft-lander performance evaluations. Part of the modification of the old 6DOF program was accomplished under this contract. Since the performance of the doppler velocity radar is critical to the success of the mission, the 6DOF program and Monte Carlo simulations were used to investigate several candidate radar mechanizations, to demonstrate the analytical techniques, and to provide background data on radar performance.

The report is arranged to present a description of the proposed mission, a description of the terminal descent guidance system, the results of the radar study, and a general description of the 6DOF program. In this way, the reader gains sequential knowledge of the need, usage, and operation of the program. Detailed user's instructions may be found in reference 1.

2

II. MISSION DESCRIPTION

Continuously-active Lander Capsule propulsion, guidance, and control (PG&C) functions are required from Orbiter separation to touchdown on the Mars surface (figure 1). One navigation, two guidance, and several attitude-control modes of operation are required to implement the sequential functions and performance requirements that are shown in the figure. The proper operation of the system is critical to the success of the soft landing mission; therefore, it must be reliable and flexible enough to compensate for variations in atmospheric density, horizontal winds, surface elevation, and surface slopes in the landing area.

A block diagram of the PG&C system is shown in figure 2. All control computations and descent sequencing signals are provided by the general-purpose digital computer.

Functional operation of the system begins 15 hr before the Lander separates from the Orbiter. Ground commands energize the system, initiate a checkout mode, and update nominal mission control parameters. These parameters include the deorbit impulse and attitude, entry attitude, and sequence signal times. During the preseparation period, the GCC checks the system and relays system-status information to the Space Flight Operations Facility (SFOF). An attitude reference is established in the GCC while the Orbiter is locked on the Sun and Canopus.

Separation is initiated by an Orbiter timer. An attitude-hold mode is used while the Lander coasts away from the Orbiter. During this 30-minute period, the Lander is oriented to the deorbit attitude. Then the deorbit engine is ignited with a timed signal and is shut down when the VRU measures the required impulse.

After the deorbit thrust phase, the Lander coasts in an attitude-hold mode until 30 minutes before entry. At that time, the Lander is oriented to the programed entry attitude. The HARA is energized before entry with a timed signal. Entry is sensed by the VRU at 0.1-g deceleration, and the control mode is changed to rate damping in all three axes. When maximum deceleration is sensed, local vertical inertial navigation equations are initialized in the GCC on the bases of a priori knowledge of velocity and attitude and the altitude determined by the HARA. At a preset altitude of 23 500 ft, as sensed by the HARA, the Ballute is deployed and control is switched to roll rate damping only. The parachuse is deployed at 14 500 ft. Six sec later the aeroshell is jettisoned and the TDLR and LARA are energized.
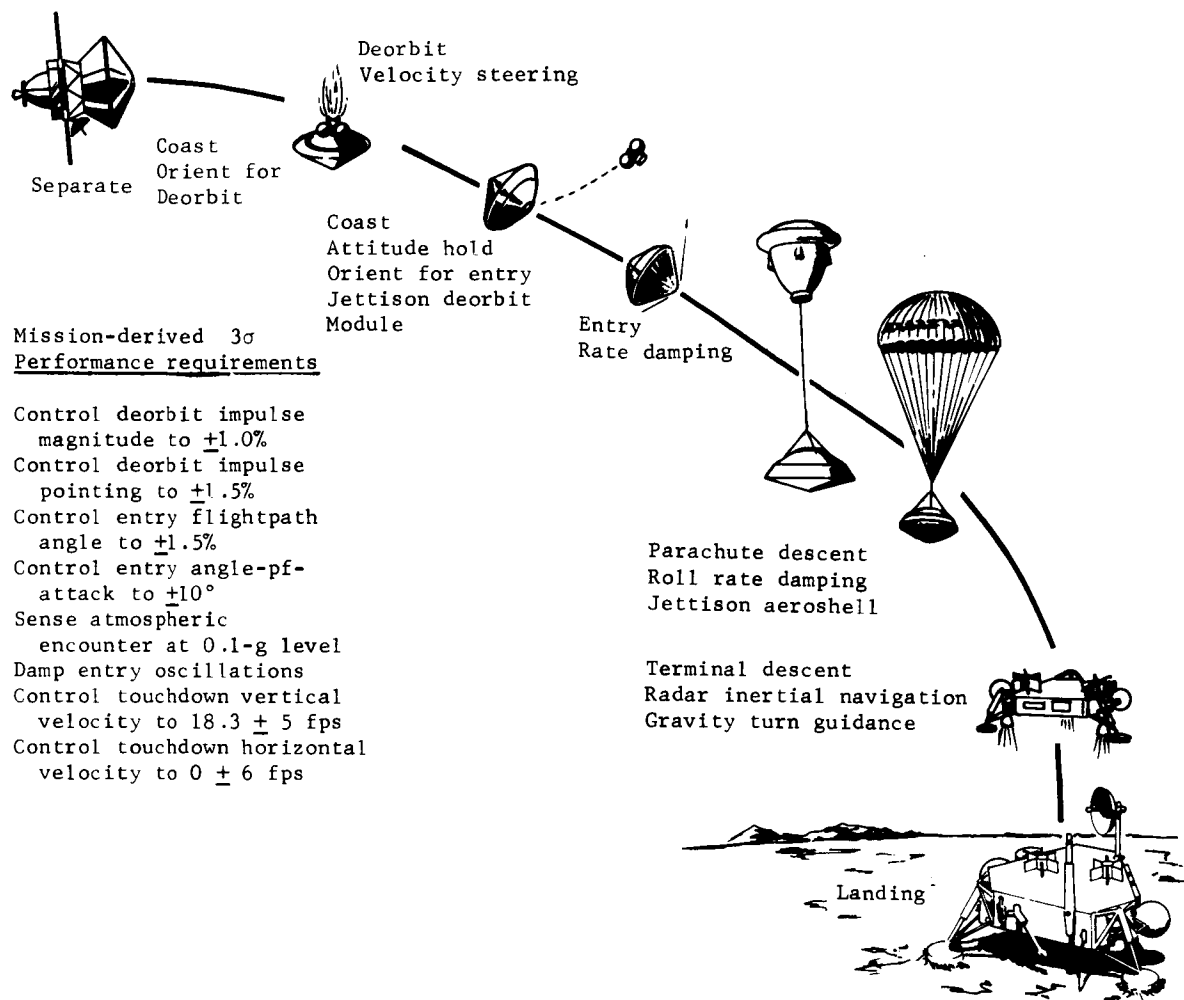
Figure 1.- Major Steps Between Orbiter Separation and Touchdown

Separate
Coast
Orient for
Deorbit

Deorbit
Velocity steering

Coast
Attitude hold
Orient for entry
Jettison deorbit
Module

Entry
Rate damping

Parachute descent
Roll rate damping
Jettison aeroshell

Terminal descent
Radar inertial navigation
Gravity turn guidance

Landing

Mission-derived 3σ
Performance requirements

Control deorbit impulse
   magnitude to $\pm 1.0\%$
Control deorbit impulse
   pointing to $\pm 1.5\%$
Control entry flightpath
   angle to $\pm 1.5\%$
Control entry angle-pf-
   attack to $\pm 10°$
Sense atmospheric
   encounter at 0.1-g level
Damp entry oscillations
Control touchdown vertical
   velocity to 18.3 ± 5 fps
Control touchdown horizontal
   velocity to 0 ± 6 fps

Figure 2.- Block Diagram of the PG&C System

4

During the parachute phase, the local vertical inertial navigation estimates of altitude and velocity are updated in the computer with radar data. At a preset altitude of approximately 3900 ft, as sensed by the widebeam LARA, the terminal engines are ignited and the parachute is jettisoned. For the rest of the descent, pitch and yaw are controlled by differentially throttling the three terminal engines, and roll is controlled with six jets on the Lander. During a 3-sec tipup maneuver after parachute release, the Lander is rotated to align the thrust vector with the velocity vector sensed by the TDLR. The Lander drops at throttle settings of 25% until the axial control curve conditions are met. At that time, the engines are throttled up to 90% and the Lander performs a gravity turn descent aimed at 10 fps at a 60-ft altitude. A constant-velocity control mode is then invoked to an altitude of 10 ft, at which time the engines are shut down and the Lander drops to the surface.

III. TERMINAL DESCENT GUIDANCE AND CONTROL

A. Guidance and Control Laws

The guidance and control laws considered in this study represent the result of a series of studies documented in references 3 thru 6. A summary of the descent guidance laws follows.

To accomplish a soft landing, the three components of the Lander's velocity measured with respect to the surface must be controlled as a function of altitude measured with respect to the surface. Gravity-turn steering has been selected as the means of controlling the lateral velocity components. This law is mechanized by rotating the vehicle about its pitch and yaw axes until the lateral body-axis velocities are zero. This causes the thrust axis to point along the total velocity vector. This steering law is simple to mechanize because local vertical sensing is not required. Gravity causes the thrust axis to rotate toward the vertical as the velocity is reduced. An arbitrary roll orientation is maintained by using an attitude-hold mode during the descent. If the components of vehicle velocity are denoted as u, v, and w along the roll, pitch, and yaw axes, respectively, then the steering signals are

$$\text{Pitch:} \quad \alpha_c = G_\alpha \, w/u \tag{1}$$

$$\text{Yaw:} \quad \beta_c = G_\beta \, v/u \tag{2}$$

$$\text{Roll:} \quad \varphi_c = 0 \tag{3}$$

where G_α and G_β are the pitch and yaw gains, respectively.

The axial component of velocity, u, is controlled by modulating the vehicle thrust to follow the preprogramed desired velocity/altitude contour shown in figure 3. After a 2-sec engine warmup, the parachute is jettisoned and a 3-sec maneuver phase is alloted for aligning the thrust and velocity vectors. The high-thrust phase is designed to command up to 90% of the available thrust; this will conserve propellant by minimizing gravity losses. The remaining 10% of available thrust is used for steering. The constant-velocity phase allows the vehicle control system to reduce the effects of dynamic control lags and errors that result from following the high-thrust phase contour before shutting down the engines.

Terminal descent contour

Propellant used, lb

Minimum velocity   Maximum velocity

(Minimum velocity)   (Maximum velocity)

Start engines

Warmup phase

Release parachute

Tipup maneuver phase

High-thrust phase

Constant-velocity phase

Engine shutdown

Altitude above surface (ft)

3900
3300
2356
520
60
10

10 18.3 100 143   376

Velocity (fps)

(Minimum velocity)	(Maximum velocity)
4	4
	6
50	86
35	
9	9
(98)	(105)

Figure 3.- Terminal Descent Contour

The contour is designed for the highest velocity condition, includes winds resulting from the parachute phase, and is shaped to account for propellant-tank pressure blowdown and specific-impulse changes. Simulations have shown that this approach allows margin for any 3σ combination of atmospheres, winds, and surface slopes (ref. 4). The minimum velocity resulting from the parachute phase occurs in the maximum-density atmosphere with zero wind. The resulting trajectory shown has a long drop phase before intersecting the design descent contour for the high-thrust phase. The propellant required for this condition is less than that required for the maximum-wind case.

The propulsion-system design parameters of blowdown ratio, maximum thrust, throttle ratio, and propellant loading are defined through descent simulations using the guidance laws described above. The thrust and blowdown ratio can be chosen to minimize the weight of the system (ref. 6). Once the maximum thrust has been established, the required throttle ratio is defined by the requirement to reach a Mars thrust-to-weight ratio of less than one during the constant-velocity descent phase. Thus

$$(1/R + 0.1) \ F/W < 1 \tag{4}$$

where R is the throttle ratio, F is the total maximum thrust, and W is the weight of the Lander on Mars. The 0.1 term in equation (4) is the margin reserved for attitude control.

The use of gravity-turn steering with a high thrust-to-weight ratio can result in high vehicle turning rates near the surface. These potential effects are minimized by using a constant-velocity descent phase and a blowdown propulsion system.

Figure 4 shows a block diagram of the Terminal Descent Guidance and Control System. Several choices exist for mechanizing the system; these will be discussed later in this report.
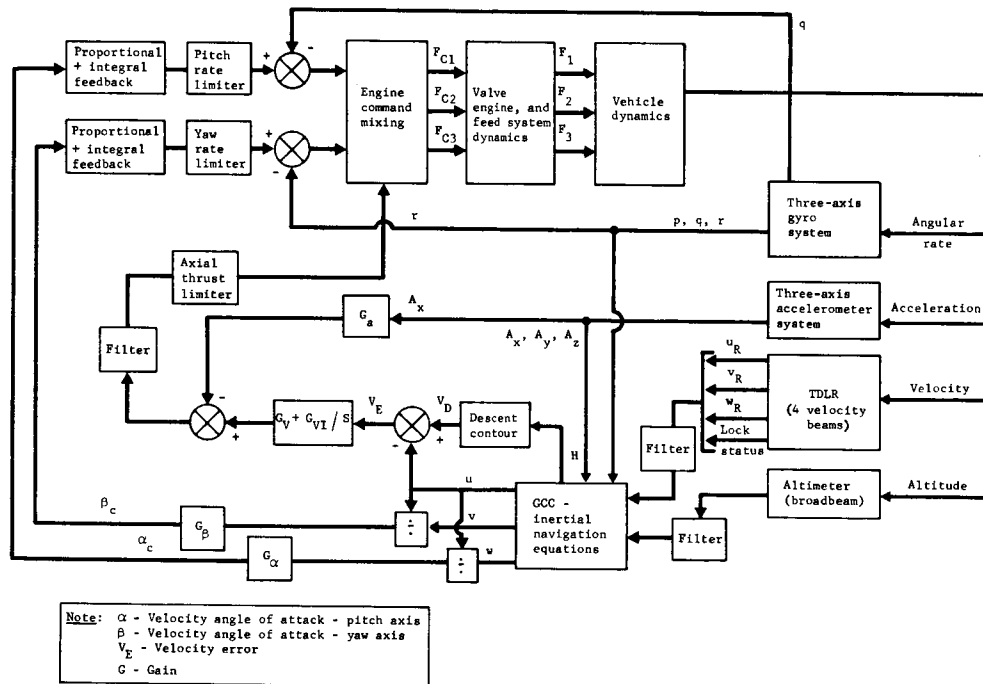
Figure 4.- Block Diagram of the Terminal Descent Guidance and Control System

As shown in the figure, the vehicle dynamic motion is sensed by the TDLR, the altimeter, and the three-axis strapdown gyro and accelerometer systems. The data from these sensors are used to generate outputs for u, v, w, and H from the radar-aided inertial navigator. The navigator equations are given below.

Velocity equations:

$$\dot{u} = A_x - qw + rv + gA_{13} + K_u \left(u_R - u \right) \tag{5}$$

$$\dot{v} = A_y + pw - ru + gA_{23} + K_v \left(v_R - v \right) \tag{6}$$

$$\dot{w} = A_z - pv + qu + gA_{33} + K_w \left(w_R - w \right) \tag{7}$$

Altitude equations:

$$\dot{Z} = A_{13} \, u + A_{23} \, v + A_{33} \, w \tag{8}$$

$$\dot{Z}_a = \dot{Z} + K_H \left(H - H_A \right) \tag{9}$$

$$H = H_o - Z_a \tag{10}$$

In these equations, u, v, w are the body-axis velocity components; u_R, v_R, w_R are the velocity components determined by the radar system; p, q, r are the attitude rates; A_x, A_y, A_z are the acceleration components; A_{13}, A_{23}, A_{33} are the computed direction cosines; H is the computed altitude; H_o is the reference altitude; H_a is the altitude determined by the altimeter; g is the Mars gravitational constant; and K_H, K_u, K_v, K_w are adjustable gains.

The attitude-rate data used in these equations are obtained by differencing the consecutive gyro-pulse counts in the digital computer. The acceleration data are obtained similarly from the accelerometer pulses. The gains K_u, K_v, K_w, and K_H are keyed to the radar-tracker lock status indicators. When a particular radar data input $\left(\text{e.g.,} \quad U_R\right)$ is invalid, the corresponding gain $\left(K_u\right)$ is set to zero. This allows the computation to proceed using inertial data. When the gains are not zero, the inertial estimates will track the radar data with a time lag of $1/K$ sec $\left(K = K_u, K_v, \text{etc}\right)$.

Three-axis accelerometer data are required to implement these equations. During the parachute phase, the inertial navigator updates the estimates of u, v, w, and H, and the lateral-axis accelerometers measure lateral accelerations caused by wind gusts.

The descent contour block shown in figure 4 is a curve-fit function of the velocity/altitude contour shown in figure 3. Because the form of this function for flight software has not yet been defined, the MOD6MV program uses a table look-up routine to generate the desired velocity from H. This desired velocity is then compared with u to generate the velocity error, V_E. The command signal to the inner acceleration control loop is

$$A_c = \left(G_V \cdot V_E \right) + \left(G_{VI} \cdot \frac{V_E}{S} \right) \tag{11}$$

where G_V is the acceleration command proportional gain, G_{VI} is the acceleration command integral gain, and S is the Laplace transform variable.

This signal is compared to A_x the acceleration sensed by the roll-axis accelerometer (assuming $G_a = 1$), and is then filtered and limited. The filter removes accelerometer noise and structural feedback; the limiter ensures that the axial control channel does not saturate the engine valves and prevent differential throttling for attitude control.

In the steering channels, a rate command inner loop ensures that the initial pitch and yaw maneuver can be accomplished at a controlled rate after the parachute is released. The command rate signal is limited so neither the gyro-torquing capability nor the radar-tracking-rate capability will be exceeded. Proportional plus integral feedback is used to allow complete nulling of α_c and β_c in the steady-state condition, even in the presence of misalignment torques. The MOD6MV simulations have shown that these integrators should not be active until after the vehicle has accomplished the initial maneuver. Unless this is done, the integrated signal tends to counteract the proportional signal, and the maneuver response is poor. After the maneuver is over, the integrators can be started to provide the desired steady-state nulling.

Stability analyses (ref. 6) have shown that lead-lag compensation is desirable in each of the inner control loops (pitch rate, yaw rate, and acceleration) to improve their stability and response. This lead-lag compensation is accomplished by using a filter transfer function.

$$G_{LL}(S) = \frac{K_L \left(S + W_o\right)}{S + W_p} \tag{12}$$

on each of the input lines to the engine command mixing block of figure 4. In equation (12), K_L is the filter gain, W_o is the filter lead break frequency, and W_p is the filter lag break frequency. In the present design (ref. 6), $W_o = 50$ rad/sec, $W_p = 300$ rad/sec, and $K_L = 6$.

The engine command mixing block consists of the following equations for a three-engine vehicle

$$B_1 = G_{p1} \cdot Pe + Te \tag{13}$$

$$B_2 = -G_{p2} \cdot Pe + G_y \cdot Ye + Te \tag{14}$$

$$B_3 = -G_{p2} \cdot Pe - G_y \cdot Ye + Te \tag{15}$$

where B_1, B_2, B_3 are the mixed command inputs to the engine valves, Pe is the pitch-channel error signal, Ye is the yaw-channel error signal, Te is the acceleration-loop error signal, and G_{p1}, G_{p2}, G_y are the mixing gains in the three engines.

These equations correspond to the engine arrangement shown in figure 5. For a symmetrical arrangment
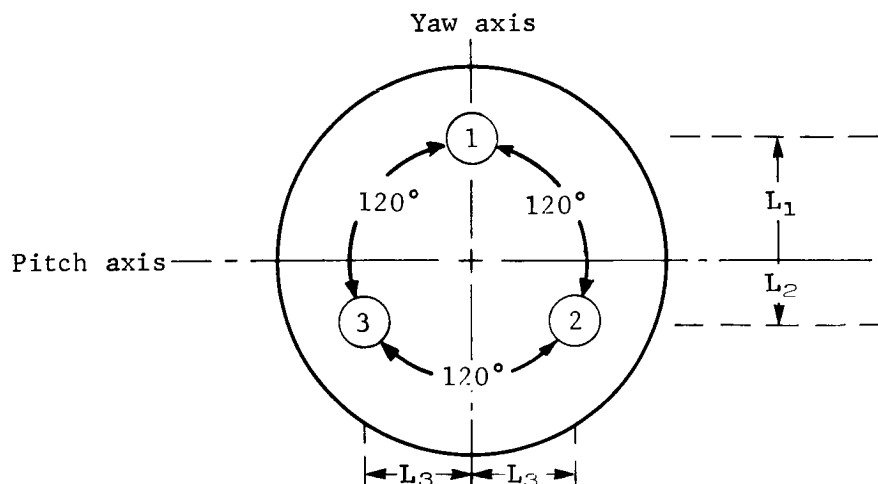
Figure 5.- Engine Arrangment

The moment arms are related by

$$L_2 = \tfrac{1}{2} L_1 \tag{16}$$

$$L_3 = \sqrt{\tfrac{3}{2}} L_1 \tag{17}$$

12

The moment and thrust equations are then

$$M_p = \left(F_1 \cdot L_1\right) - \left(F_2 \cdot L_2\right) - \left(F_3 \cdot L_2\right) \tag{18}$$

$$M_y = \left(F_2 \cdot L_3\right) - \left(F_3 \cdot L_3\right) \tag{19}$$

$$F = -F_1 - F_2 - F_3 \tag{20}$$

where M_p is the pitch moment, M_y is the yaw moment, F is the total thrust of the engines and F_1, F_2, F_3 are the individual engine thrusts.

G_{p1}, G_{p2}, and G_{p3} should be chosen to eliminate cross-coupling between the control channels. We can do this by letting

$$F_i = B_i \tag{21}$$

and using equations (13) thru (15) and (18 thru (21) to construct the matrix equation shown below.

$$
\begin{bmatrix} M_p \\ M_y \\ F \end{bmatrix} =
\begin{bmatrix} L_1 & -L_2 & -L_2 \\ 0 & L_3 & -L_3 \\ -1 & -1 & -1 \end{bmatrix}
\begin{bmatrix} G_{p1} & 0 & 1 \\ -G_{p2} & G_y & 1 \\ -G_{p2} & -G_y & 1 \end{bmatrix}
\begin{bmatrix} Pe \\ Ye \\ Te \end{bmatrix}
$$

$$
=
\begin{bmatrix}
\left[\left(G_{p1} \cdot L_1\right) + \left(2 \cdot G_{p2} \cdot L_2\right)\right] & 0 & \left[L_1 - \left(2 \cdot L_2\right)\right] \\
0 & \left(2 \cdot G_y \cdot L_3\right) & 0 \\
\left[-G_{p1} + \left(2 \cdot G_{p2}\right)\right] & 0 & -3
\end{bmatrix}
\begin{bmatrix} Pe \\ Ye \\ Te \end{bmatrix}
\tag{22}
$$

Since by equation (16) $L_2 = \tfrac{1}{2} L_1$ we see that choosing

$$G_{p1} = 2 \cdot G_{p2} \tag{23}$$

will yield a diagonal matrix which decouples the control channels. Furthermore, to make the pitch and yaw channels have equal gain through the mixing and engine elements, let

$$G_y = \frac{\sqrt{3}}{2} G_{p1} \tag{24}$$

13

The dynamics of all the components in the terminal descent control system are well known, with the possible exception of the engine-throttling dynamics. Preliminary engine-throttling tests performed by Martin Marietta with nitrogen-saturated propellant show that the engine equivalent-throttling-time constant is on the order of 15 msec or less. The recommended control loop mechanization can be made stable and responsive with any postulated engine dynamics (up to a time constant of 100 msec) because all the other components in the system have fast responses, including the available throttle valves (fig 6).
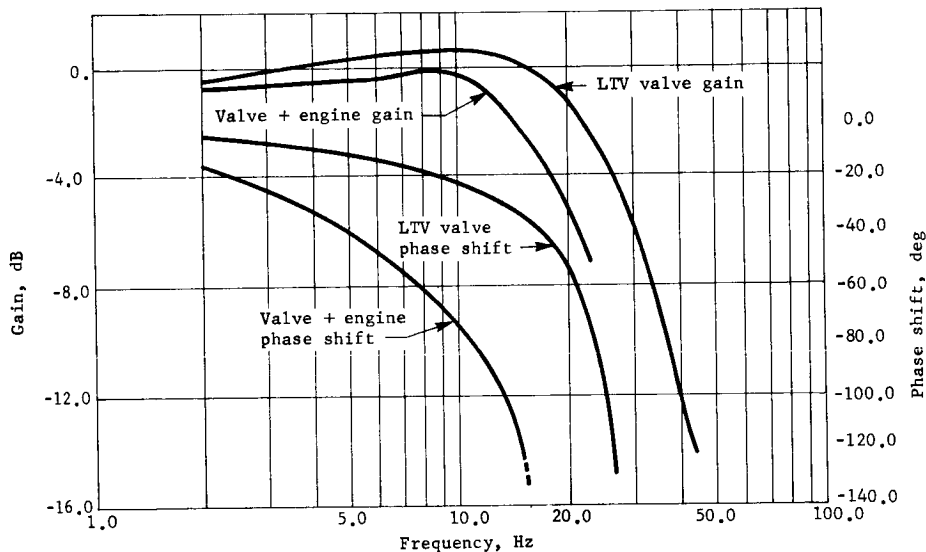
Figure 6.- Frequency Response to Input Commands

The engines operate in a blowdown mode, which means their thrust (and therefore the gain in the inner loops) decreases as a function of the propellant used. The control loops are designed to have sufficient stability margin and to be stable and responsive at all operating gains, without requiring gain changing as a function of the propellant-tank pressure. The radar-aided inertial control loop mechanization enhances the stability and the speed of response of the control loops because the main control signals do not have to be filtered through a low-frequency noise filter (see ref. 5). Figure 7, which shows the root loci for the inner and outer control loops in the radar-aided inertial mode, illustrates that all dominant closed-loop poles are stable and well-damped. This was confirmed in the 6-D digital computer simulations performed on the control system. As evidenced in the plots of pitch rate and position versus time, the response of the attitude channels is fast and stable. The axial channel also· has a fast response. In these analyses, the valve transfer function was defined by a second-order linear model, and the engine, by a first-order model.

Legend:

▢	Closed-loop poles
L	Low gain
H	High gain
×	Open-loop pole
○	Open-loop zero
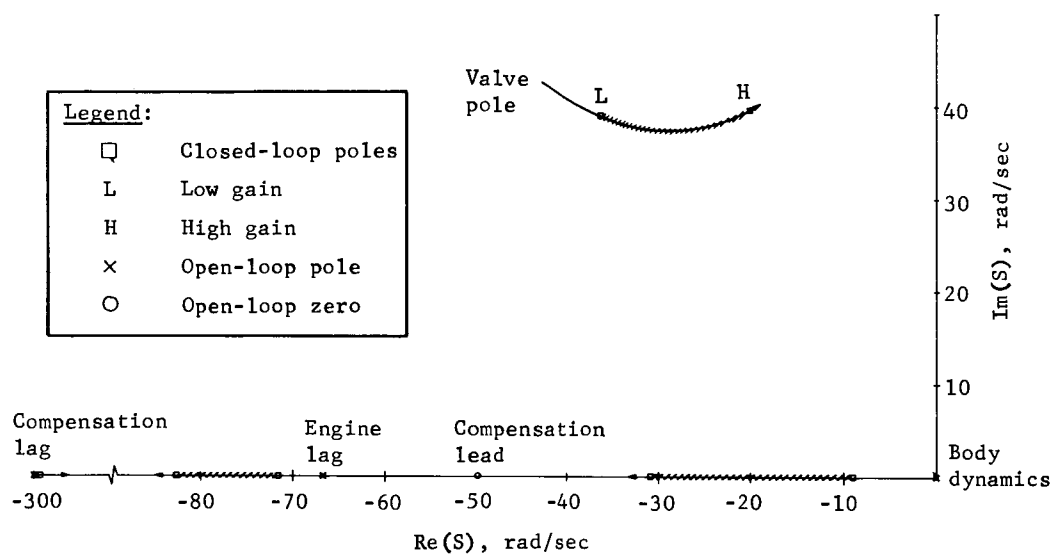
(a) Pitch-Yaw Control Inner Rate Loop Root Locus
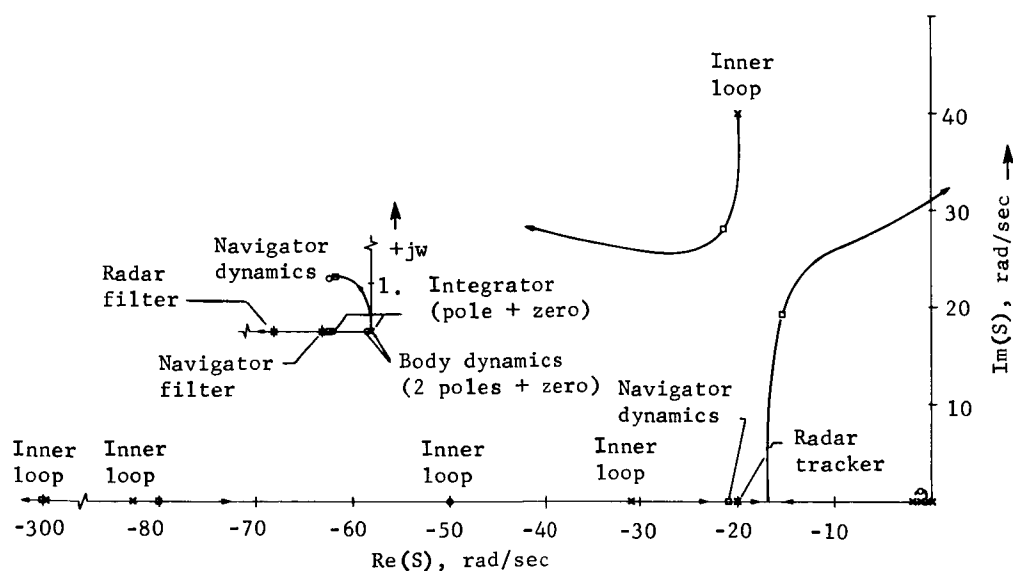
(b) Pitch-Yaw Control Outer Radar-Aided Inertial Loop Root Locus, High-Gain Case

Figure 7.- Root Locus Plots for the Inner and Outer Control Loops, System Operating in the Radar-Aided Inertial Mode

Valve pole ✕   L   H

Legend:
- □   Closed-loop poles
- L   Low gain
- H   High gain
- ✕   Open-loop pole
- ○   Open-loop zero

40

30

Im(S), rad/sec

10

Compensation lag			Engine lag	Compensation lead		Accelerometer filter lag	

-300   -80   -70   -60   -50   -40   -10

Re(S), rad/sec
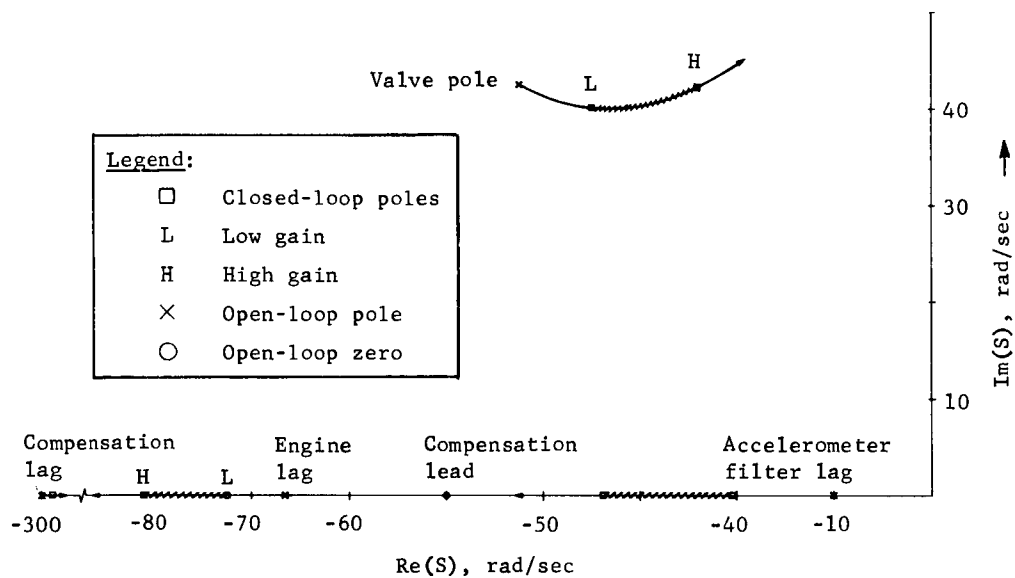
(c)   Velocity Control Inner Loop Root Locus

✕ Inner loop

40

Im(S), rad/sec

30

Navigator filter
Navigator dynamics
+jw
-1.
20
-2.   -1.
Body dynamics

Navigator dynamics

10

Radar filter

Inner loop	Inner loop			Inner loop		Inner loop			Radar filter

-80   -70   -60   **-50**   -40   -30   -20   -10

-50 ı, rad/sec
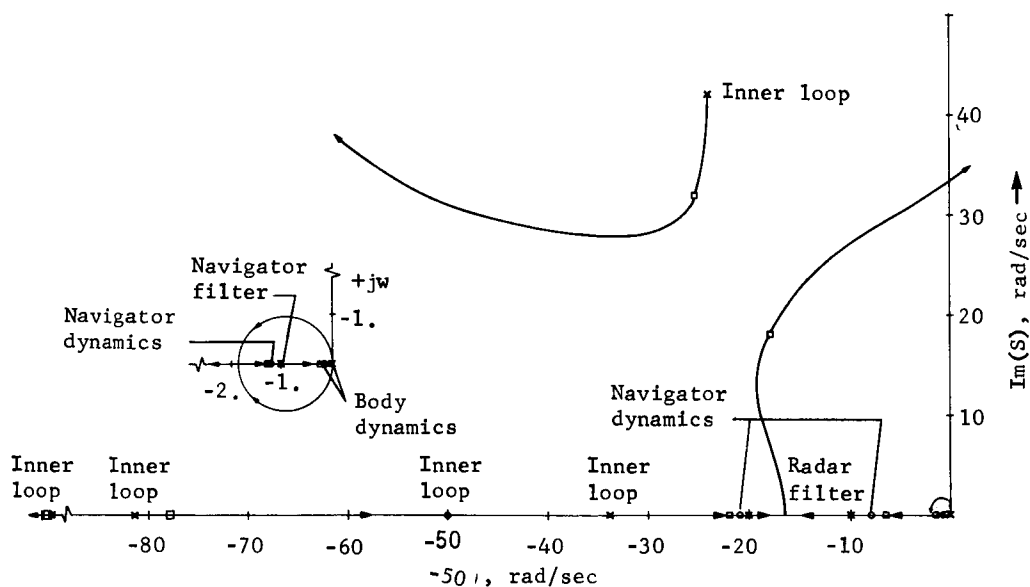
(d)   Velocity Control Outer Radar-Aided Inertial Loop Root Locus, High Gain Case

Figure 7.- Concluded

16

B. Alternative System Mechanization

The block diagram in figure 4 showed a system that employed the outputs of a radar-aided inertial navigator for steering and descent-contour guidance. Alternatively, the outputs of the radar $\left(u_R, \ v_R, \ \text{and} \ w_R\right)$ and the altimeter $\left(H_A\right)$ could be used directly for this purpose. This direct method is called operation in the radar prime mode. Stability analyses (refs. 3 thru 6) have shown that for operation in the radar prime mode, special control-loop compensation is required to counteract the effects of having the radar noise-smoothing filters directly in the steering channels. The compensation subsystem, which uses integrals of the gyro rate outputs q and r, is shown in figure 8. τ is the time constant for the filter. This subsystem is inserted (fig. 4) between the radar and the command signals α_c and β_c when the system operates in the radar prime mode. It has also been shown (ref. 4) that if the radar operates in the prime mode, none of the radar components $\left(u_R, \ v_R \ \text{or} \ w_R\right)$ can be absent for longer than a few msec or vehicle control will be lost. Thus, in the radar prime mode, the inertial navigator must be used as a backup to handle radar-dropout periods. In this case, equations (5) thru (10) are solved and the outputs are substituted for

u_R, v_R, w_R, and H_A when the radar lock-status flags indicate the loss of a signal.

Figure 9 shows the 6DOF simulation results for a system operating in the radar-aided inertial mode. Figure 10 shows the results for a system operating in the radar prime mode with inertial backup. Notice the difference in the effect of radar noise on the vehicle's thrust response. When the system is operating in the radar-aided inertial mode, it is about four times less sensitive to radar noise.

Since the radar did not unlock on these runs, the radar prime mode did not use inertial navigator data except during the tip-up phase, when the attitude rates exceeded 10 deg/sec. This is a logic test in the simulation, since for high vehicle rates, the radar data lags significantly. Figures 9 and 10 show slight trajectory differences because, in each run, the navigator was initialized with errors. Even so because of radar data updating, these errors are reduced as time increases.
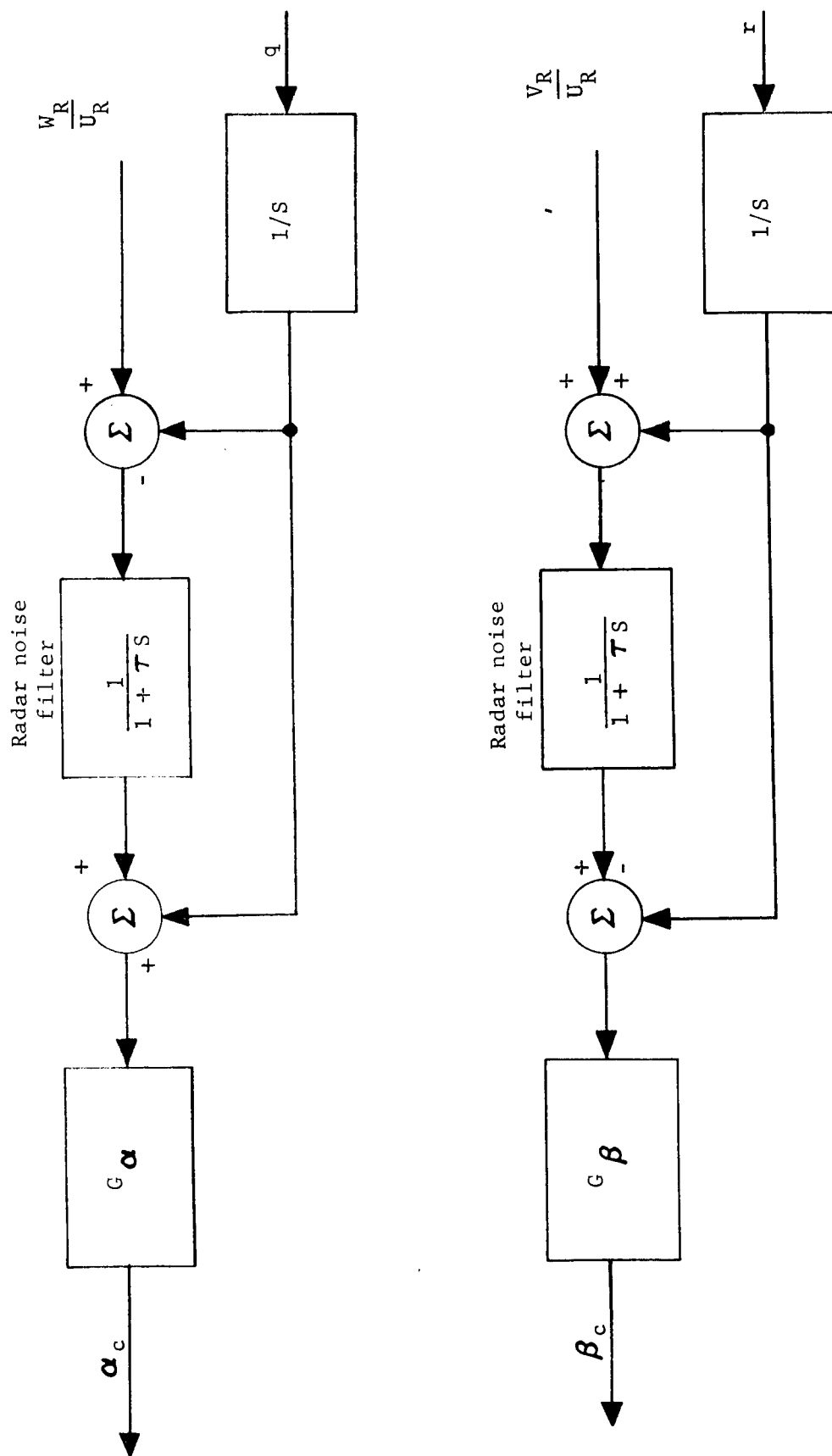
Figure 8.- Block Diagram of the Steering Channel Control-Loop Compensation Subsystem

18
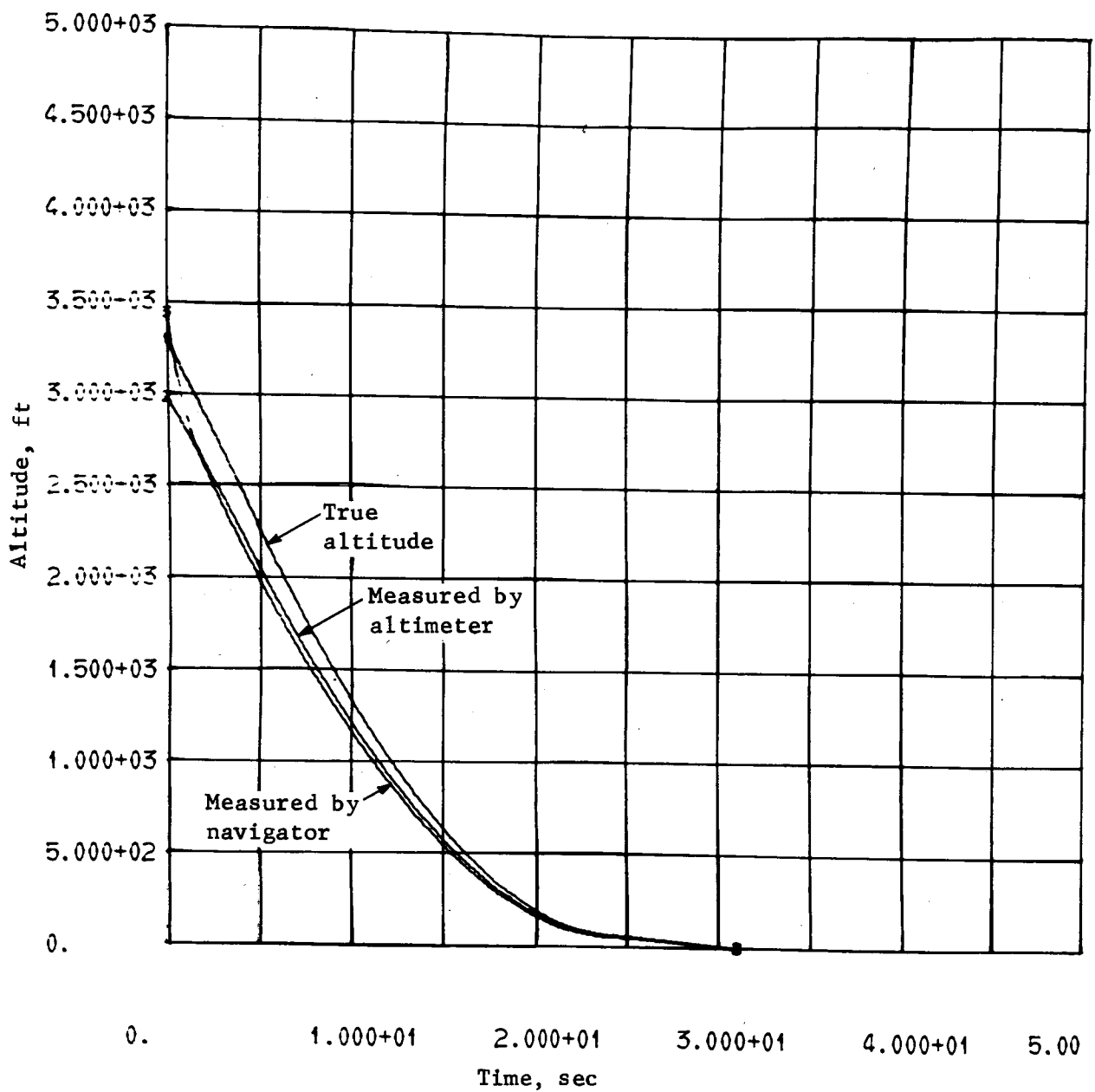
(a) Altitude vs Time

Figure 9.- 6DOF Simulation Results; System Operating in Radar-Aided
Inertial Mode
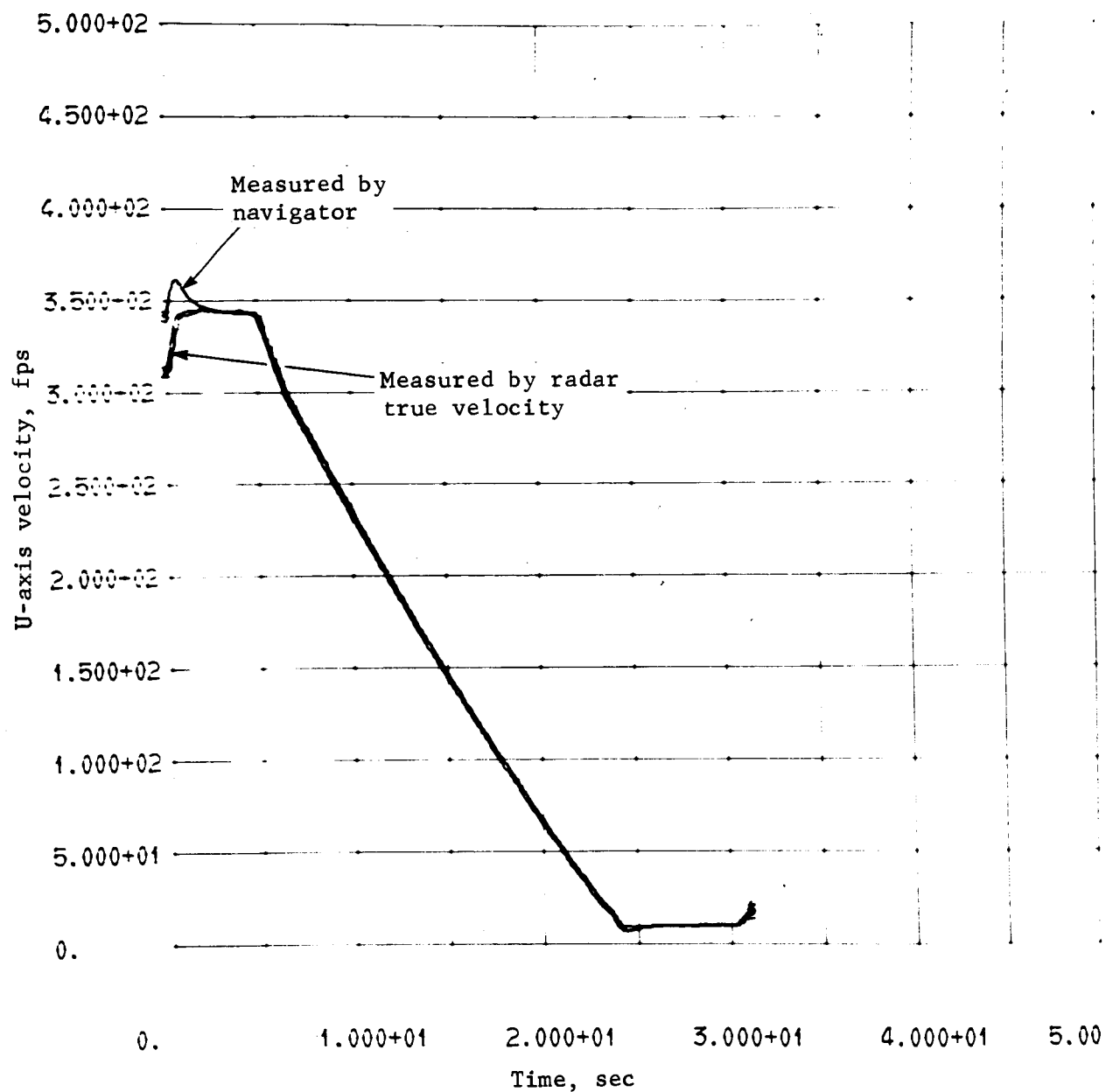
(b) U-Axis Velocity vs Time
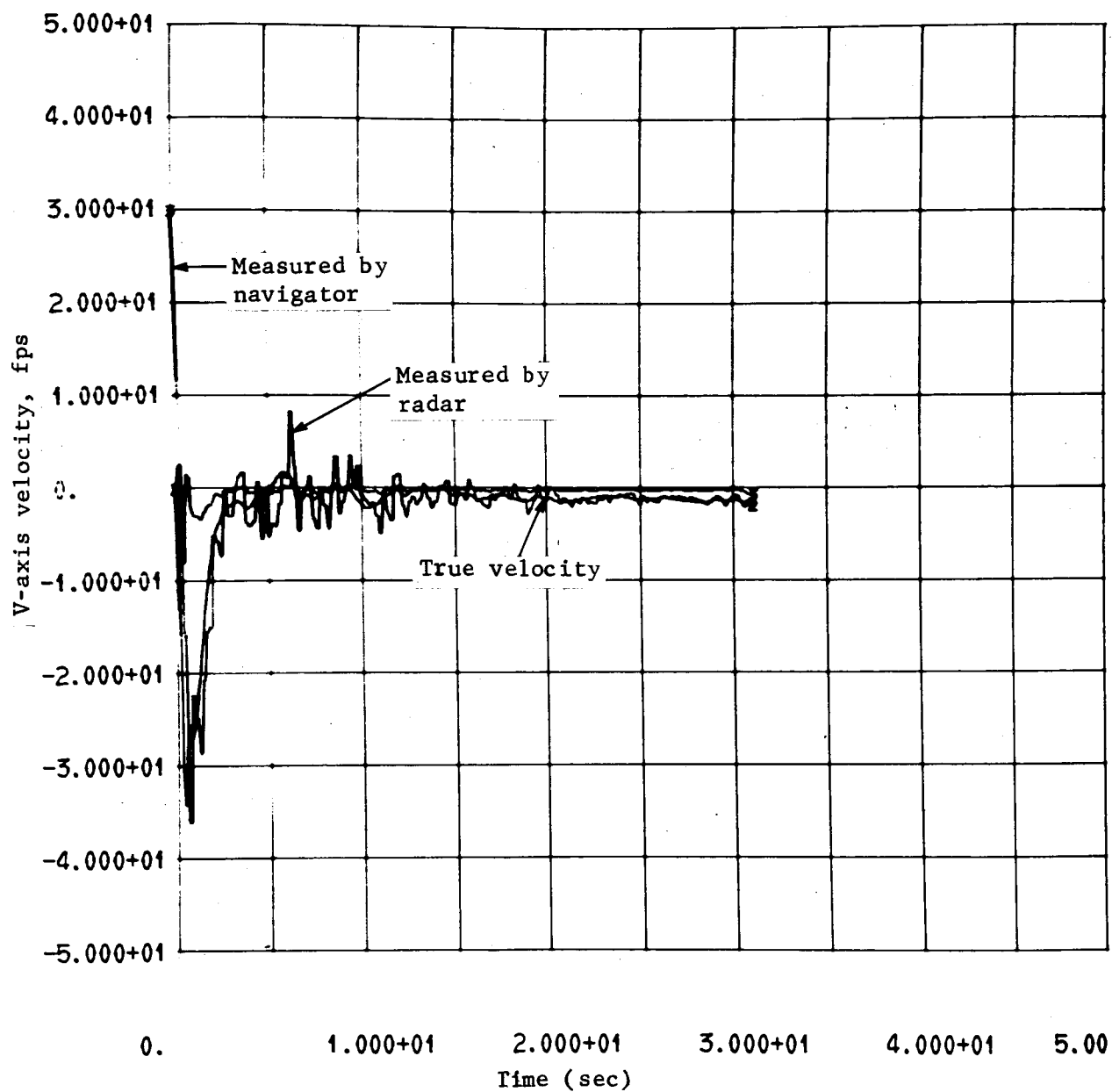
Figure 9.- Continued

(c) V-Axis Velocity vs Time
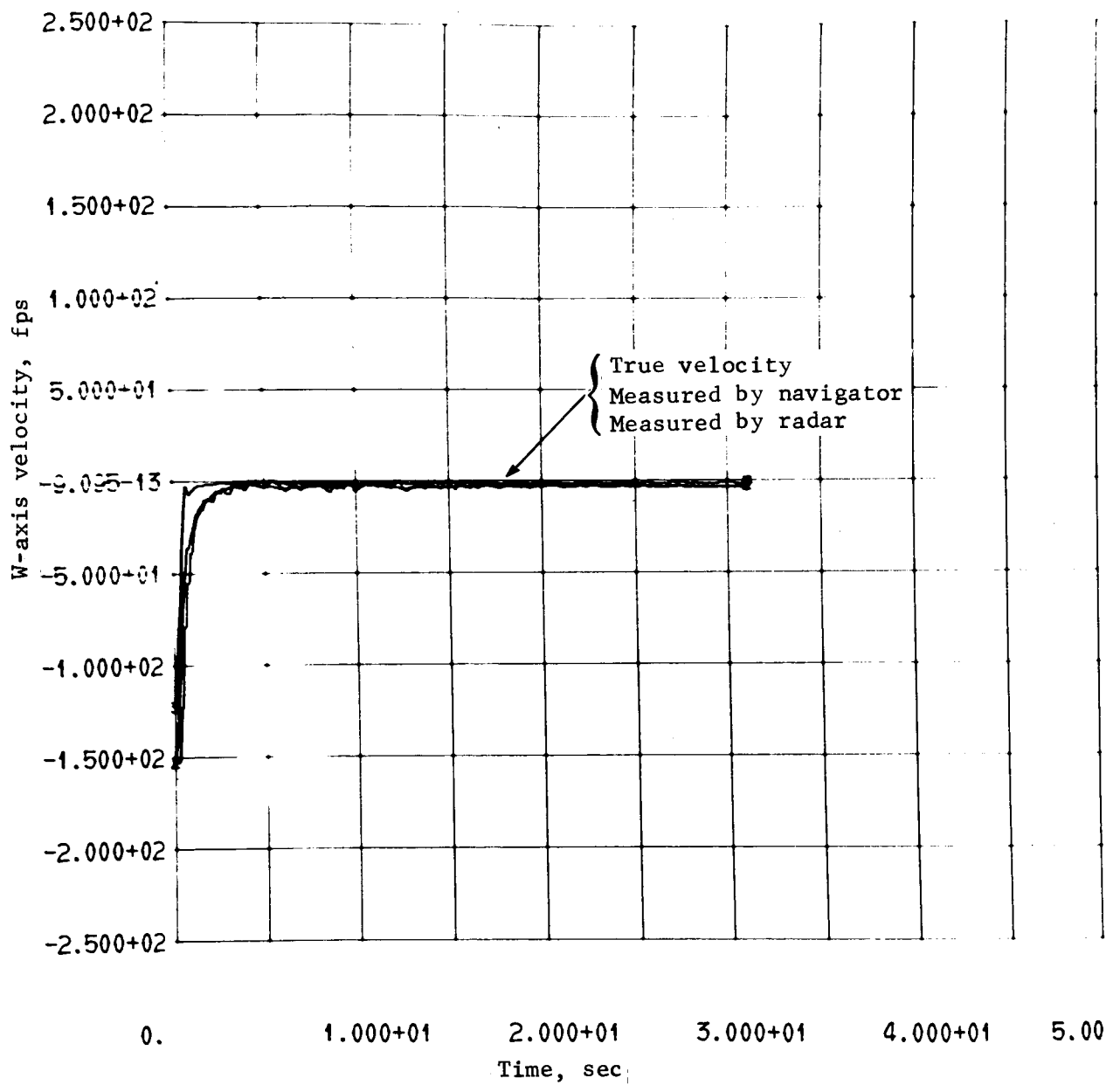
Figure 9.- Continued

(d) W-Axis Velocity vs Time
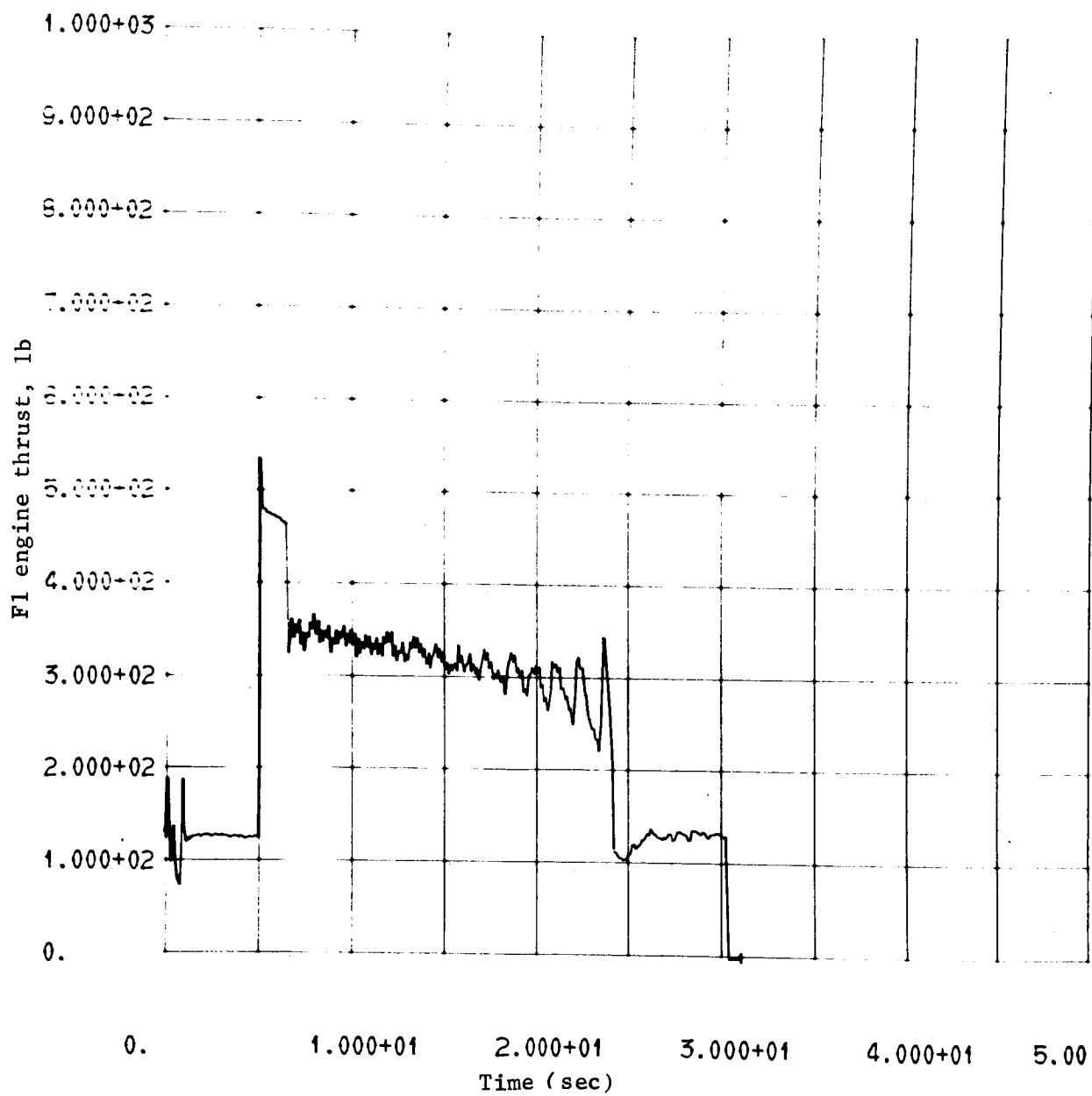
Figure 9.- Continued

(e) F1 Engine Thrust vs Time

Figure 9.- Continued
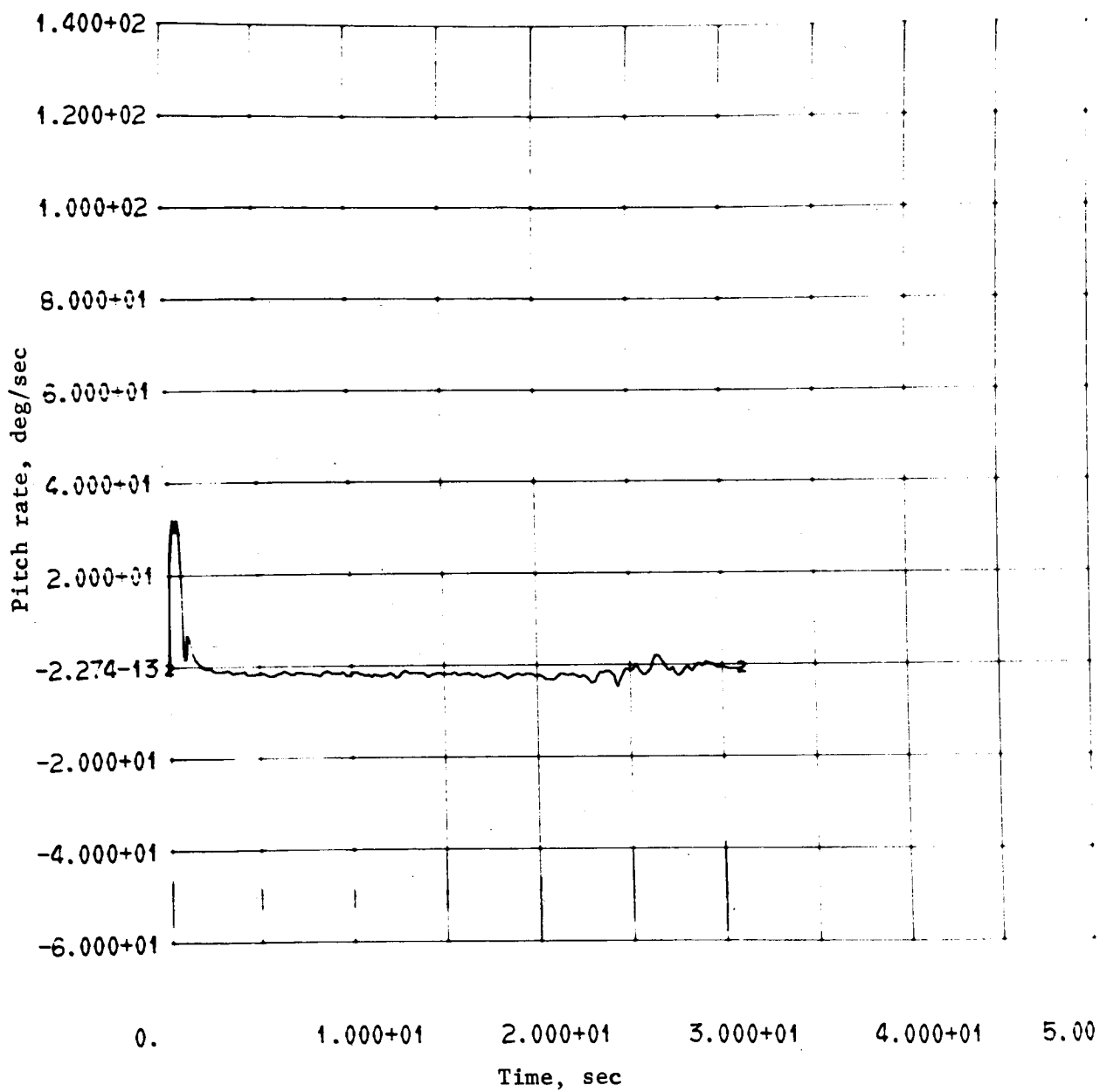
(f) Pitch Rate vs Time
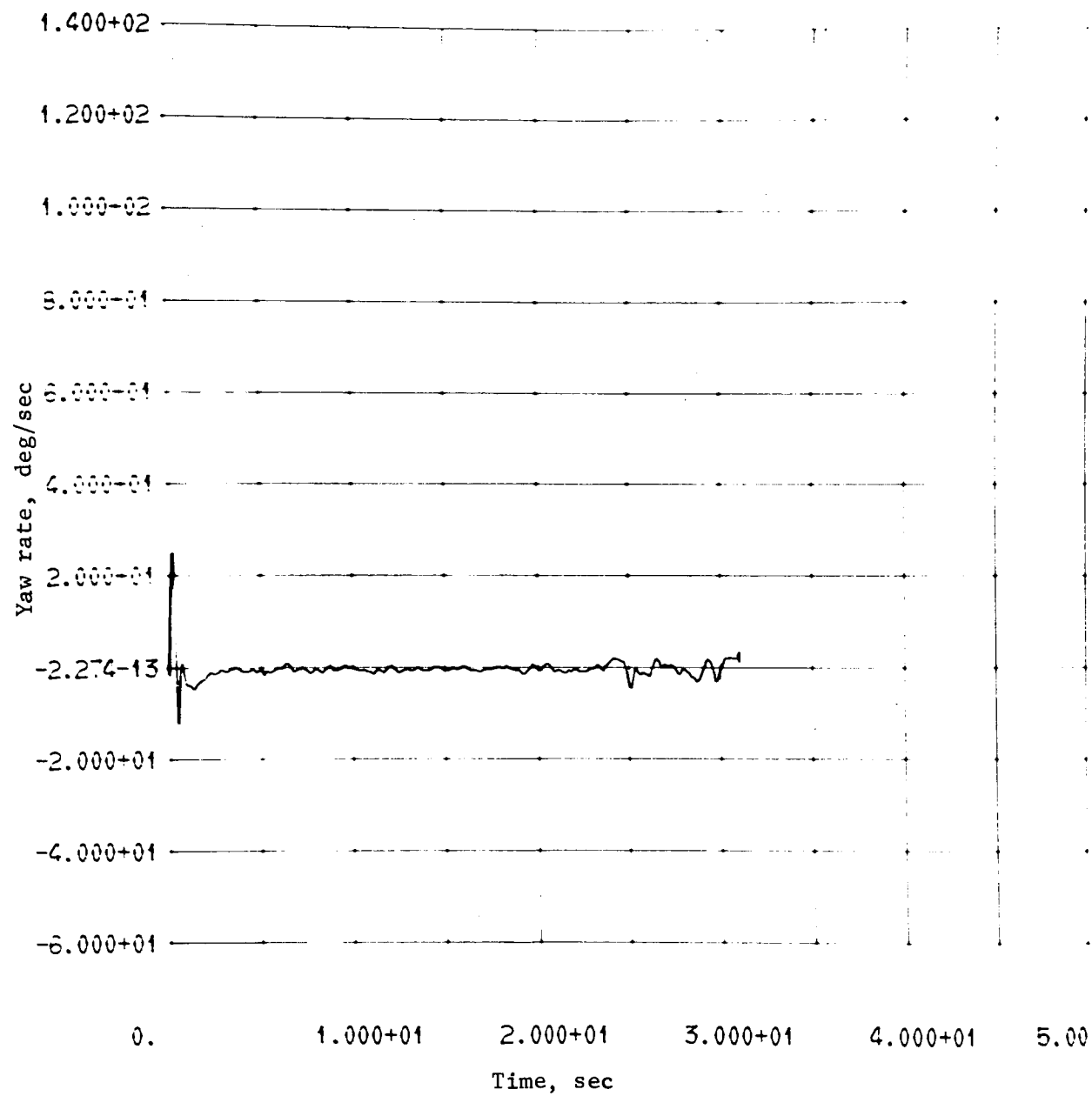
Figure 9.- Continued

(g)   Yaw Rate vs Time
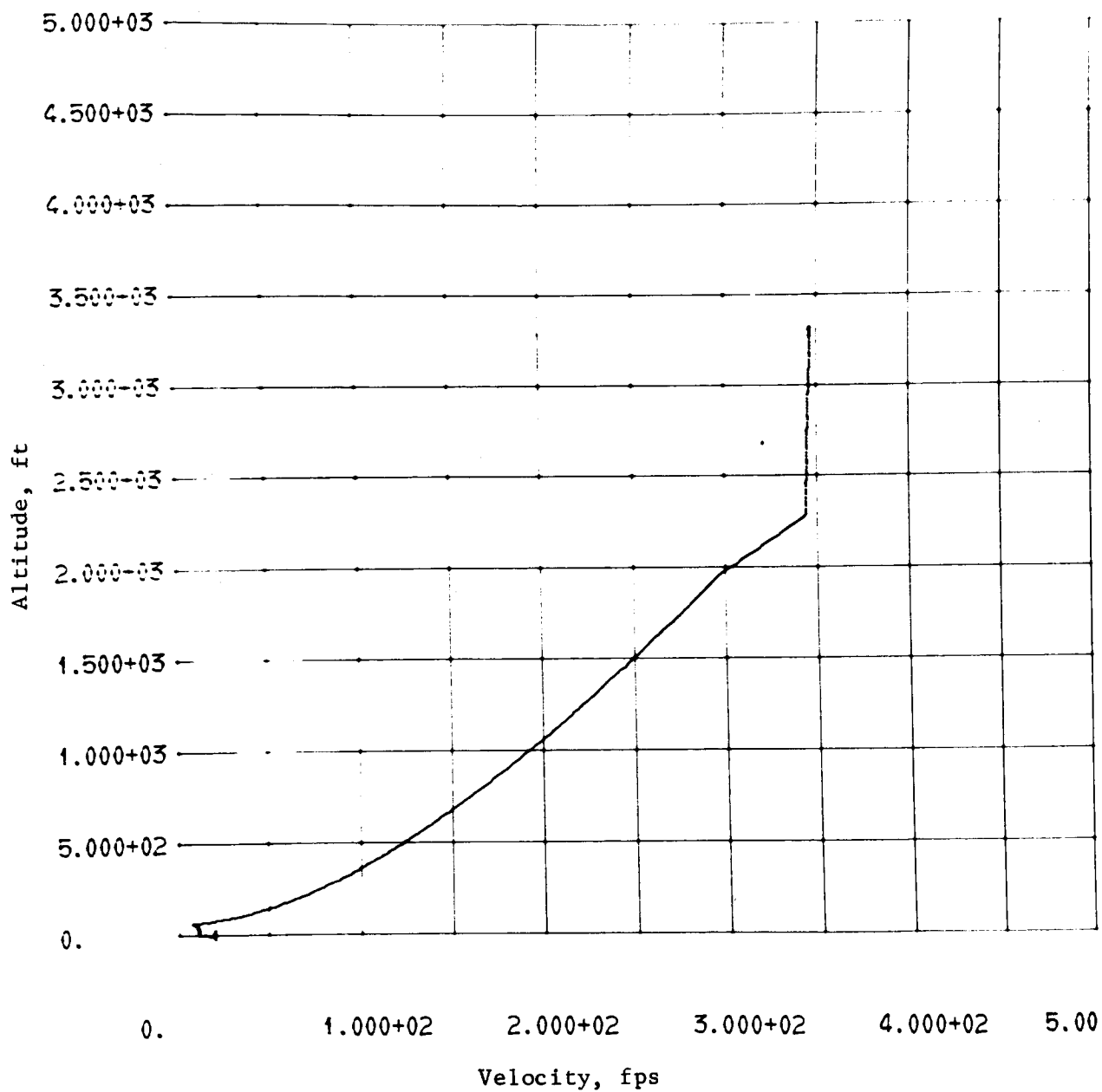
Figure 9.- Continued

(h) Altitude vs Velocity

Figure 9.- Concluded
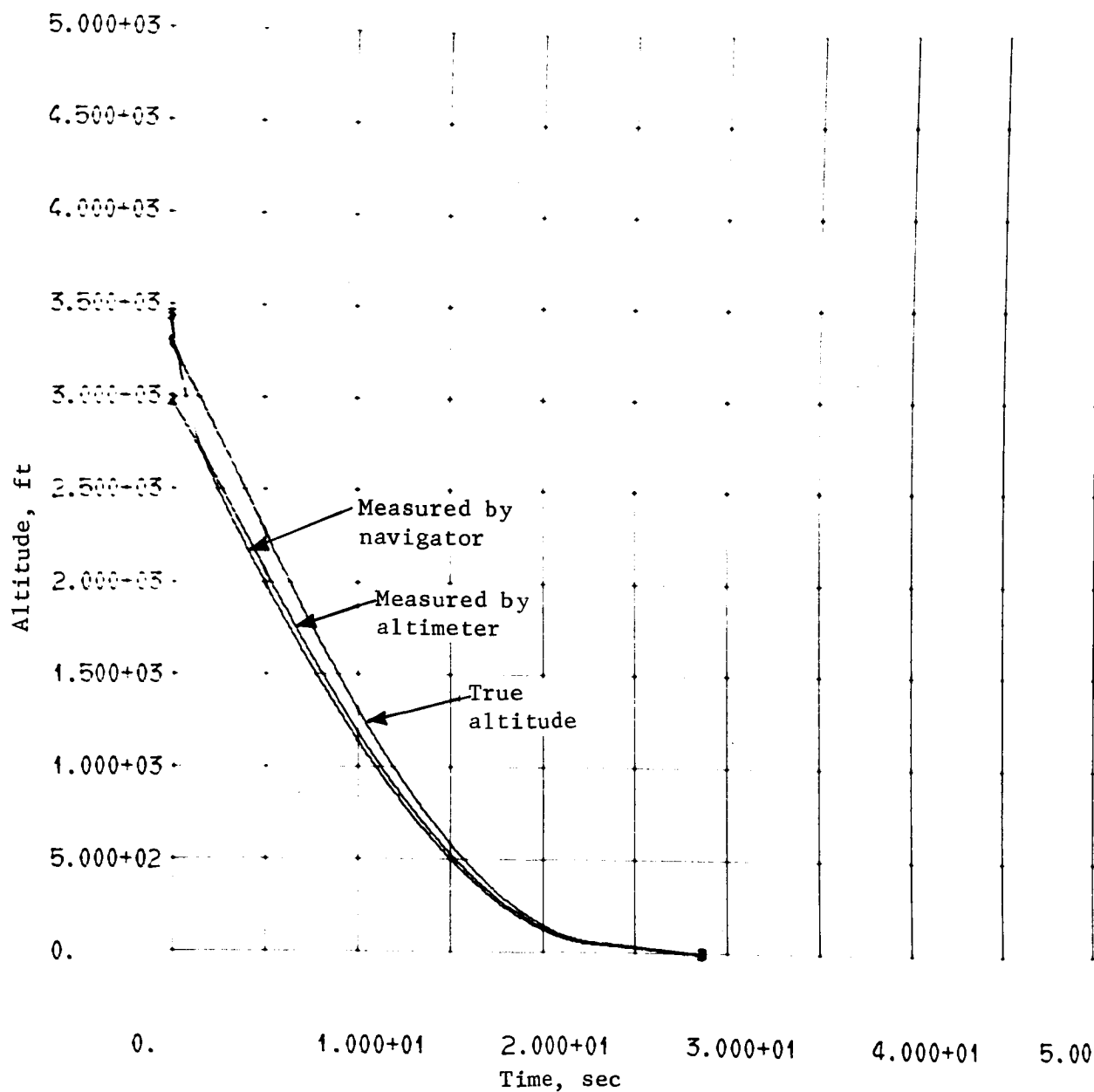
(a) Altitude vs Time

Figure 10.- 6DOF Simulation Results; System Operating in Radar Prime Mode with Inertial Backup
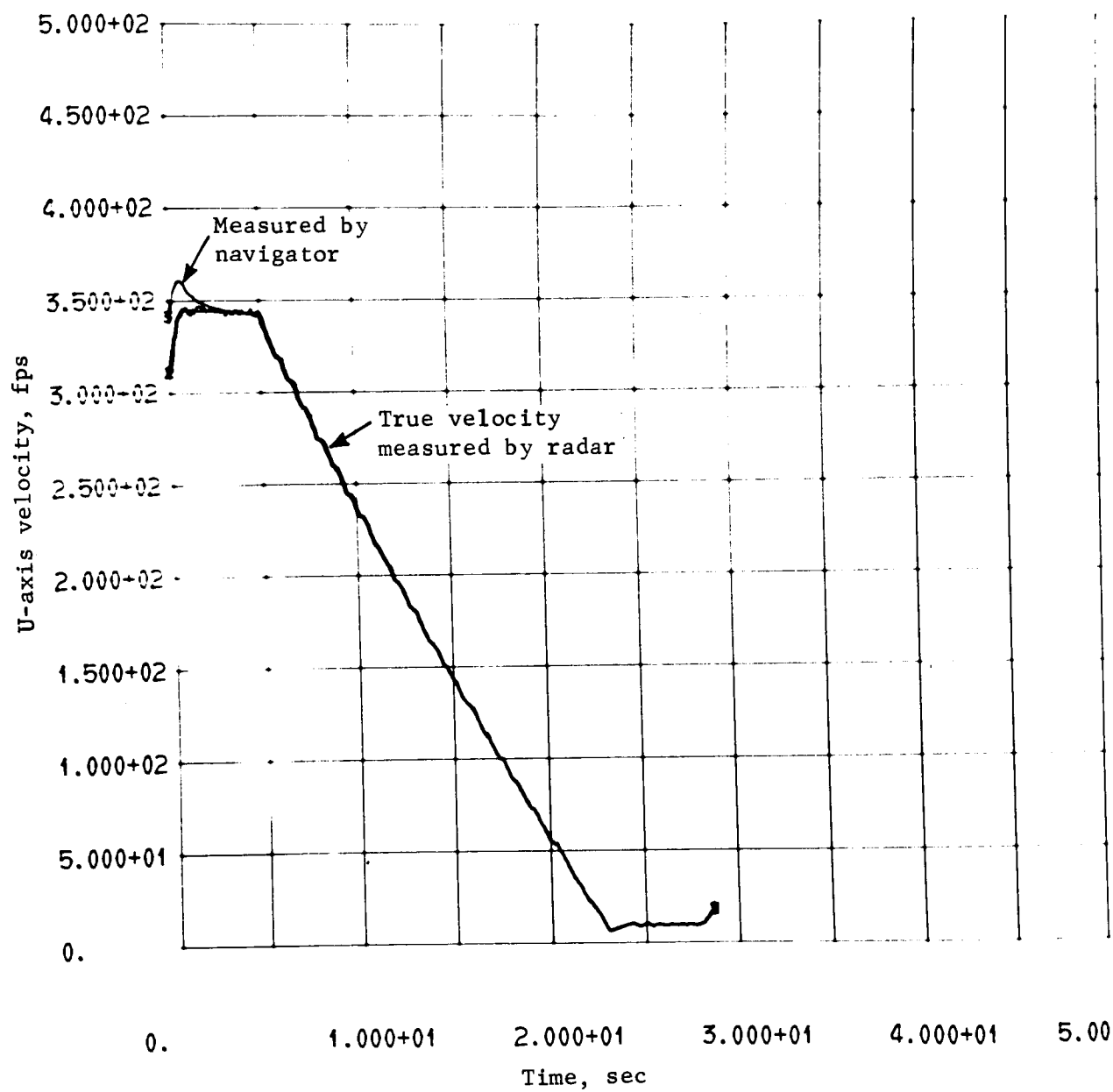
(b) U-Axis Velocity vs Time

Figure 10.- Continued
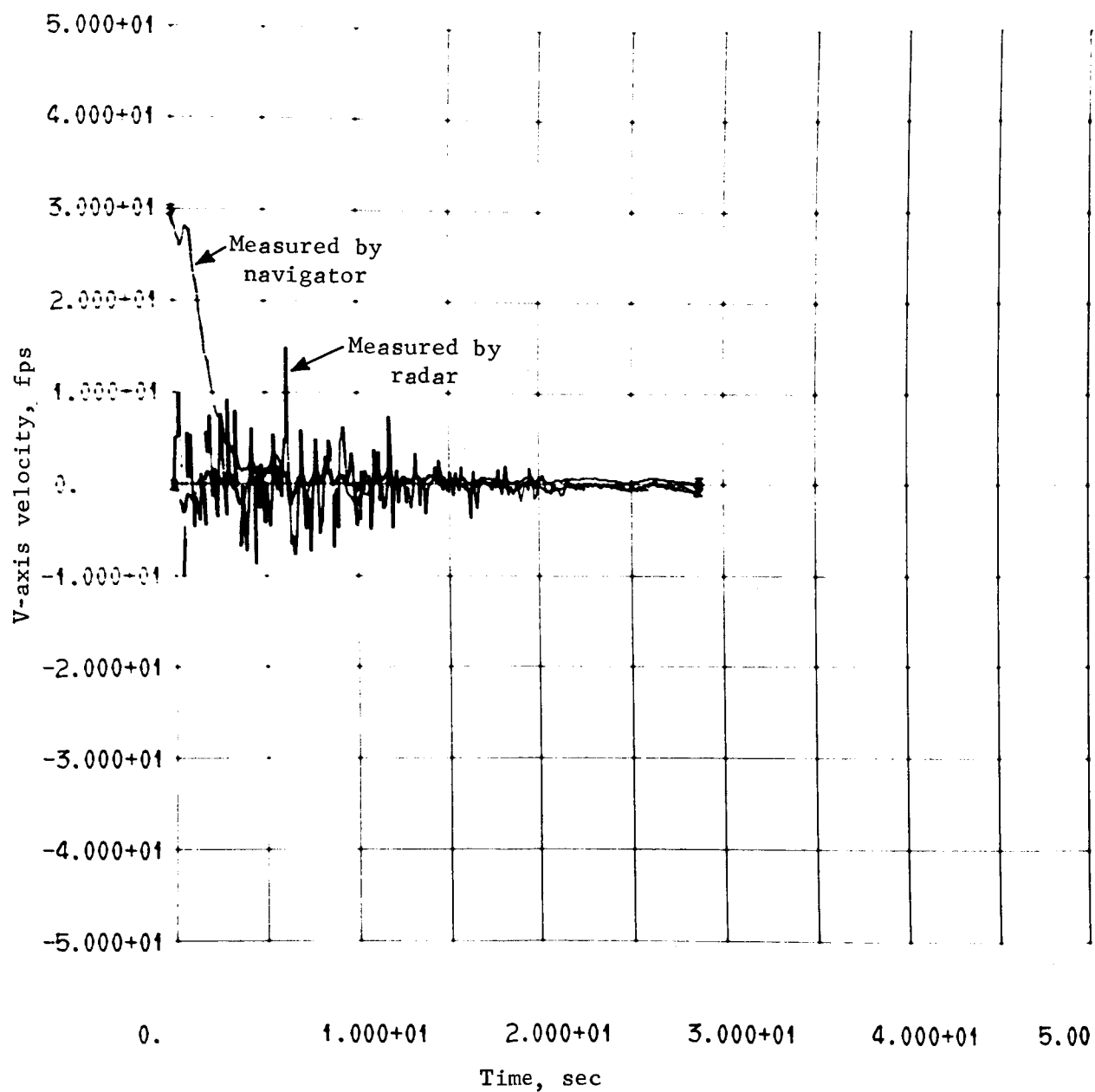
(c) V-Axis Velocity vs Time

Figure 10.- Continued
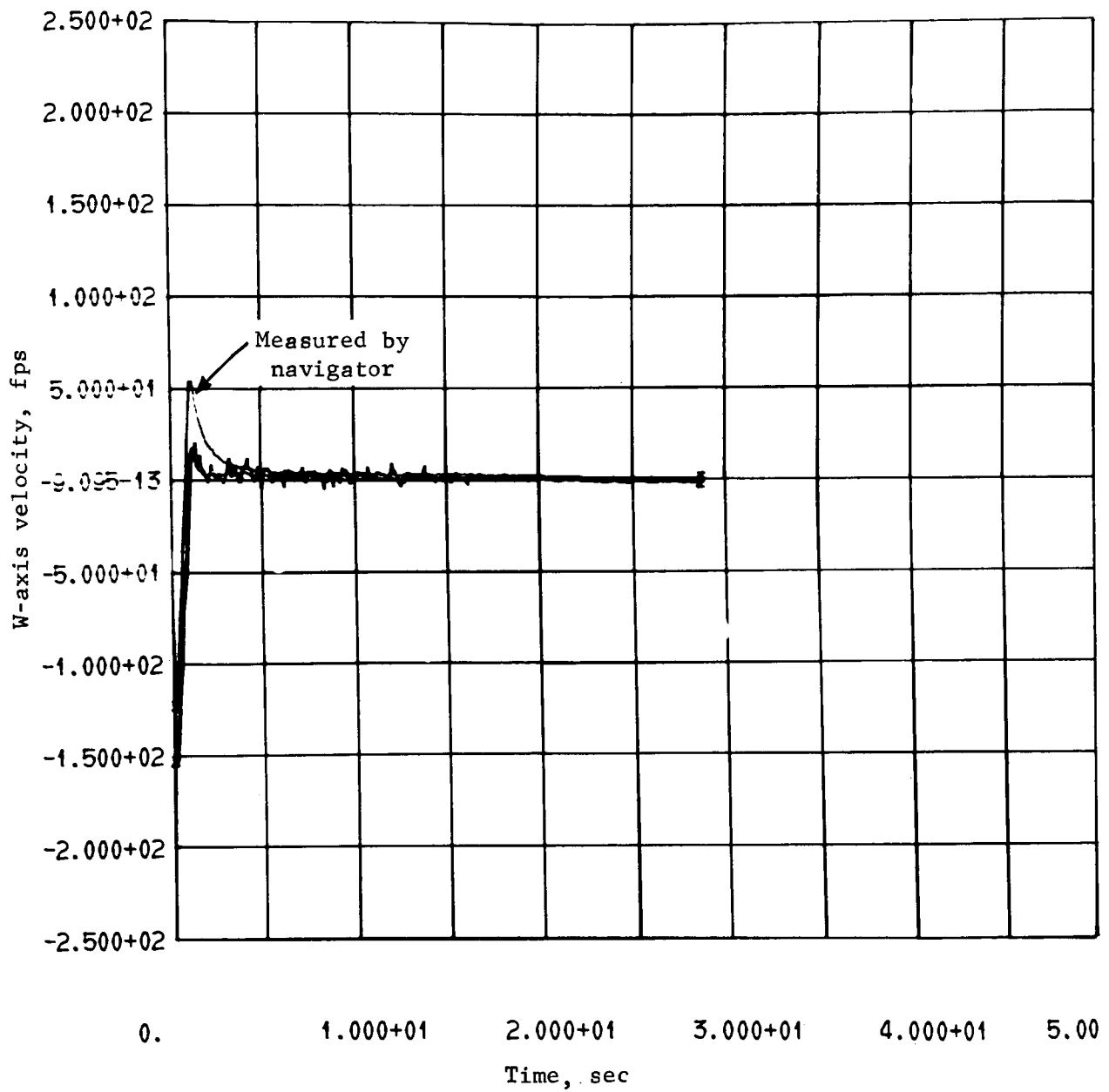
(d) W-Axis Velocity vs Time

Figure 10.- Continued
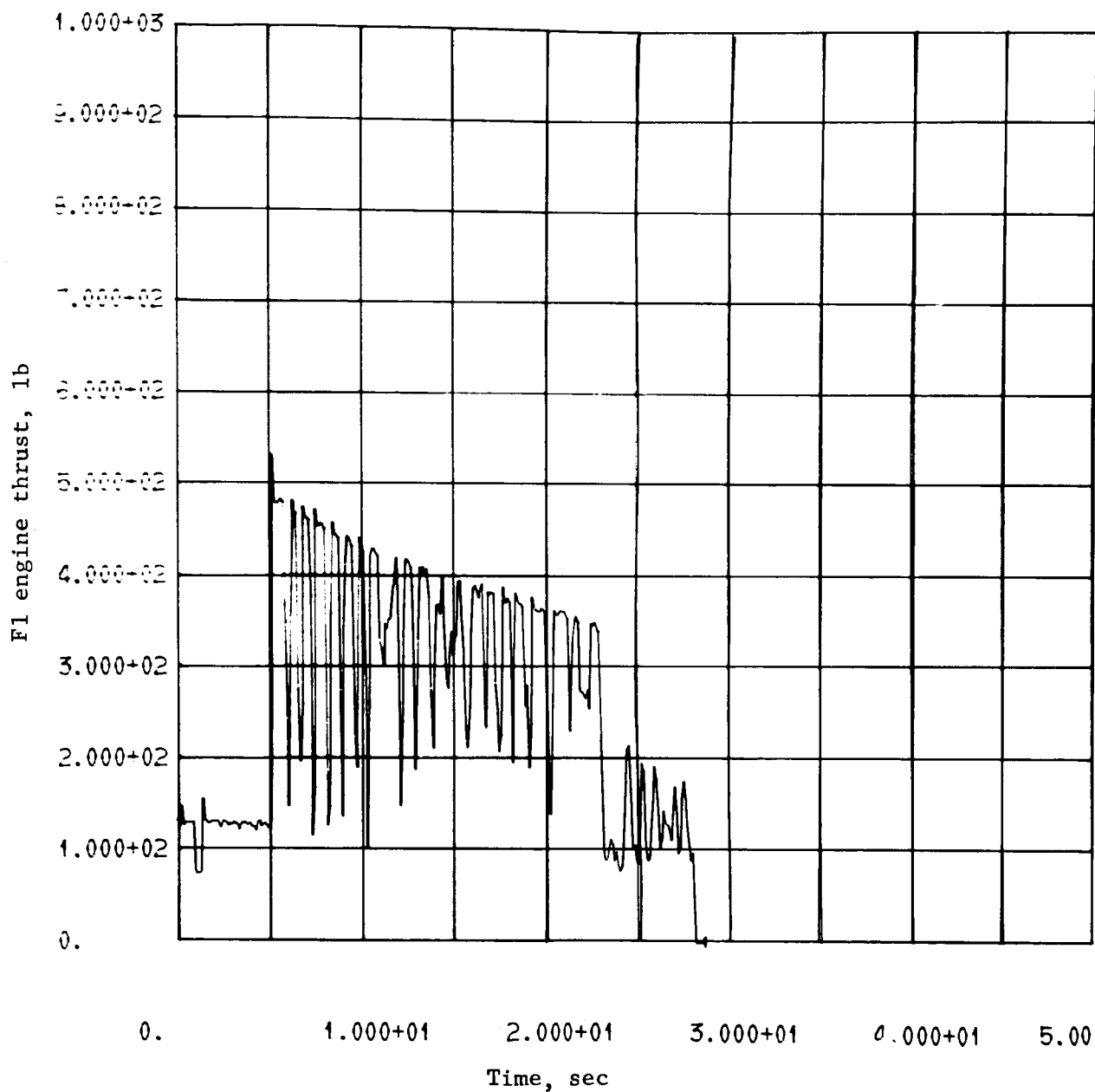
(e) F1 Engine Thrust vs Time

Figure 10.- Continued
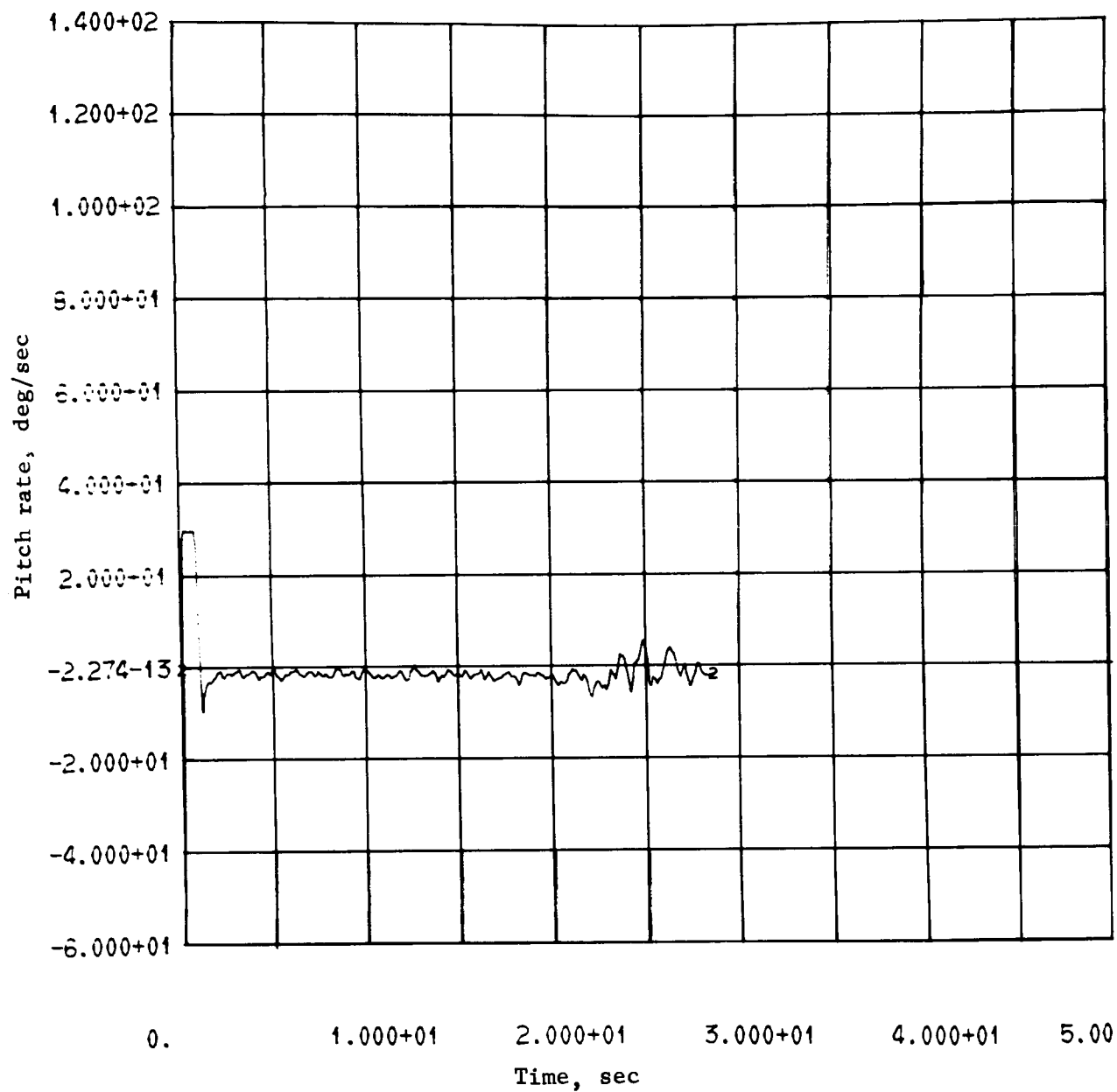
(f) Pitch Rate vs Time

Figure 10.- Continued
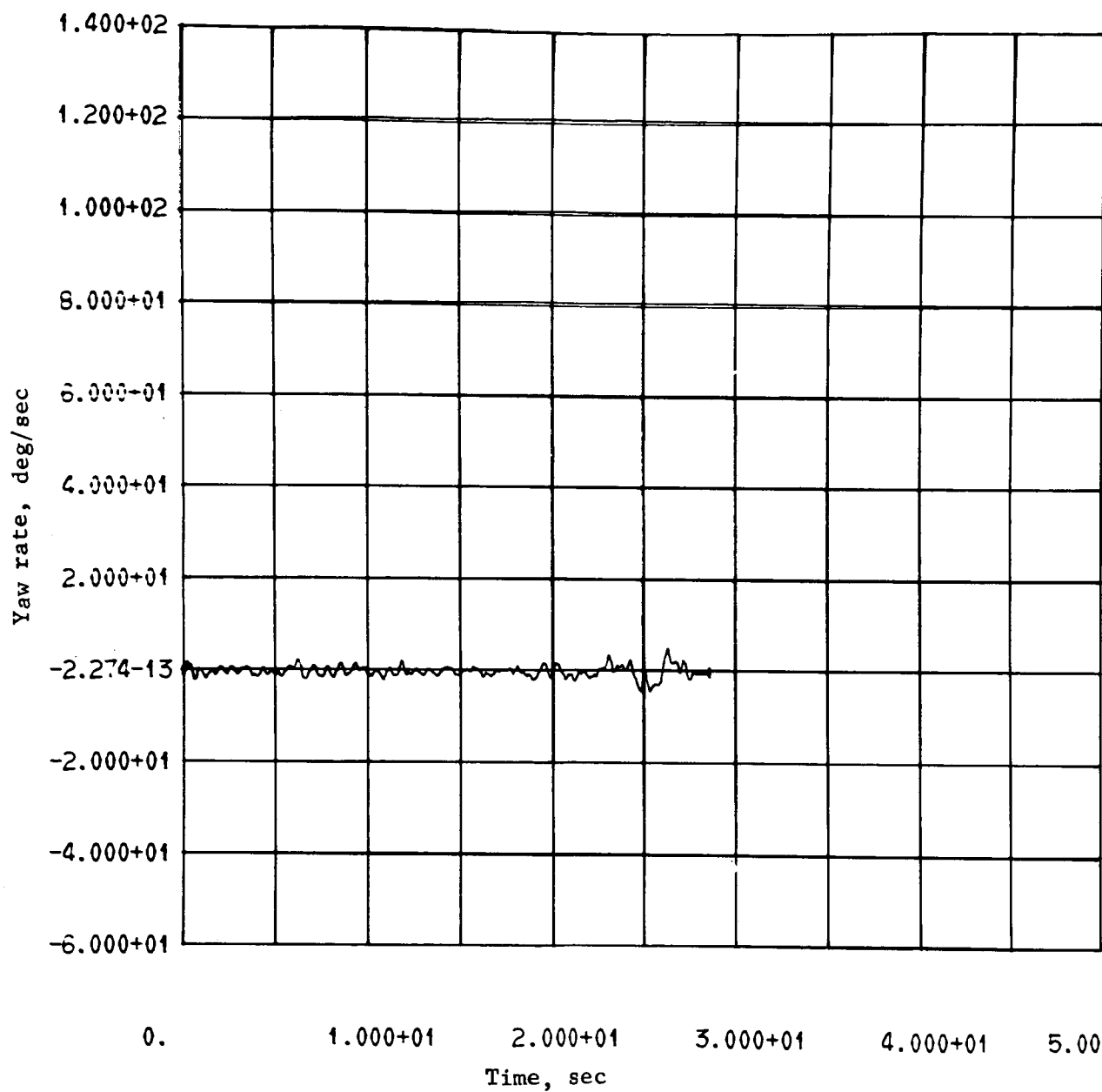
(g) Yaw Rate vs Time

Figure 10. - Continued
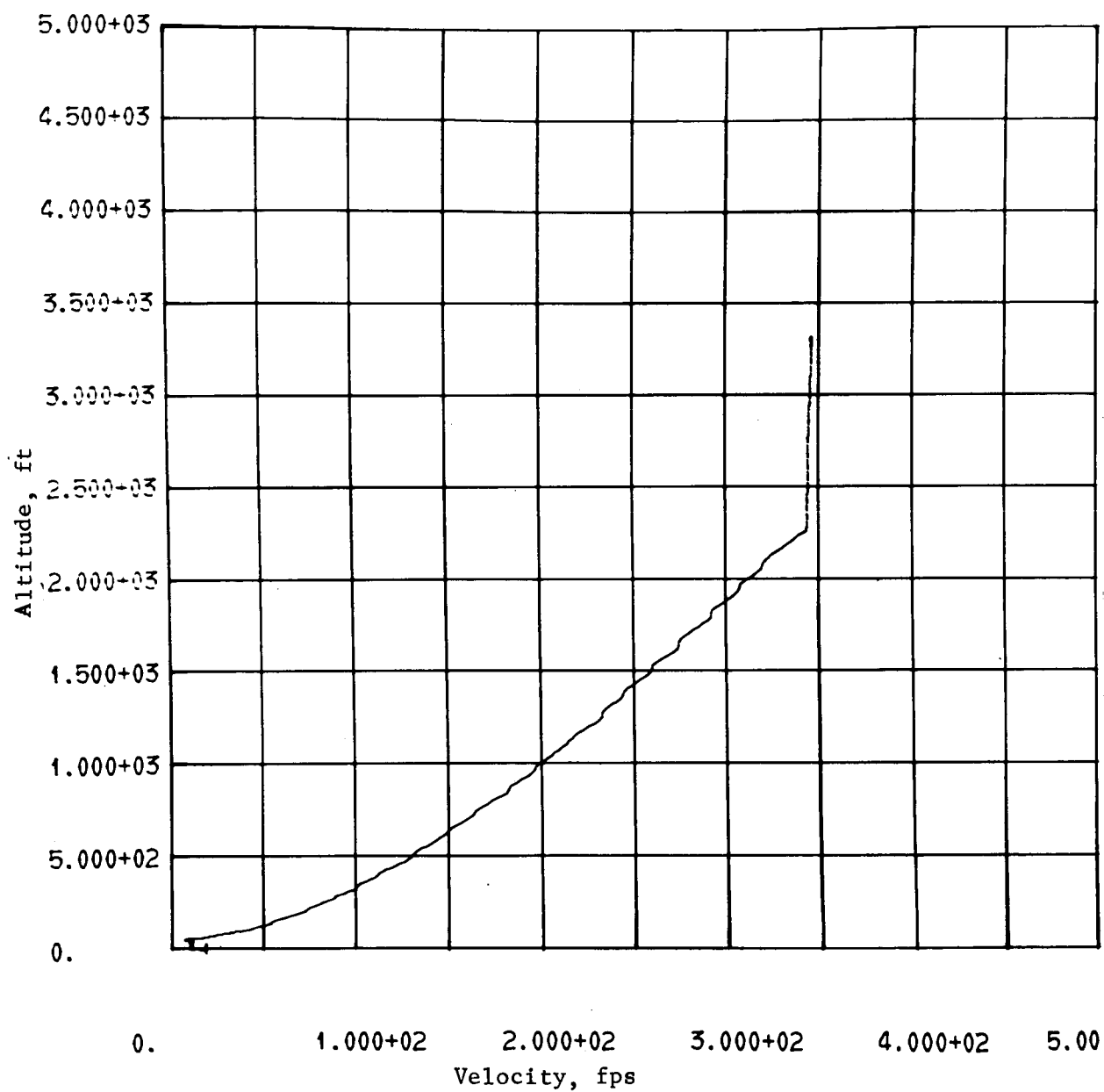
(h) Altitude vs Velocity

Figure 10.- Continued

A second alternative mechanization which we have considered involves using slant range of the radar instead of a broadbeam altimeter measurement for descent-contour guidance and for initiating the terminal-descent phase. As far as descent-contour guidance is concerned, it makes little difference whether we use range or altitude, although a single range beam is somewhat more sensitive to surface-slope variations than the altimeter measurement. Figure 11 shows 6DOF simulation results for a radar-aided inertial system using range measurements.

In this simulation, the Lander did not land successfully. Instead, because of the surface slope, the range had a large positive error. As a result, the Lander did not follow the descent contour during the early stages of the descent, and the thrust-to-weight ratio of the vehicle would have had to be increased for the vehicle to land successfully.

C. Inertial Navigator Analysis

Two methods of mechanizing the inertial navigator have been investigated. The first method, given by equations (5) thru (10), was based on a straight-forward solution of the vehicle translation equations of motion in the rotating-body-axis coordinate system. The errors in the outputs of the inertial system are then controlled by comparing them to the radar outputs and feeding back the differences through gains (Ku, Kv, etc) that are selected via simulation and a control stability analysis. The solution of equations (5) thru (10) requires three elements of a direction cosine matrix A, which relates the vehicle-body-axis coordinate system to the local vertical. This matrix solution is mechanized in the vehicle's digital computer by integrating the following equations:

$$\dot{A}_{11} = (A_{21} \cdot r) - (A_{31} \cdot q) \qquad (25)$$

$$\dot{A}_{12} = (A_{22} \cdot r) - (A_{32} \cdot q) \qquad (26)$$

$$\dot{A}_{13} = (A_{23} \cdot r) - (A_{33} \cdot q) \qquad (27)$$

$$\dot{A}_{21} = (A_{31} \cdot p) - (A_{11} \cdot r) \qquad (28)$$

$$\dot{A}_{22} = (A_{32} \cdot p) - (A_{12} \cdot r) \qquad (29)$$

$$\dot{A}_{23} = (A_{33} \cdot p) - (A_{13} \cdot r) \qquad (30)$$

$$\dot{A}_{31} = (A_{11} \cdot q) - (A_{21} \cdot p) \qquad (31)$$

$$\dot{A}_{32} = (A_{12} \cdot q) - (A_{22} \cdot p) \qquad (32)$$

$$\dot{A}_{33} = (A_{13} \cdot q) - (A_{23} \cdot p) \qquad (33)$$
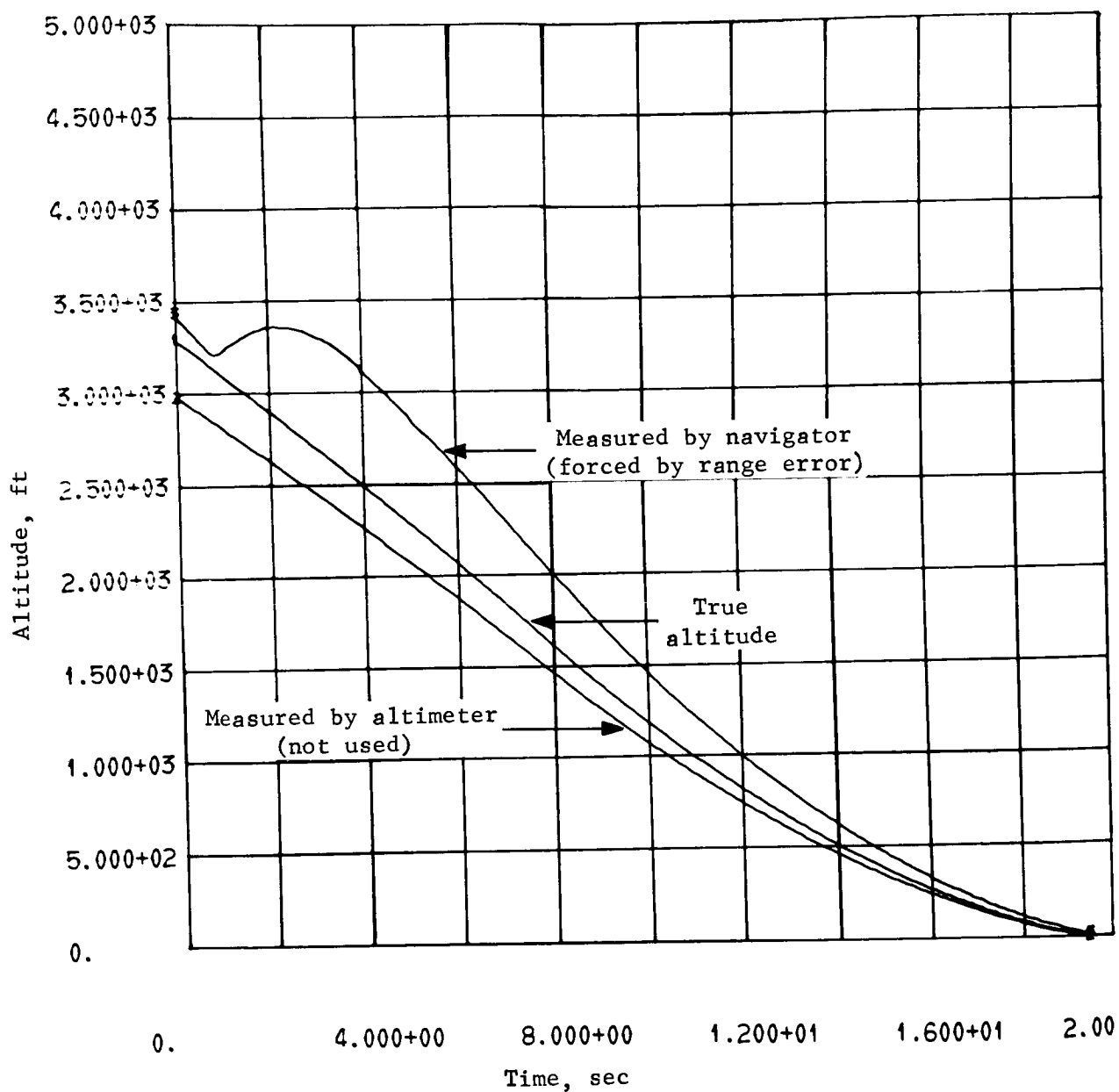
(a) Altitude vs Time

Figure 11.- 6DOF Simulation Results, System Operating in Radar-
Aided Inertial Mode Using Range Measurements
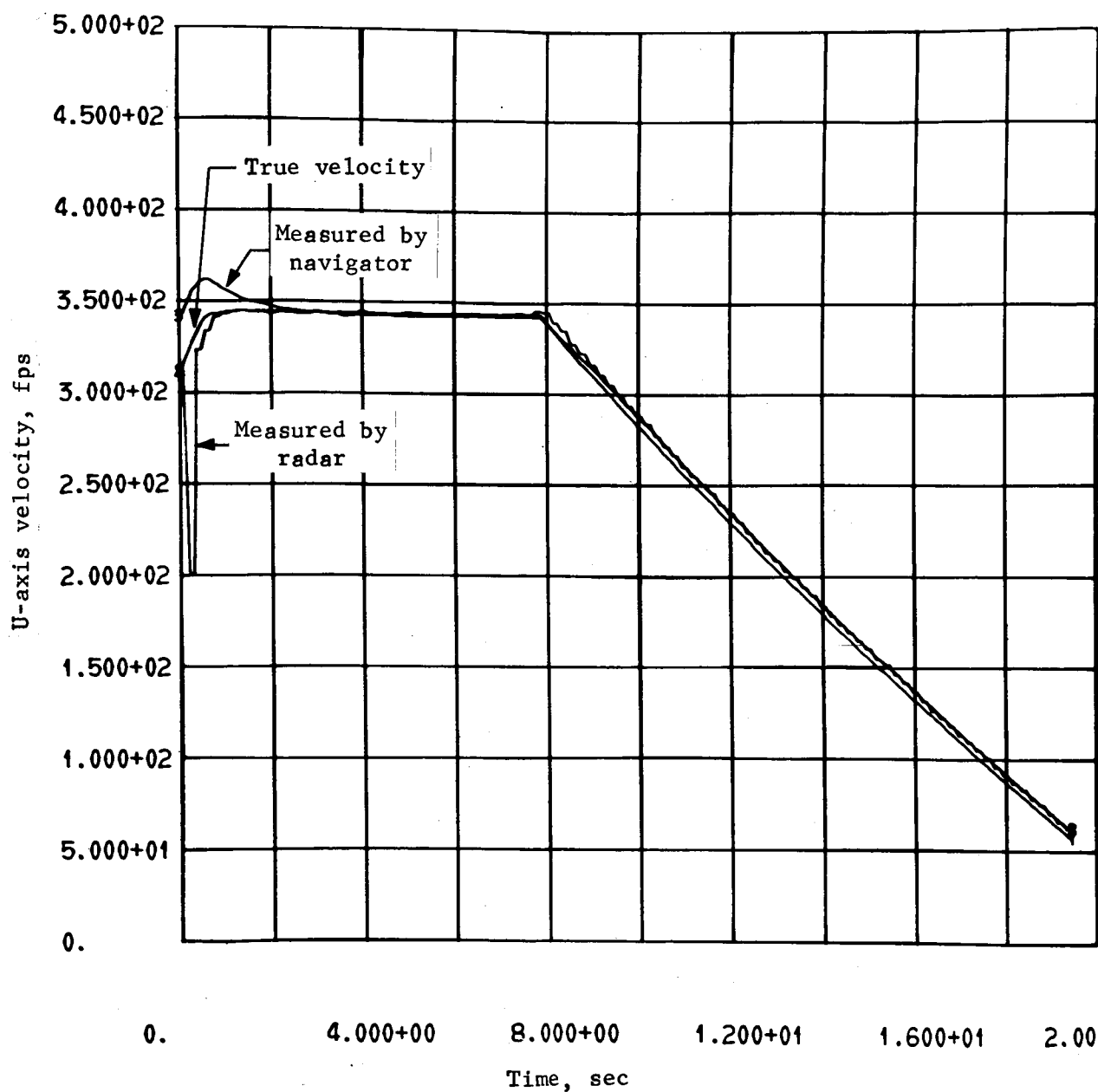
(b) U-Axis Velocity vs Time

Figure 11.- Continued
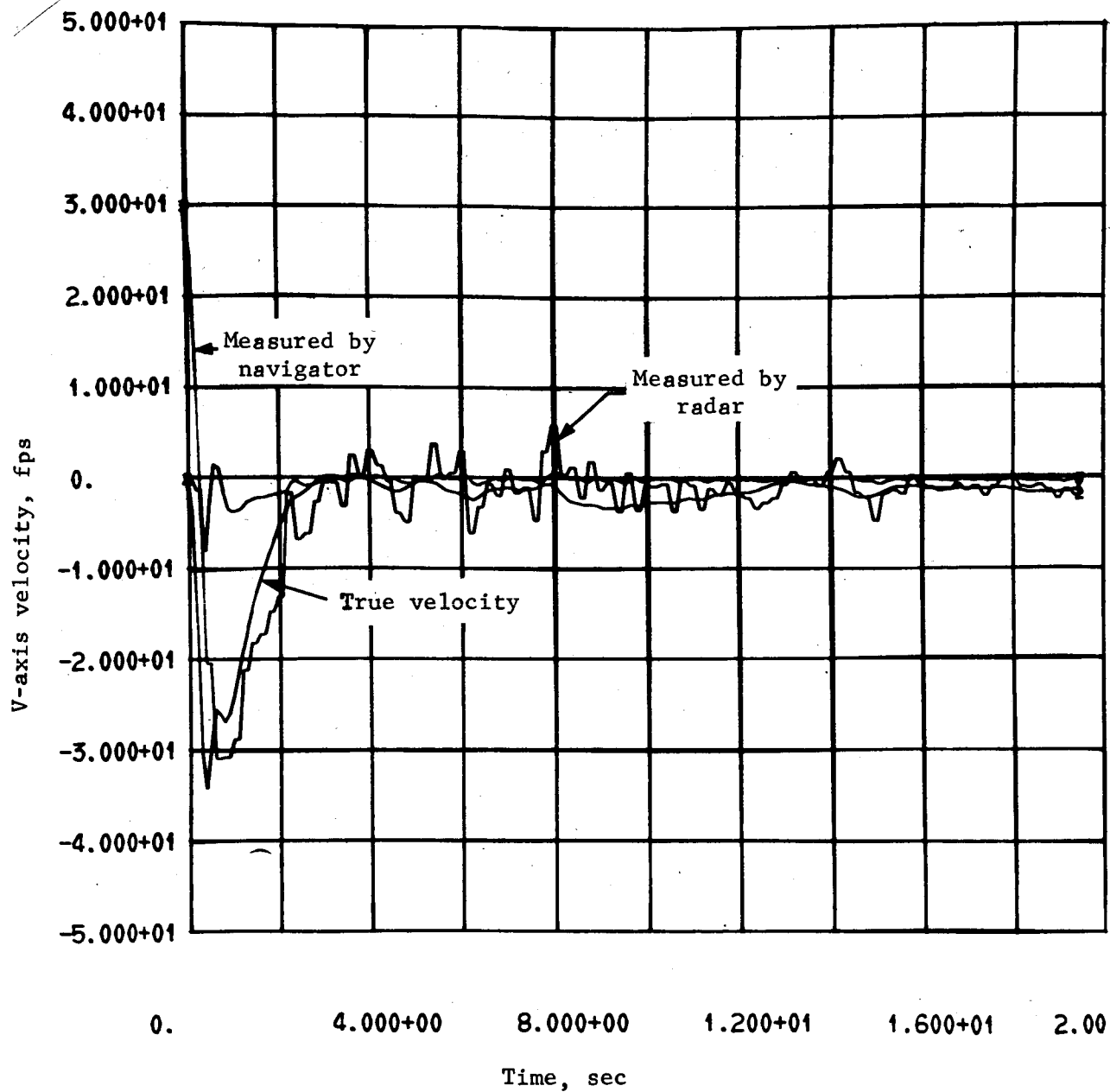
(c) V-Axis Velocity vs Time

Figure 11.- Continued

(d) W-Axis Velocity vs Time

Figure 11.- Continued

Y-axis: F1 engine thrust, lb

Y-axis labels: 5.500+02, 5.000+02, 4.500+02, 4.000-02, 3.500-02, 3.000-02, 2.500+02, 2.000+02, 1.500+02, 1.000+02, 5.000+01

Saturated at 90%

X-axis labels: 0.   4.000+00   8.000+00   1.200+01   1.600+01   2.00

Time, sec
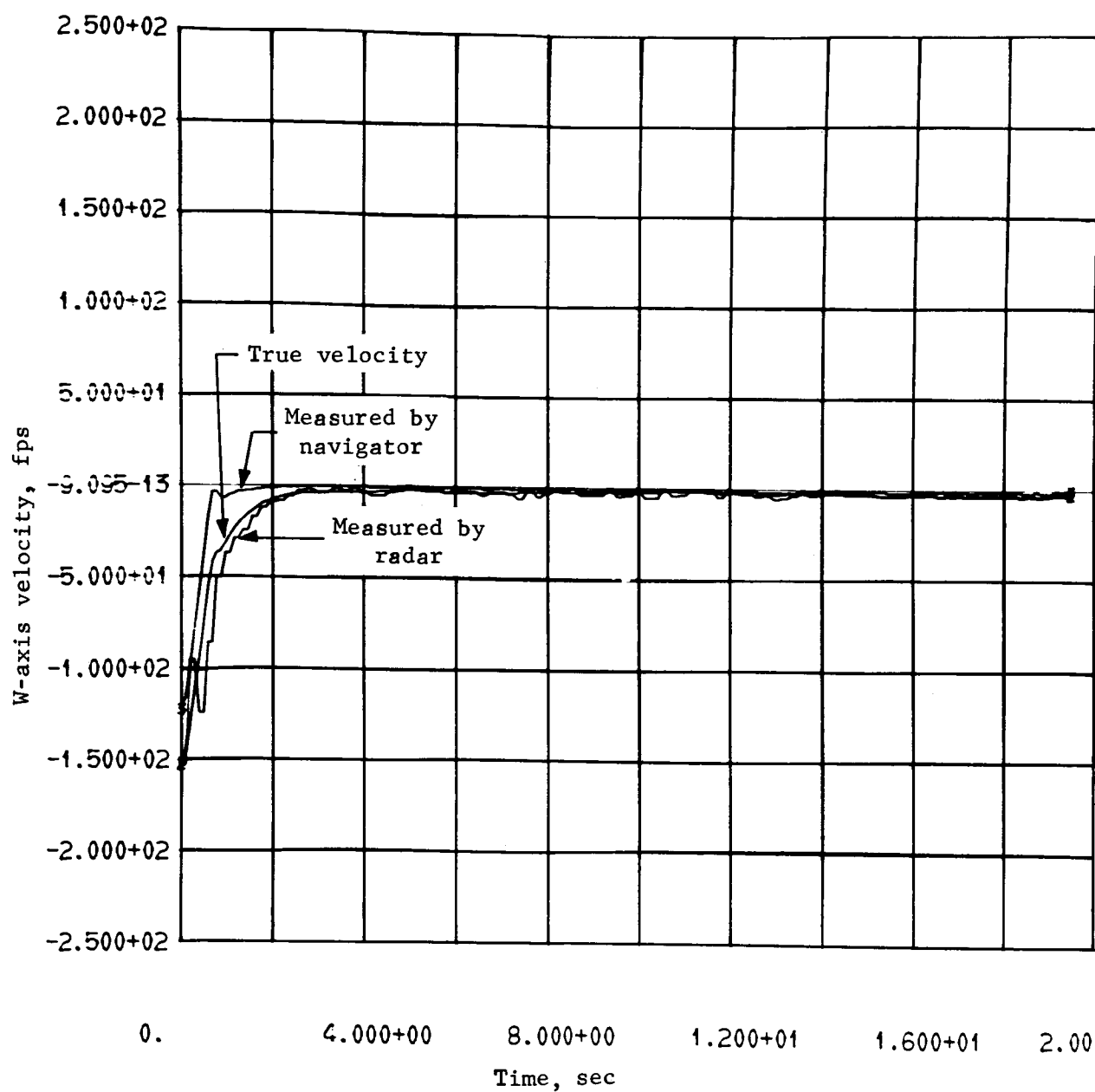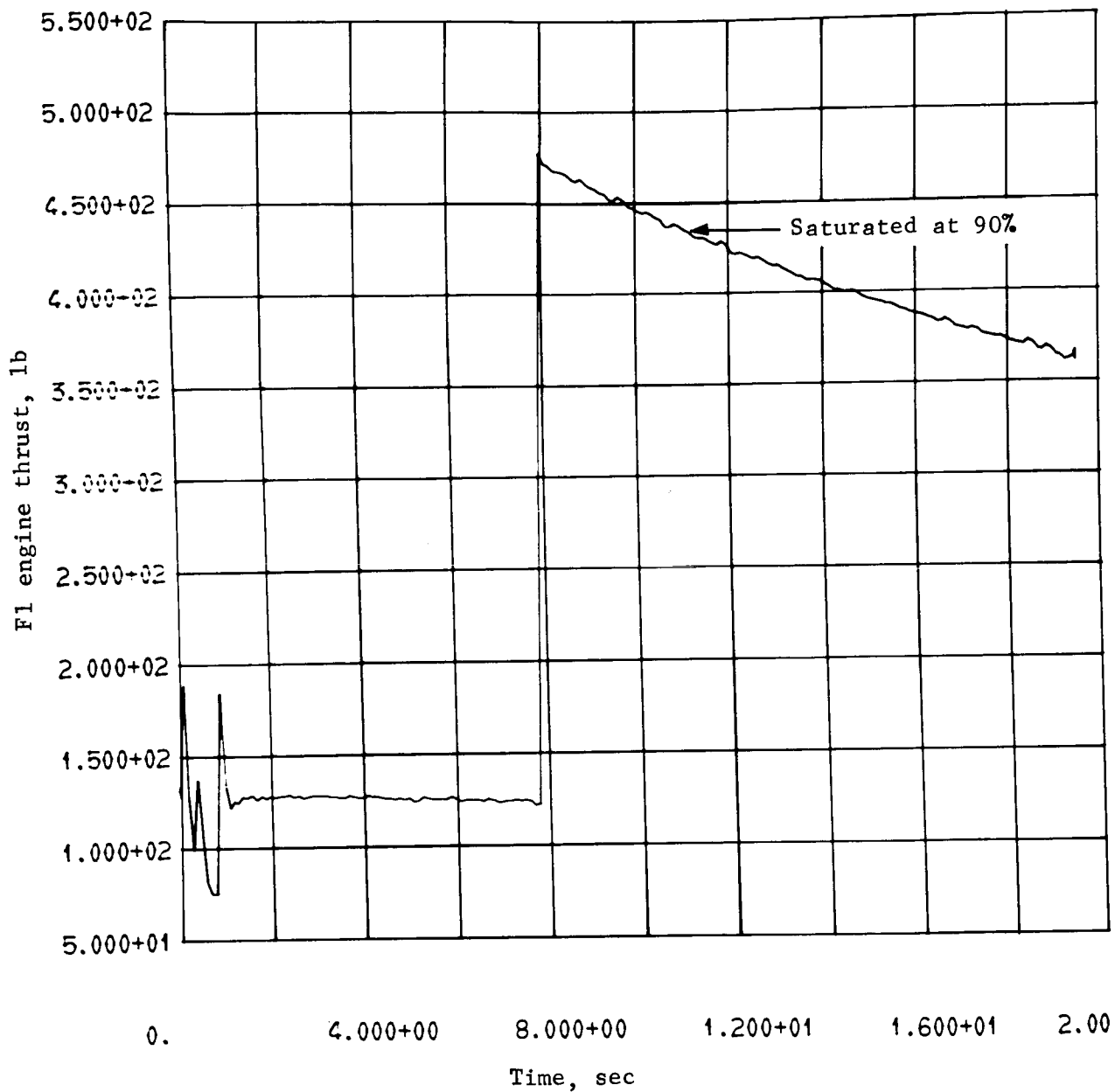
(e) F1 Engine Thrust vs Time

Figure 11.- Continued
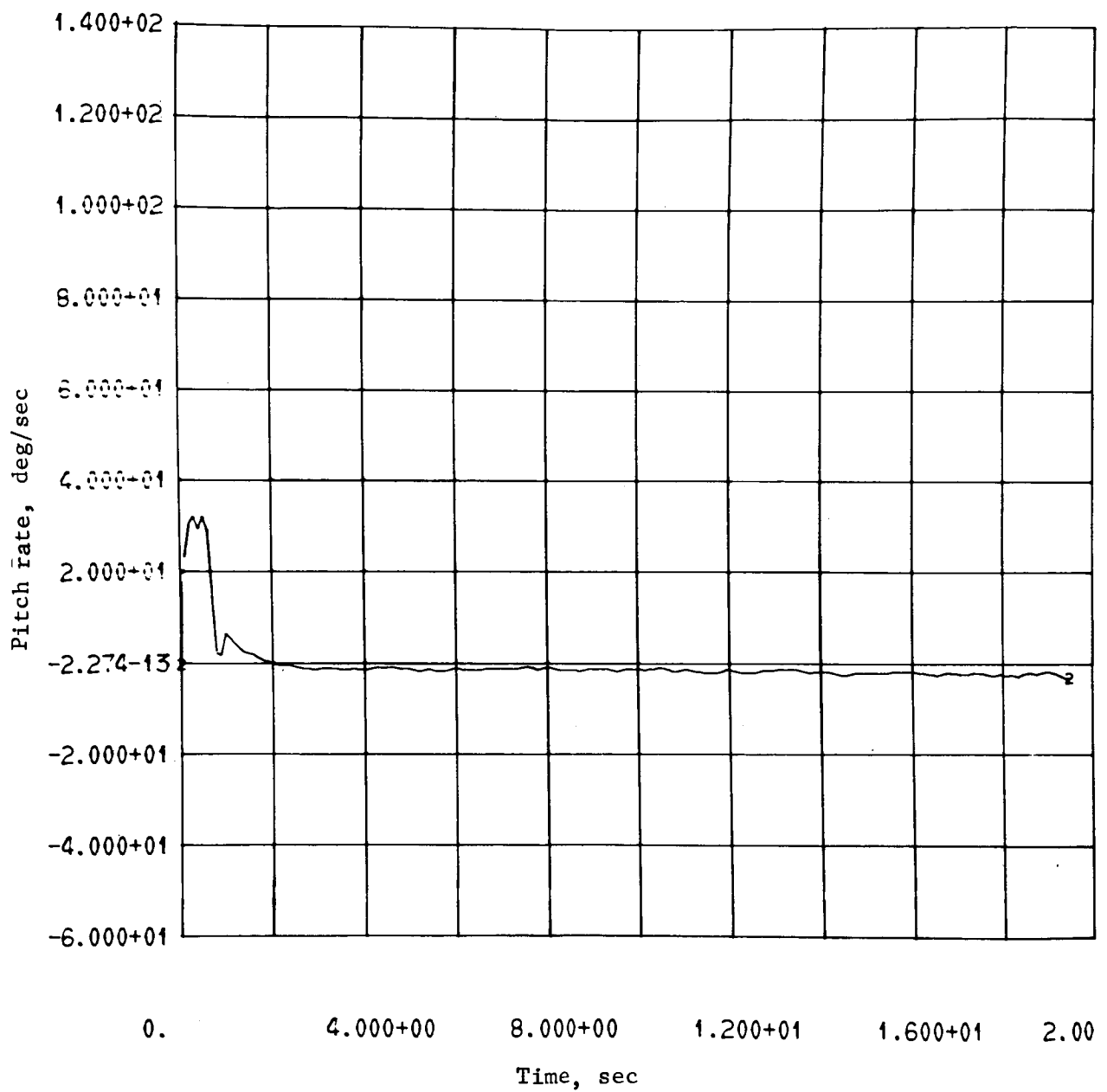
(f) Pitch Rate vs Time

Figure 11.- Continued
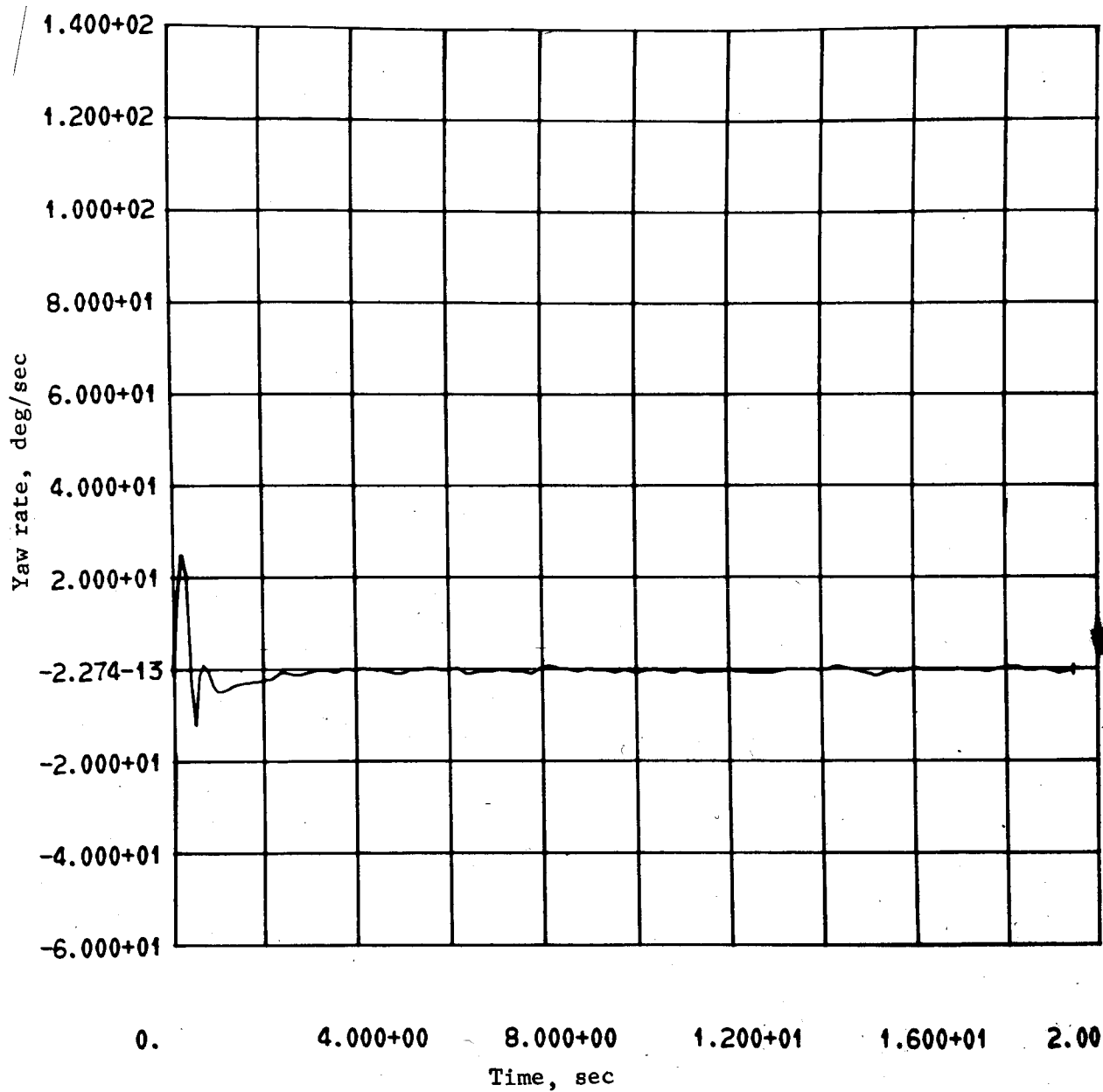
(g) Yaw Rate vs Time

Figure 11.- Continued
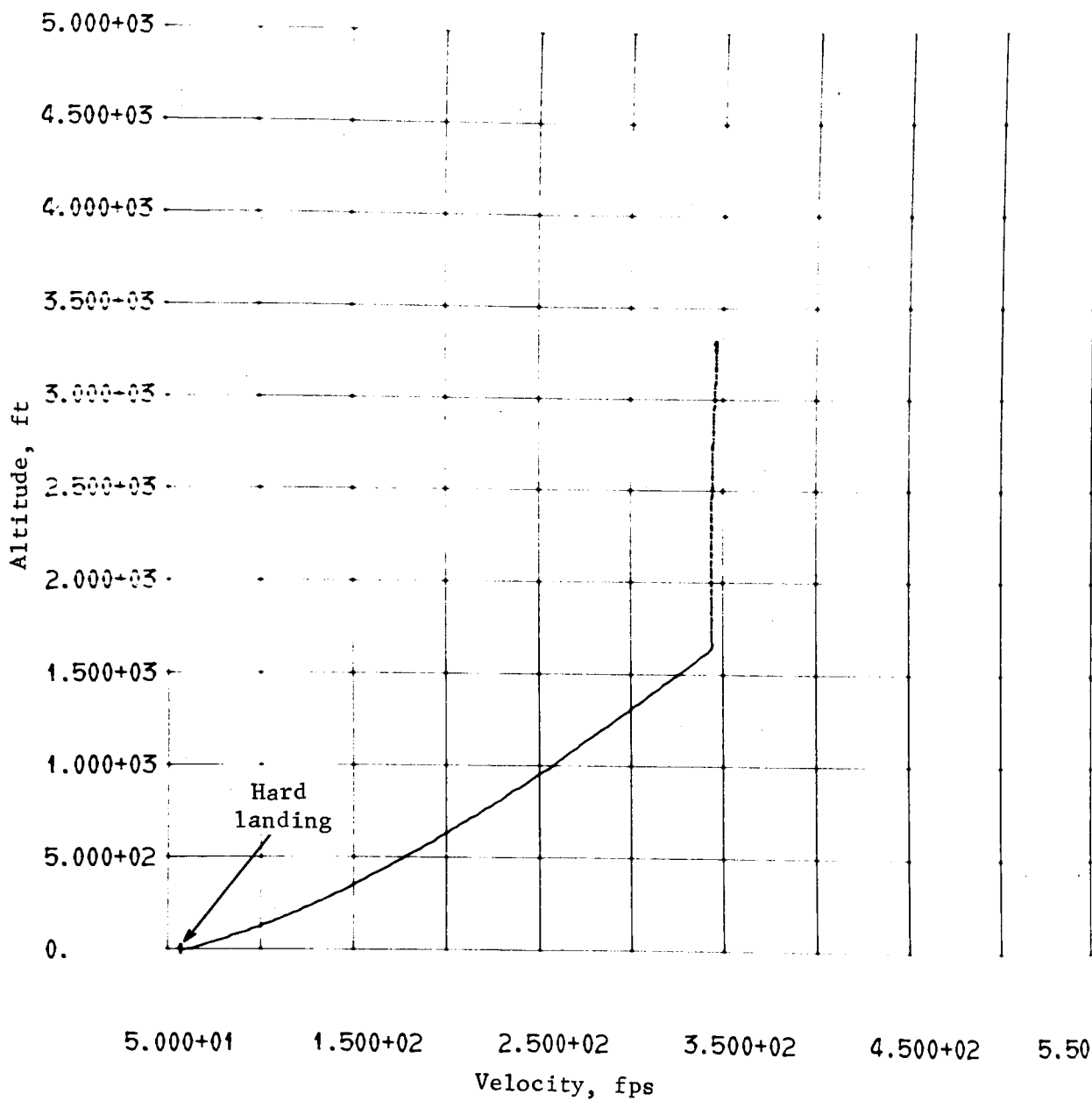
(h) Altitude vs Velocity

Figure 11.- Concluded

The transformation equation is then

$$\begin{bmatrix} X_b \\ Y_b \\ Z_b \end{bmatrix} = [A] \begin{bmatrix} X_I \\ Y_I \\ Z_I \end{bmatrix} \qquad (34)$$

where X_b, Y_b, and Z_b are the vehicle roll, pitch, and yaw axes, respectively, and X_I, Y_I, and Z_I are the local vertical coordinates $\left(Z_I \text{ points down}\right)$.

Though only A_{13}, A_{23}, and A_{33} are required in equations (5) thru (10), the digital computer will still be able to compute the entire A matrix. This is because equations (25 thru (33) must be solved during the deorbit phase to relate the body axes to the Sun-Canopus coordinate system of the orbiter. Thus, the A matrix computations must be reinitialized at some point so that they represent the transformation shown in equation (34).

A good choice for this point is near the maximum-deceleration point during the entry. At this point, the angle-of-attack oscillations will be negligible, so that vehicle's roll axis will lie along the velocity vector. Figure 12 shows the range of values that the flight path angle can have at maximum deceleration. γ_M is the angle the velocity vector makes with respect to the local horizontal. If the vehicle is targeted for an entry angle, γ_E, of 16 deg, the 3σ dispersion in this number can be ~1.5 deg, as shown. The total dispersion of γ_M is then ~3.7 deg (worst case). If the effect of the entry angle dispersion (~2.8 deg) is root-sum-squared with the effect of the atmosphere (~1.4 deg) the 3σ dispersion in γ_M is ~3.1 deg. This error includes the effect of variations in the downrange distance due to variations in the atmospheric density. It can be reduced in the future by three methods:

1) Reducing the errors in γ_E that result from orbit determination errors;

2) Refining the atmospheric model;

3) Using inertial navigation to compensate for variations in the downrange angle.

44
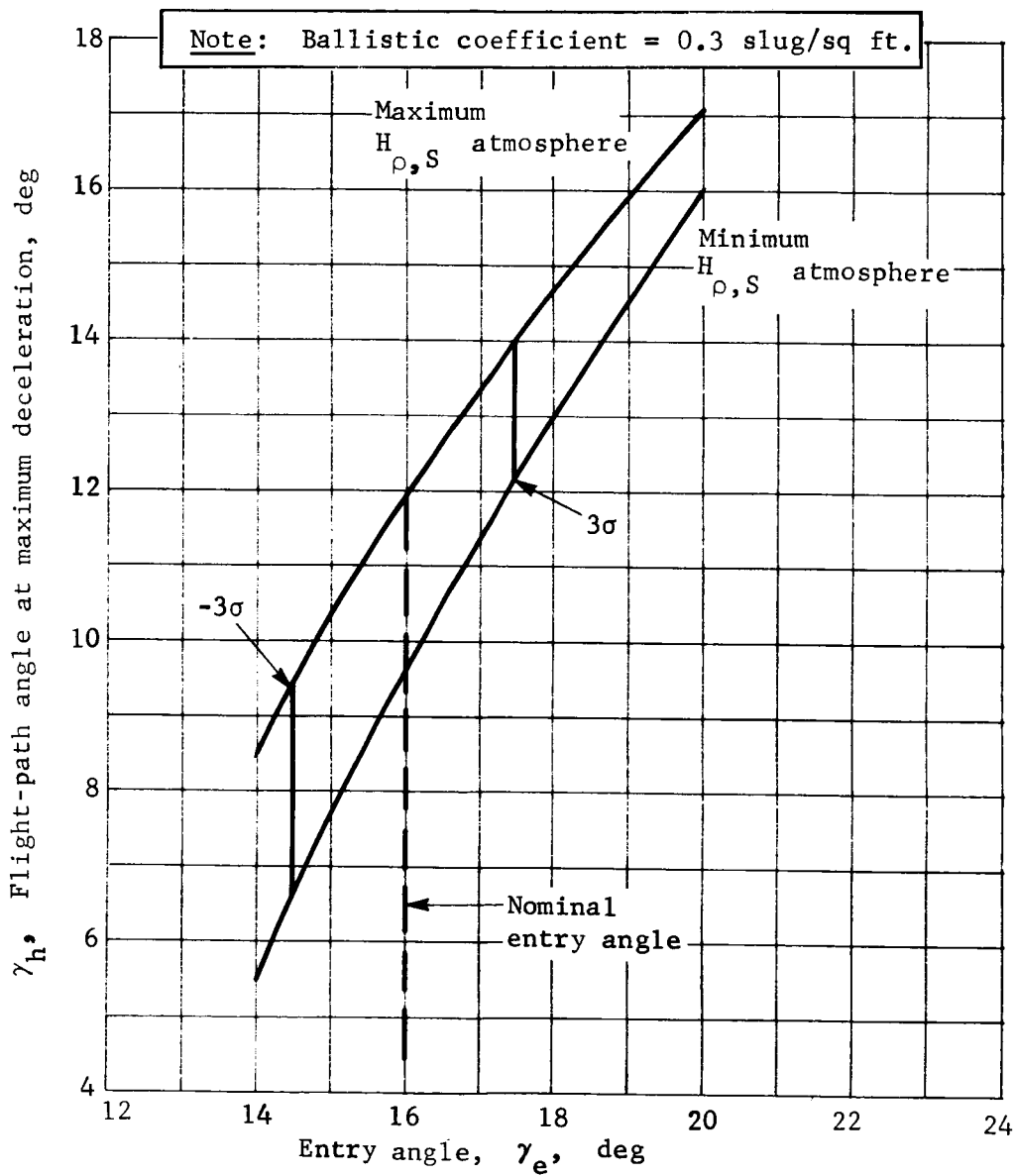
Figure 12.- Flight-Path Angle at Maximum Deceleration vs Entry Angle

Further studies will define how much the 3.1-deg error can be reduced. Note that this error will occur only in the pitch plane. The yaw error will be much smaller. The method of updating the roll attitude is based on the fact that the vehicle's yaw gyro rate will be zero if the pitch axis is horizontal. This is due to the normal gravity turn rate of the trajectory, which is as high as 1/2 deg/sec.

In equations (5) thru (10), u, v, w, and H are initialized by being set equal to the first valid radar data that are received; then, the solution of the equations begins from that point. This is the simplest means of obtaining adequate performance from the inertial navigator.

The second method considered for the mechanization of the inertial navigator was based on the use of a Kalman filter. This was done:

1) To determine whether the more-complex, Kalman-filter approach was better from an operational standpoint;

2) To determine whether the Kalman filter could be used to update the A matrix.

A previous study on this subject (ref. 7) indicated that the Kalman-filter approach (see Appendix A) could produce safe landings with fewer than three Doppler radar beams operating. However, because that study was conducted for a nominal gravity-turn trajectory and did not consider the random effects of wind velocity, surface slope, and atmospheric density, the use of a nominal trajectory may be misleading. The approach used in this study was to mechanize a quasi-linear Kalman filter and simulate its operation in the MOD6MV program. This eliminates the assumption of a particular nominal trajectory.

The structure of this filter approach is shown in figure 13. An inspection of figure 13 shows that the only basic difference between using the Kalman filter and solving equations (5) thru (10) is that the Kalman filter generates a matrix of time-variable feedback gains, whereas a diagonal constant matrix $\left(K_u, \; K_v, \; K_w, \; K_H\right)$ is used in equations (5) thru (10). We estimated that programing the Kalman-filter approach would require about 500 additional locations in the GCC.

A further discussion of the modeling procedure is given in Appendix A. The results are briefly summarized on
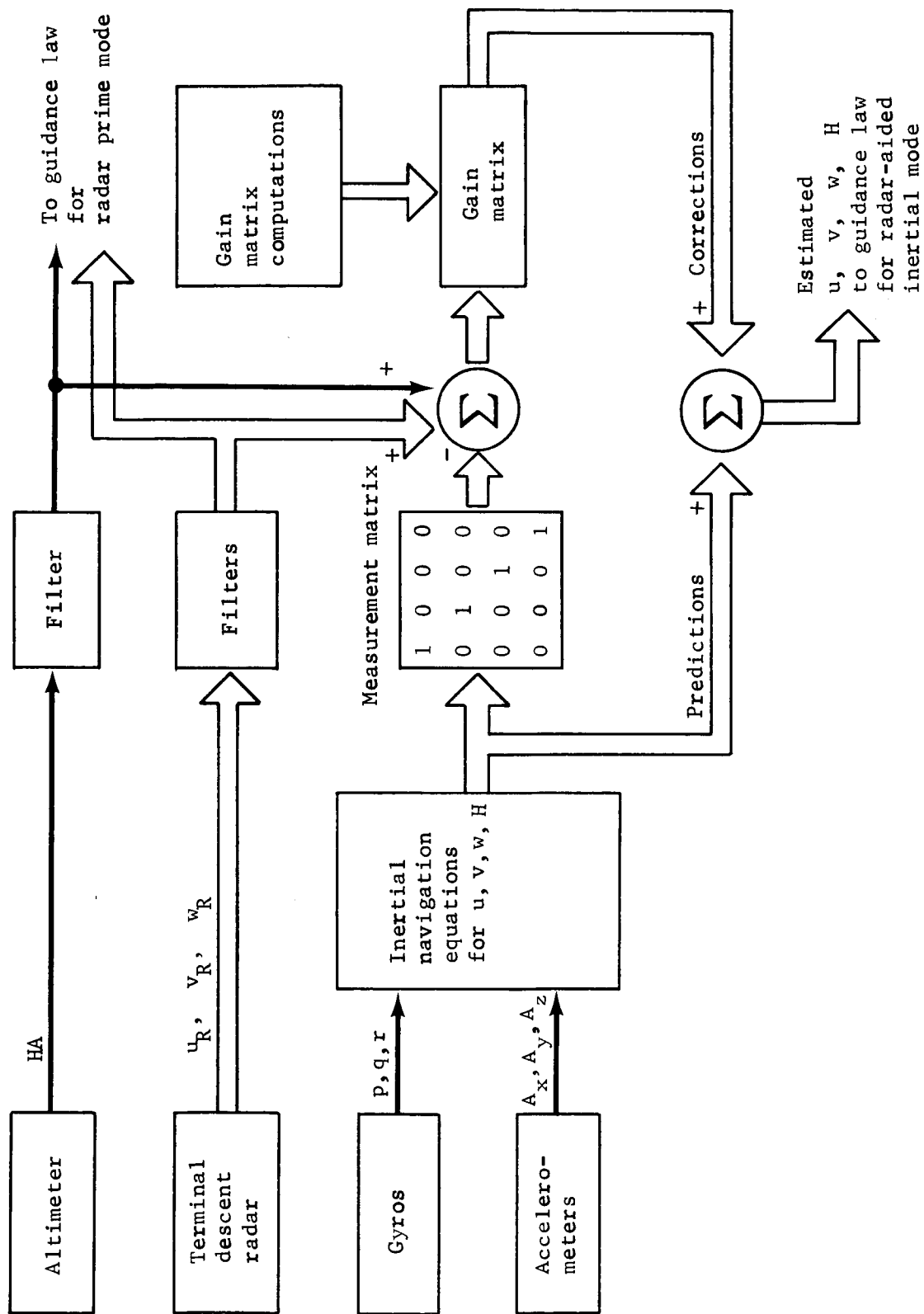
Figure 13.- Mechanization of the Kalman Inertial Navigator

1) The Kalman filter inherently initializes the inertial outputs with the first valid radar data.

2) The Kalman filter appears to give more accurate estimates of u, v, w, and H during the first several sec of operation than the simple approach.

3) Special care must be taken to keep the Kalman filter from ignoring the radar data as time progresses. If this is not done, there will be data saturation (undetectable errors in the inertial estimates).

4) More accurate inertial estimates do not produce a major payoff in terms of the descent performance, since the quality of the radar data improves with decreasing altitude anyway.

5) The expansion of the Kalman filter from four states (u, v, w, and H) to seven (u, v, w, H, A_{13}, A_{23}, and A_{33}) was considered unnecessary in light of comment 4, particularly since doing so would have significantly increased the computer requirements.

The errors of the inertial navigator can be estimated by referring again to equations (5) thru (10). The error sources and the resulting acceleration errors are shown in table 1.

TABLE 1.- INERTIAL SYSTEM ACCELERATION ERRORS

Error Source	Error Equation	Error Magnitude[a], ft/sec^2	Axis
Accelerometer bias (400 µg)	E = Bias	0.005	All
Accelerometer Scale Factor (1/4%)	$E = S_f \cdot A_x$	0.125	Axial
Gyro drift (1 deg/hr)	E = u • Drift	0.0024	Lateral
Attitude error[b] (10 deg)	E = g • sin 10°	2.1	Lateral
[a] u = 500 fps, A_x = 50 ft/sec^2; p, q, r, v, w, Ay, Az = 0. [b] Radar unlocked.			

48

Table 1 shows that, in the absence of radar data, there will be significant errors in the lateral velocity channels (v and w), and the side velocity will increase 2.1 ft/sec. These results were substantiated using the MOD6MV program. Thus, the inertial system should be considered only as a short-term memory device for extrapolating data during radar-dropout periods.

When the radar is locked, the attitude error produces a lateral velocity bias. This can be derived from equations (5) thru (10) by considering A_z, p, and q to be zero and A_{33} to equal the sine of the error angle ϵ.

$$\dot{w} = g \sin \epsilon + K_w \left(w_R - w \right) \tag{35}$$

The transfer function of this equation is

$$w = \frac{g \sin \epsilon + \left(K_w \right) \left(w_R \right)}{S + K_w} \tag{36}$$

In the steady state (S = 0), we wish to obtain $w = w_R$ which will be true only if $\epsilon = 0$. When $\epsilon = 10°$ and $K_w = 1$, the steady-state error in w will be

$$E_w = \frac{g \sin \epsilon}{K_w} = 2.1 \text{ fps.} \tag{37}$$

K_u, K_v, K_w, and K_H have been set equal to 1 in studies to date. Further studies should determine whether these gains can be increased to decrease the effect of the attitude error.

D. Radar Requirements

Requirements must be established for the operating range, accuracy, probability of unlock, and probability of false lock before selecting the final design of the radar. Analyses have been conducted to define these requirements.

The point on the trajectory at which accuracy is most critical is where the engine cuts off just above the surface. The accuracy to which the cutoff conditions can be met affects not only the design of the landing structure, but also the associated probability of a successful landing, as well as the amount of surface heating from the engines. Figure 14 shows the vertical impact velocity as a function of cutoff conditions. The shaded area is the range of conditions obtained using 3σ cutoff conditions of:

Altitude = 10 ft ± 5 ft;

Velocity = 10 fps ± 3 fps.

The currently specified values of the parameters important to landing success are shown in table 2. The expected performance is based on the performance of the modified LM radar. Other proposed designs would also be expected to meet these requirements.

TABLE 2.- EFFECT OF RADAR ERRORS ON LANDING CONDITIONS

	Attitude, deg	Attitude rate, deg/sec	Vertical velocity, fps	Horizontal velocity, fps	Altitude, ft
Nominal engine cutoff	0	0	10.0	0	10.0
Nominal impact	0	0	18.3	0	0
Desired accuracy at cutoff (3σ)	1.0	5.0	3.0	5.0	5.0
Expected performance (3σ)	1.2	3.6	0.7	1.0	2.5
Desired accuracy at impact (3σ)	6.0	5.0	5.0	6.0	--
Expected performance (3σ)	4.8	3.6	2.1	1.0	--

At higher altitudes, the accuracy is not as critical as it is near cutoff. The 3σ high-altitude accuracy requirements are shown below:

Altitude or
slant range: ±4.5% or 5 ft (whichever is greater);

Velocity: ±4.5% or 3 fps (whichever is greater).
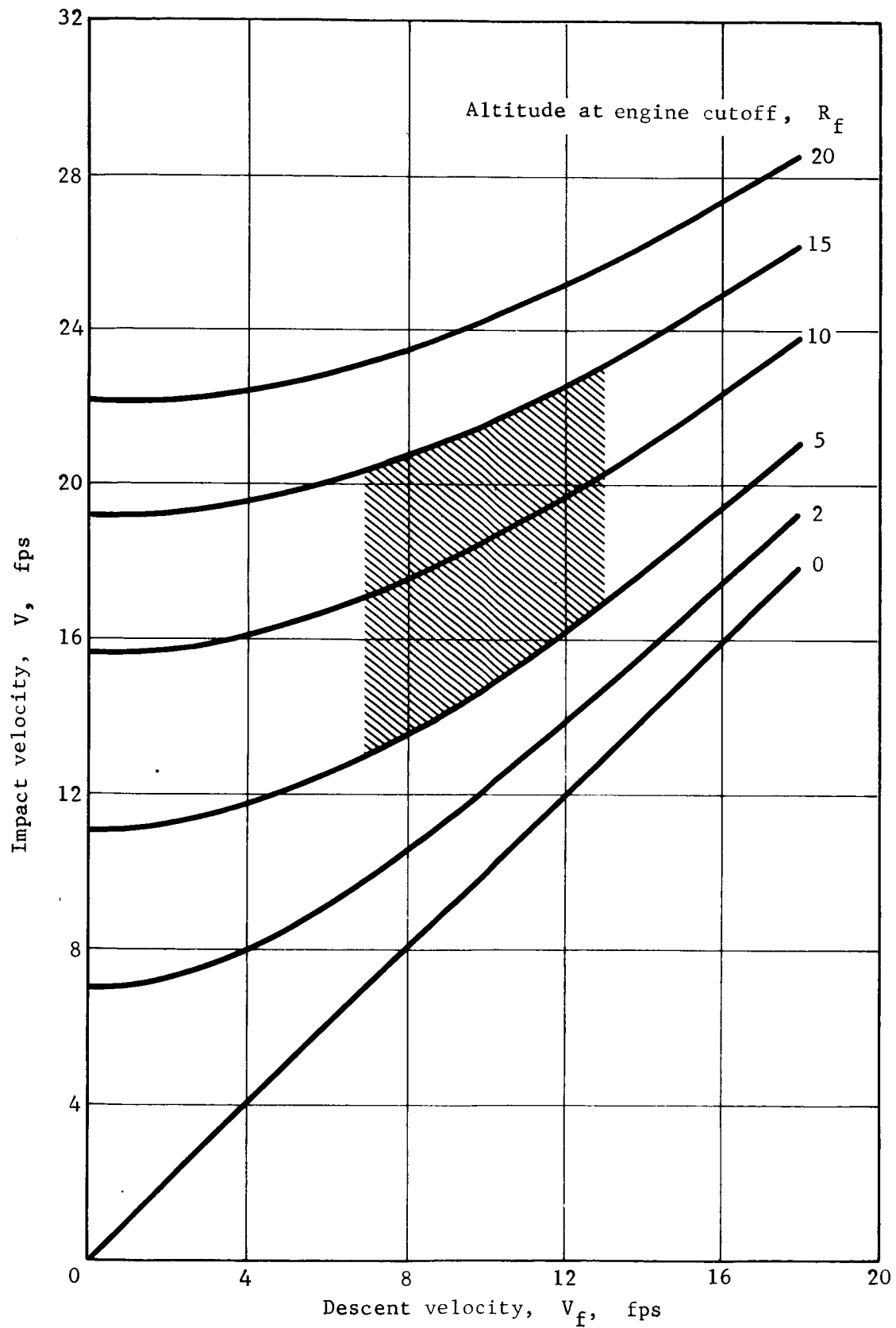
Figure 14.- Lander Impact Velocity vs Descent Velocity
at Engine Cutoff

The maximum velocity that will be measured by the radar is 600 fps. This velocity occurs during the parachute phase. Based on the above requirement, the 3σ maximum velocity error is 27 fps, which is not significant when combined with random wind velocities on root-sum-squared (RSS) basis. Other MOD6MV simulations conducted during this study have shown that successful landings can be achieved with initial velocity errors up to 30 fps, and that the 3σ altitude or range error due to radar tolerances of 4.5% at the vernier ignition altitude of 4000 ft is 180 ft. Because successful landings have been simulated with initial errors of up to 150 ft, we feel that the specified accuracies are adequate for guidance purposes.

The operating range of the radars depends on the overall trajectory of the vehicle and the design of the aerodynamic decelerator. The radars should be designed to overlap the staging altitudes to allow for some later adjustments in the trajectory. The LARA and the TDLR should operate between 20 000 and 10 ft for velocities ranging from 1000 fps to zero. The HARA should operate between 200 000 and 10 000 ft for velocities ranging from 20 000 to 500 fps.

The probability of obtaining valid radar data has been studied using Monte Carlo techniques. These will be described later in this report. An important question to be answered is: how long can we tolerate the loss of radar data? This question must be considered in terms of the alternative guidance modes described previously.

Simulations conducted with the system operating in the radar prime mode have shown that the mission will be unsuccessful if one of the velocity components (one beam of a 3-beam radar or two beams of a 4-beam radar) unlocks during the tip-up maneuver (see ref. 4). Therefore, a suitable short-term backup mode is required. The best backup mode is to use is an inertial navigator. Without the navigator backing up the system, the radar would be required to have a 99.7% probability of maintaining the radar locks during the tip-up maneuver.

The mission can also be a failure if the radar does not detect the altitude at which the vernier engines should ignite (4000 ft) during the parachute-descent phase. To preclude such a failure, the LM radar, when operating in the radar prime mode, should have a 99.7% probability of locking on the range beam and two of the velocity beams.

If the system operates in the radar-aided inertial navigation mode, or in the radar prime mode with an inertial backup, these requirements can be relaxed. Since the inertial navigator is a short-term memory and data extrapolator, intermittent radar samples can be tolerated. During the parachute descent, near vernier-ignition altitude, the vertical velocity of the vehicle will be between 100 and 300 fps. Then, if the 3σ velocity accuracy is 4.5%, the maximum velocity error will be 13.5 fps (table 3) and the drag acceleration will be about one Mars g. Table 3 shows how the altitude error and the velocity error will accumulate if radar data are lost for various times. The table shows that the axial velocity can be lost for up to 2 minutes with negligible effect. However, if the altitude data and lateral velocity data are lost for more than 10 sec, significant errors accumulate. Consequently, we recommend that, before the vernier engines ignite, at least one valid signal be received during the following intervals:

Altitude data: 10 sec or less;

Lateral-velocity data: 10 sec or less;

Axial-velocity data: 120 sec or less.

These recommendations may be restated as follows: before the Lander descends to 4000 ft, valid radar data should be received more frequently than this; and, furthermore, the probability of receiving these data (i.e., the probability of locking the required number of radar beams) should be at least 0.997.

For the terminal-descent phase, the errors shown in table 3 are essentially the same during the initial part of the trajectory. Only the accelerometer error is higher; this is because the measured acceleration increases from about 1 g to about four g. However, if radar data are lost for less than 10 sec, the accelerometer error is still negligible. Since the terminal-descent phase lasts less than 40 sec in any case, it would be desirable to update the radar data more often than every 10 sec.

Table 4 shows how the altitude error and the velocity error will accumulate as the result of radar losses during the constant-velocity descent phase. Using a 3σ landing velocity of 6 fps, we see that a 3-sec loss of radar data in that channel is acceptable. However, using the specified requirements for altimeter and TDLR accuracy (see table 3), we see that the altimeter must provide data until the vernier engines shut down in order to hold the altitude accuracy to ±5 ft. If the axial-velocity data were accurate to 2 fps and the altitude to 2 ft, then the altimeter data could be lost for up to 2.5 sec. The axial velocity can be measured with this accuracy since it is the average calculated from at least two radar beams. The feasibility of limiting the range error to 2 ft depends on the mechanization that is chosen.

TABLE 3.- 3σ NAVIGATOR ERRORS DURING THE PARACHUTE-DESCENT PHASE

Radar Unlock Time, sec	Axial velocity errors[a], fps			Altitude errors[a], ft				Lateral velocity errors, fps		
	TDLR[b]	Accelerometer[c]	RSS	Altimeter[d]	TDLR[b]	Accelerometer[c]	RSS	TDLR[e]	Attitude[f]	RSS
0	13.5	0	13.5	180	0	0	180	11	-2.1	11.2
1	13.5	.03	13.5	180	13.5	.015	180	11	0	11.0
5	13.5	.15	13.5	180	67.5	.37	191	11	8.4	13.8
10	13.5	.3	13.5	180	135.0	1.5	225	11	18.9	21.9
30	13.5	.9	13.5	180	405.0	13.5	443	11	60.9	62.0
60	13.5	1.8	13.6	180	810.0	54.0	830	11	123.9	124.0
120	13.5	3.6	14.0	180	1620.0	216.0	1640	11	250.0	250.0

[a]Gravity and attitude errors negligible.

[b]Vertical velocity = 300 fps, 3σ radar accuracy = 4.5%.

[c]Axial acceleration = 12.3 ft/sec^2, 3σ accelerometer accuracy = 0.25%.

[d]Altitude = 4000 ft, 3σ altimeter or range accuracy = 4.5%.

[e]Lateral velocity = 250 fps (worst case), 3σ radar accuracy = 4.5%.

[f]3σ attitude error = 10°.

TABLE 4.- 3σ NAVIGATOR ERRORS DURING THE CONSTANT-VELOCITY DESCENT PHASE

Radar unlock time, sec	Altitude errors[a], ft			Lateral velocity errors[a], fps		
	Altimeter	TDLR	RSS	TDLR	Attitude[b]	RSS
0	5.0	0	5.0	3.0	-2.1	4.7
1.0	5.0	3.0	5.8	3.0	0	3.0
2.0	5.0	6.0	7.8	3.0	2.1	4.7
3.0	5.0	9.0	10.3	3.0	4.2	5.2
4.0	5.0	12.0	13.0	3.0	6.3	7.0
5.0	5.0	15.0	15.8	3.0	8.4	8.9

[a]Altitude < 100 ft, velocity < 67 fps, axial-velocity error = 3 fps, gravity and accelerometer errors negligible.

[b]Attitude error = 10°, navigator gain = 1.

From these studies, we determined that the radar data should be updated every three sec or less when the altitude of the Lander is less than 100 ft. When the altitude is between 100 and 4000 ft, the update interval, t_{ud}, can be calculated from equation (38).

$$t_{ud} = \frac{7}{3900} (H - 100) + 3 \tag{38}$$

In there is a false lock, such as a main-lobe-to-cross-lobe lock or a side-lobe-to-side-lobe lock, the radar will put out false data that will be interpreted by the navigator as correct data. As documented in the next chapter, simulations have shown that a cross-lock condition which persists longer than three sec can cause loss of the vehicle. Thus, the probability of having a false lock for longer than 3 sec should be less than 0.003.

IV. MODIFIED LM RADAR STUDY

Considerable effort was made to investigate the application of the Lunar Module (LM) radar and a modified version of it (the Mod-LM radar) for the Mars Lander mission. Among the tools used were the static Monte Carlo programs and the MOD6MV program. The results of these analyses are documented in references 4 thru 6; but, for convenience, this chapter contains a summary of the principal results of those simulations and a description of the results obtained using the time-correlated Monte Carlo program.

The geometry of the LM and Mod-LM radar beams is shown in figure 15.
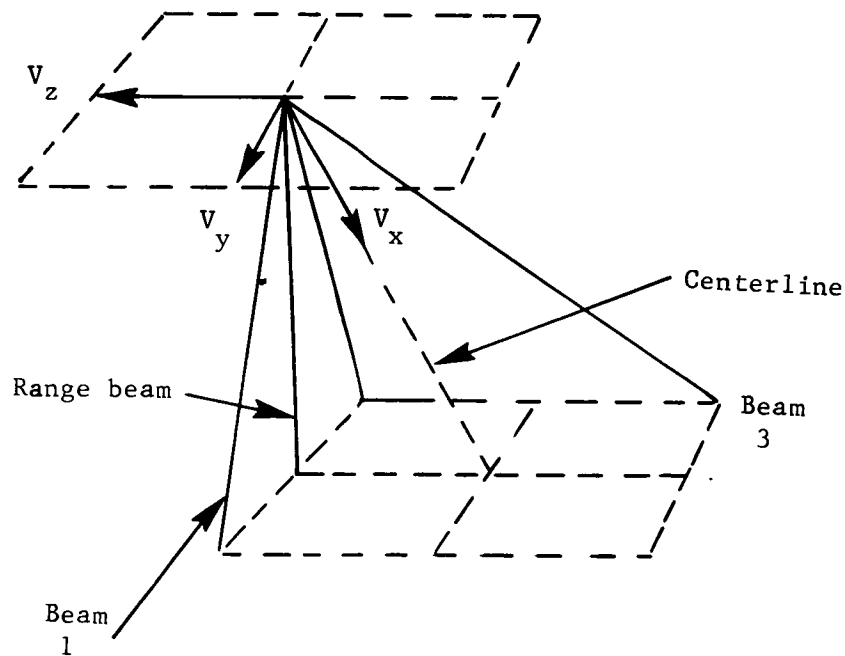
Figure 15.- Beam Geometry for the LM and Modified LM Radar System

The Mod-LM radar is a cw/FM-cw radar that uses three independent velocity trackers and one range tracker. Velocity compensation is required from Beams 1 and 3. The LM and Mod-LM radar parameters are compared in table 5.

TABLE 5.- LM AND MODIFIED-LM RADAR PARAMETERS

Parameter	LM radar	Mod-LM radar
Transmitter power, dBW	-13.0	-13.0
Losses, dB	-1.8	-1.8
Receiver sensitivity	a	b
Antenna gain, dB	28.0	28.0
Maximum beam width, deg	7.5	7.3
Minimum beam width, deg	3.7	3.7
Carrier frequency in velocity channel, GHz.	10.51	10.51
Carrier frequency in range channel, GHz . .	9.58	9.58
Sawtooth modulation frequency in range channel, Hz	[c]130.0	[c]130.0
Upper high-mode search limit, KHz	d	[e]12.0
Lower high-mode search limit, KHz	f	[e]0
Upper low-mode search limit, KHz	[e]7.4	[e]6.0
Lower low-mode search limit, KHz	[e]-5.24	[e]0
Acquisition time, sec	6	3
Mode-switching attitude, ft	2500	1250
High-mode filter bandwidth, Hz	2800	600
Low-mode filter bandwidth, Ha	400	400

[a]Velocity-dependent (3-dB signal-to-noise ratio used as criterion).

[b]Velocity-dependent (3-dB signal-to-noise ratio used as criterion). More sensitive than LM radar.

[c]Frequency-modulated.

[d]52.0 KHz for Beams 1 and 2, 70.0 KHz for Beam 3.

[e]For all four beams.

[f]-41.0 KHz for Beams 1 and 2, -20.0 KHz for Beam 3.

The modifications made to the LM radar included adding a centered range beam, decreasing its search time, increasing its sensitivity, obtaining parallel data output on a per beam basis, and using a new range criterion for mode change. Note that before a production model of the Mod-LM radar can be heat-sterilized, 24 of the 104 components and 51 of the 124 types of material that are not compatible must be changed. These changes were not included in the simulations of the Mod-LM radar.

A. Summary of Previous Results

The four techniques used to determine the application of the Mod-LM radar were:

1) Tracking analyses (to determine the effect of changing the doppler frequency and the range);

2) Error analyses (to qualify the noise models being used and to determine the effect of noise on the vehicle);

3) Monte Carlo analyses (to determine the probability of detecting various radar beams); and

4) 6DOF terminal-descent simulations (to determine noise, mode-switching, and system effects).

The tracking rate capability of the Mod-LM radar is summarized in table 6. The only area of concern was the tendency of the range beam to unlock in the high mode during tip-up maneuvers.

TABLE 6.- TRACKING RATE ANALYSIS RESULTS, MODIFIED LM RADAR

Program	Velocity beam		Range beam	
	High mode	Low mode	High mode	Low mode
Parachute[a]	OK	Does not exist	OK	Does not exist
Tip-up[a]	OK	Does not exist	Break lock[b]	Does not exist

[a] Parachute and tip-up rates = 30 deg/sec.

[b] Break lock at 30 deg/sec occurs at an incidence angle of 60 deg (verified in 6D runs).

To qualify the noise models being used, the MOD6MV program was "frozen" at various points along the trajectory (indicated in the upper half of table V-3) and a large number of samples were taken of the tracker output and resulting body velocities. These data, in turn, were reduced statistically to probability density functions. The resulting root-mean-square (rms) levels were compared with data generated by Robert Harrington of Ryan Aeronautical Co, San Diego, California, at the same trajectory points. The results were the same (tables 7 and 8). The effect of radar noise on the vehicle may be seen in table 8. Note that when the system operates in the radar prime mode, the specified condition at engine cutoff is not met for attitude rate.

TABLE 7.- ERROR ANALYSIS RESULTS

Time	3σ radar error, fps		
	X-axis	Y-axis	Z-axis
Vernier engine ignition	1.65	7.2	4.5
Tipup	1.1	4.2	3.0
Contour point	.9	3.6	1.8
Vernier engine cutoff	.2	.8	0.5

TABLE 8.- 3σ EFFECT OF ERRORS ON SYSTEM PARAMETERS AT VERNIER ENGINE CUTOFF

Parameter	Operating mode of system		Specified cutoff errors
	Radar Prime Mode	Radar Inertial Mode	
Attitude rate, deg/sec	12.6	3.6	5.0
Attitude, deg	4.2	1.2	1.0
Horizontal landing velocity, fps	1.0	1.0	6.0
Vertical landing velocity, fps .	2.1	2.1	3.0

Monte Carlo analyses were used to investigate the probabilities of beams unlocking, crosslobe lockups, and incorrect range for the Modified LM radar. The results of these analyses are shown in table 9 and in figures 16 and 17. The parametric conditions for the analyses were: altitude = 4000 ft; nominal pitch angle = 20 deg from the vertical, 3σ ground slope = 34 deg, 3σ wind velocity = 146 fps, and 3σ attitude dispersion caused by wind gust = 22.4 deg.

The probabilities of a single beam becoming unlocked or supplying incorrect range data were analyzed for the upper and lower surface-reflectivity models specified in reference 8 over the range of velocities caused by variations in the atmospheric models.

TABLE 9.- CROSS-LOBE LOCK STATISTICS

Conditions		Total cases	Three main lobe locks	Cross-lobe conditions per beam[a]	Cross-lobe locks
V_t	σ_0				
100	Minimum	1000	606	0	0
200	Minimum	1000	933	0	0
300	Minimum	1000	978	0	0
100	Maximum	1000	988	560	4
200	Maximum	1000	1000	1450	0
300	Maximum	1000	1000	2136	0

[a]A cross-lobe condition occurs when the cross-lobe power is above the detector threshold present in the beam. The tracker may or may not be locked to the main beam signal under this condition (see Chapter VI, Section A).

Figure 16 shows that it is impractical to operate the existing or Modified-LM radar in a primary radar control mode if all three velocity beams are used on a continuous basis. However, it may be possible to operate the Modified-LM radar in the radar-aided, inertial-control mode, even though some risk of mission failure is implied by the high probability of beam unlock, particularly for the lower boundary of reflectivity characteristics and low velocities.

The probability of having range errors is so high, even for the Modified-LM radar, that it cannot be used to measure altitude for engine ignition and parachute release. This means that a separate widebeam altimeter or the range along each beam, is needed. The results of the cross-lobe lock study, which was made at various velocity conditions, are shown in table 9.
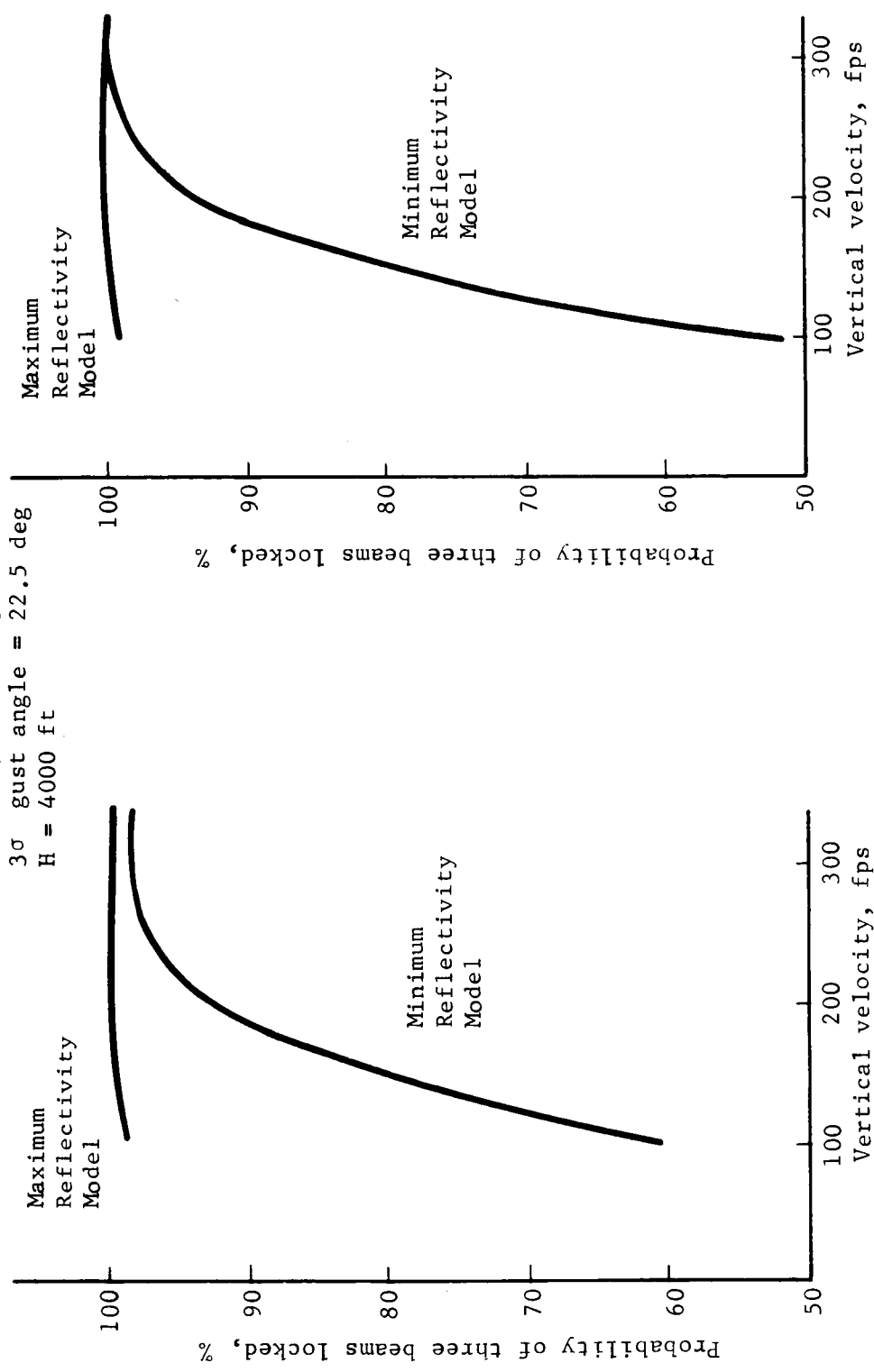
Figure 16.- Monte Carlo Analysis Results: Beam Lock Probability, Modified LM Radar System

θ_t = 20 deg

H = 4000 ft

Minimum reflectivity model
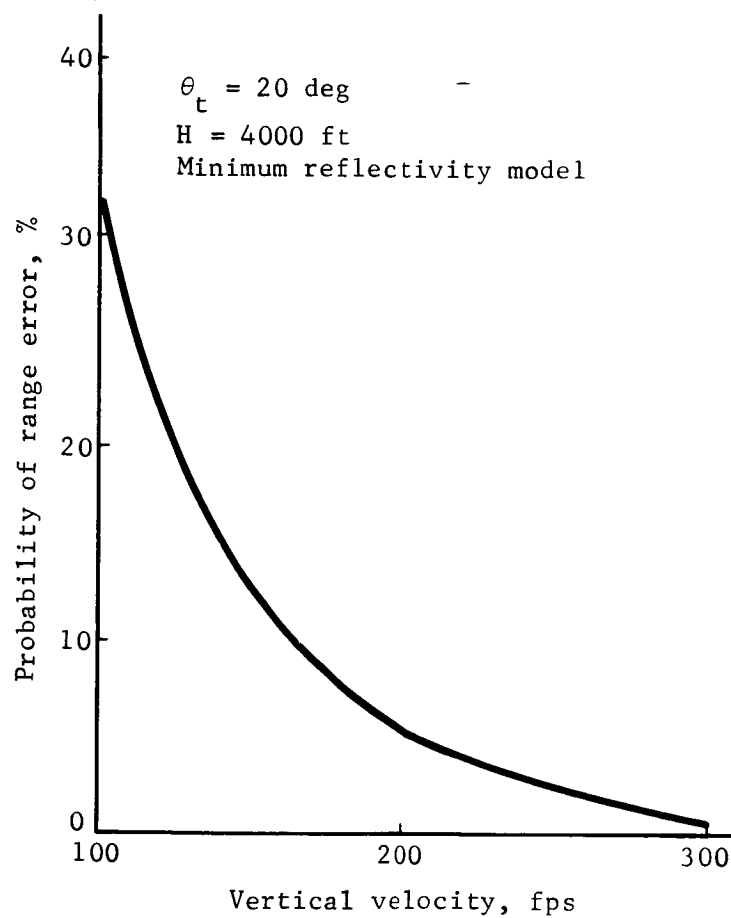
Figure 17.- Monte Carlo Analysis Results: Range Error Probability, Modified LM Radar System

Using a cross-coupling threshold of -28.9 dB (an average from five flight LM radars), the study shows that the conditional probability of cross-lock is 32% for V_T = 100 fps, based on the maximum reflectivity curve. The conditional probability, $P(c/u)$, is expressed in terms of the probability of a beam unlock, $P(u)$, and the joint probability of a cross-lobe lock occurring simultaneously with a beam unlock, $P(c,u)$. A cross-lobe lock is catastrophic to the mission unless the condition can be detected and compensated for. Figures 18a thru 18d show that this should be done in less than three sec. This condition is hard to detect, because there are widely-varying dynamic changes on the parachute and capsule during the terminal-descent phase.

Because of the major changes needed to use the LM radar for the Mars Lander mission and the uncertainties of operational risk, a new radar system should be developed.

The machine plots shown in figures 18a thru 18d are examples of the type of evaluation that was done with the MOD6MV program. The Beam 2 radar signal was suppressed (forced) below its threshold to determine if the radar would cross-lock, and if so, how long the main beam radar signal would have to be below the threshold and the beam cross-locked to cause mission failure. By varying the length of time the main beam signal was suppressed, it was shown that three sec is critical. The plots show that cross-locking Beam 2 to a side to make its direction that of Beam 1, while suppressing the main beam signal for three sec caused the vehicle to crash with very high side velocities. The main beam signal was suppressed eight sec into the terminal descent and allowed to return at 11 sec. The vehicle had been driven off so far, due to the error caused in velocity by the cross-lock, that the main beam spectrum was no longer in the tracker bandwidth, and the radar remained cross-locked until the vernier engines cut off.

A large number of MOD6MV runs were made to determine the compatibility of the Mod-LM radar with respect to acquisition time, beam dropout, tracking rates, radar noise, mode switch, etc. Many of these results are documented in reference 4.
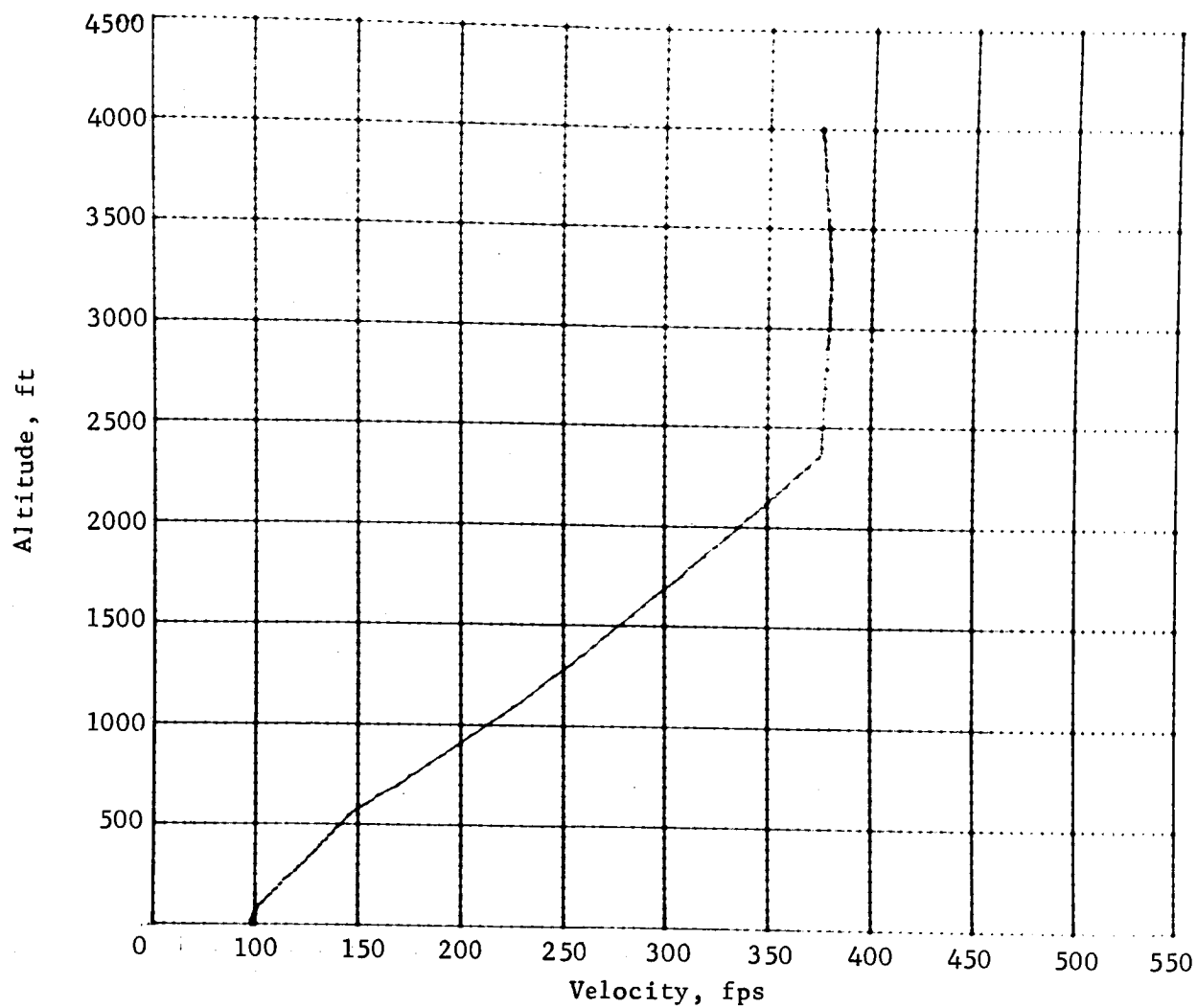
(a) Altitude vs Velocity

Figure 18.- Monte Carlo Analysis Results: Effect of Main Beam Suppression
on Velocity, Modified LM Radar System
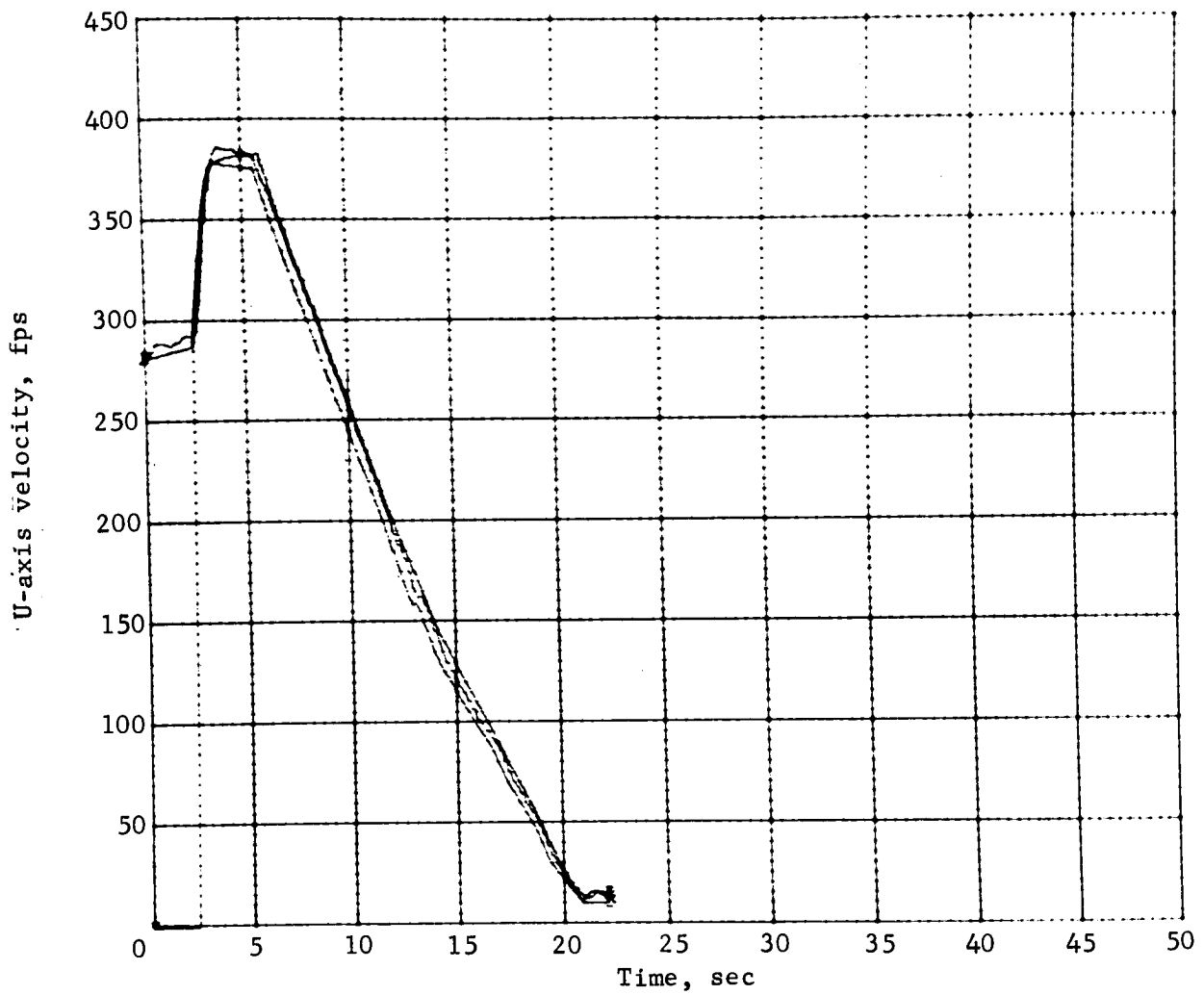
(b) U-Axis Velocity vs Time

Figure 18.- Continued
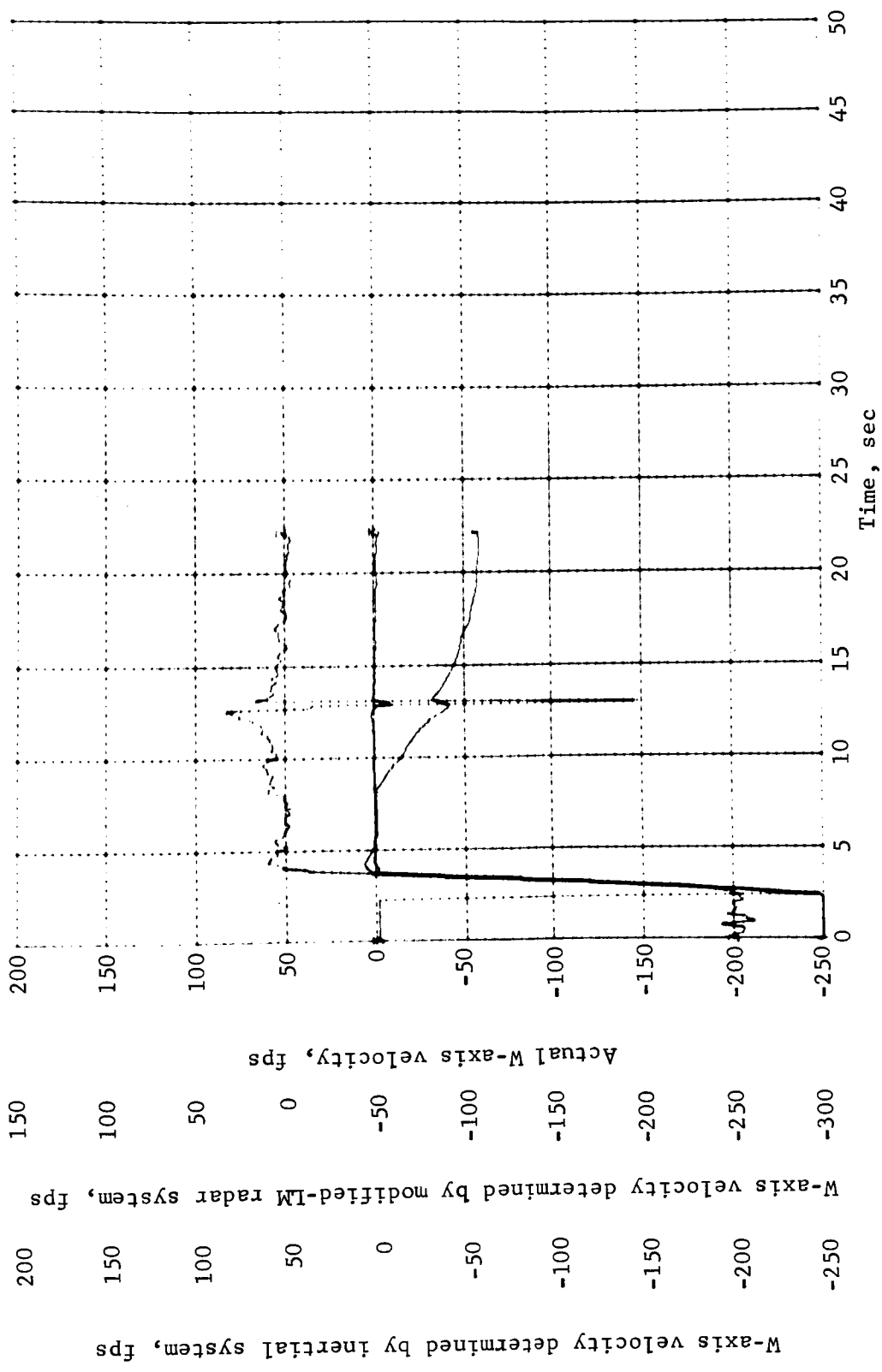
(c) W-Axis Velocity vs Time

Figure 18.- Continued

67
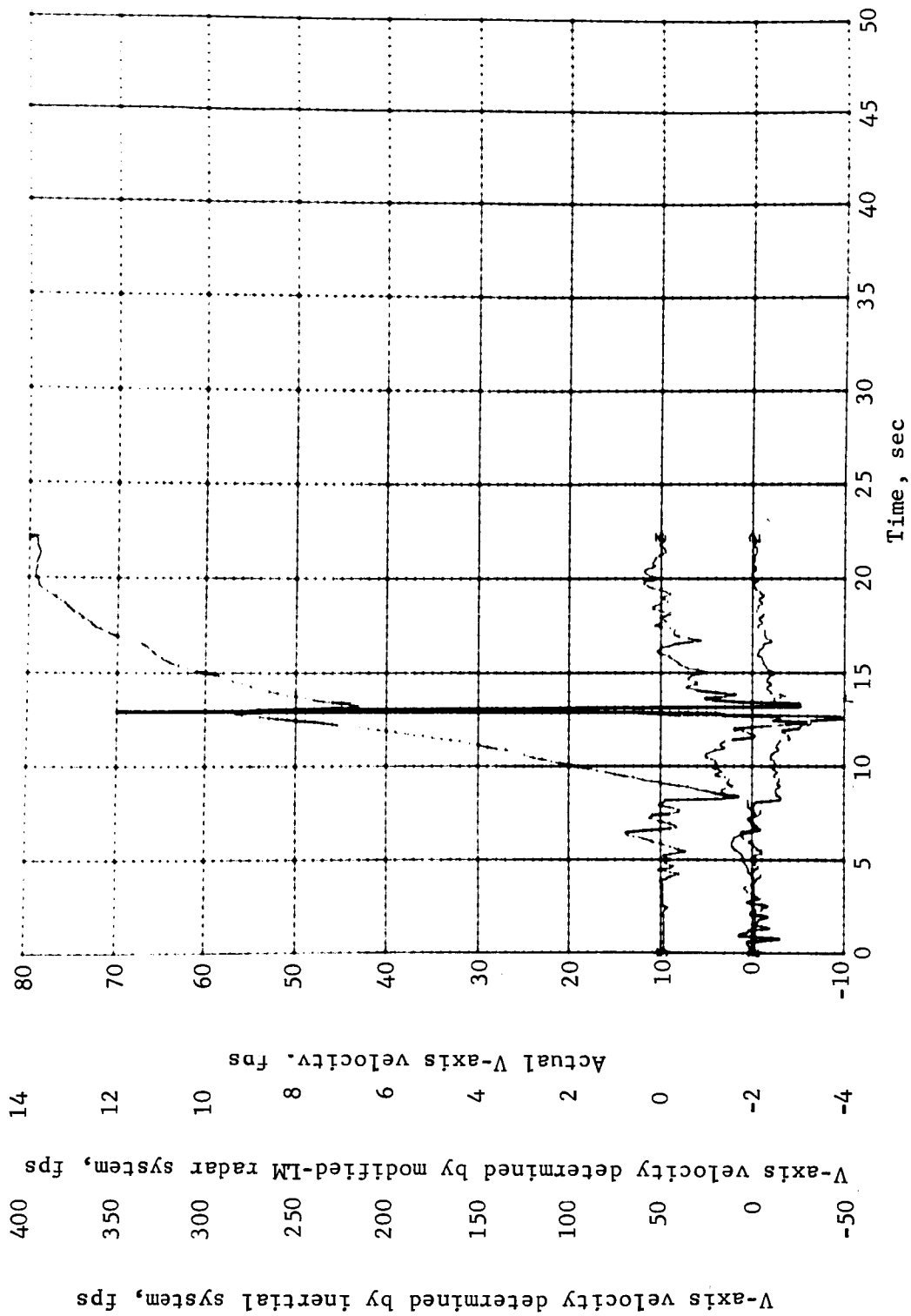
(d) V-Axis Velocity vs Time

Figure 18.- Concluded

68

B. Time-Correlated Monte Carlo Analysis Results

Table 10 summarizes the data obtained with the time-correlated Monte Carlo program described in Appendix B. The data are from four computer runs -- i.e., the tip-up and parachute programs run with the upper and the lower bounds of the reflectivity model defined in reference 8 (see fig. 23). Each block of data in table 10 is numbered for reference in later discussions.

Four types of probability data are presented: the data labeled "length of time that three beams are locked" give the probability that three beams will be locked or cross-locked for T sec somewhere on the trajectory (T is plotted from zero to the maximum time that occurred in the random trajectories computed); the data labeled "length of time ... before vernier engines ignite give the probability that beams will be locked or cross-locked before the vehicle descends to 4000 ft. (These data are plotted out only to the minimum trajectory time).

Table 11 indicates the mean, maximum, and minimum durations of the trajectories sampled with the two programs.

The data generated in figures 19 thru 21 are for 3-, 4-, and 5-beam radars and are based on the MOD-LM radar parameters. The 3-beam system has a lamda pattern, the 4-beam system has a square pattern, and the 5-beam system has four beams in a square pattern plus a centered beam.

As one might expect, the probability that three beams will be locked increases with the number of beams being used. This can be seen by examining table 10. To determine what beam configuration is optimum, a tradeoff is required between the number of beams and the transmitter power. Figure 24 shows that the probability of locking 3 beams of a 3-beam radar is less than the probability of locking three beams in a 4-beam system whose transmitter power is nine dB less.

Because of the increased power required for a 3-beam system to have a lock-on probability equal to that of a 4-beam system, it is more reasonable to choose a 4-beam system. In addition, we feel that the G&C requirement can still be met using a 4-beam system.

TABLE 10.- TIME-CORRELATED MONTE CARLO RESULTS

Probability vs	Reflectivity model			
	Maximum		Minimum	
	Parachute program	Terminal descent program	Parachute program	Terminal descent program
Length of time that three beams are locked (3-beam radar)	figure 19a [1]	figure 19b [5]	figure 19c [9]	figure 19d [13]
Length of time that three beams are locked (4-beam radar)	figure 19a	figure 19b	figure 19c	figure 19d
Length of time that three beams are locked (5-beam radar)	figure 19a	figure 19b	figure 19c	figure 19d
Length of time that Beam 1 is cross-locked	figure 20a [2]	No cross-locks [6]	No cross-locks [10]	No cross-locks [14]
Length of time that Beam 2 is cross-locked	figure 20b	No cross-locks	No cross-locks	No cross-locks
Length of time that Beam 3 is cross-locked	figure 20c	No cross-locks	No cross-locks	No cross-locks
Length of time that Beam 4 is cross-locked	figure 20d	No cross-locks	No cross-locks	No cross-locks
Length of time that Beam 5 is cross-locked	No cross-locks	No cross-locks	No cross-locks	No cross-locks
Length of time that three beams are locked before vernier engines ignite (3-beam radar)	figure 21a [3]	100% for T < 25 sec [7]	figure 21b [11]	100% for T < 25 sec
Length of time that three beams are locked before vernier engines ignite (4-beam radar)	figure 21a	100% for T < 25 sec	figure 21b	100% for T < 25 sec
Length of time that three beams are locked before vernier engines ignite (5-beam radar)	100% for T < 37 sec	100% for T < 25 sec	figure 21b	100% for T < 25 sec
Length of time that Beam 1 is cross-locked before vernier engines ignite	figure 22 [4]	No cross-locks [8]	No cross-locks [12]	No cross-locks [16]
Length of time that Beam 2 is cross-locked before vernier engines ignite	figure 22	No cross-locks	No cross-locks	No cross-locks
Length of time that Beam 3 is cross-locked before vernier engines ignite	figure 22	No cross-locks	No cross-locks	No cross-locks
Length of time that Beam 4 is cross-locked before vernier engines ignite	figure 22	No cross-locks	No cross-locks	No cross-locks
Length of time that Beam 5 is cross-locked before vernier engines ignite	No cross-locks	No cross-locks	No cross-locks	No cross-locks
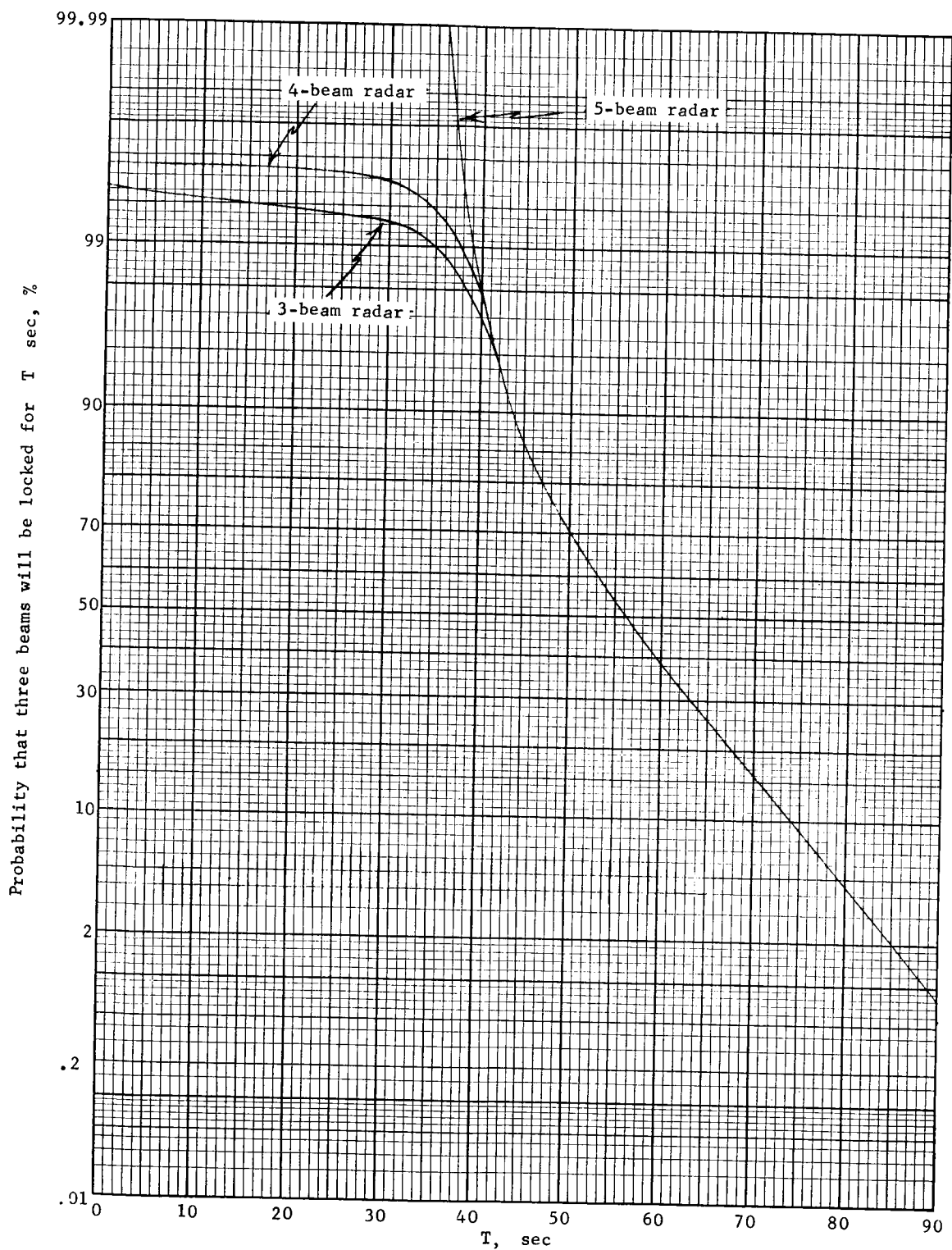
(a) Parachute Phase, Maximum Reflectivity Model

Figure 19.- Time-Correlated Monte Carlo Analysis Results: Probability That
Three Modified LM Radar Beams Will Be Locked for T sec
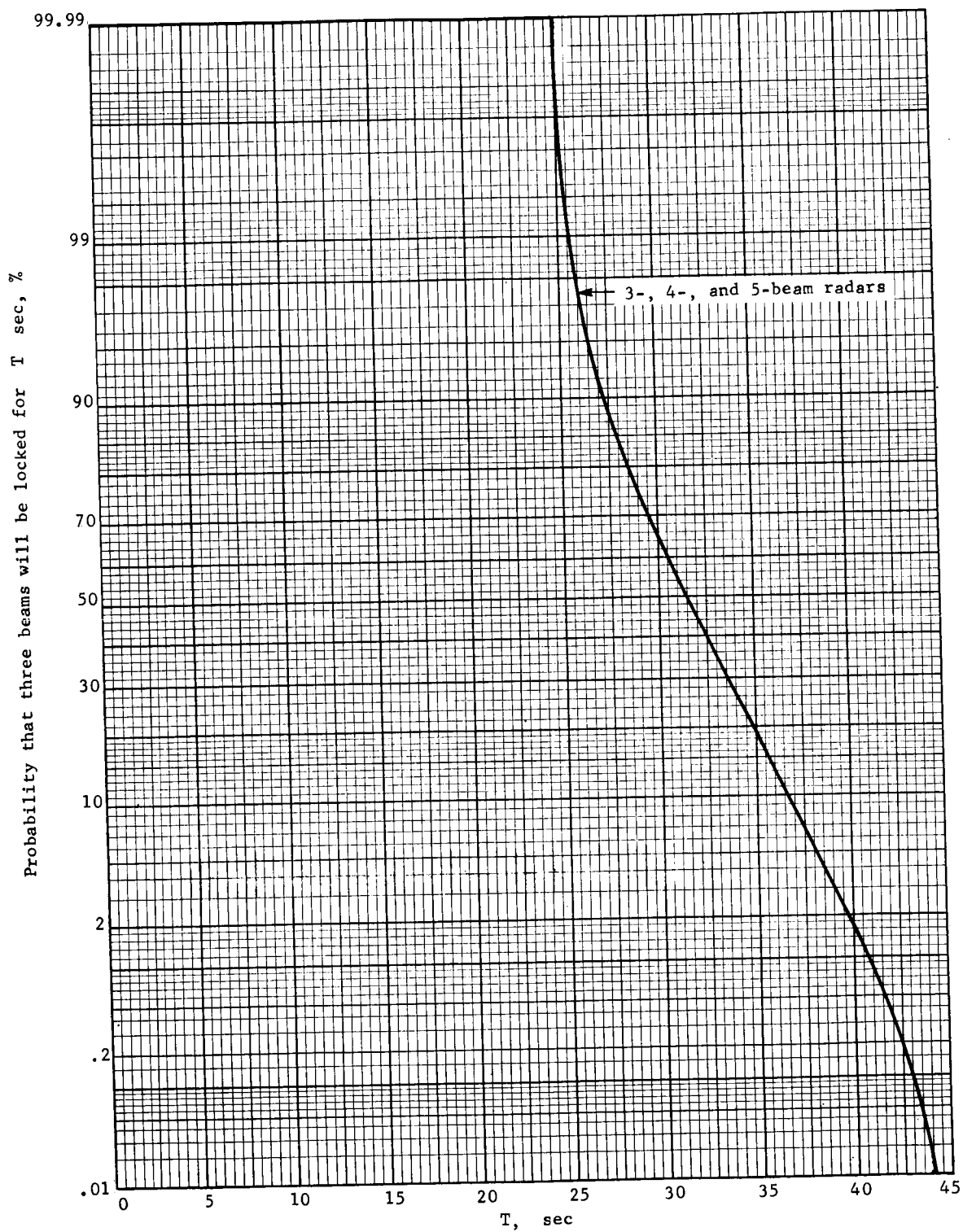
(b) Terminal Descent Phase, Maximum Reflectivity Model

Figure 19.- Continued

(c) Parachute Phase, Minimum Reflectivity Model

Figure 19.- Continued

73
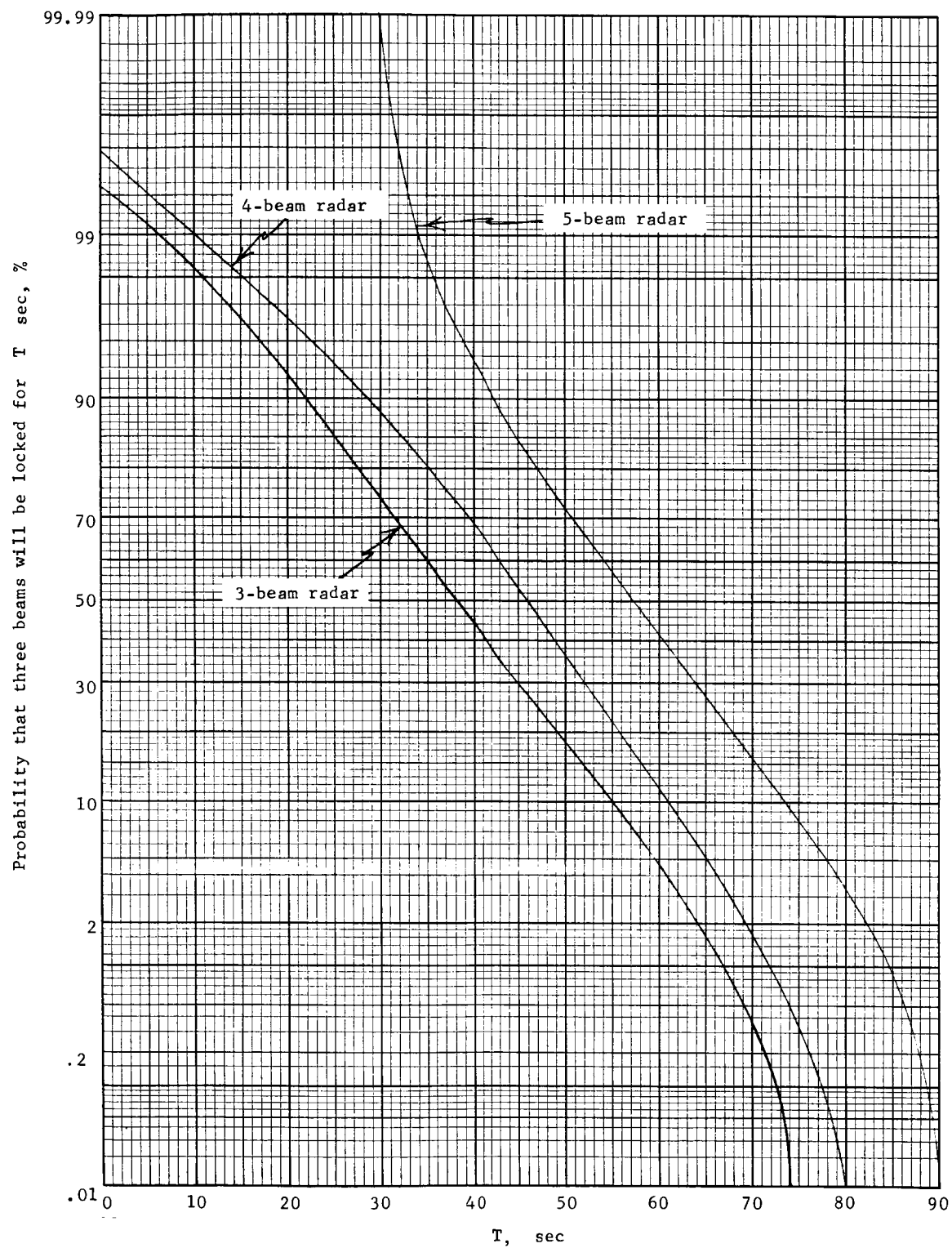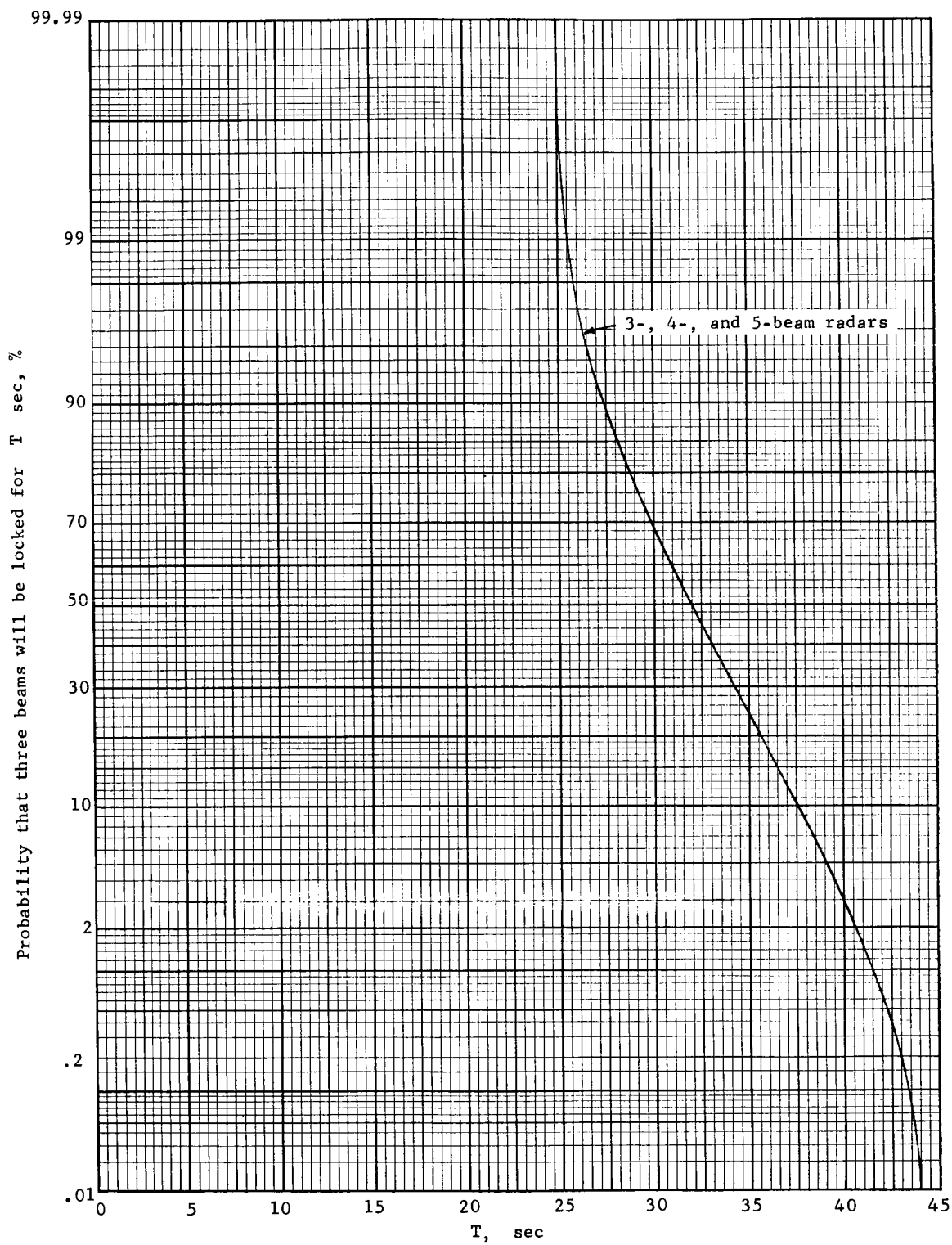
(d) Terminal Descent Phase, Minimum Reflectivity Model

Figure 19.- Concluded
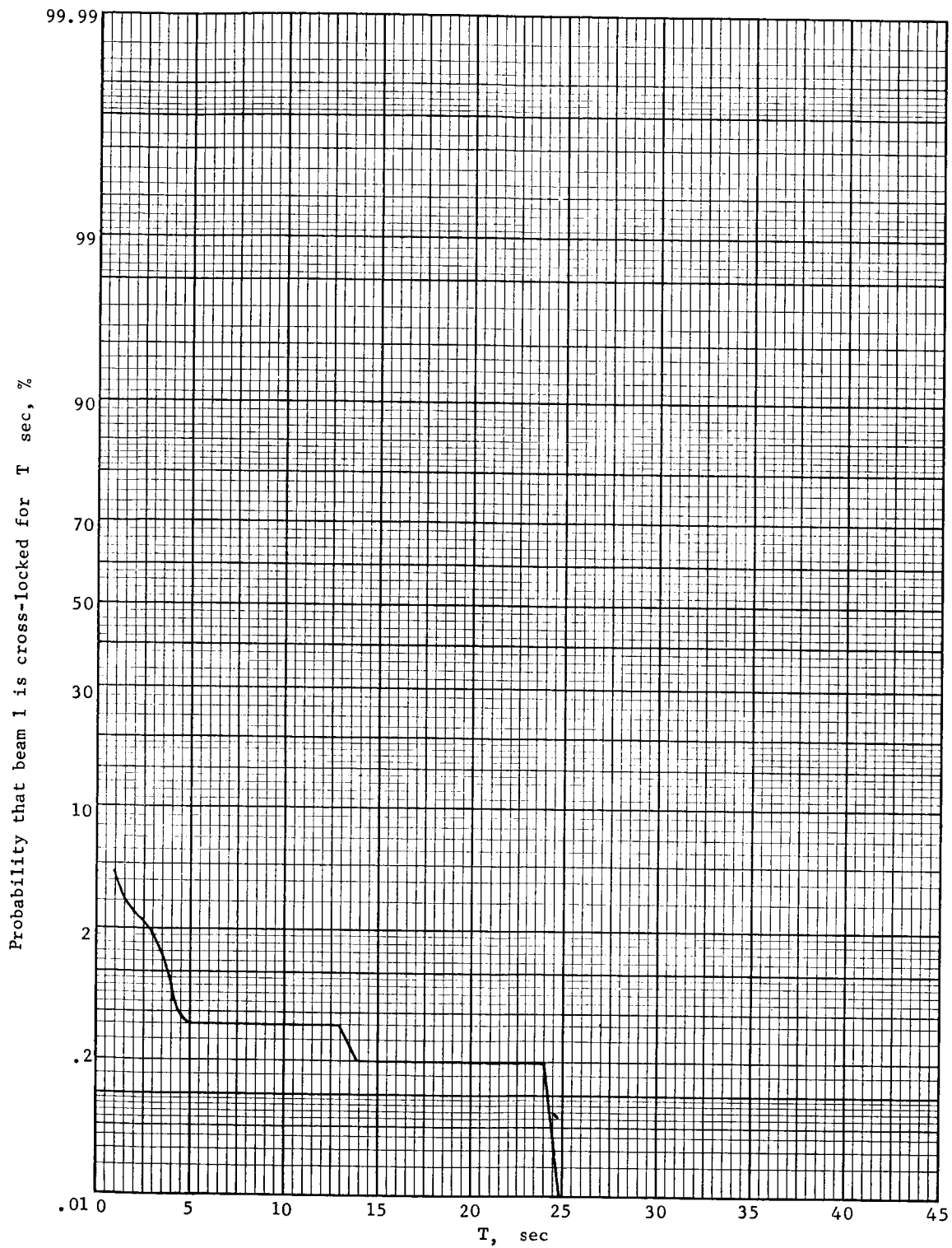
(a) Parachute Phase, Maximum Reflectivity Model, Beam 1

Figure 20.- Time-Correlated Monte Carlo Analysis Results: Probability That Individual Modified LM Radar Beams Will Be Cross-Locked for T sec
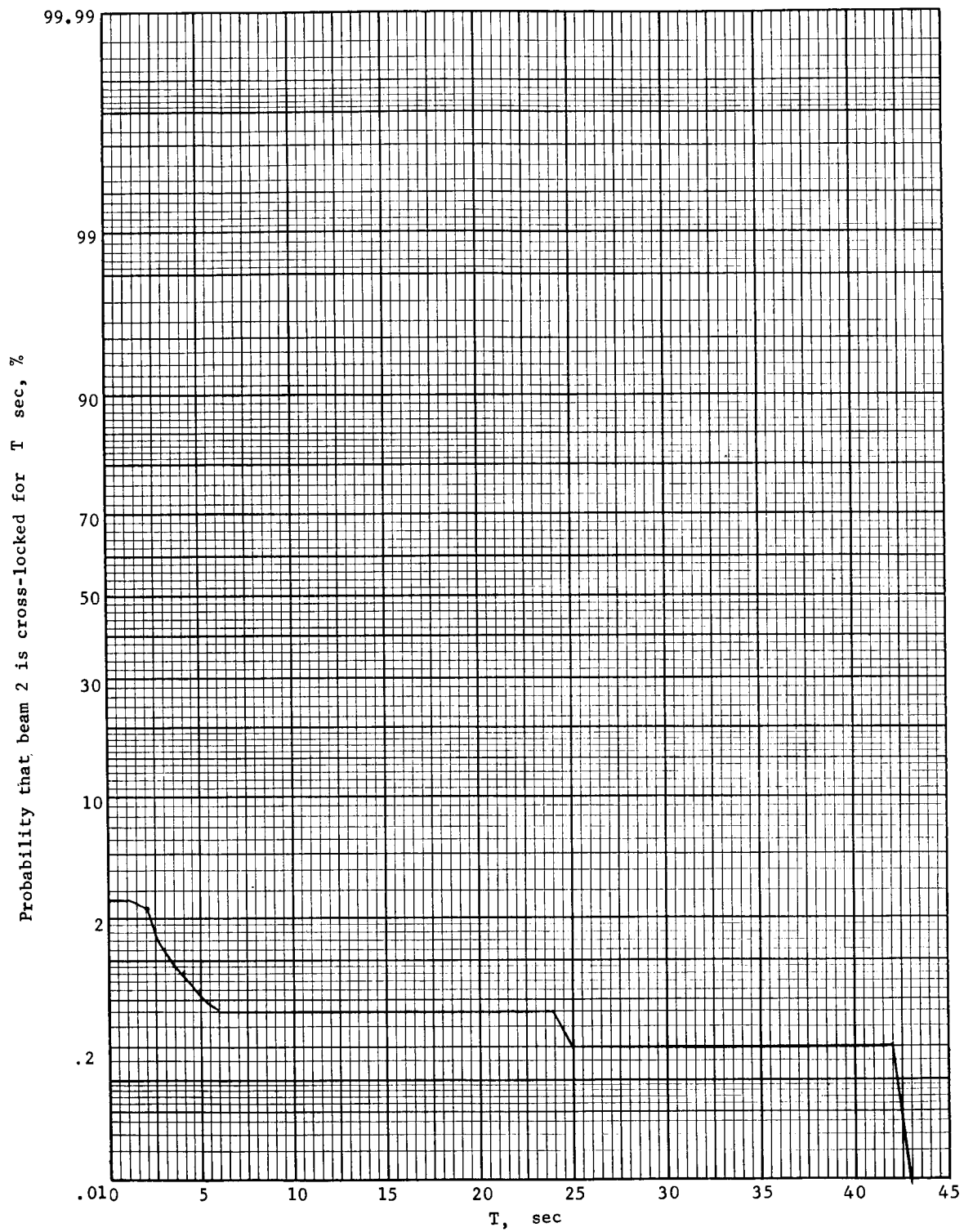
(b) Parachute Phase, Maximum Reflectivity Model, Beam 2

Figure 20.- Continued
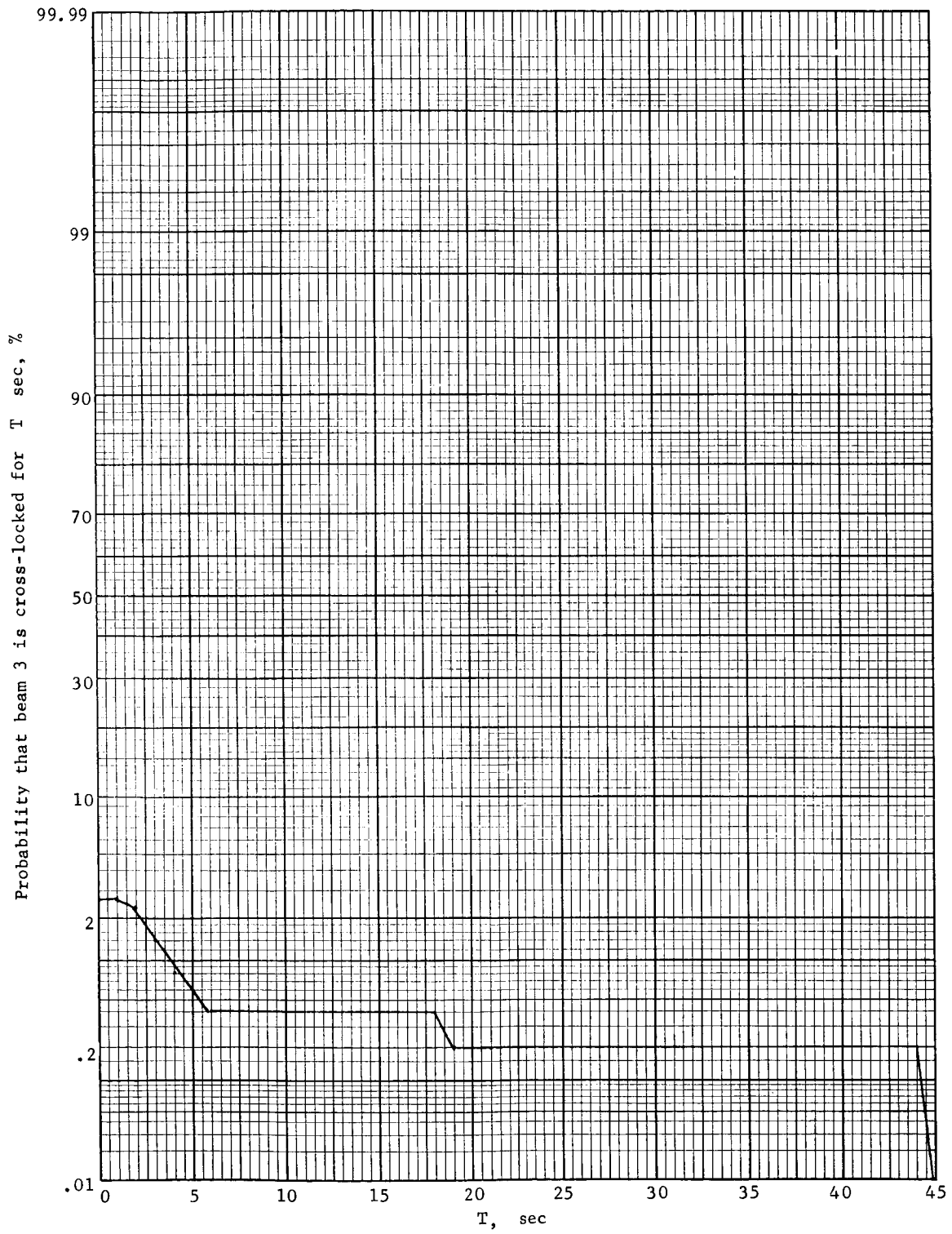
(c) Parachute Phase, Maximum Reflectivity Model, Beam 3

Figure 20.- Continued
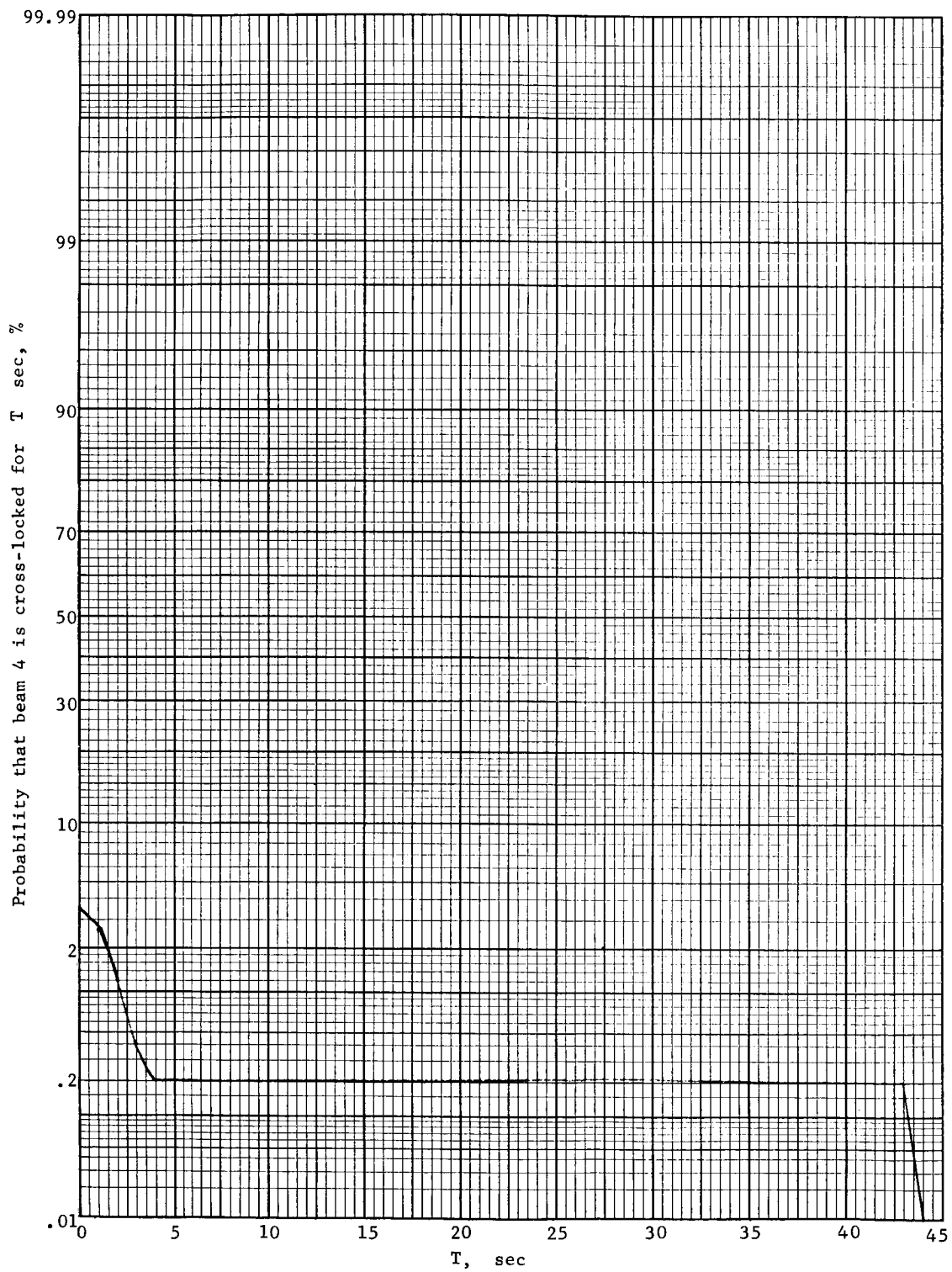
(d)   Parachute Phase, Maximum Reflectivity Model, Beam 4

Figure 20.- Concluded
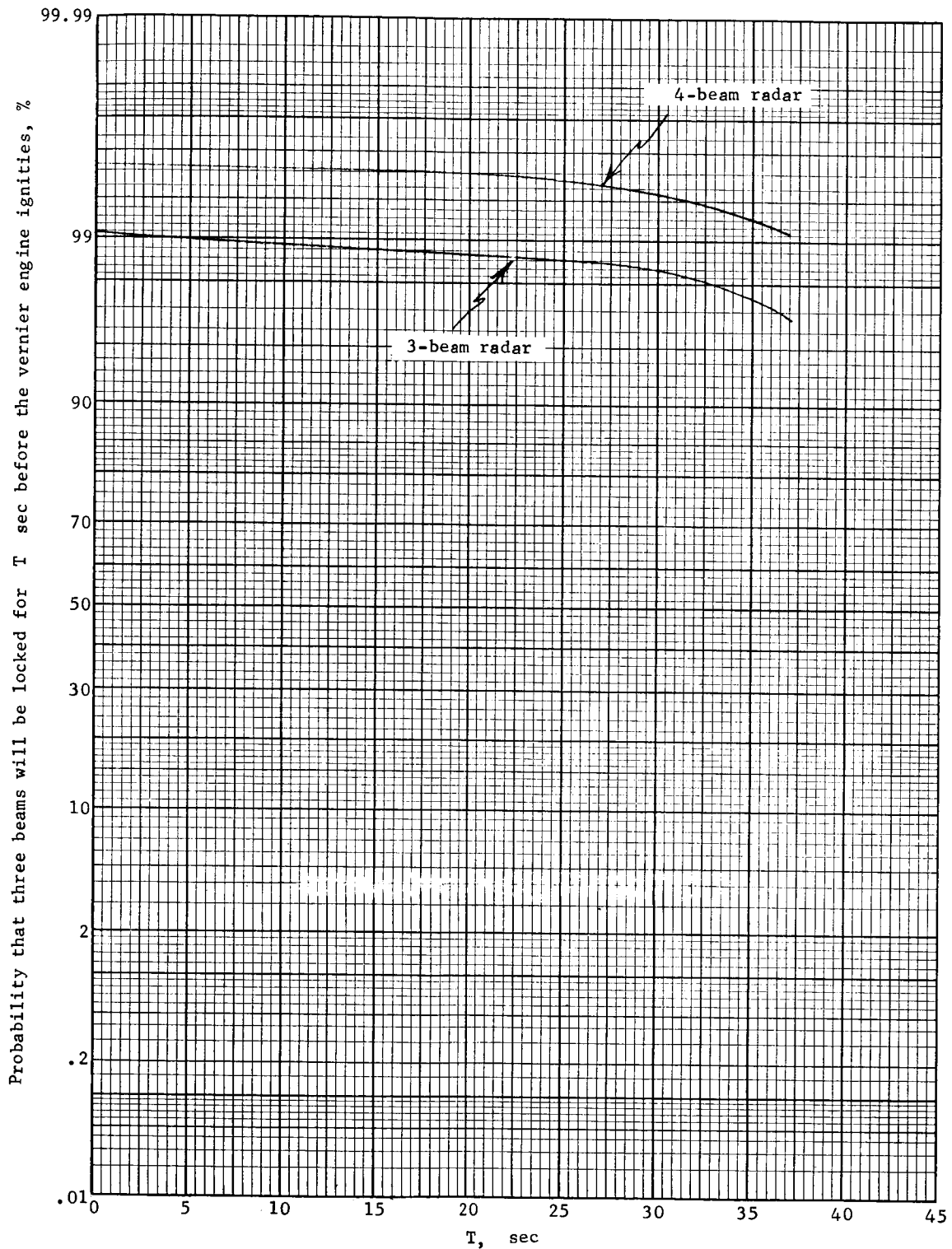
(a) Parachute Phase, Maximum Reflectivity Model

Figure 21.- Time-Correlated Monte Carlo Analysis Results: Probability That Three
Modified LM Radar Beams Will Be Locked for T sec Before the Vernier
Engine Ignites
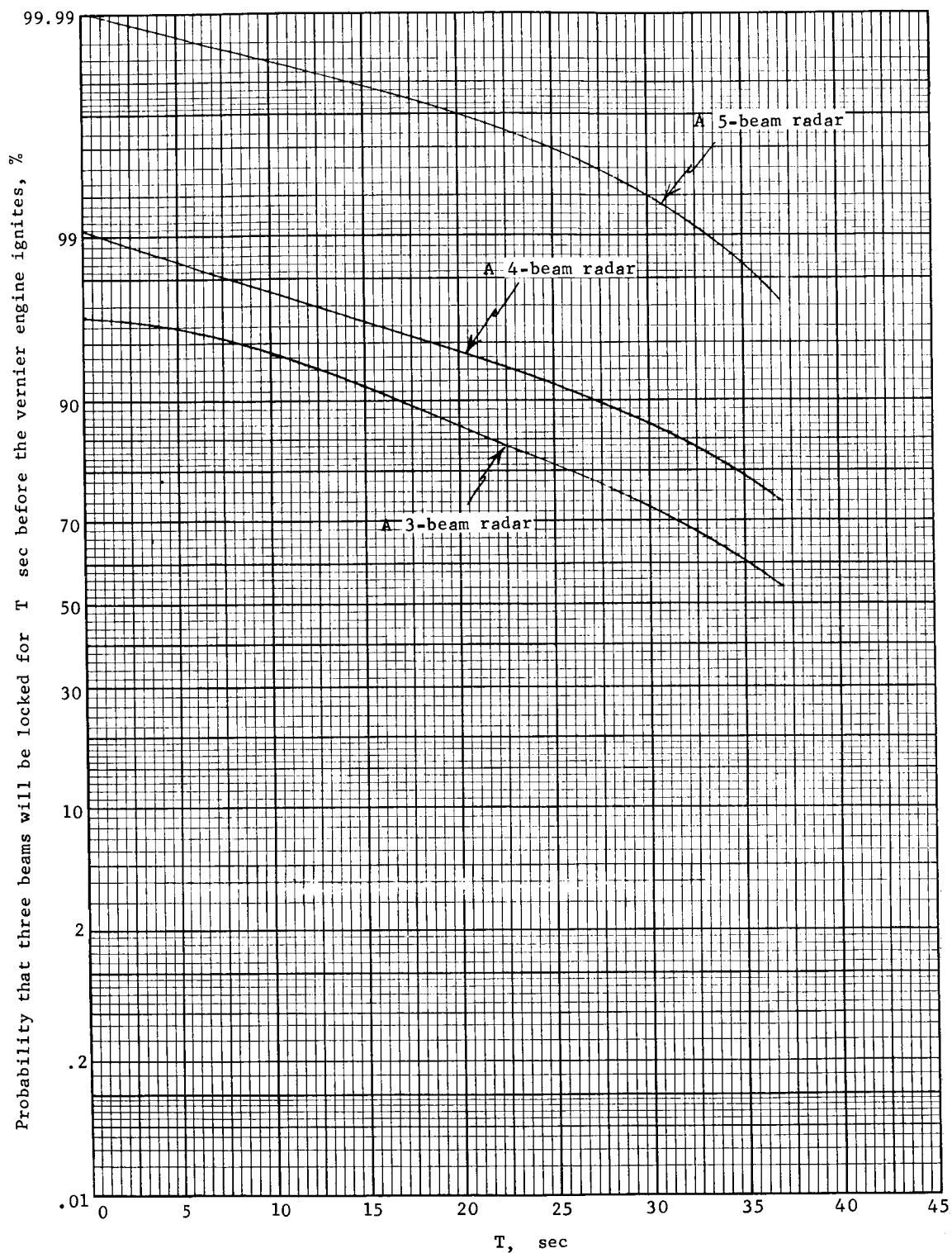
(b) Parachute Phase, Minimum Reflectivity Model

Figure 21.- Concluded
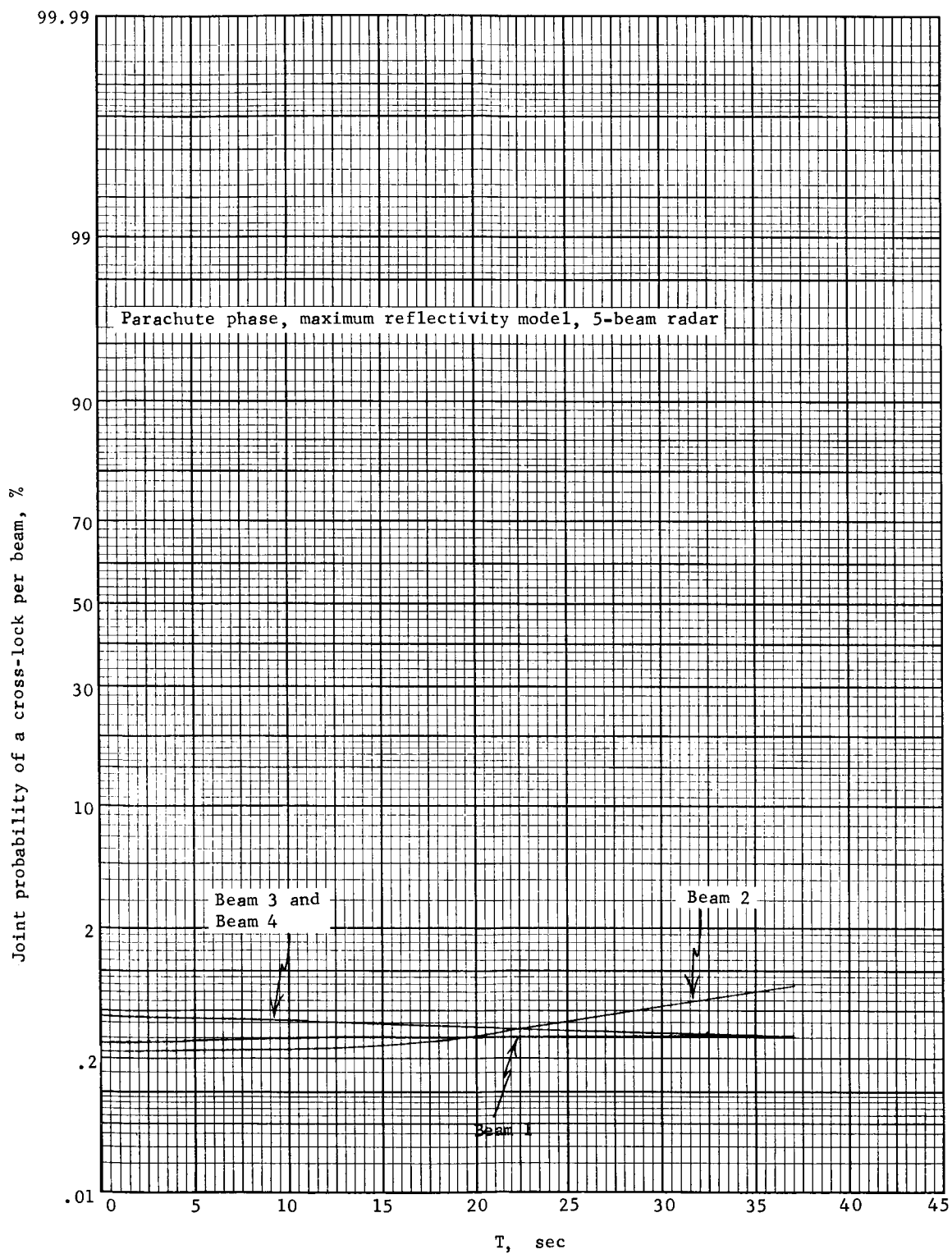
Figure 22.- Time-Correlated Monte Carlo Analysis Results: Probability That
Individual Modified LM Radar Beams Will Be Cross-Locked for
T sec Before The Vernier Engine Ignites

81
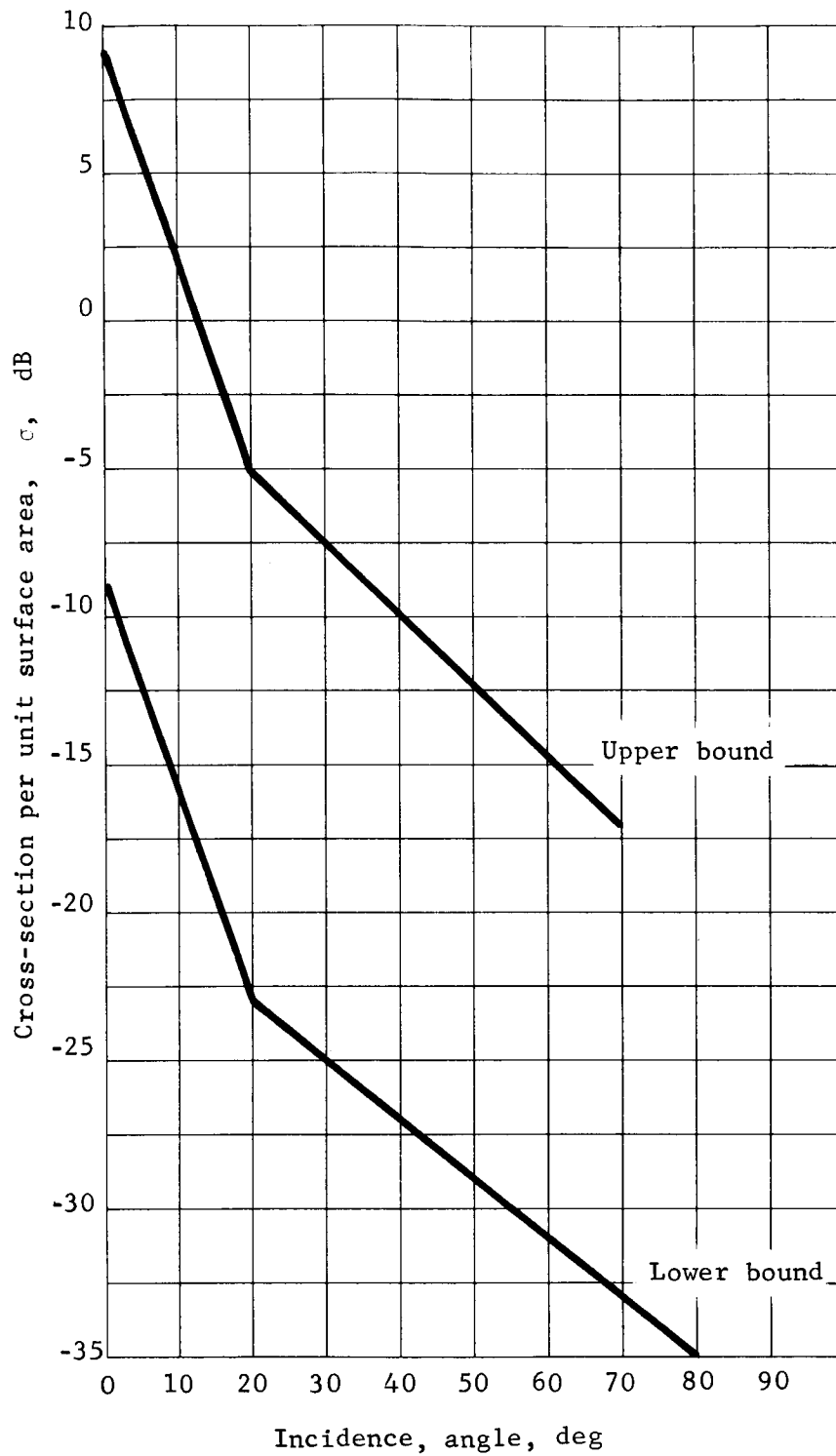
Figure 23.- Terrain Reflectivity Model Defined in the
Mars Engineering Specification
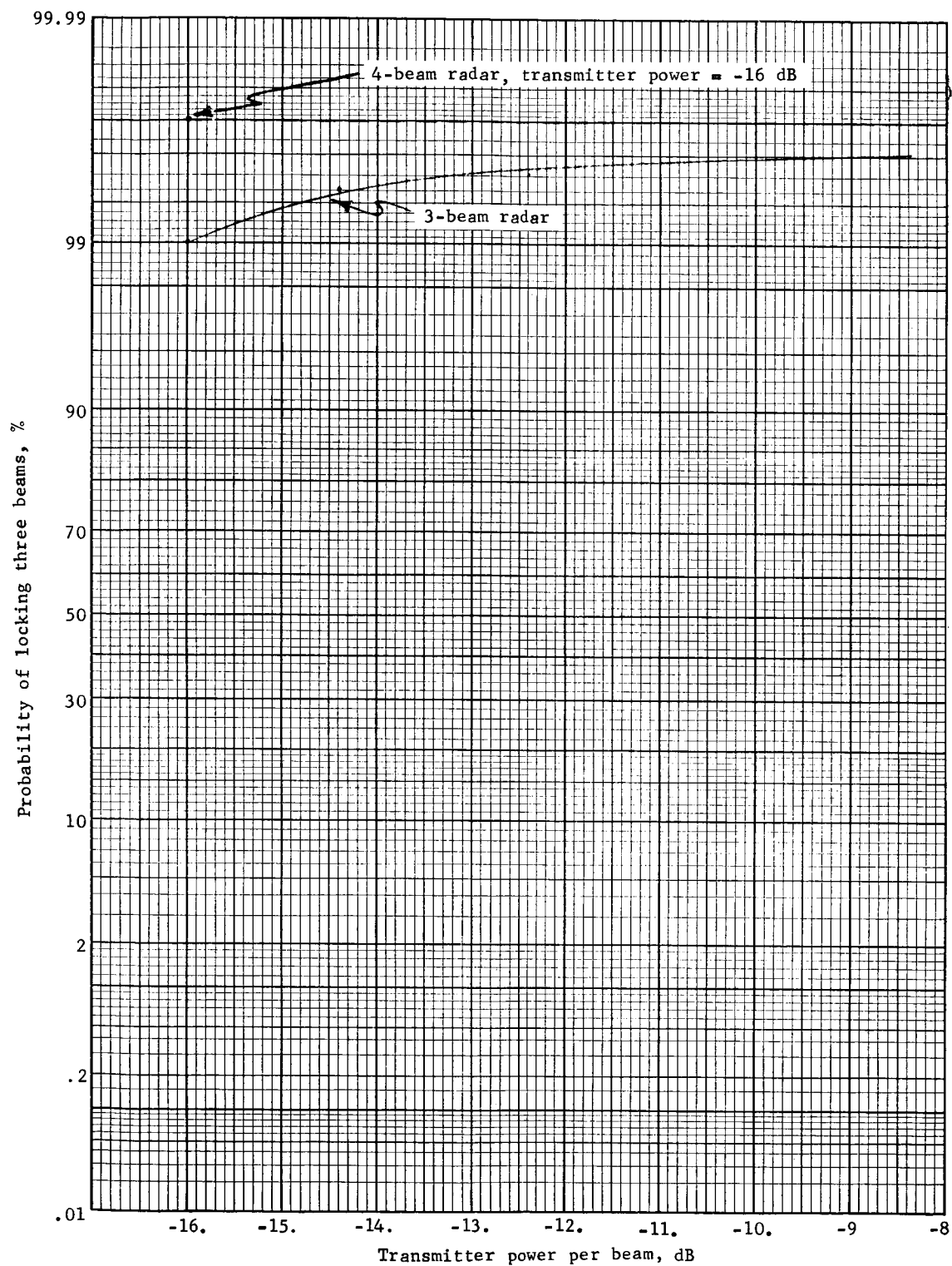
Figure 24.- Time Correlated Monte Carlo Analysis Results: Probability of
Locking Three Modified LM Radar Beams vs Transmitter Power

TABLE 11.- TRAJECTORY TIMES

Program	Trajectory time, sec		
	Mean	Maximum	Minimum
Terminal descent	33	45	27
Parachute	60	97	37

For the parachute descent and the maximum reflectivity model, all beams are locked or cross-locked at an altitude of 4000 ft (see Blocks 3 and 4 of table 10). However, the G&C requirement of one valid 3-beam update every 10 sec (see Section III-D) cannot be met with either the 3-, 4-, or 5-beam radar, because of the high number of cross-locks. At first glance, it would seem that the 5-beam system for which there is a 100% probability that three beams will be locked for 37 sec before reaching the altitude at which the descent engine ignites, would be adequate; however, there is no practical means for detecting which of the beams is providing good data (i.e., it is not feasible to detect which beams are cross-locked).

From Block 11 of table 10, we see that the probability of locking three beams before the Lander descends to 4000 ft is very low; only the 5-beam radar system gives a reasonable probability. Note, however, that there are no cross-locks (Block 12).

With a 4-beam radar we are 2.7% more likely to lock three beams at 4000 ft, and 21% more likely to lock three beams 37 sec before the Lander reaches 4000 ft, than if we use a 3-beam radar system.

If we use the parachute descent program and the minimum reflectivity model (Block 1 of table 10), we see that there is a 99.2%, 99.7%, and 100% probability of having three beams locked for at least 30 sec for the 3-, 4-, and 5-beam radars respectively. For the minimum reflectivity model (Block 9), the probabilities of locking three beams for the same length of time (30 sec) are 70.7% for the 3-beam radar, 89% for the 4-beam radar and 100% for the 5-beam radar. Only with the 5-beam radar are three beams locked for a satisfactory length of time.

During the terminal-descent phase, all radars will have, three beams locked with 100% probability for the 27 sec before the engine cuts off, for both the maximum and minimum reflectivity models. The probabilities for the total time that three beams will be locked for each type of radar system are indicated in Blocks 5 and 13.

Actual cross-locks occurred during the parachute descent, using the maximum reflectivity model (Blocks 2 and 4). Most of these occurred for only a short time, such as when a wind gust tipped the vehicle and caused a beam to unlock and then cross-lock. However, a few times (two trajectories/beam), the beams cross-locked during the initial search and remained cross-locked until the Lander descended to 4000 ft. As mentioned before, this situation is not tolorable.

In summary then:

1) With the reflectivity models of figure 23, the MOD-LM radar gave satisfactory probabilities both for having three beams locked and for having no cross-locks during the terminal descent.

2) During the parachute descent, using the maximum reflectivity curves, the 4- and 5-beam radars gave satisfactory probabilities of locking three beams; however, for both systems, there were an intolerable number of cross-locks.

3) The results obtained using the minimum reflectivity curve indicate that none of the radars performed satisfactorily. Accordingly, we made another time-correlated Monte Carlo run using a reflectivity model supplied by Dr. Richard F. Broderick (see figure 25). The upper-bound curve shown in this figure produces the greatest number of unlocks and was used in this new run. The radar that was simulated was a cw radar similar to the MOD-LM radar. The results of this analysis (figures 26 and 27) show that for the 4-beam radar, the probability of locking three beams satisfied the G&C requirement, and that, for the 5-beam radar, the probability of having three beams locked for the 37 sec before the Lander descended to 4000 ft was 100%.
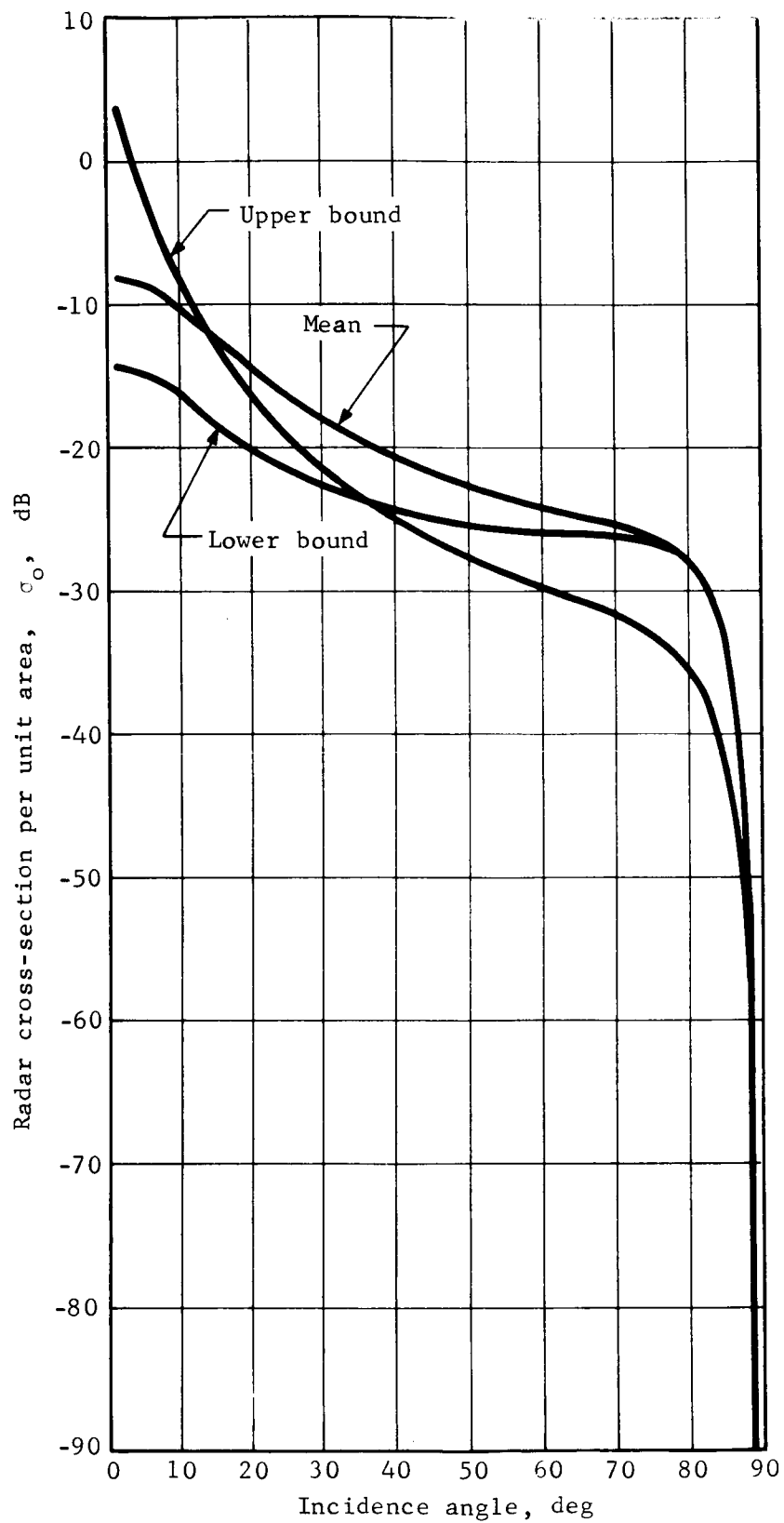
Figure 25.- Reflectivity Model Used in the Second
Time-Correlated Monte Carlo Analysis

3-, 4-, and 5-beam radars
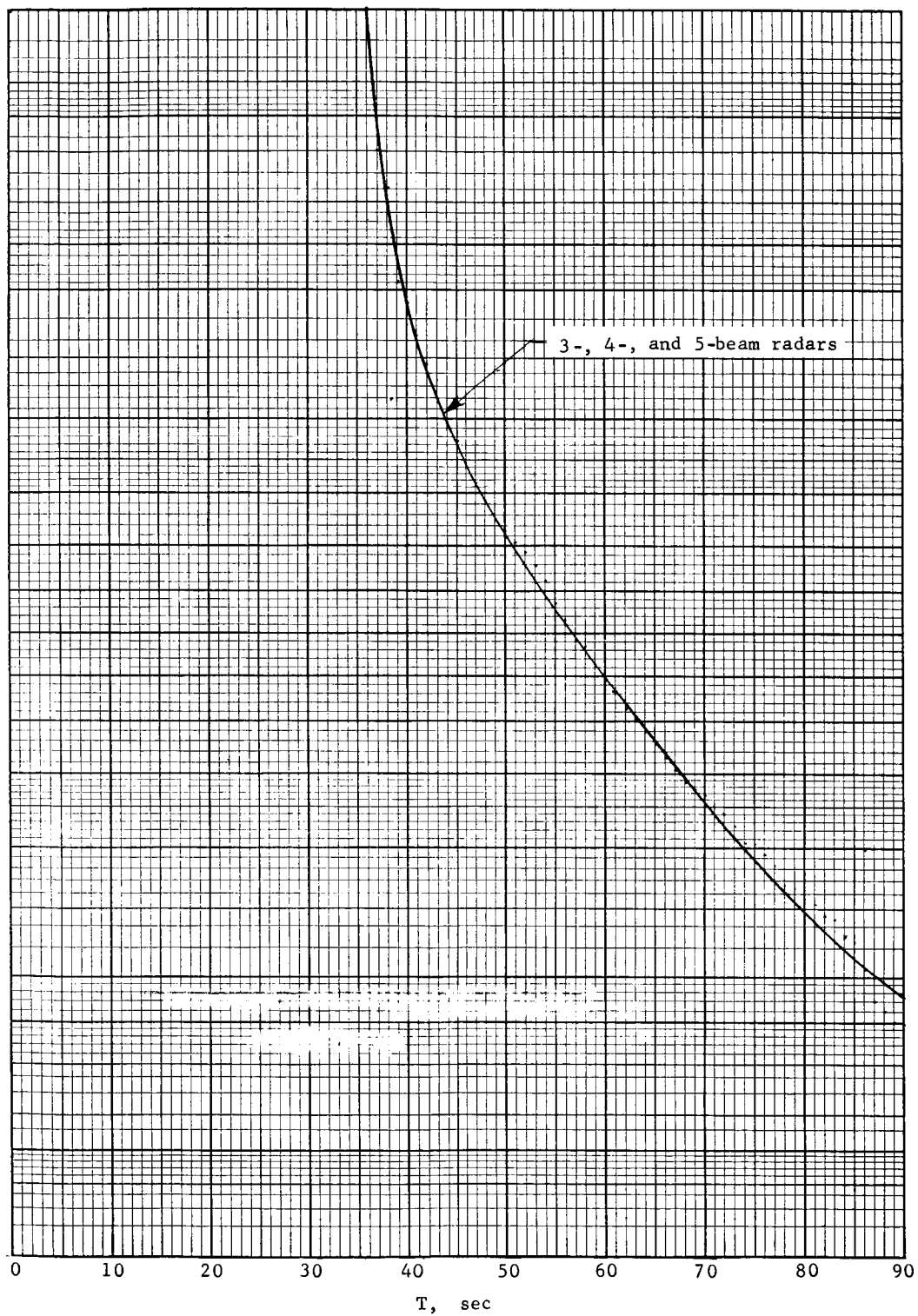
Parachute phase, maximum reflectivity model from figure 25

Figure 26.- Second Time-Correlated Monte Carlo Analysis Results: Probability That Three J_o Radar Beams Will be Locked for T sec
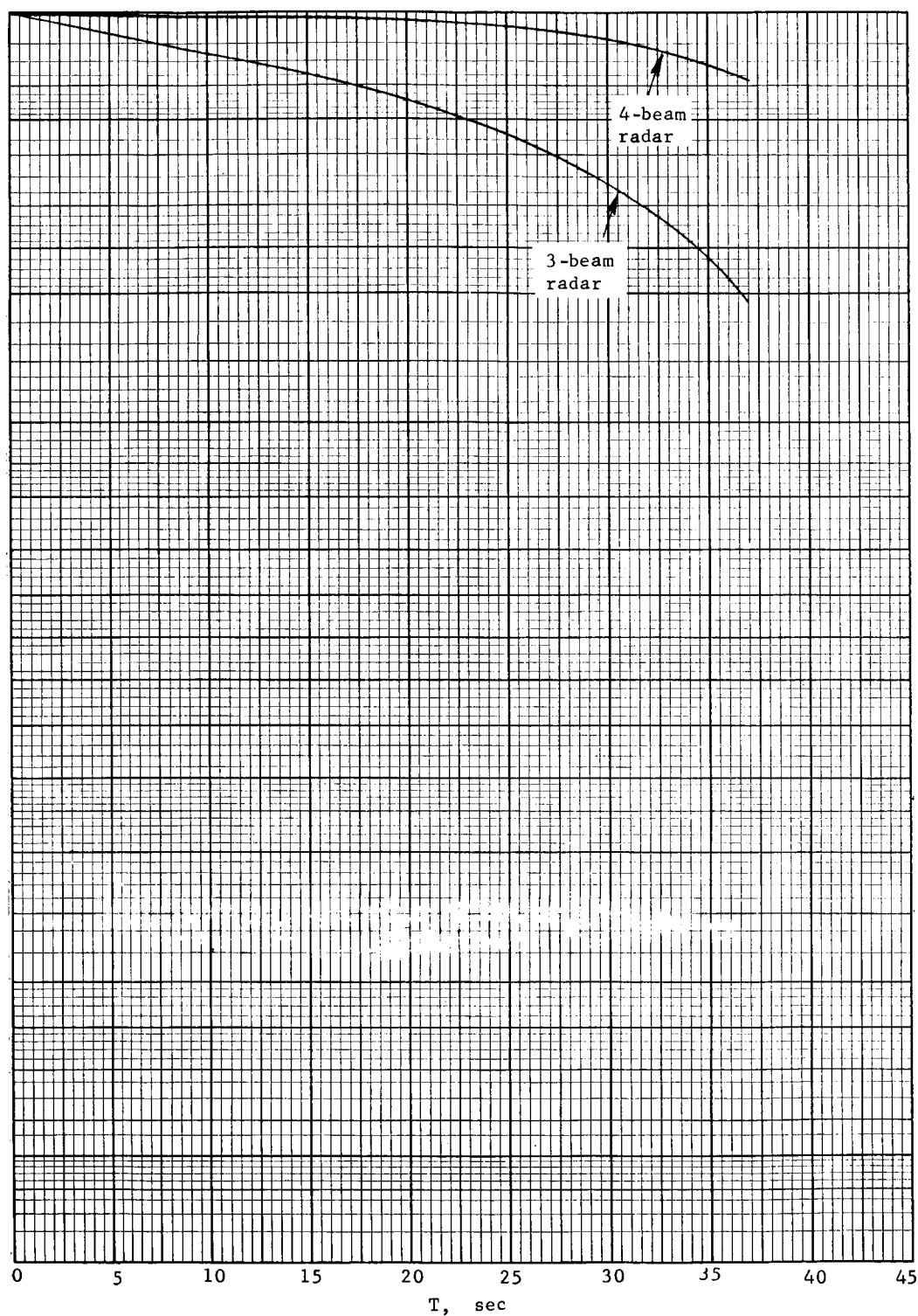
Parachute phase, maximum reflectivity model from figure 25

Figure 27.- Second Time-Correlated Monte Carlo Analysis Results:
Probability that Three J_o Radar Beams will be Locked
for T sec Before the Vernier Engine Ignites

4) Most cross-locks existed for a very short time; however, when they occurred during the initial acquisition, they were apparently maintained throughout the terminal descent. Such cross-lock conditions are intolerable.

5) The 4-beam radar that had a square beam pattern will meet the G&C requirements and appears to be the best choice in terms of the tradeoff of transmitter power and the probability of having three beams locked.

V. BESSEL SIDEBAND RADAR STUDY

A technique to achieve isolation from receiver mixer noise (a consideration for the velocity sensor) is frequency modulation of the carrier. The following is an evaluation of a Bessel sideband radar in which data is processed at the J_1 sideband.

The radar is a modified AN/APN-187 Doppler radar system. The general characteristics of this radar are: a 4-beam sequential lobing system; a time-shared sine-cosine tracker; Bessel-J_1 sideband data processing; a program bandwidth for the tracking filter; and sequential frequency modulation on two frequencies.

A. Radar Math Modeling

A block diagram of the J_1 radar circuitry that was simulated in the MOD6MV is shown in figure 28. The following is a description of the detailed parameters and calculations contained in each block.

1. <u>Beam switching (Block A)</u>.- The beam-switching rate of the radar is 24 Hz. This rate is maintained in the simulation by a counter that switches beam positions every 1/96 sec. The radar as modeled uses the MOD-LM velocity-beam geometry shown in figure 15.

2. <u>Modulation frequency switching logic (Block B)</u>.- The transmitter sequentially switches between 148 and 161.5 KHz at a rate of 12 Hz. A counter is used to switch these modulation frequencies every 1/12 sec.

3. <u>Bessel coefficient (Block C)</u>.- The Bessel function generator used is a subroutine called BESJ taken from reference 9. The Doppler processing is done at the frequency of the J_1 sideband. The argument for the Bessel function is

$$2(I) \sin (2\pi R/\lambda) \tag{39}$$

where the deviation index I is 1, the range in the beam is R, and the wavelength of the carrier λ is 0.074 ft.

4. <u>Geometry (Block D)</u>.- The selected ground slope is read into the program and is used to define a unit vector $\overline{\mu}_n$ perpendicular to the terrain. Then, the incidence angle of each beam is calculated in the following manner:
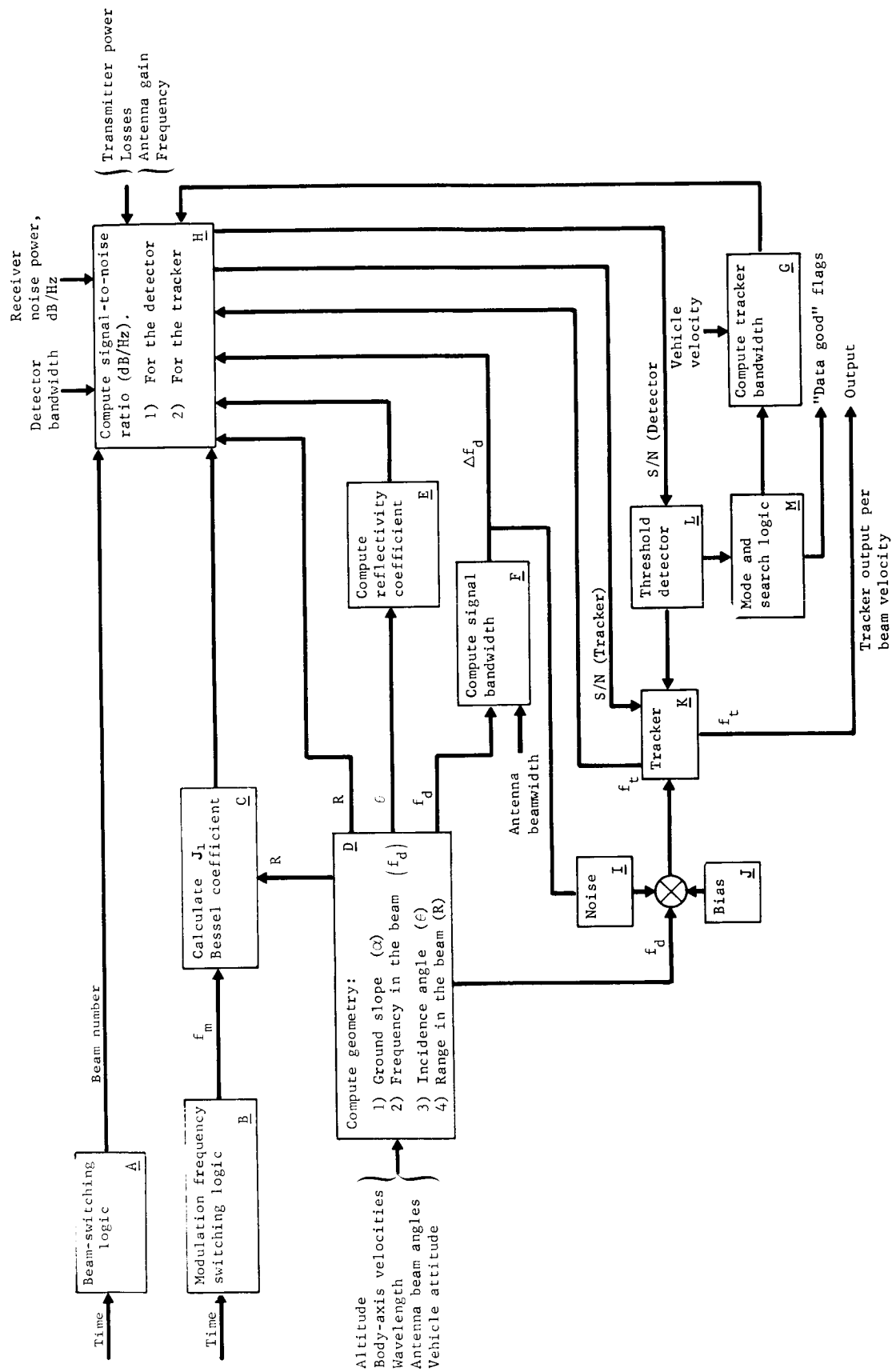
Figure 28.- Block Diagram of the J_1 Radar Circuitry

$$\left[\overline{\mu}_{Ij}\right] = [\underline{A}]^T \left[B_j\right] \left(\overline{\mu}_{Bj}\right), \quad \text{where } j = 1, 2, 3 \qquad (40)$$

$$\cos \theta_j = \overline{\mu}_{Ij} \cdot \overline{\mu}_n \qquad (41)$$

where $\left[\mu_{Ij}\right]$ is the pointing direction of the jth beam in inertial coordinates, $[\underline{A}]^T$ is the body- to inertial-coordinate-system transformation matrix, $\left[\underline{B}_j\right]$ is the jth beam to body-coordinate-system transformation matrix, $\overline{\mu}_{Bj}$ is the jth beam unit vector expressed in body coordinates, and θ_j is the incidence angle associated with the center beam propagation vector.

The range along each beam is obtained from equations (42) and (43).

$$R = D/\cos \theta; \qquad (42)$$

$$D = \overline{X} \cdot \overline{\mu}_n \qquad (43)$$

where $\overline{X}$ is the position vector of the vehicle and D is the perpendicular distance from the vehicle to the terrain.

The Doppler frequencies of the beam are calculated by: (1) transforming the inertial velocities of the vehicle into body-axis velocities; (2) transforming the body-axis velocities into beam velocity components; and (3) converting beam velocities into Doppler frequencies.

$$\overline{V}_B = [\underline{A}] \, \overline{V}_I \qquad (44)$$

$$V_{B1} = \overline{\mu}_{B1} \; ; \; \overline{V}_B \qquad (45)$$

$$V_{B2} = \overline{\mu}_{B2} \; ; \; \overline{V}_B \qquad (46)$$

$$V_{B3} = \overline{\mu}_{B3} \; ; \; \overline{V}_B \qquad (47)$$

where $[\underline{A}]$ is the inertial- to body-coordinate-system transformation matrix, $\overline{V}_I$ is the vector that expresses the inertial velocity of the vehicle, $\overline{V}_B$ is the velocity of the vehicle expressed in body coordinates, and V_{B1}, V_{B2}, and V_{B3} are the velocities of Beams 1, 2, and 3, respectively.

The Doppler frequencies are:

$$f_{dj} = 2V_{Bj}\big/\lambda_{dj} \qquad\qquad (48)$$

where f_{dj} is the Doppler frequency in a beam and λ_{dj} is the wavelength of that beam.

5. Reflectivity model (Block E).- The reflectivity model used for this MOD6MV radar simulation is shown in figure 23. The two bounds shown in the figure include all the reflectivity models that have been proposed for the lunar surface. A curve-fit was obtained for each bound (the respective equations are keyed on input).

6. Signal bandwidth (Block F).- The spectral bandwidth of a Doppler signal is calculated as follows:

$$\triangle f_d = \frac{2\triangle\gamma}{\lambda}\,\left|\overline{V}_B\right|\,\sin\gamma \qquad\qquad (49)$$

where $\triangle\gamma$ is the average 3-dB beamwidth of the antenna (0.069 radians), $\left|\overline{V}_B\right|$ is the maximum velocity of the vehicle relative to the reflecting surface, and γ is the angle between the centerline of the beam and the velocity vector.

Thus, the spectrum bandwidth is proportional to the component of velocity perpendicular to the beam-pointing direction, as modified by the 3-dB beamwidth of the antenna. The spectrum is assumed to be Gaussian.

7. Tracker bandwidth (Block G).- The tracker of the J_1 radar contains filters whose bandwidths depend on the mode in which the radar is operating. The radar can operate in three different modes:

Mode 1 -- Initial search mode in which the filters have a bandwidth equivalent to the maximum expected Doppler frequency (16 000 Hz)

Mode 2 -- Final phase of search during which the filters have a bandwidth 1/8 of that in Mode 1 (2000 Hz)

Mode 3 -- Normal track mode during which the filters have a bandwidth which is proportional to the velocity

94

When the J_1 radar operates in Mode 3, we have assumed that the velocity vector is always centered in the beam pattern. The filter bandwidth is then programed as the product of a coefficient times the total velocity of the vehicle. The coefficient is

$$C = 2\Delta\gamma \sin \gamma \qquad (50)$$

where $\Delta\gamma$ is the beamwidth of the antenna (4 deg) and γ is the beam splay angle (20 deg).

8. Signal-to-noise ratio (Block H).- Two signal-to-noise (S/N) ratios are computed: one for the tracker filters and the other for the threshold detector. The latter has a fixed bandwidth of 100 Hz. The S/N ratio may be defined in a peak-power, spectral-density sense. From figure 29, the S/N ratio according to this definition would be SI/NO. This definition was maintained in the simulation.
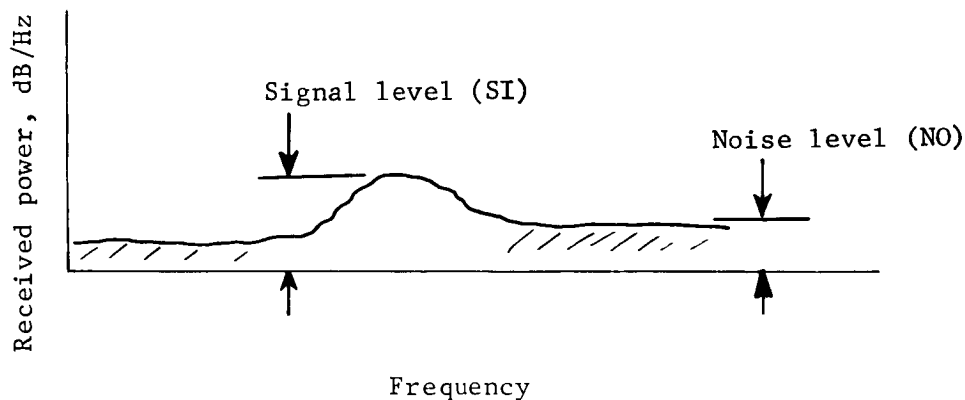
Figure 29.- Power Spectral Density Used in the J_1 Radar Simulation

The received power may be calculated from equation (51).

$$PR = \frac{P_t \; \lambda^2 \; G \; W \; \sigma_o \; L \; E}{(4\pi)^2 \; R^2 \; \cos \theta} \qquad (51)$$

where PR is the power received, P_t is the transmitter power (167 mW), λ is the carrier-frequency wavelength (13.325 GHz), G is the antenna gain (30 dB), W is the antenna weighting factor (3.5 dB), σ_o is the relative cross-section of the radar, L is the total microwave loss (5.1 dB), and E is the Bessel coefficient. The noise spectral density (dB/Hz) is calculated from equation (52).

$$\frac{dB}{Hz} = KTN \tag{52}$$

where K is Boltzmann's constant, $T = 290°K$, and N is the receiver noise (9 dB).

Next, the received power is numerically integrated for the tracker filters and for the detector. As demonstrated in figure 30, the signal spectrum and filter responses ideally have rectangular shapes. Power integration is required when the tracking rates induce a lag between the output of the voltage control oscillator (VCO) and the incoming Doppler signal.
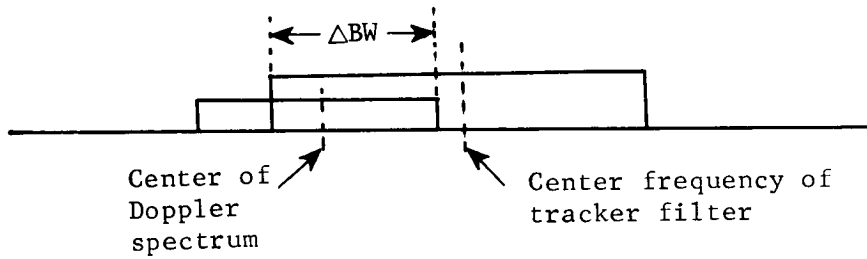
Figure 30.- Idealization of Received Power

When this situation is detected in the simulation, the received power is modified as shown in equations (53) and (54).

$$P_{RT} = PR + 10 \log\left(\frac{\triangle BW_t}{\triangle f_d}\right) \tag{53}$$

$$P_{RD} = PR + 10 \log\left(\frac{\triangle BW_D}{\triangle f_d}\right) \tag{54}$$

where P_{RT} is the signal power in the tracking filter bandwidth, $\triangle BW_t$ is the proportional bandwidth of the signal in the tracking filter (see fig. 30), $\triangle f_d$ is the signal bandwidth, P_{RD} is the signal power in the detector, and $\triangle BW_D$ is the proportional bandwidth of the signal in the detector (see fig. 41).

To obtain an approximate estimate of the peak power level of the signal spectrum in the tracker and in the detector, the powers

P_{RT} and P_{RD} are divided by $\triangle BW_t$ to obtain dB/Hz. Then, the S/N ratio can be obtained from equation (52).

9. Fluctuation noise (Block I).- The statistical character-istics of the tracker output are obtained by adding the appropriate noise to the Doppler frequency f_d. Because the signal is assumed to have a Gaussian distribution, the rms level of the frequency jitter σ and the correlation time of the noise τ are functions of the Doppler spectral bandwidth.

$$\sigma = \frac{\triangle f_d}{2} \tag{55}$$

$$\tau = \frac{1}{\pi \triangle f_d} \tag{56}$$

10. Bias (Block J).- Although we could have added biases to the signal, we did not; the outcome of the simulation was predicta-ble and nothing would have been gained by including them.

11. Tracker (Block K).- As shown in equation (57), the closed-loop transfer function of the J_1 tracker was represented by a first-order lag.

$$1/(1 + \tau s) \tag{57}$$

where $\tau = 0.3$ sec.

12. Threshold detector (Block L).- The threshold detector was modeled to allow a different criterion (input variable) for each mode; 3 dB is the criterion for normal tracking.

13. Mode and search logic (Block M).- If a beam becomes un-locked on the proposed system, all beams go into Mode 1. During this search, the bandwidth of the tracker filter is held wide open for one sec. If, at the end of one sec, all beams are above the threshold, then the radar goes to Mode 2; if not, the radar is held in Mode 1 for another sec. If the radar is operating in Mode 2 and at any time during a 1-sec interval all the beams are above the threshold value, the tracker immediately switches to Mode 3; but, if at the end of one second this has not occurred, then the tracker reverts to Mode 1 (see table 12).

The only signal driving the VCO is the error signal of the discriminator (i.e., when the radar is first turned on, the VCO will be randomly positioned, and is not driven in a search mode).

TABLE 12.- TRACKER MODES

Mode	Function	Tracker filter bandwidth, Hz	Time, sec
1	Initial search	16 000	1
2	Search	2 000	<1
3	Normal track	Variable	

The flags that indicate "data good" are also provided by the logic.

B. MOD6MV Results

The J_1 radar, as it was modeled here, was not found to be acceptable. The simulation showed that:

1) The bandwidth of the detector was too narrow (100 Hz); break-lock conditions frequently existed due to noise spikes and tracker lags.

2) The variable-bandwidth filter in the tracker does not work well; the coefficient cannot be determined unless we assume an angular distance between the velocity vector and the centerline of the beam exists. The angle assumed must be equal to the beam splay angle; but, even so, this causes the filter bandwidth to be too narrow whenever the roll axis of the vehicle is not aligned with the velocity vector.

3) The detector has no memory (i.e., momentary fading of the signal causes the radar to break-lock immediately).

4) The tracker is not allowed to break-lock on one beam. Consequently, if the signal to a beam is lost, all channels must revert to Mode 1.

Figures 31a thru 31c are shown in order to clarify the above conclusions. These curves were obtained from computer runs of the MOD6MV. The shaded areas in the figures represent the times at which the beams were locked. This run imposed very moderate conditions -- no ground slope, and a low velocity (initially 150 fps) in a vertical descent from 4000 ft -- and there should have been no tendency for the radar to break-lock. Nonetheless, numerous break-locks did occur, because the noise and acceleration momentarily drove the signal out of the tracker and detector bandwidths. Since the tracker had no memory, break-locks on all beams occurred immediately.
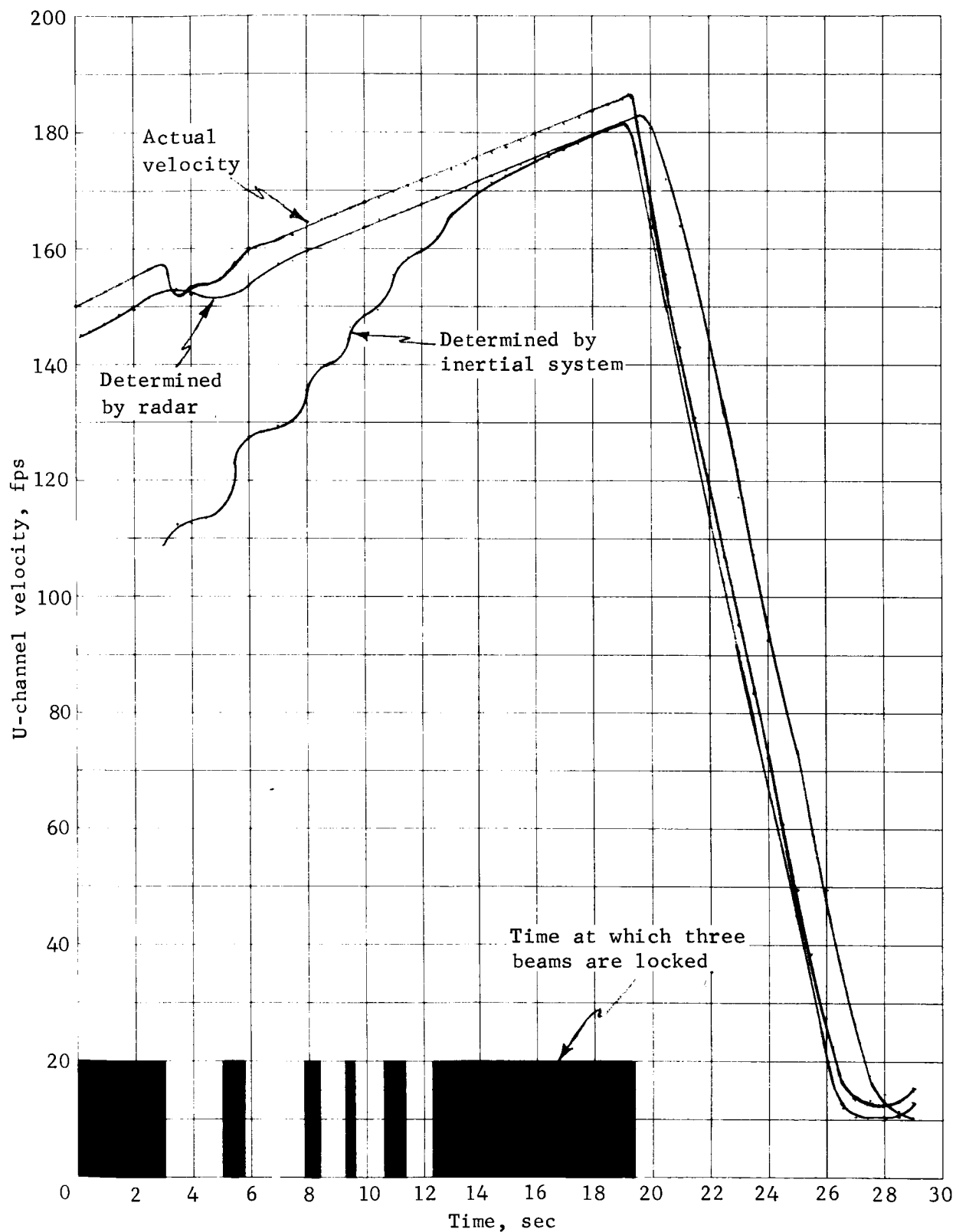
(a) U-Channel Velocity vs Time

Figure 31.- MOD6MV Computer Program Results: Effect of Beam Locking on Velocity, J_1 Radar System
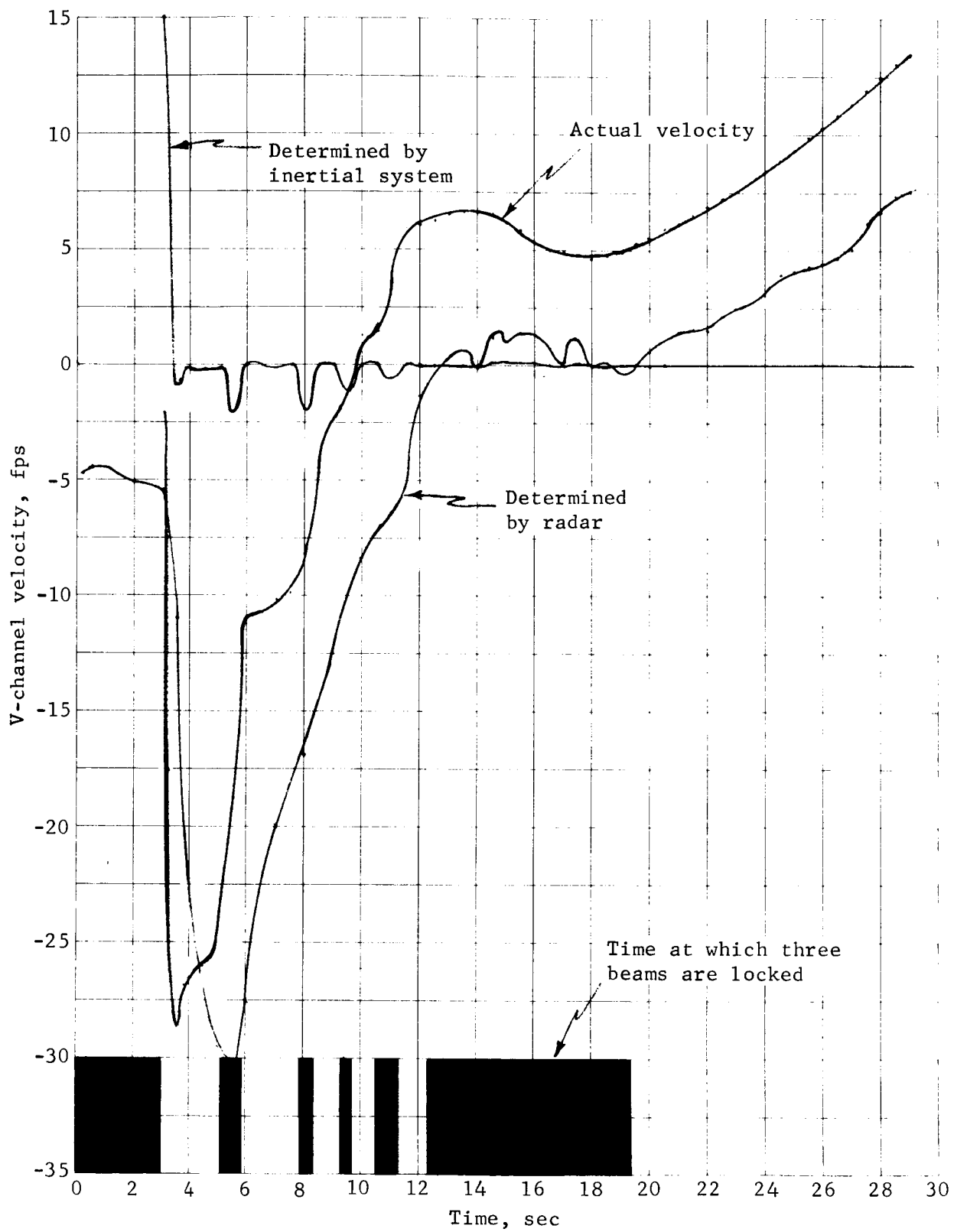
(b)   V-Channel vs Time

Figure 31.- Continued
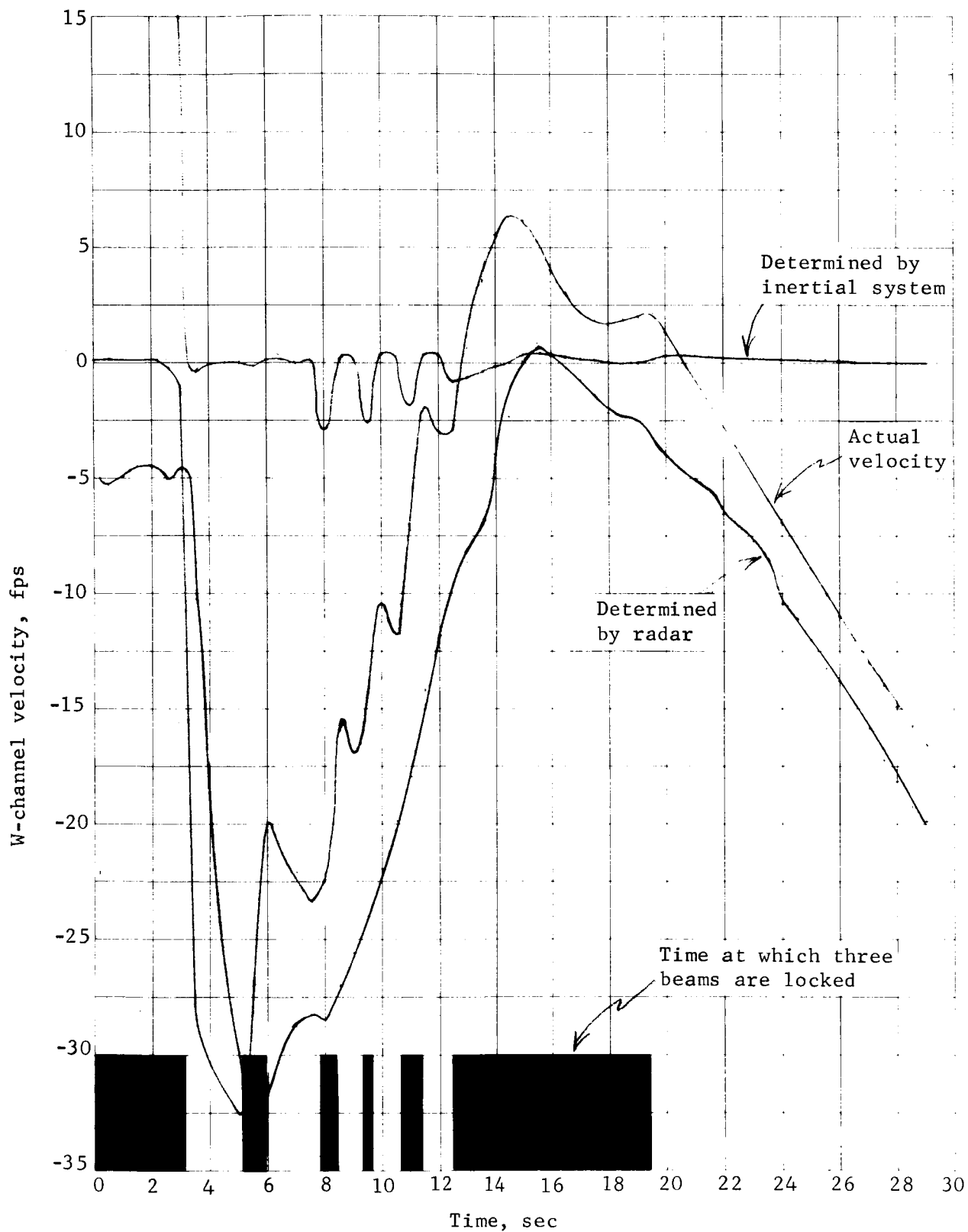
(c) W-Channel Velocity vs Time

Figure 31.- Concluded

C. Monte Carlo Analysis Results

The static Monte Carlo program described in Appendix C was used to determine the probability of data loss (break lock) for the J_1 radar. Each time a beam was unlocked, all beams were considered to be unlocked. The results of this analysis are shown in figure 32.
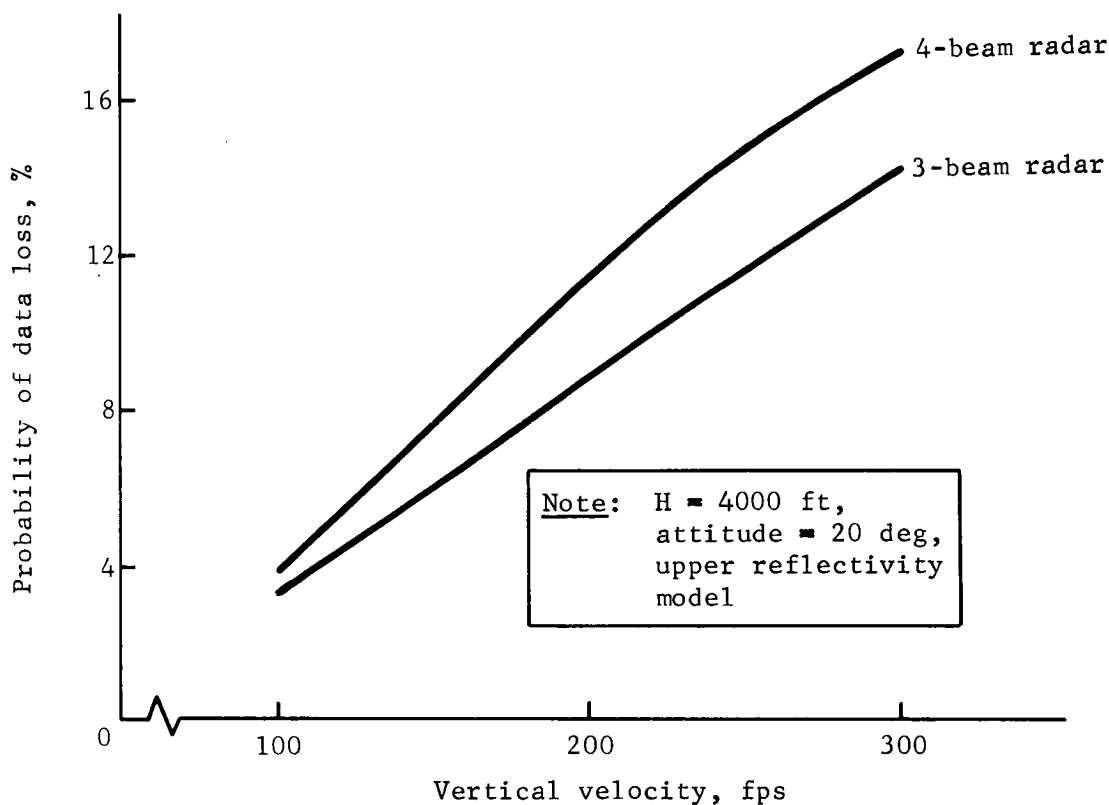
Figure 32.- Static Monte Carlo Analysis Results: Probability of Data Loss for the J_1 Radar System

The reflectivity model used is the same as shown in figure 23. The figure indicates that there is a high probability of losing data. Some of the reasons for this are:

1) A range hole occurs at 6400 ft (see fig. 33);

2) As a result of sequential lobing, the efficiency factor is -6 dB;

3) Each time a channel unlocks, all beams are declared unlocked;

4) Whenever a break-lock occurs with one-frequency modulation, an additional efficiency factor of -3 dB is used.

In contrast to these results, using the minimum reflectivity model resulted in a loss of data 100% of the time.

Figure 33 shows that, during the descent, the J_1 radar has a range hole at about 3000 ft. This was probably responsible for some of the unlocks shown in figure 31.
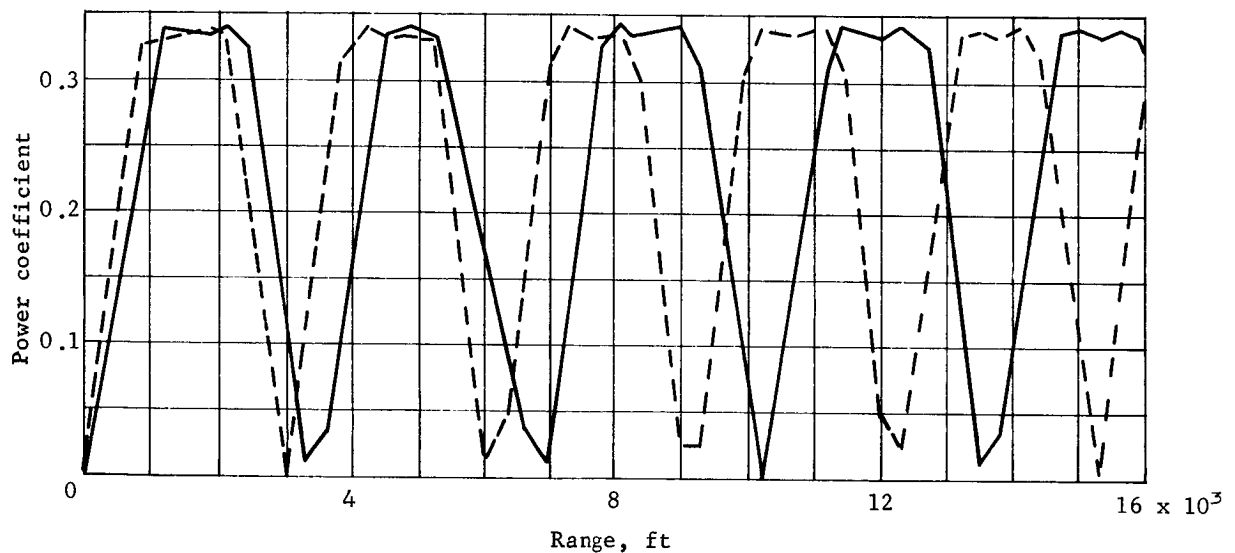
Figure 33.- Bessel Power Coefficients for the J_1 Radar System

The preceding Monte Carlo and MOD6MV results are presented in response to the contract task to model and analyze a Bessel sideband radar. The particular design used in this evaluation turned out to be poorly suited to the mission. However, certain features and approaches which were used are attractive, and further evaluation should be made with better-chosen parameters. Unfortunately, time did not permit an iterative design analysis during this study.

VI.   ALTERNATIVE RADAR MECHANIZATION STUDY

A.   Radar Modeling and Approach

The static Monte Carlo program described in Appendix C was used as a tool for obtaining tradeoff data with regard to modulation techniques and cross-coupling. Three modulation techniques can be considered for the TDLR. These are: (1) continuous wave $\left(cw-J_o\right)$ modulation; (2) Bessel sideband (J_1) modulation; and (3) interrupted continuous wave (ICW) modulation. To compare the three modulation techniques, three static Monte Carlo radar subroutines were created, each representing one type of radar. Each radar was modeled in such a way that the parameters which were not dependent on modulation technique were equivalent.

The following were equal for each radar:

Antenna gain = 25 dB

Transmitter power = -16 dBw

Carrier frequency = 13.33 GHz

Total losses = -8 dB

Noise figure = 11 dB

Tracker bandwidth = 600 Hz

In addition, an S/N criterion of 3 dB was used for determining a lock condition (for each of the three systems).

The bases for tradeoff were: the probability of locking three beams; the probability of cross-locking; the probability of conditional cross-locking; the probability of side lobe locking; and the probability of conditional side lobe locking.

Cross-locking refers to locking a channel to the side lobe signal of a receiver that coincides with the main beam of a transmitter. Conditional cross-locking occurs when a side lobe signal of a receiver is above a threshold value and the channel is locked to the main beam signal (again the side lobe of a receiver coincides with the main lobe of a transmitter). Side lobe locking occurs when a channel is locked to a received side lobe signal and the side lobe of a receiver coincides with the side lobe of a transmitter. Conditional side lobe locking occurs when received energy at the side lobe is above the threshold and the channel is locked to the main beam signal.

The tradeoff criteria will be to determine, for each modulation technique, the side lobe levels that will prevent side lobe locking at the vernier-engine-ignition altitude and the side lobe level (or isolation due to frequency diversity) that will be required to prevent cross-locking at the vernier-engine-ignition altitude.

The J_o radar was used as a baseline for establishing the S/N criteria on the receiver noise figure and the tracker bandwidth. Note the receiver sensitivity curve shown in figure 34. A curve-fit for each of the curves of figure 34 was obtained and used as a detector model for the J_o radar. Since these curves are based on a 3-dB S/N threshold, that threshold was used for the other two radars as well. The wide-band mode of the J_o system specifies a tracker filter bandwidth of 600 Hz. Since this mode includes the major portion of the expected range at Doppler frequencies, this bandwidth (BW) was used consistently to calculate the tracker noise level in the other two systems. Note that if the wide-band-mode receiver sensitivity curve is extrapolated to higher frequencies, it would probably level off at approximately -162 dB. Figure 34 also indicates that the noise level is about -165 dB.

From this, then, we can use equation (58) to calculate an equivalent noise figure at high frequencies for the J_o system.

$$N_{Eq} = KTBN \qquad (58)$$

where K is Boltzman's constant, $T = 290°$, B is the bandwidth of the tracker, and N is the receiver noise. The noise is 11 dB. This value was used to calculate the noise power for the ICW and J_1 systems.

Each modulation technique forces a unique degradation to the required signal power for normal acquisition and tracking. Due to mixer noise in the J_o system, the signal power must be expressed as a function of velocity (see fig. 34). The ICW system suffers an efficiency loss of approximately 4 dB, due to the duty cycle and receiver blanking. The J_1 system, besides operating on reduced sideband power, is range-sensitive (see fig. 33), so the parameters used for the J_1 modulation were a deviation index of one and sequential switching of two modulation frequencies (148 and 161.5 KHz); in addition, if the power received using one of the modulation frequencies resulted in a signal below the detector threshold, then the power received using the remaining modulation frequency was degraded by 3 dB, due to the 50% duty cycle that would result.

106
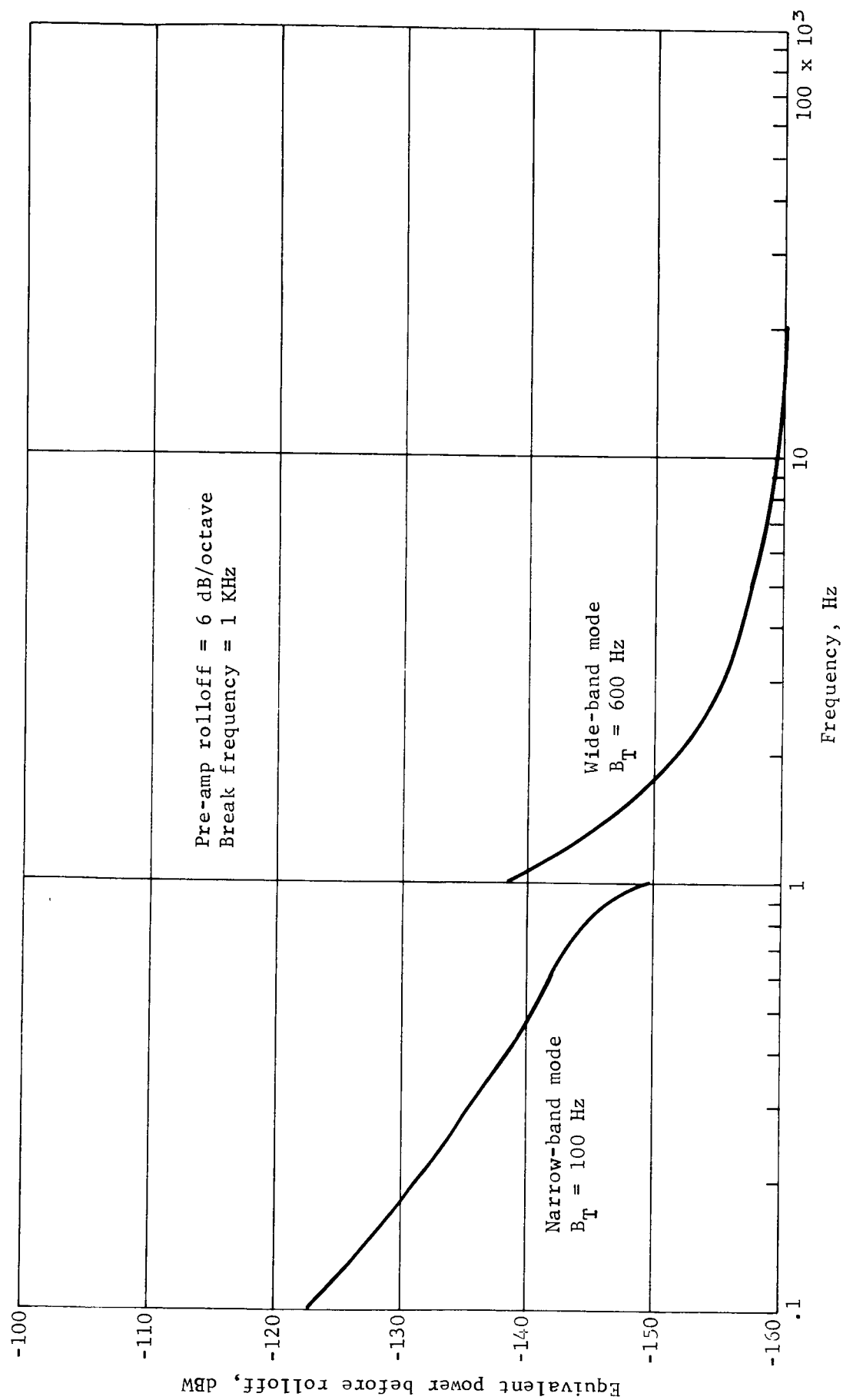
Figure 34.- Acquisition Sensitivity of the J_o Radar Receiver

If a sequential lobing radar had been used it would have had
an efficiency loss of 6 dB; because of this we assumed that such
a radar would transmit 6 dB more power. Hence, the results that
will be shown here for the J_1 system are valid for either a
time-dependent or simultaneous lobing system.

The reflectivity models used for the static Monte Carlo runs
described here are shown in figure 25. These models were furnished
by Dr. Richard F. Broderick, and are felt to be representative of
the radar cross-section for the 4000-ft altitude at which these
computer runs were made.

The Monte Carlo program provides the following types of data:
(1) the probabilities of having one, two, three, and four beams
unlocked (equivalent to the probabilities of having four, three,
two, and one beam locked); (2) the conditional probability of
having a cross-lock (i.e., the probability that the received power
from a side lobe is above the threshold); and, (3) the joint prob-
ability of having a cross-lock (the probability that a main beam
is unlocked at the same time that a cross-lock occurs).

In determining the probabilities of having locks and condi-
tional locks, data were obtained for a 4-beam radar whose beams
were separated by 90 deg and whose splay angles were 20 deg. The
side lobe-side lobe data were obtained for a main beam splayed at
20 deg with three side lobes in a plane defined by the centerline
of the main beam and the roll axis of the vehicle, as shown in
figure 35.
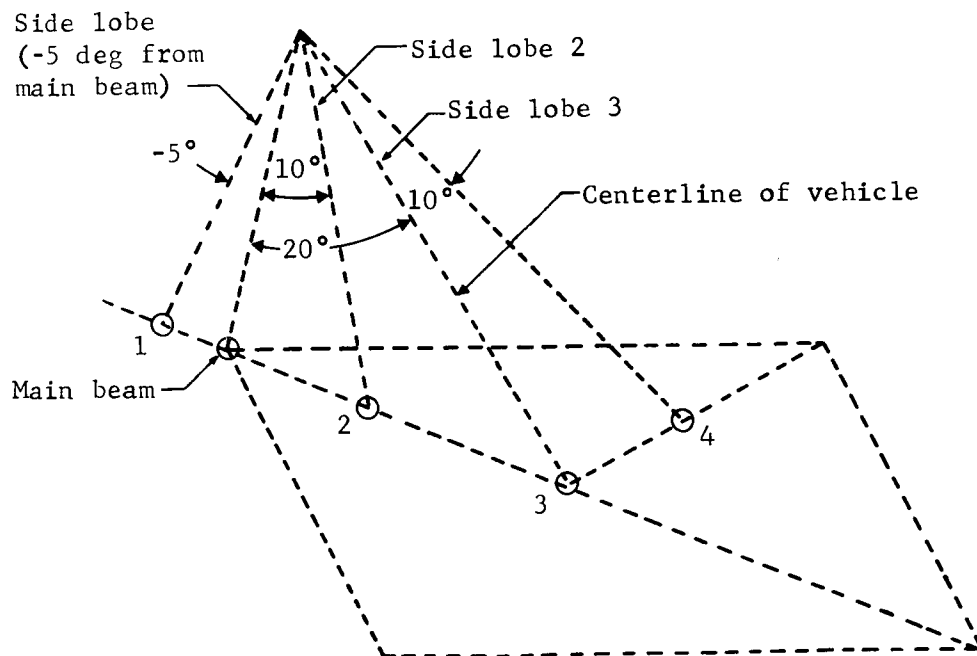
Figure 35.- Side Lobe Configuration Used in the Static Monte
Carlo Tradeoff Analysis

108

The data obtained from this configuration are applicable whenever
a side lobe of the main beam lies within a volume formed by ro-
tating the center line of side lobe 1 about the centerline of the
vehicle. This is so because the Monte Carlo program selects
random values for the roll of the vehicle, the ground slope
azimuth, and the wind azimuth. For example, the statistics for
a side lobe of the main beam positioned at 4 in figure 35 will
be the same as those for side lobe 2. The results of this in-
vestigation will be described in the following section.

B. Comparative Monte Carlo Results

The results of the static Monte Carlo computer runs are shown
in figures 36 and 37. The radar parameters and reflectivity
models that were used in these runs have been described in the
previous section. The random variables are shown in table 13.
All runs were made at an altitude of 4000 ft.

TABLE 13.- RANDOM VARIABLES USED IN THE
STATIC MONTE CARLO TRADEOFF ANALYSIS

Parameter	Distribution	3σ Value
Horizontal wind	Gaussian	146 fps
Ground slope	Gaussian	34 deg
Attitude due to wind gusts	Gaussian	22.4 deg
Vehicle roll	Uniform $\pm$ 180°	
Ground slope azimuth	Uniform $\pm$ 180°	
Wind azimuth	Uniform $\pm$ 180°	

To determine the probabilities of cross-coupling for the
various side lobe-to-main lobe combinations, the following param-
eters were used: upper and lower reflectivity models (see fig.
25); terminal velocity and nominal attitude paired as 100 fps and
0 deg, 200 fps and 10 deg, and 300 fps and 20 deg; and the tip-
up and parachute Monte Carlo programs. In the past, the terminal
velocity and the nominal attitude had been paired as 100 fps and
20 deg, 200 fps and 20 deg, and 300 fps and 20 deg; but in using
the time-correlated Monte Carlo program we noted that the first
two paired conditions do not exist.

The results of this run are shown in figures 36a thru 36ℓ.
The side lobe-side lobe data are shown in figures 37a thru 37f,
and were obtained using the upper reflectivity model, a terminal
velocity of 300 fps, and a nominal attitude of 20 deg for both
the tip-up and the parachute programs.
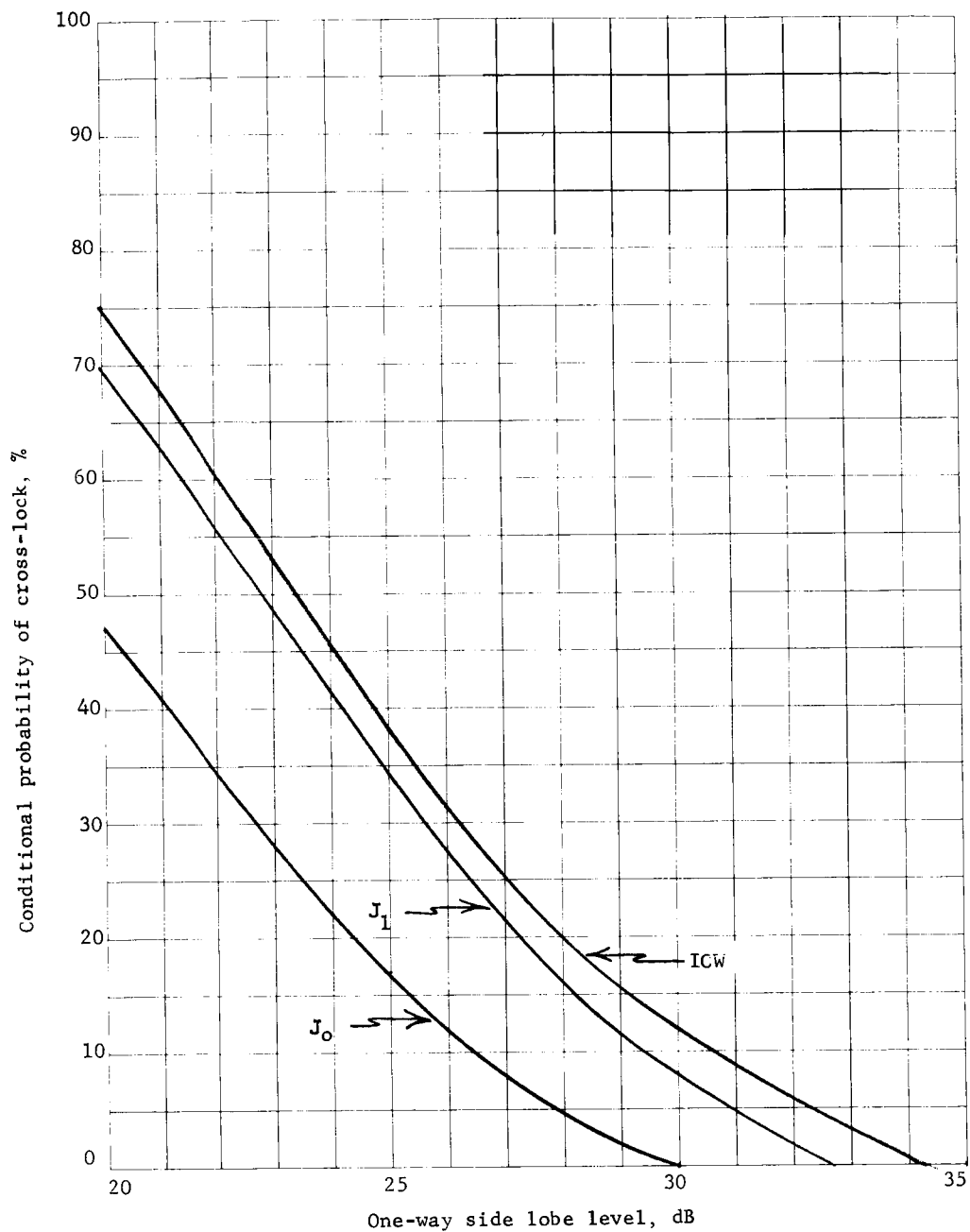
(a) Parachute Program, Lower Reflectivity Model, Terminal Velocity = 300 fps,
      Nominal Pitch Attitude = 20 deg

Figure 36.- Static Monte Carlo Tradeoff Analysis Results: Conditional Probability
            of Cross-Lock at Vernier Engine Ignition
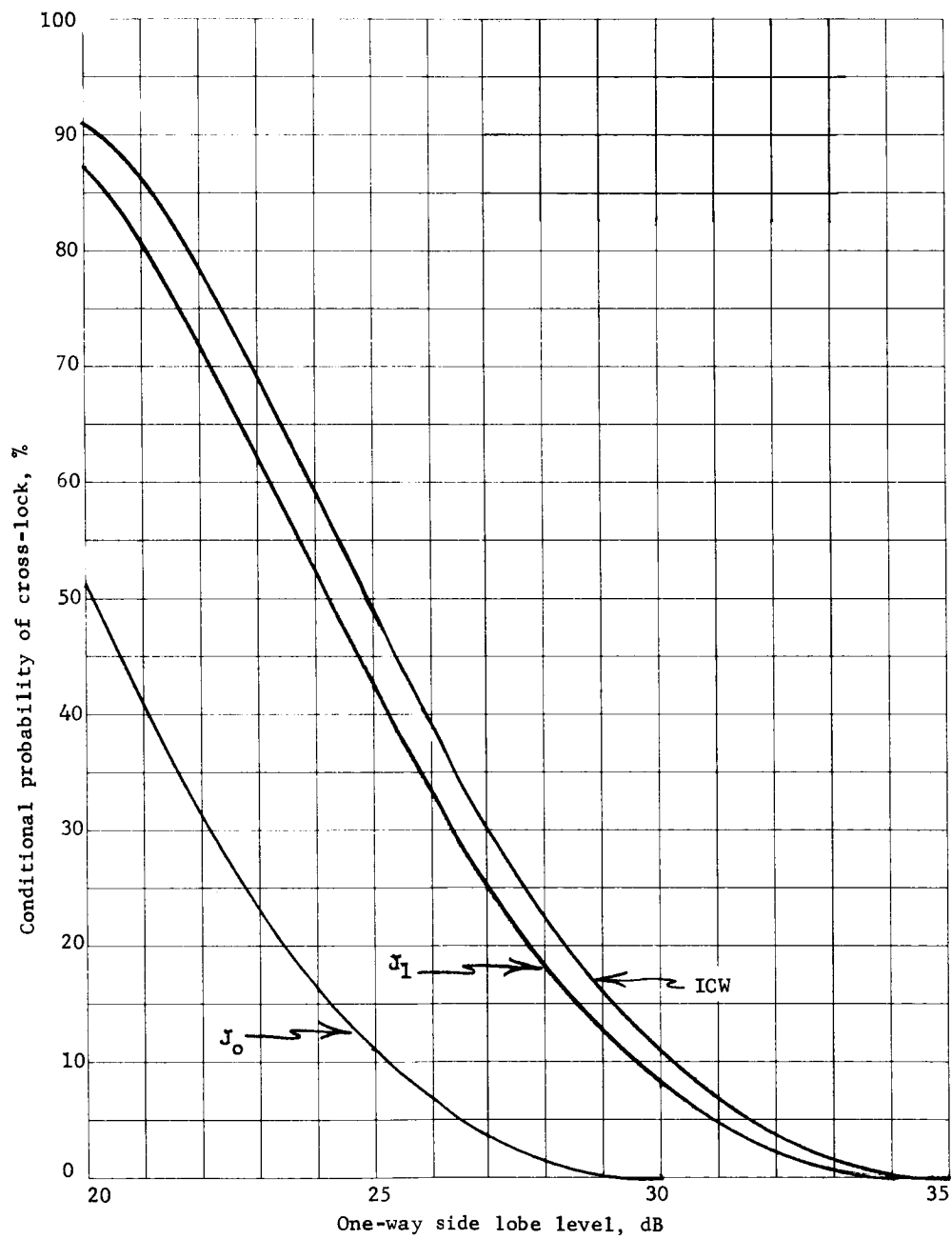
(b) Parachute Program, Lower Reflectivity Model, Terminal Velocity - 200 fps, Nominal Pitch Attitude = 10 deg

Figure 36.- Continued
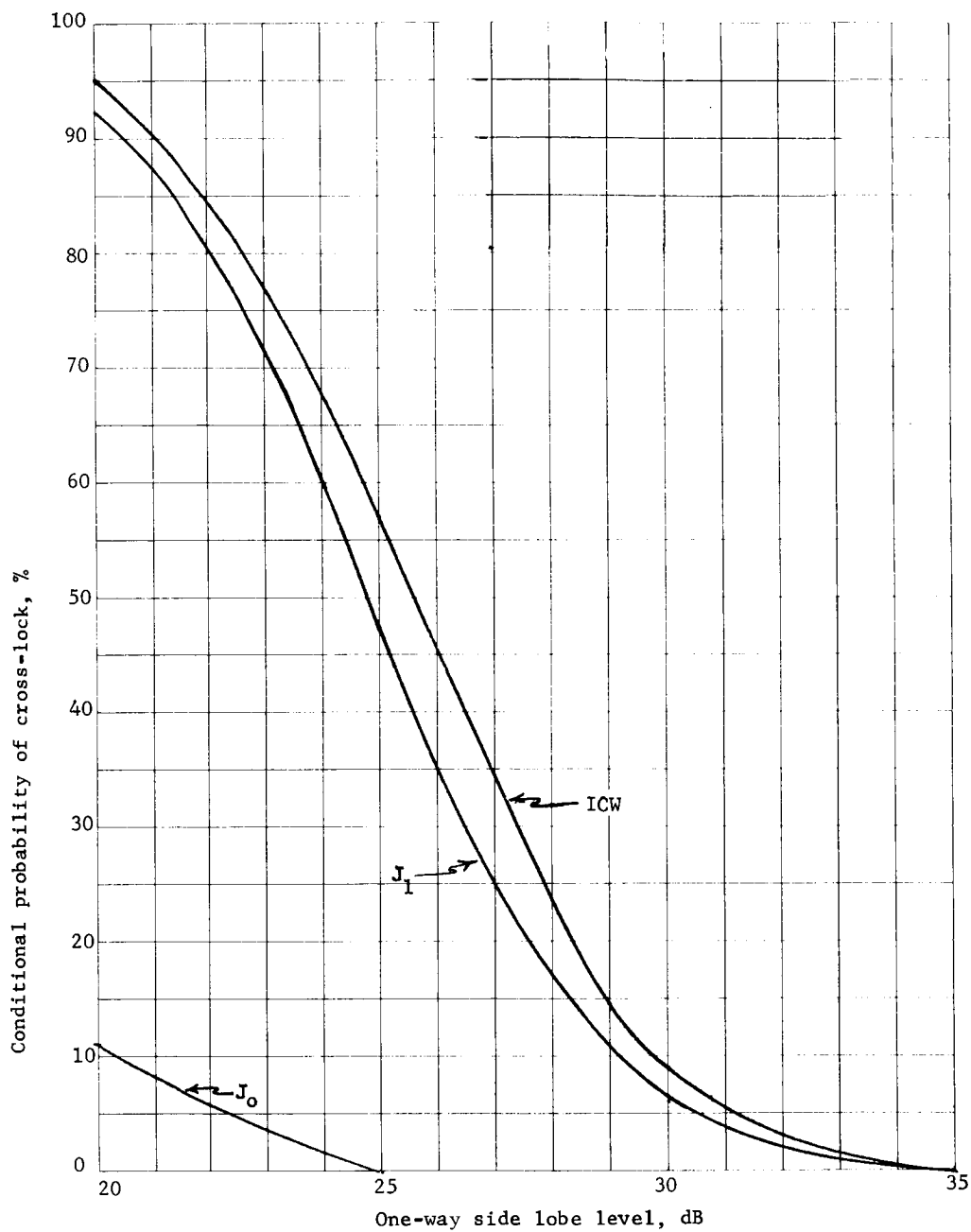
(c) Parachute Program, Lower Reflectivity Model, Terminal Velocity = 100 fps, Nominal Pitch Attitude = 0 deg

Figure 36.- Continued
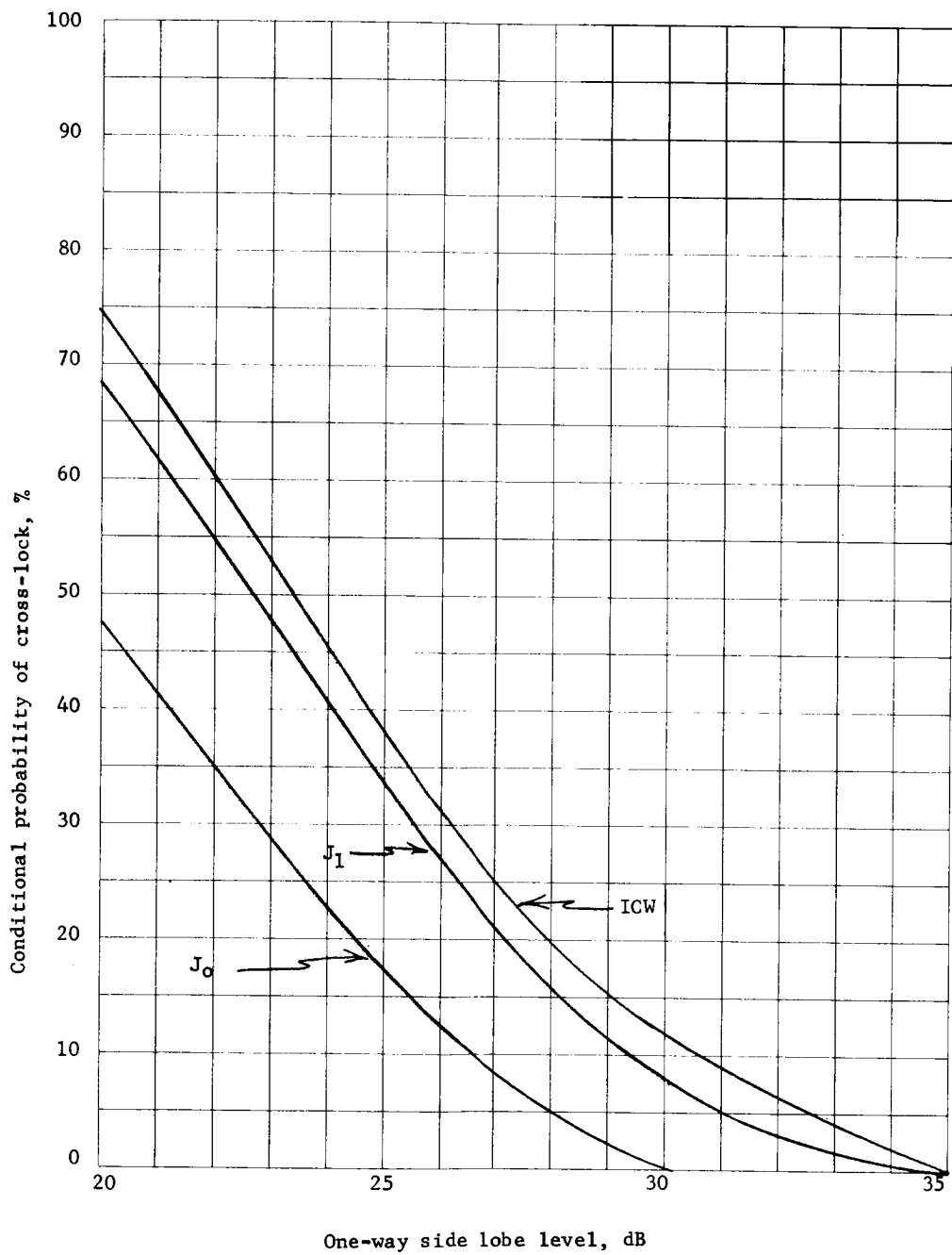
(d) Tip-Up Program, Lower Reflectivity Model, Terminal Velocity = 300 fps, Nominal Pitch Attitude = 20 deg

Figure 36.- Continued
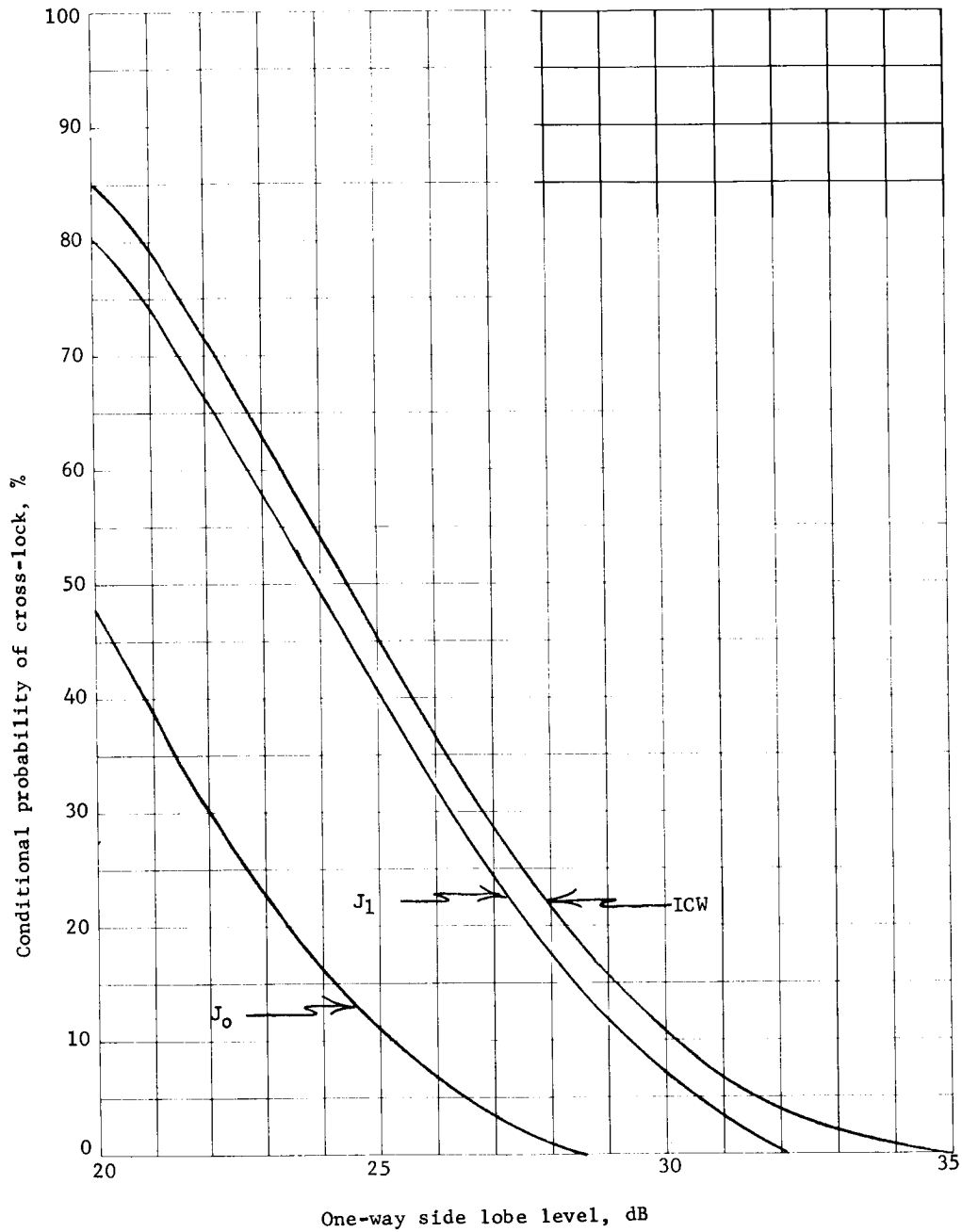
(e) Tip-Up Program, Lower Reflectivity Model, Terminal Velocity = 200 fps, Nominal Pitch Attitude = 10 deg

Figure 36.- Continued
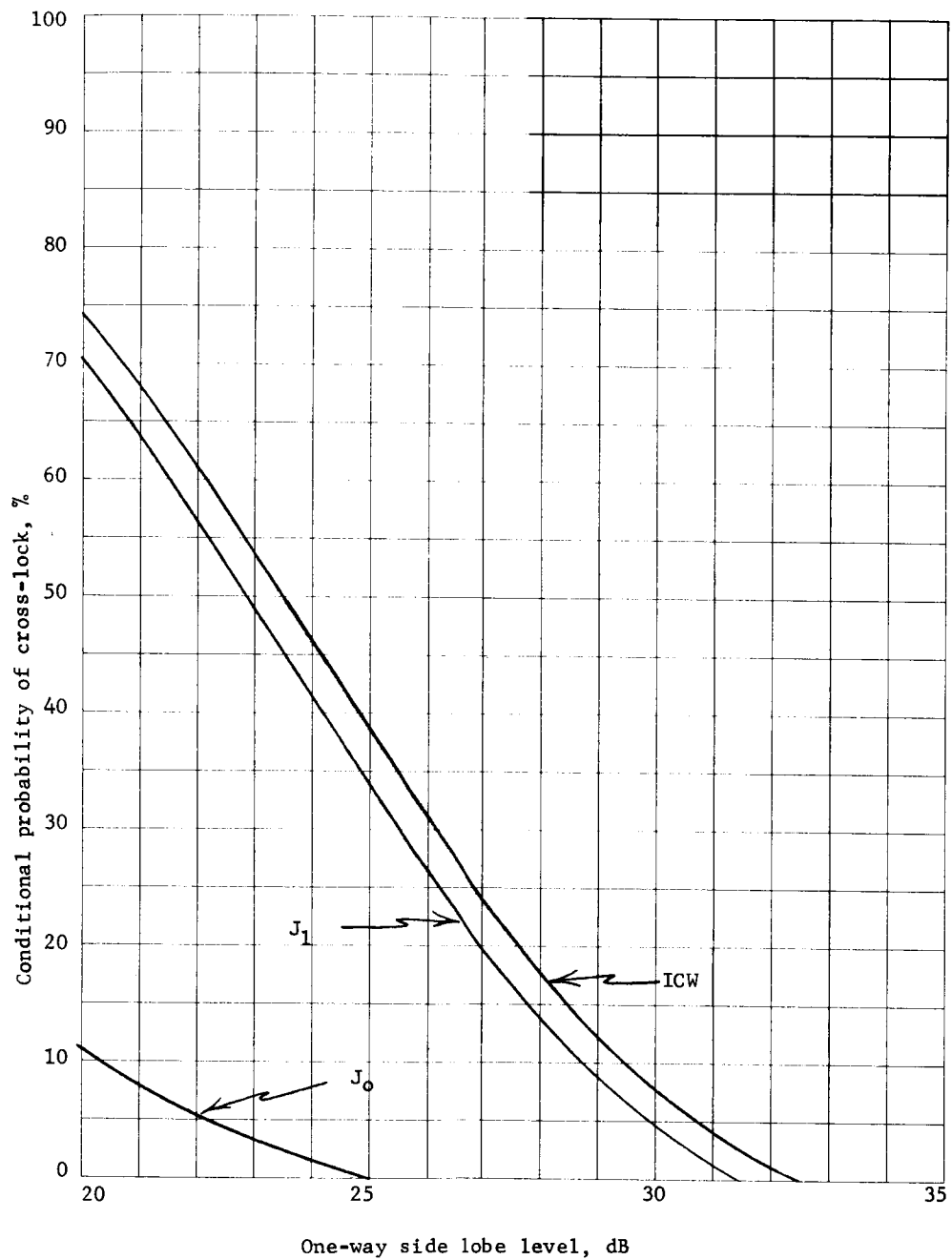
(f) Tip-Up Program, Lower Reflectivity Model, Terminal Velocity - 100 fps,
     Nominal Pitch Attitude = 0 deg

Figure 36.- Continued
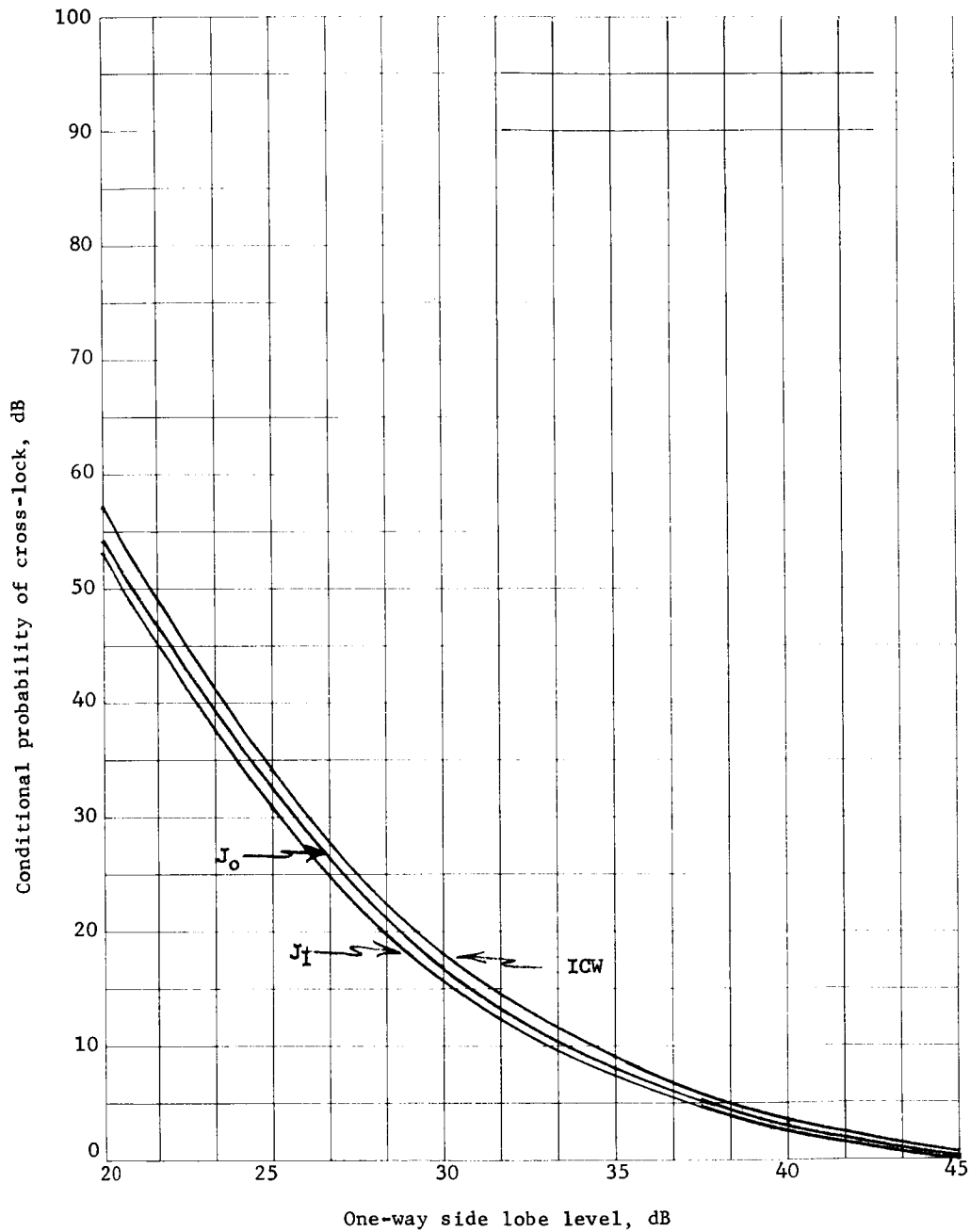
(g) Parachute Program, Upper Reflectivity Model, Terminal Velocity = 300 fps, Nominal Pitch Attitude = 20 deg

Figure 36.- Continued
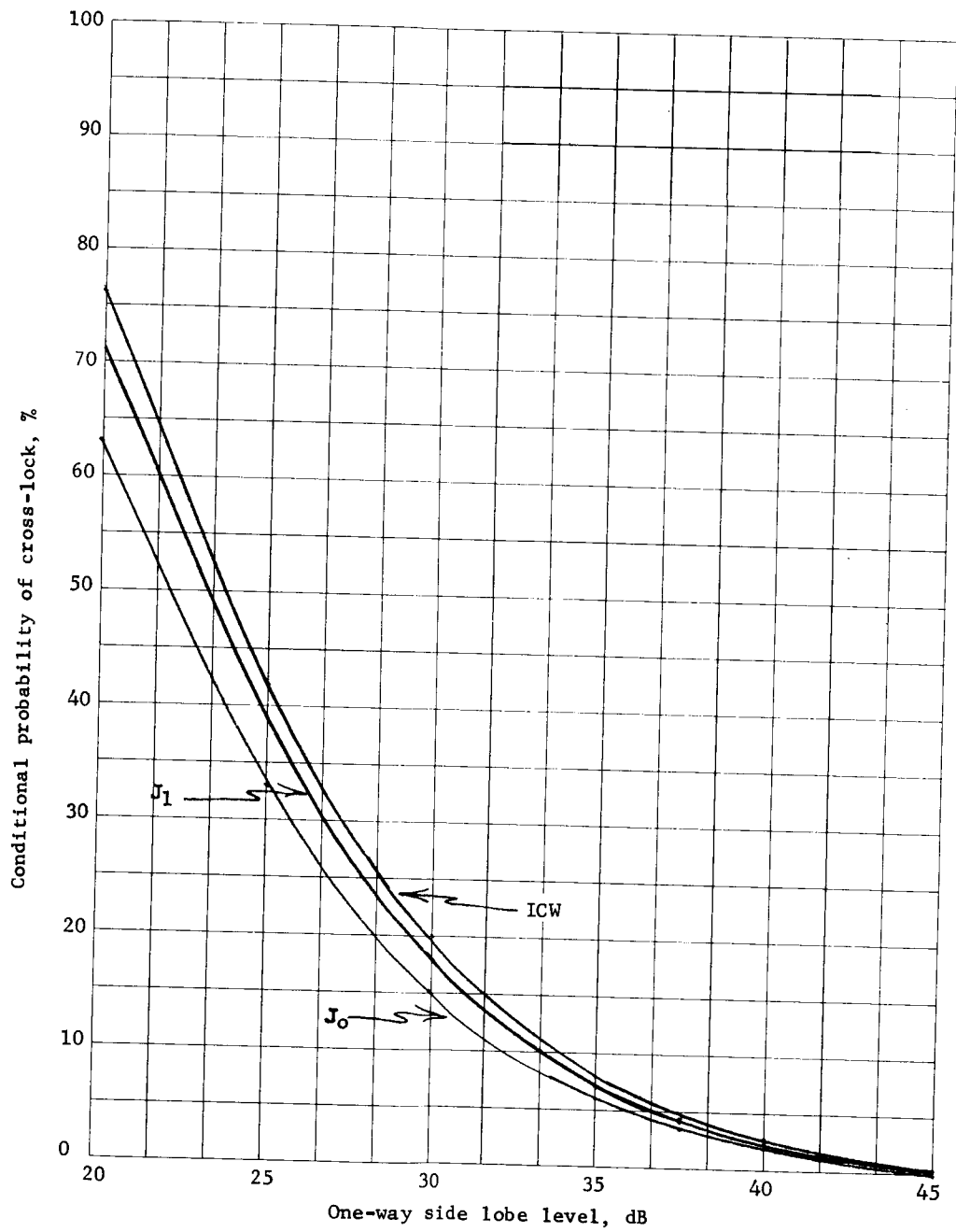
(h) Parachute Program Upper Reflectivity Model, Terminal Velocity = 200 fps, Nominal Pitch Attitude = 10 deg

Figure 36.- Continued
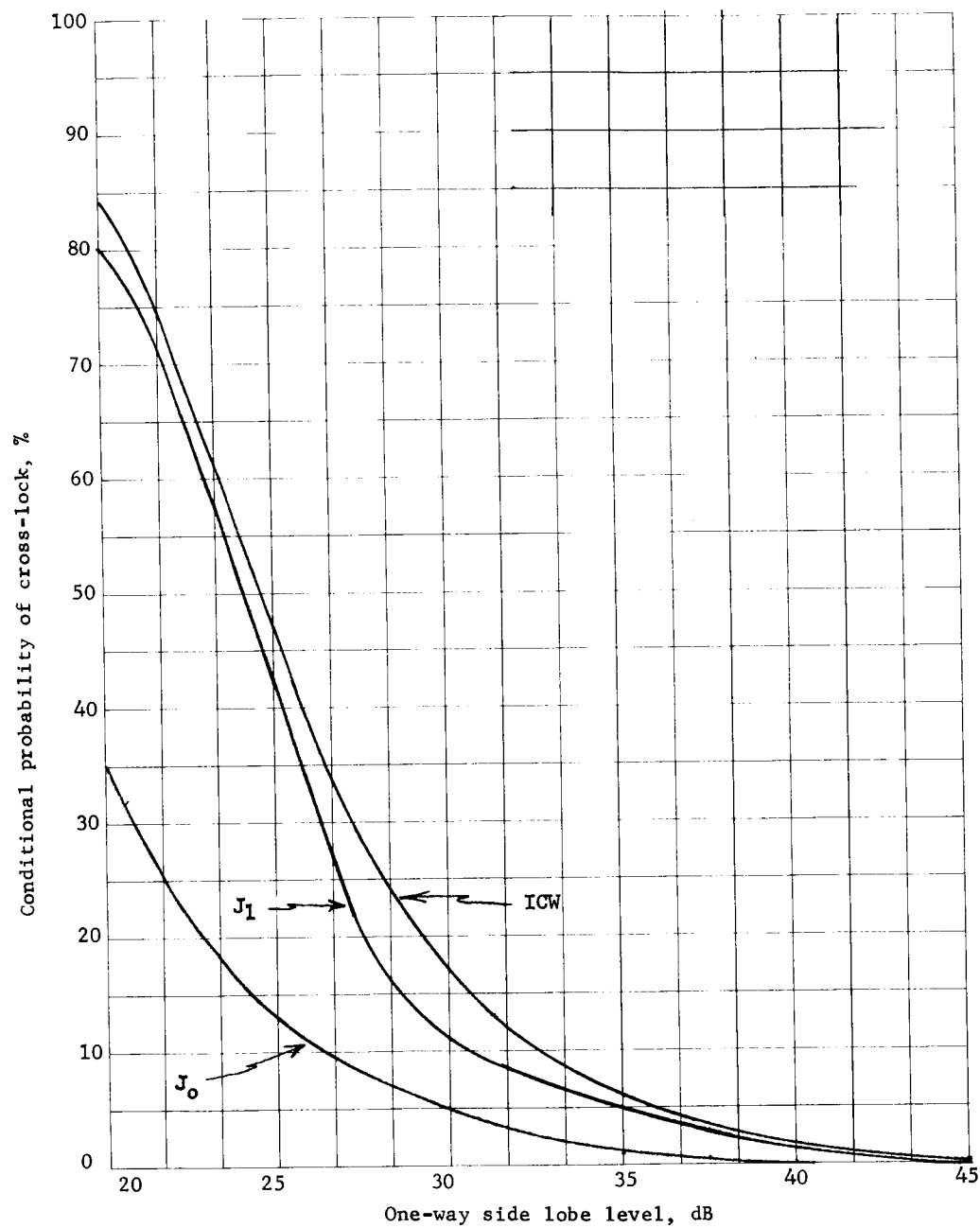
(i) Parachute Program Upper Reflectivity Model, Terminal Velocity = 100 fps, Nominal Pitch Attitude = 0 deg

Figure 36.- Continued
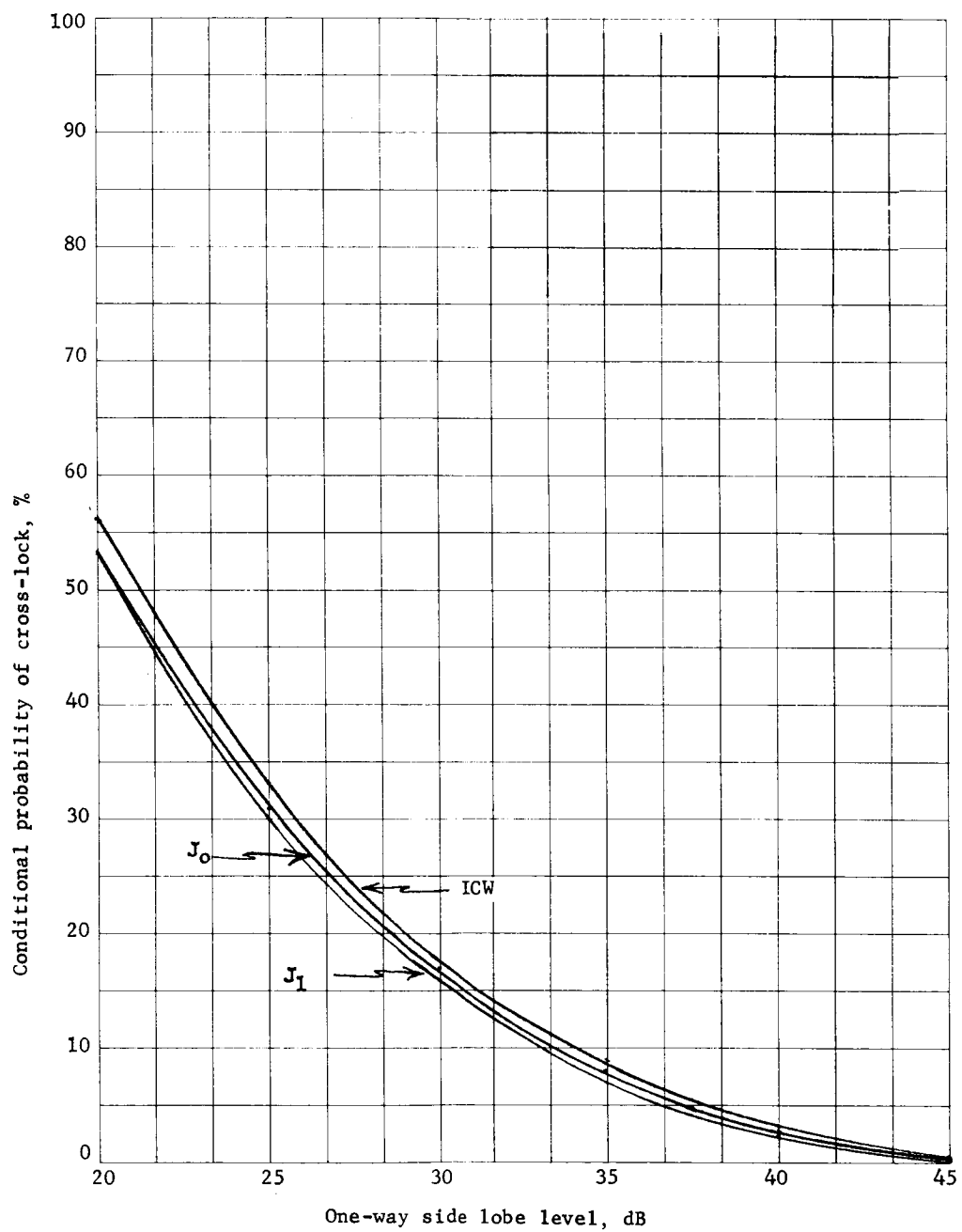
(j) Tip-Up Program, Upper Reflectivity Model, Terminal Velocity = 300 fps,
     Nominal Pitch Attitude = 20 deg

Figure 36.- Continued

(k) Tip-Up Program, Upper Reflectivity Model, Terminal Velocity = 200 fps, Nominal Pitch Attitude = 10 deg

Figure 36.- Continued

120

One-way side lobe level, dB
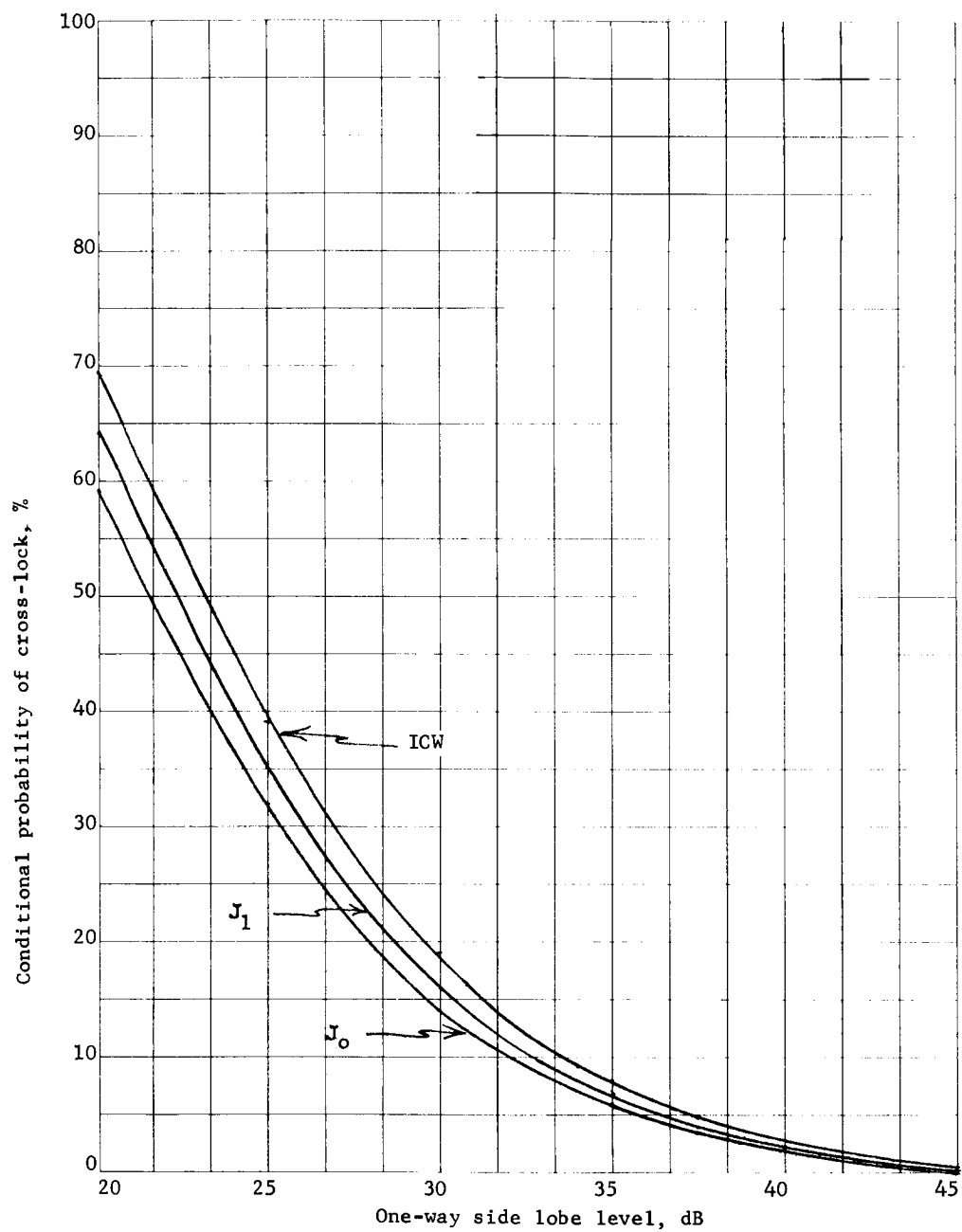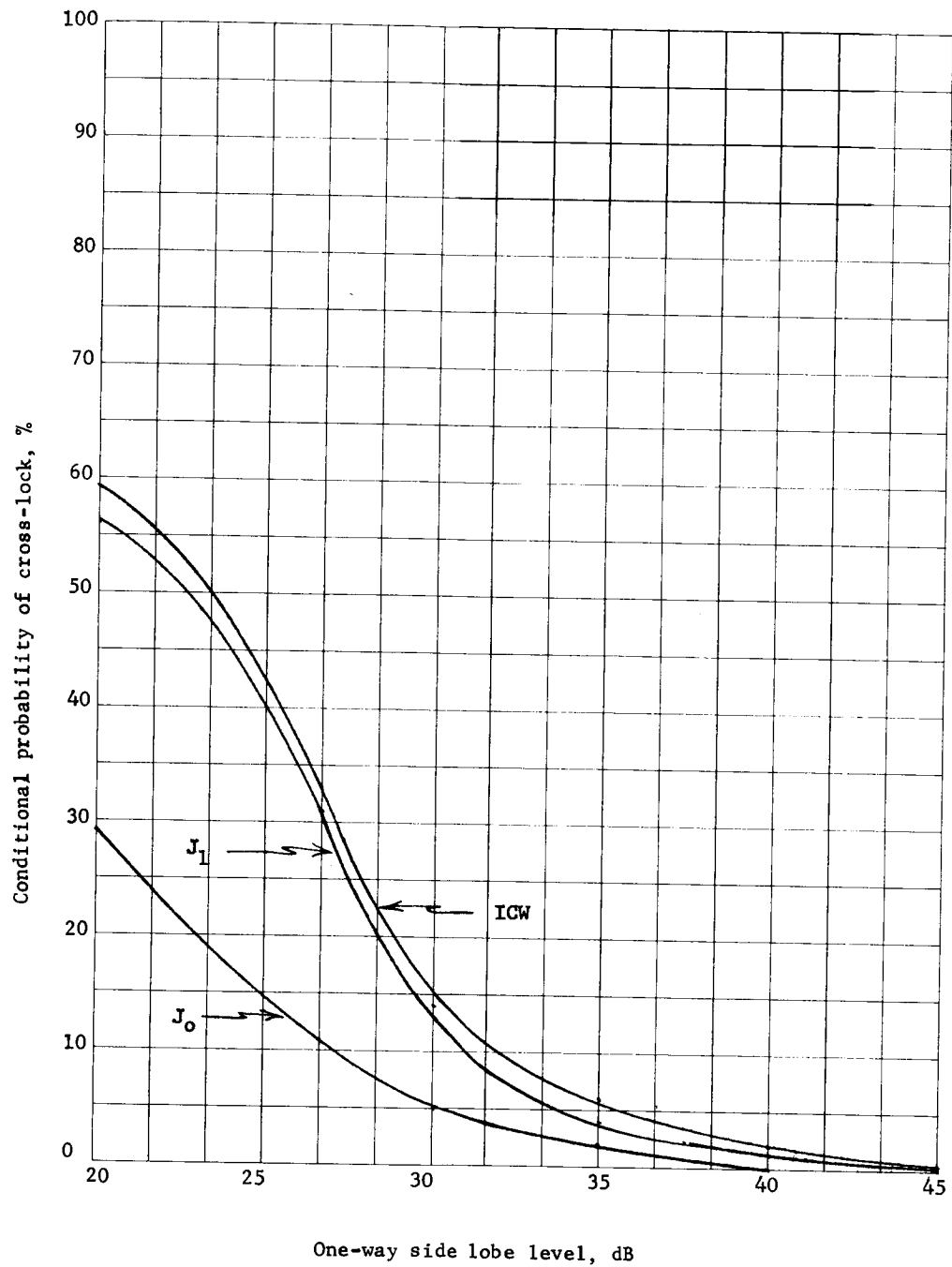
(1) Tip-Up Program, Upper Reflectivity Model, Terminal Velocity = 100 fps, Nominal Pitch Attitude = 0 deg

Figure 36.- Concluded
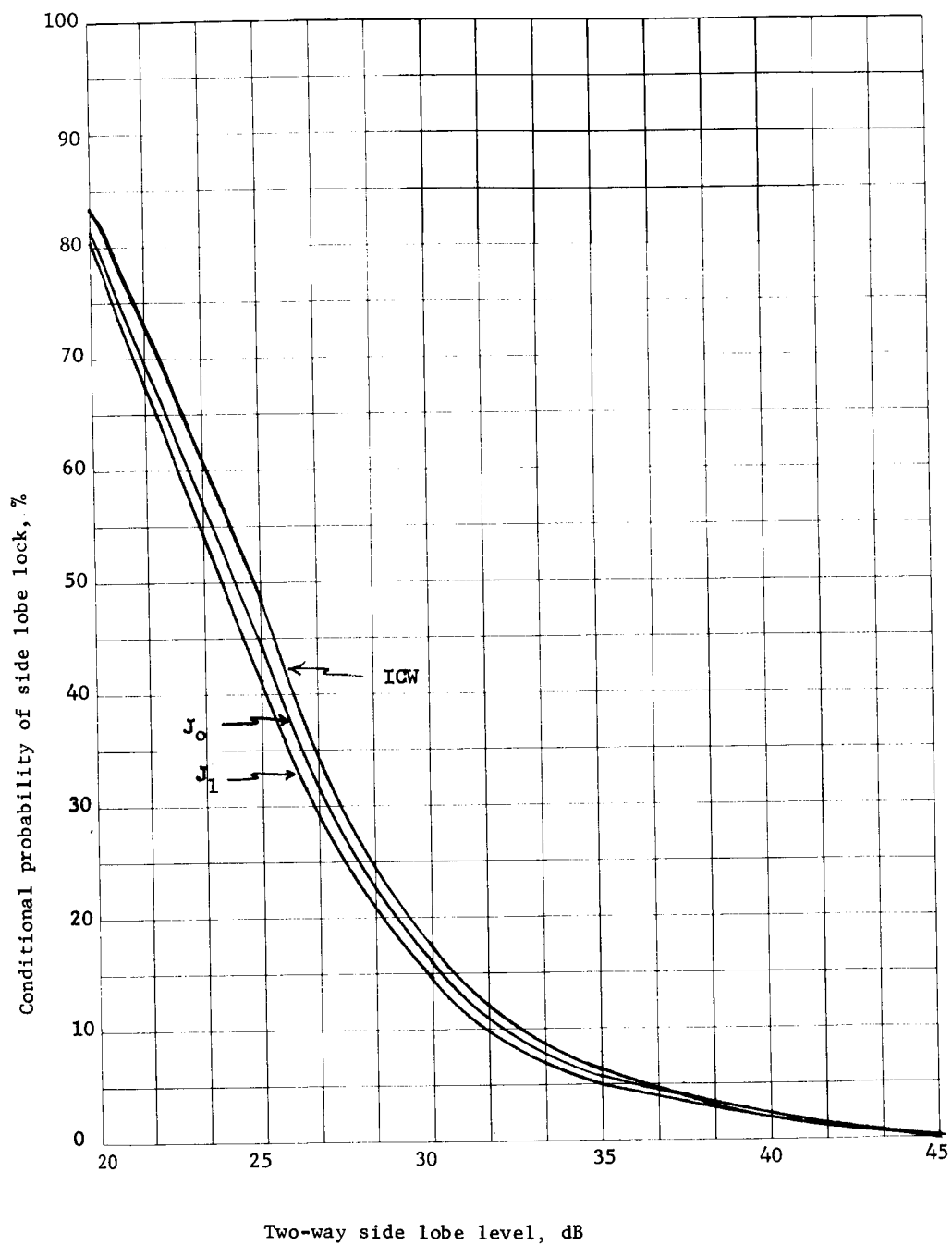
(a) Parachute Program, Side Lobe 20 deg from Main Beam

Figure 37.- Static Monte Carlo Analysis Results: Conditional Probability
of Side-Lobe Lock at Vernier Engine Ignition, Calculated Using
Upper Reflectivity Model with Terminal Velocity = 300 fps and
Nominal Pitch Attitude = 20 deg
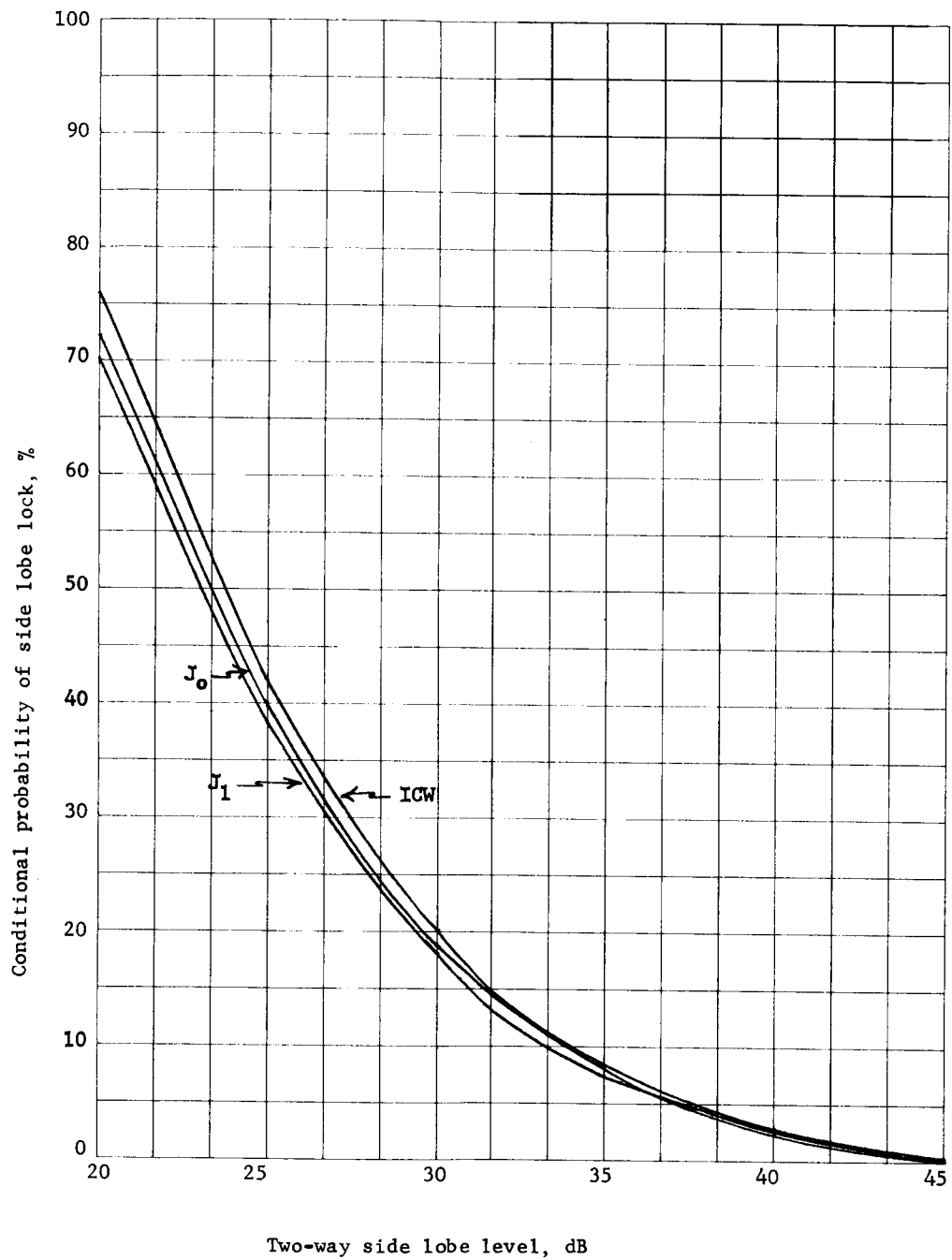
Two-way side lobe level, dB

(b)   Parachute Program, Side Lobe 10 deg from Main Beam

Figure 37.- Continued

Two-way side lobe level, dB
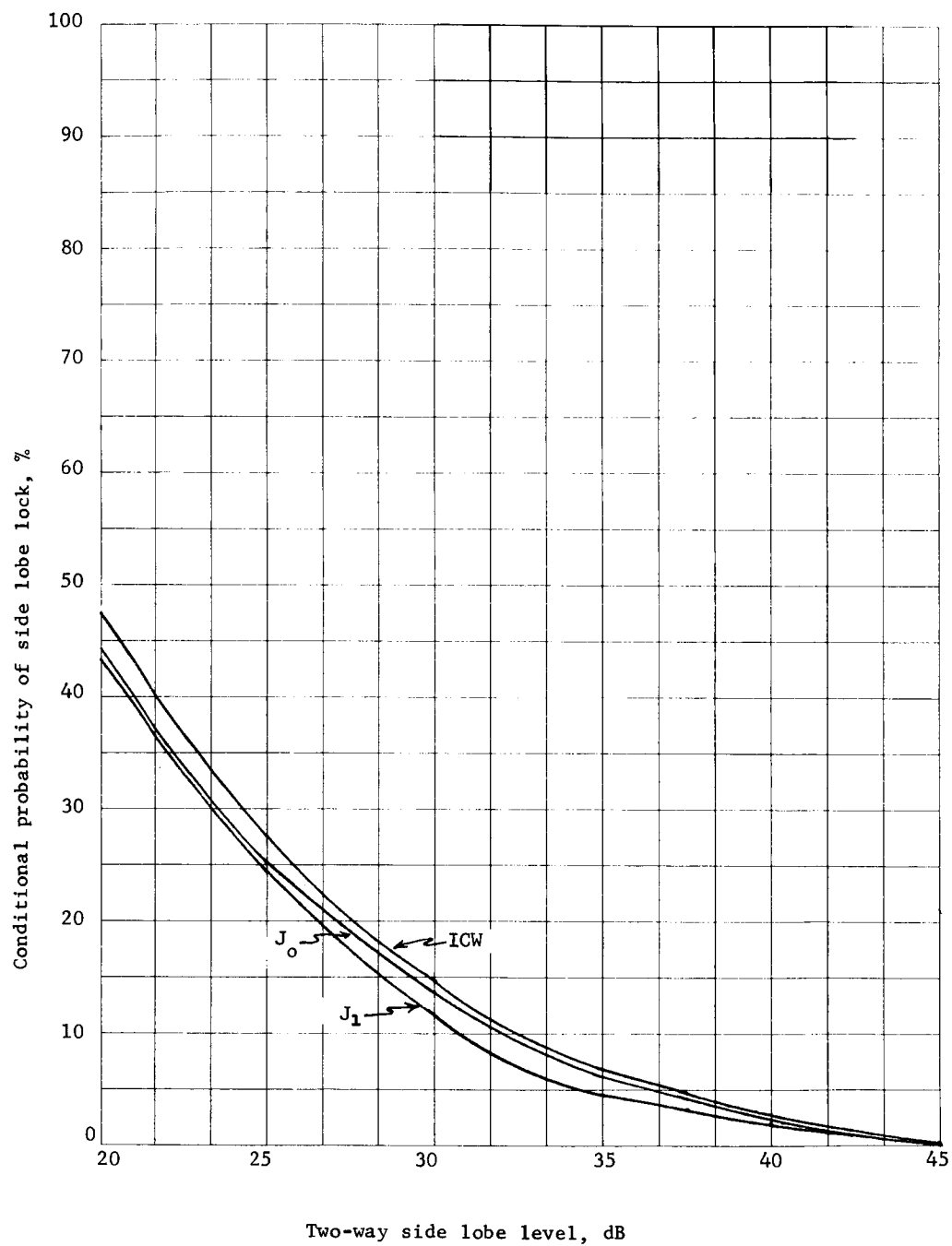
(c) Parachute Program, Side Lobe -5 deg from Main Beam

Figure 37.- Continued
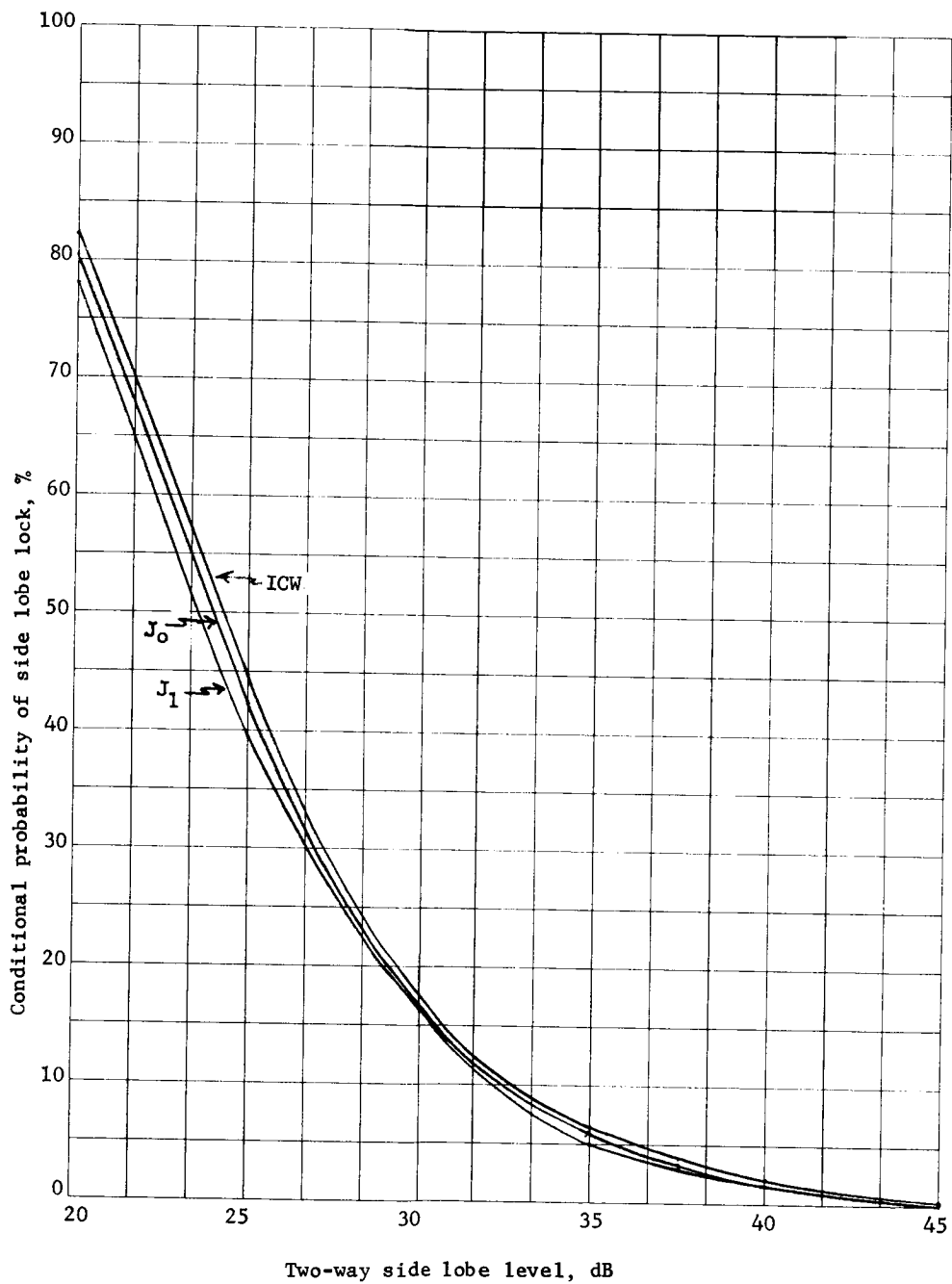
(d) Tip-Up Program, Side Lobe 20 deg from Main Beam

Figure 37.- Continued

(e) Tip-Up Program, Side Lobe 10 deg from Main Beam

Figure 37.- Continued

Two-way side lobe level, dB
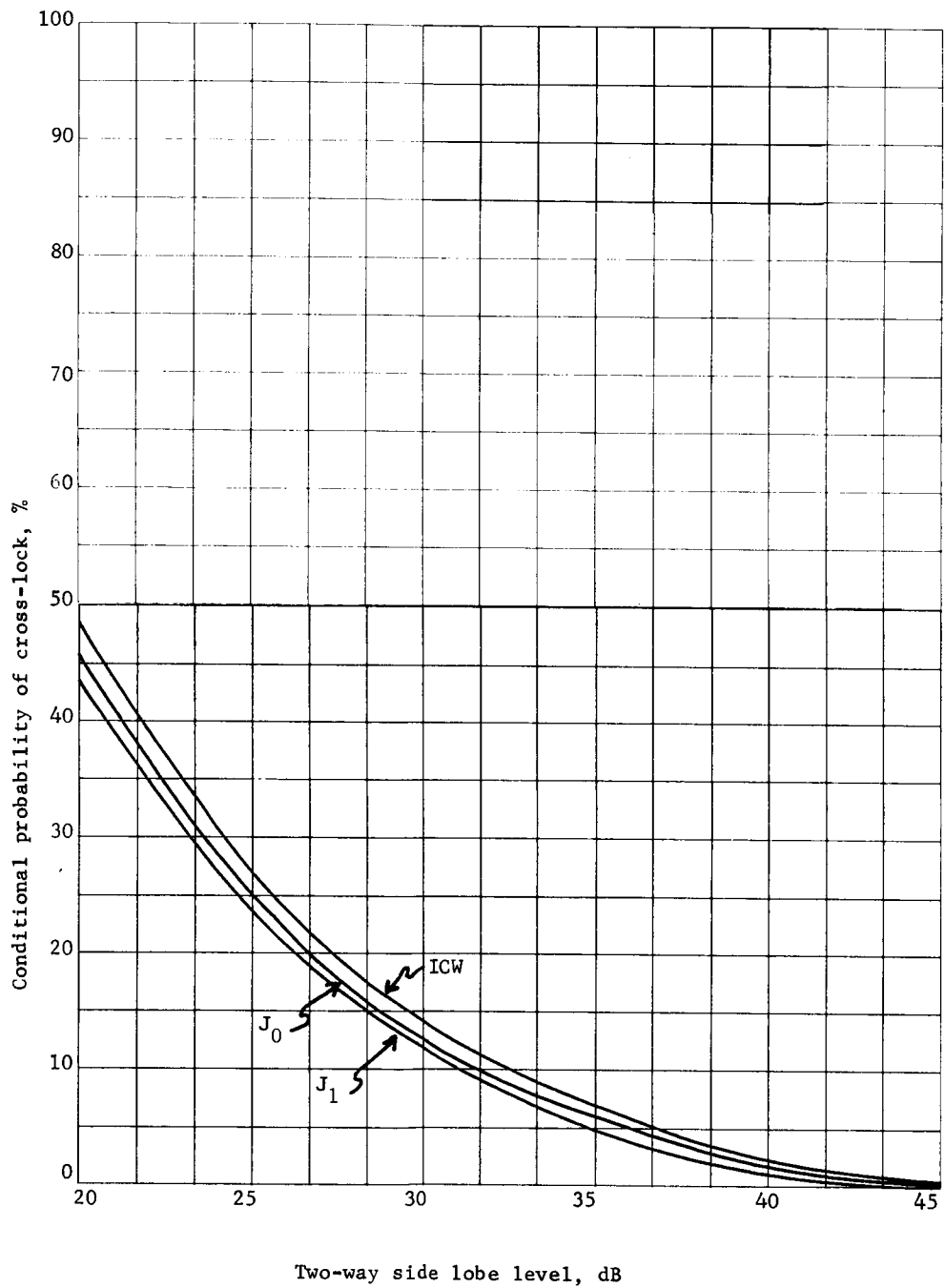
(f) Tip-Up Program, Side Lobe -5 deg from Main Beam

Figure 37.- Concluded

Table 14 indicates the results of the first part of the modulation tradeoff (i.e., the probability of having three and four beams locked for a 4-beam radar). Note that the different modulation techniques produce nearly the same results. It appears that the most favorable radar is the ICW, the next most favorable is J_1 radar, and the least favorable radar is the J_o. It should be pointed out that some data (not shown) were taken using a transmitter power of -10 dB for each radar, and there was even less perceptible difference between the modulation techniques at that power level. The beam unlocks are due to large incidence angles (ICW), large incidence angles and low velocities $\left(J_o\right)$, and large incidence angles and range holes (J_1).

TABLE 14.- PROBABILITY OF FOUR BEAMS LOCKED/PROBABILITY OF THREE BEAMS LOCKED FOR 4-BEAM RADARS IN PERCENT

Program	Model	V_T, fps	θ_T, deg	Modulation technique		
				J_1	J_o	ICW
Tip-up	Upper reflectivity	100 200 300	0 10 20	99.8/100 100/100 100/100	99.9/100 100/100 100/100	99.9/100 100/100 100/100
Tip-up	Lower reflectivity	100 200 300	0 10 20	98.8/100 100/100 100/100	98.9/100 100/100 100/100	99.7/100 100/100 100/100
Parachute	Upper reflectivity	100 200 300	0 10 20	99.8/100 100/100 100/100	99.3/100 100/100 100/100	99.9/100 100/100 100/100
Parachute	Lower reflectivity	100 200 300	0 10 20	99.8/100 100/100 100/100	98.9/100 99.9/100 100/100	99.9/100 100/100 100/100

Table 15 indicates that the J_o modulation technique is more susceptible to cross-locks. This implies that conditions under which the J_o system unlocks and cross-locks (side lobe-to-main lobe) are zero Doppler conditions, to which the other radars are not susceptible.

TABLE 15.- NUMBER OF CROSS LOCKS AS A FUNCTION OF SIDE LOBE LEVEL[a]

One-way side lobe level, dB	Modulation technique		
	J_1	J_0	ICW
20	1	10	1
25	1	9	1
30	1	6	1
35	1	3	1
37.5	0	2	0

[a]Terminal velocity = 100 fps, nominal attitude = 0 deg, upper reflectivity model, parachute program.

On the other hand, figures 36a thru 36ℓ show that, in general, the J_0 system is less susceptible to conditions of cross-lock than either the J_1 or ICW. The data indicate that if the one-way side lobe level is approximately 45 dB, there is virtually no possibility of having a cross-lock on any of the radars (for the parameters used in this analysis). Although it is difficult to achieve a one-way side lobe level of 45 dB in the direction of the main beams of the transmitter for a 4-beam system (the mean for 5-beam LM radars is 28.9 dB), each transmitter could be set at a different carrier frequency, so that the isolation would be greater than 80 dB.

Figures 37a thru 37f show the probabilities of having conditional side lobe locks. Although the difference in susceptibility here is practically insignificant, the J_1 system is the least susceptible and the ICW is the most susceptible. Note that side lobes with small splay angles are more susceptible to locks when the two-way side lobe level is less than 25 dB. In practically all cases, having a two-way side lobe level slightly greater than 45 dB would eliminate the possibility of a side lobe lock at altitudes of 4000 ft and above (for the radar parameters used).

In conclusion:

1) With regard to the probability of maintaining a radar lock, there is no significant difference between the modulation techniques.

2) There is no significant difference between the modulation techniques, with respect to side-lobe power levels, for eliminating side-lobe locking conditions to an altitude of 4000 ft.

3) Excluding the consideration of time diversity, there is no significant difference between the modulation techniques with regard to the isolation or side-lobe level required to prevent cross-lobe locking to an altitude of 4000 ft.

4) A computer run was made with the time-correlated Monte Carlo parachute program using the parameters of a J_o system and the corresponding isolation determined here (that would exclude cross-locks to an altitude of 4000 ft). No cross-lock conditions existed during the 500 parachute trajectories that were run. These results are shown in figures 26 and 27.

C. Radar System Comparison

Before deciding which modulation method to mechanize in the system, we first need to consider the characteristics of each method. This will allow us to select a method that will not be too complex to implement. The ICW system uses a servoed pulse repetition frequency (PRF) to avoid altitude holes (which would otherwise occur when the PRF equals the Doppler frequency) and maintain the proper 50% duty cycle. To maintain the 50% duty cycle, the slant range must be measured along the velocity beam. But because there is a high probability that a beam may unlock as a result of large attitude excursions, and an uncertainty as to which beam will do so, the slant range on each of the four velocity beams must be measured. Although this minimizes the need for a LARA, it increases the complexity of the four range channels that must be included in the basic velocity-measuring system to maintain the theoretical efficiency of the system.

The reference system for the J_1 modulation is the APN/187 FM/cw radar system. This particular system circumvents the need for frequency diversity by using time diversity, in which the respective velocity beams are sampled at a 24-Hz scan rate. It operates on a single frequency, which permits the formation of a multiple-beam pattern in which each beam can be sampled at the scan rate. The RF separation frequency from the carrier will also allow us to use an interleaved aperture array, in which the receiver and transmitter array elements are interlaced. As shown in Appendix D, this reduces the original 60-dB isolation between the receiver and transmitter antennas significantly (to between 18 and 22 dB).

But because the first-order Bessel function (J_1) does not have the isolation of a higher-order Bessel function $(J_2$ or $J_3)$, the use of an interleaved-antenna array becomes questionable. In addition, the effect of the interlaced components is to increase the side-lobe levels of the multiple beams about the center of the aperture. As the reflectivity curves reach a maximum value about the vertical or nadir, this particular antenna system is more susceptible to side-lobe lockups than one that uses a side-by-side aperture array.

The time-diversity system has an additional advantage: it is the lightest. Its disadvantages -- of using single channel (which creates operational as well as reliability problems) and its high probability of having a beam unlock, are overcome by using the additional RF beam to increase the probability of having three beams locked. Had it been only a single-channel system, however, the high probability of having a single beam unlock would cause there to be a high probability that the total system (four beams) would unlock.

For application to the Mars Lander, we recommend that individual receiver channels be used to ensure a high probability of locking three beams. Due to the previously-mentioned consequences of having the interleaved-antenna array operating at a single frequency, a time-diversity system has little or no advantage over a frequency-diversity system for the Mars Lander mission.

The J_0 system has a weight disadvantage, because an additional quadrature preamplifier must be provided to maintain sign sense; however, this disadvantage may be offset somewhat by using solid-state transmitters (these might be susceptible to either AM or FM bandwidth and transient requirements in the ICW or FM/cw

systems). The high-pass filter in the preamplifier, which atten-
uate diode noise in the mixer and spectral impurities in the trans-
mitter, makes this system more susceptible to beam unlocks as the
velocities decrease toward the zero Doppler region. However, this
same preamplifier rolloff characteristic tends to minimize side-
lobe and cross-lobe lockups, in that the unwanted signals from
the side lobes occur in the proximity of the zero Doppler region,
where the reflectivity curves peak at the nadir.

Due to the criticality of providing altitude information from
4500 ft to engine cutoff (10 ft), we studied methods of using the
TDLR to provide a backup range measurement. As previously dis-
cussed, the ICW radar system utilizes a range measurement at the
upper altitudes to properly servo the PRF; but as the altitude
decreases to about 500 ft, the transmitted pulse eclipses the
received pulse and makes this method of modulation inoperative.
To compensate for this effect, the ICW modulation is augmented by
an FM/cw modulation whenever the altitude is below 500 ft.

For this latter case, and for the J_1 FM/cw modulated system,
the range is generally determined by measuring the phase differ-
ence between the Bessel sideband of the transmitted and received
signals.

The S/N ratio for the FM/cw system is

$$\left.\frac{S}{N}\right|_{FM/cw} = \frac{P_w \, G \, \lambda^2 \, \sigma_o \, J_n^2 \, (M)}{(4\pi R)^2 \, L \, KT \, B_t \, \overline{NF} \, \cos \theta} \tag{59}$$

where

$$M = 2m \, \sin \left(2\pi f_m \frac{R}{C}\right) \tag{60}$$

and the phase or range accuracy can be expressed as

$$\left(\Delta R\right)_{1\sigma} = \frac{C}{\sqrt{2 \, \frac{S}{N}}} \tag{61}$$

where

$$C = (989 \text{ feet}/2\pi) \left(1 \text{ MHz}/n \, f_m\right) \tag{62}$$

Upon substituting the S/N term into equation (61), we obtain

$$\left(\Delta R\right)_1 = \left(\frac{R}{J_n(M)}\right) \left(\frac{4\pi C}{\lambda}\right)\sqrt{\frac{L\ K\ T\ B_t\ \overline{NF}\cos\theta}{P_w \cdot G\ \sigma_o}} \tag{63}$$

where n refers to the order of the Bessel sideband. From equation (63) we can see that, as the argument M of the Bessel function varies with respect to range, the one-sigma range error $\Delta R_{1\sigma}$ will also vary as a function of range unless one of two conditions are met: either the range measurement interval for R must be selected in such a way that the slope of the decreasing range is the inverse of the slope of the Bessel function $J_n(M)$ for the selected argument, or the S/N ratio must be very large (S/N $\gg$ 1). In the latter case, the large S/N ratio extends through the receiver to the final phase measurement.

The other well-known technique for measuring range involves generating a linear sawtooth waveform, of the form

$$E(t) = A(t)\cos\left(W_c\ t + \tfrac{1}{2}\mu t^2\right) \tag{64}$$

where

$$\frac{-t}{2} \leq t \frac{\leq t_p}{2}$$

Although the range is measured using a phase-measuring device, the frequency spectrum of the sawtooth waveform includes several Bessel sidebands, which constitute a rectangular frequency spectrum. The number of significant sidebands $\Delta F/f_r$ is the ratio of the peak frequency deviation ΔF to the repetition frequency f_r, and the contribution beyond this limit is insignificant. For the upper sidebands, the spectrum function can be expressed as

$$F(M)\Big|_u = \sum_{n=0}^{\infty} \epsilon_n\ J_n(M) \tag{65}$$

and, for the lower sidebands, as

$$F(M)\Big|_t = \sum_{m=1}^{\infty} J_m(M) \tag{66}$$

where the Neumann coefficient ϵ_n is equal to one when $n=0$, but is equal to two otherwise, and the upper and lower sidebands are related as

$$J_n(M) = (-1)^m J_m(M) \tag{67}$$

By combining the upper and lower sidebands, we obtain the identity

$$J_o(M) + 2\sum_{n=1}^{\infty} J_{2n}(M) = 1 \tag{68}$$

which shows that the S/N expression for the linear sawtooth wave is independent of variations in the altitude.

Thus the range may be measured either using a single Bessel sideband on each beam of the velocity sensor or a single-beam linear FM/cw modulation; however, the linear FM/cw modulation technique is essentially independent of variations in the slant range.

Another consideration for the Mars Lander mission is the susceptibility of the radar system to surface effects. Since the exact characteristics of the local terrain are unknown, the nominal and "worst-case" surface characteristics must be estimated and incorporated into surface reflectivity curves. Three reflectivity curves were used in the simulation: an upper curve, which was determined from the specular component; a mean curve, which represented an unsloping, diffuse surface with no surface slope; and a lower curve, which represented the contribution from a sloping, diffuse surface. The probability density function, which describes the percentage of specular and diffuse surface components within a beamwidth-illuminated area, can then be determined from a knowledge of the Martian local terrain or an assumed reference terrain. A brief description of the reflectivity curves is given in Appendix E.

134

As the altitude decreases and the diagonal distance across the beamwidth-illuminated area becomes comparable to the surface decorrelation distance of a rough terrain, amplitude variations occur in the Doppler time video (see ref. 10). In addition, exceedingly large objects, whose effective radar cross-sections are large in comparison to other objects within the beamwidth, can produce large chirp signals that have different slopes than those from objects at the centroid of a homogeneous illuminated area. The above conditions tend to produce either excessive fading or strong signals that cause the tracker to be pulled off the Doppler centroid for short periods of time. Although this effect is common to all forms of modulation, we observed that not all of the reference systems had provisions to minimize this effect.

Because there is a short time constant in the TDLR tracker, so that it can perform over rapidly-varying trajectories, the tracker must have a memory circuit with a suitable time constant to prevent the recycling that might result from these instantaneous interruptions.

VII. TERMINAL DESCENT SYSTEM MODELING

A. General Description

The 6DOF terminal descent computer program that generated the results shown in this report has been used by Martin Marietta since about June, 1967. It has been under continual evolution as the Mars Lander mission became better defined and as the mathematical modeling of components such as the radar and the propulsion system became more detailed. The latest version of this program is being documented as a part of this contract and shall be referred to as MOD6MV. Detailed flow charts, module diagrams, symbol definitions, and FORTRAN listings are documented in reference 1. This chapter summarizes the program, the mathematical models used, and the operational features. Some of this material is repeated in reference 1.

The functional part of the program, which simulates vehicle dynamics and components, is made up of building blocks called modules. Though a module is actually a subroutine in the general programing sense, in this program the term is used to designate these major building blocks to separate them from the executive subroutines and other miscellaneous subroutines. There are five groups of modules:

> Aerodynamics: A1 thru A5
>
> Control or computer: C1 thru C10
>
> Dynamics: D1 thru D5
>
> Geodetic: G1 thru G6
>
> Sensors: S1 thru S10

The user may place any FORTRAN models or operations he chooses in any of these modules and designate the modules to be executed in any run by using input data cards.

The executive structure of the program consists of the main program and the subroutines required to set up and terminate runs, read input data, write output data, set up plots, and perform other housekeeping functions. The user very rarely needs to get into the details of the executive routines. Occasionally, he may need to use certain of the executive subroutines to switch from one phase of the run to another, such as switching from the parachute-descent phase to vernier engine ignition or terminal-descent staging.

Figure 38 shows a flow block diagram of the program as it is used during terminal descent. Starting with G1, the modules are called in the order shown to compute the derivatives of the differential equations and the other related variables. Then the executive calls the integrator (FOMS/AMRK), CNTR, OUPT, etc, as shown. The integrator can use either a simple first-order integrator with derivative averaging (FOMS) or fourth-order Adams-Moulton or Runge-Kutta integrators (AMRK) by specifying the form during his input. He may also choose between generating random numbers having either a uniform or Gaussian probability density function for use in any module (e.g., for radar noise and output quantization).

If he desires, he may include lander aerodynamics by calling Modules G3, A1, and A2 into the simulation between G1 and G5. The flexibility of the program is demonstrated by noting that the use of Modules G1, G3, A1, A2, G5, D1, and D2 and appropriate input data will yield a 6DOF entry vehicle simulation. This has been done several times for Mars Lander or Venus missions, with start-up and checkout times of less than two weeks.

The mathematical modeling used in Modules A, G, and D is described in the next chapter and in reference 1. The next section describes the modeling for the cw linear FM ranging-type radar. The modeling associated with Modules C3, C4, and C5 has been covered in Chapter III, with the exception of the propulsion system portion of C5, which is presented in Section C of this chapter. In general, the modeling duplicates the system block diagram shown in figure 4 and is based on the following assumptions:

1) Inertial sensor dynamics and quantization effects are neglected.

2) Accelerometer measurement errors and gyro drift errors are constants (g-sensitive effects are neglected).

3) The lag portion of the lead-lag network is too high in frequency to be simulated economically in a digital simulation, so only the lead portion is included with the valve dynamics.

4) All filters in the system are first-order.

5) The valve short-term transient dynamics are assumed to be second order, and there are no nonlinearities, except for position- and rate-limiting.

6) Time lags in the engine and feed system are too short to be simulated.

7) Engine misalignments and unbalanced aerodynamics are ignored.

138
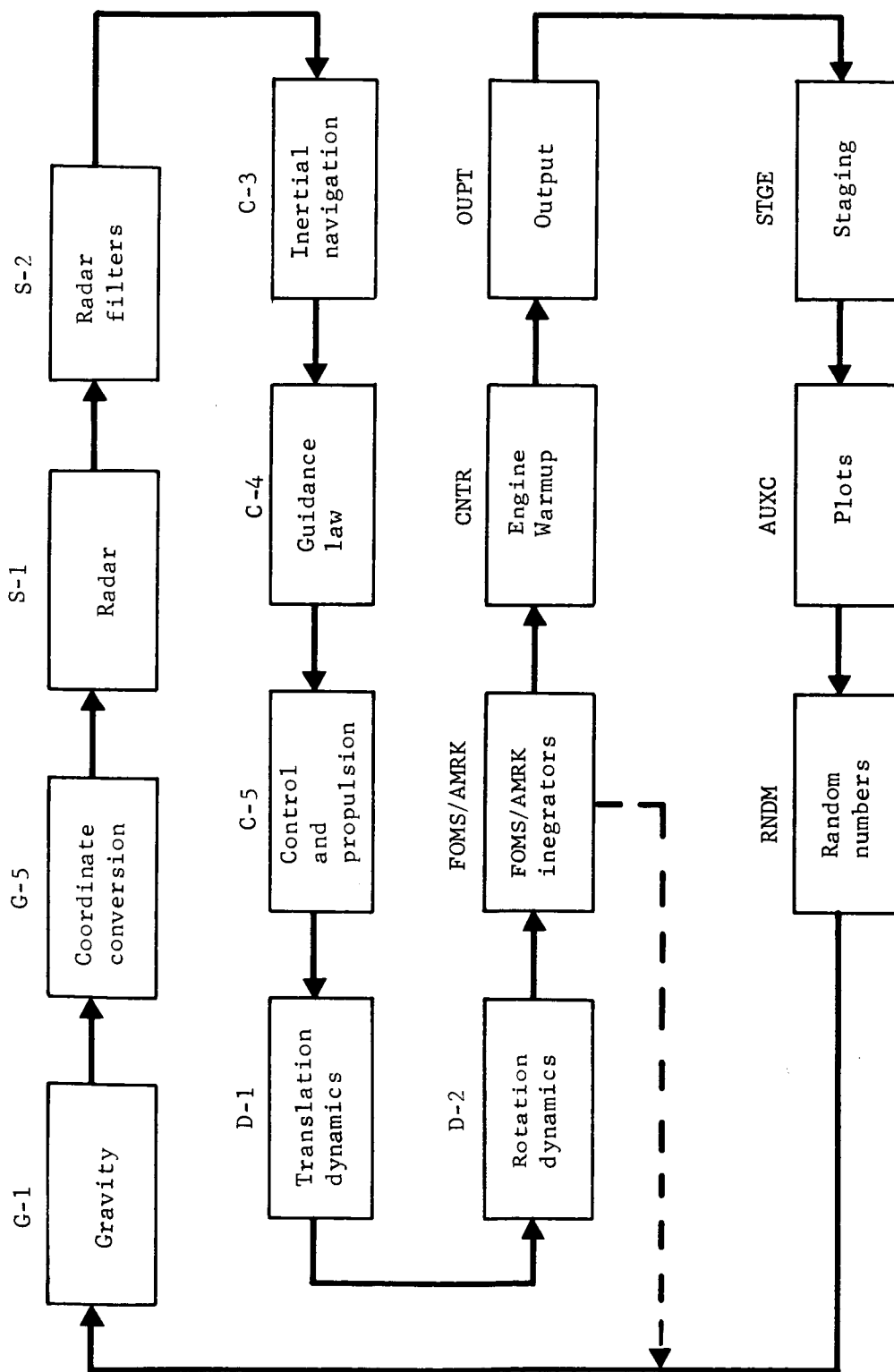
Figure 38.- Flow Block Diagram of the MOD6MV Computer Program as Used During Terminal Descent

B. Radar Model

The approach used in simulating the MOD-LM radar was that of a black box or functional simulation, as opposed to a one-to-one type of modeling. The following will describe the math models used in the simulation; as a guide to this discussion, a block diagram of the simulation is shown in figure 39 (the following text will refer to block A, B, etc, from this figure).

Figure 39 is representative of the flow of calculations carried out on a per beam basis within 6DOF simulation program. Figure 40 indicates the relative beam geometry. Note that the range beam appears in the center of the beam pattern; this is a recommended change to the system, and the LM radar has been evaluated with the range beam in this position.

1. Doppler and range frequency calculation (Block A).- The in-beam Doppler frequency and range frequency are calculated by: (1) transforming the inertial velocity of the vehicle into body-axis velocities; (2) transforming the body-axis velocity components into antenna-beam velocity components; (3) converting the velocity components along the beam into Doppler frequencies; (4) converting the inertial position of the vehicle into the position in the vehicle-centered coordinate system; and (5) transforming the position in the body-axis coordinate system into a component along Range Beam 4.

a. In-beam velocities: The in-beam velocities are obtained by solving equations (69) thru (75).

$$\vec{V}_B = \overline{A}\ \vec{V}_I \tag{69}$$

$$V_{B1} = \vec{\mu}_{B1} \cdot \vec{V}_B \tag{70}$$

$$V_{B2} = \vec{\mu}_{B2} \cdot \vec{V}_B \tag{71}$$

$$V_{B3} = \vec{\mu}_{B3} \cdot \vec{V}_B \tag{72}$$

$$V_{B5} = \vec{\mu}_{B5} \cdot \vec{V}_B \tag{73}$$
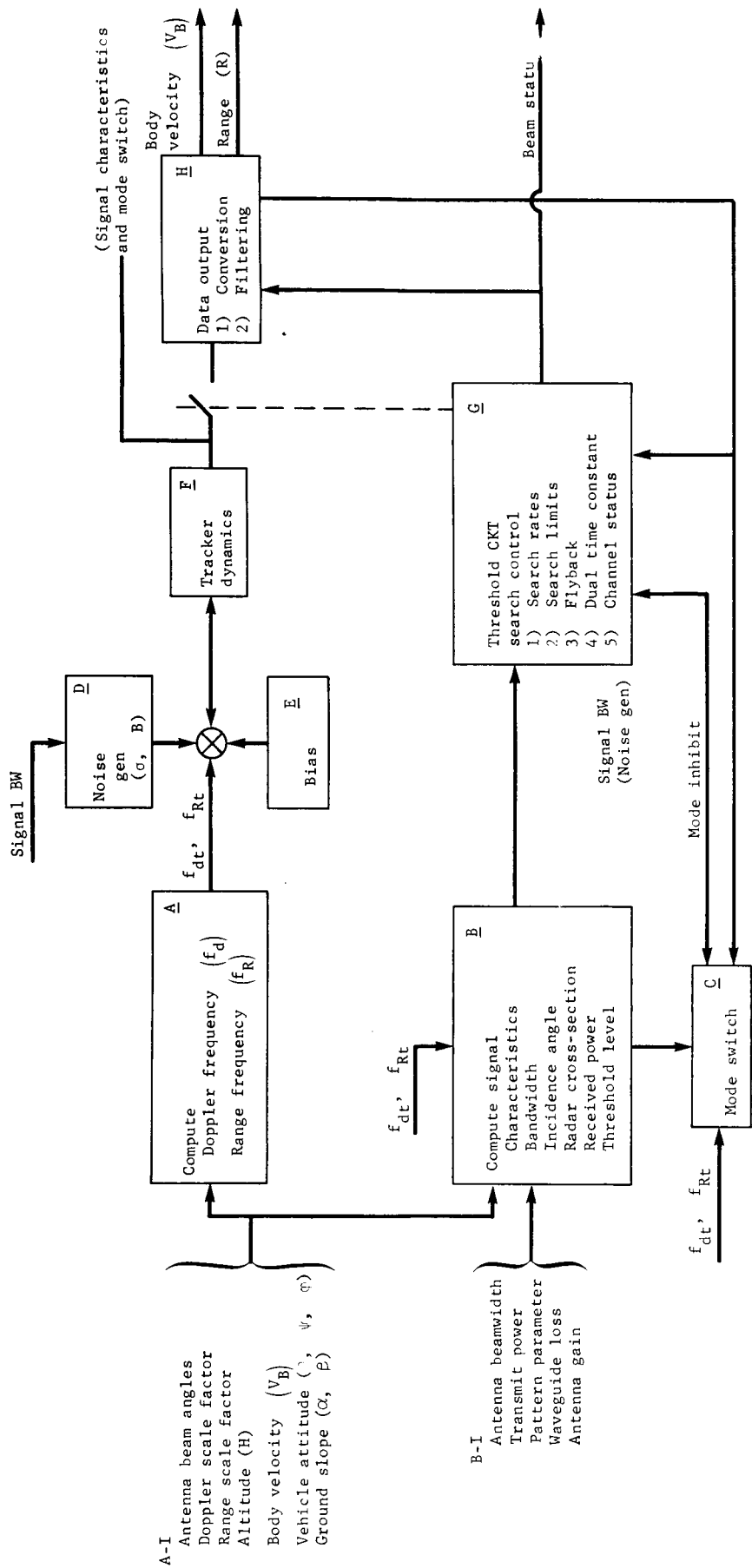
Figure 39.- Flow Block Diagram of the Calculations for Each Beam, Modified LM Radar Simulation

141
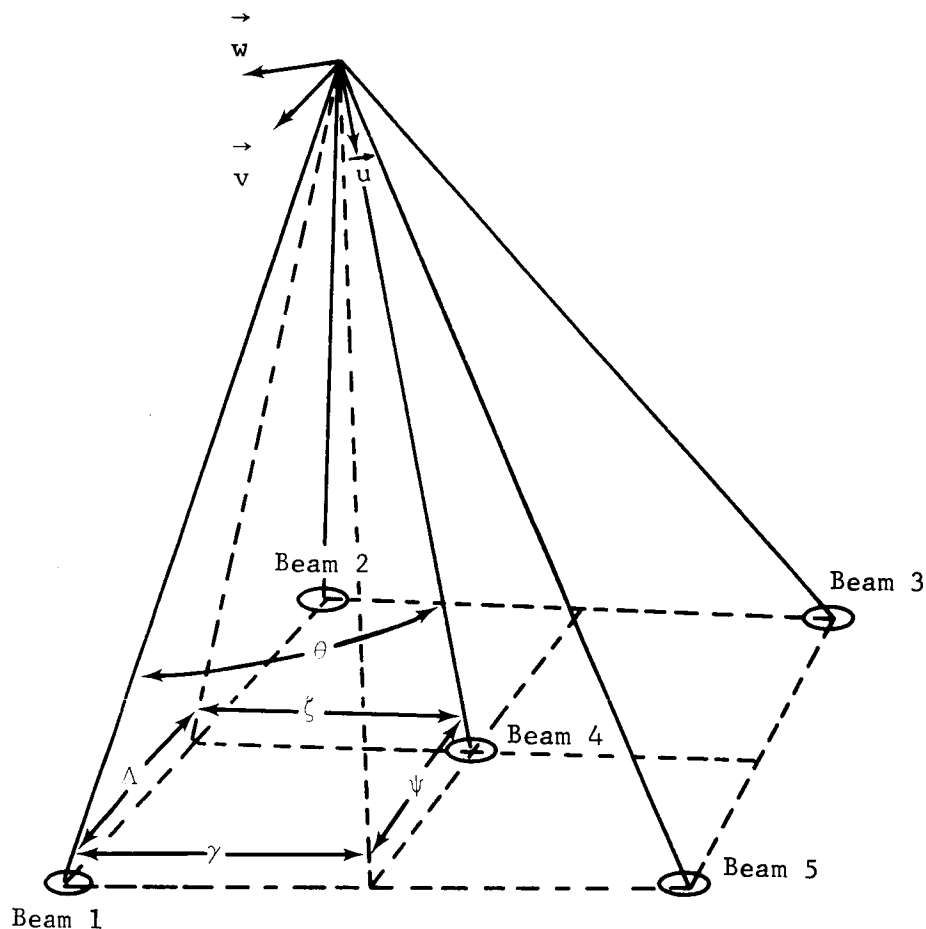
Note: 1. Beam 4 is the range beam. Con-
           figuration angles of Beams 2 and
           3 are nominally identical to those
           of Beam 1. Beam 5 only transmits.
       2. ζ = 20° 22' 48", Λ = 13° 59' 22",
           θ = 24° 33', ψ = 14° 53', and
           γ = 19° 45'.

Figure 40.- Definition of Beam Pointing Angles with Respect to Vehicle
Body Coordinates, Modified LM Radar Simulation

where $\bar{A}$ is the inertial- to body-coordinate-system transformation matrix; $\vec{V}_I$ is the vector expressing the inertial velocity of the vehicle; $\vec{V}_B$ is the velocity of the vehicle expressed in body coordinates; $\vec{\mu}_{B1}$, $\vec{\mu}_{B2}$, $\vec{\mu}_{B3}$ and $\vec{\mu}_{B5}$ are the unit vectors along Beams 1, 2, 3, and 5 in the body coordinate system; and V_{B1}, V_{B2}, V_{B3}, and V_{B5} are the components of the vehicle's velocity along Beams 1, 2, 3, and 5.

b. Range: For ranges, where

$$R = D/\cos \theta_4 \tag{74}$$

$$\bar{\mu}_{I4} = \bar{A}^T \bar{B}_4 \bar{\mu}_{B5} \tag{75}$$

$$\cos \theta_4 = \bar{\mu}_{I4} \cdot \bar{\mu}_N \tag{76}$$

$$D = \bar{X} \cdot \bar{\mu}_N \tag{77}$$

and $\bar{A}^T$ is the body- to inertial-coordinate-system transformation matrix; $\bar{B}_4$ is the beam 4- to body-coordinate-system transformation matrix; $\bar{\mu}_{B4}$ is the unit vector in body coordinates along the Beam 4 pointing direction; $\bar{\mu}_N$ is the unit vector normal to the terrain; $\bar{\mu}_{I4}$ is the Beam 4 pointing direction in inertial coordinates; θ_4 is the incidence angle for Beam 4; $\bar{X}$ is the vector for the position of the vehicle; D is the perpendicular distance from the vehicle to the ground; R is the slant range of the range beam (Beam 4).

c. Doppler frequencies: The simulation is based on assuming an infinite ground plane, which can slope in a defined direction. Then equation (78) is used to obtain the Doppler frequencies for the velocity beams.

$$f_d = \frac{2 V_{Bi}}{\lambda} \tag{78}$$

where V_{Bi} is the velocity of the beam and λ is the wavelength of the beam.

d. Range beam frequency: Equation (79) is used to obtain the range beam frequency.

$$f_R = KR + \frac{2\ V_{B4}}{\lambda} \tag{79}$$

where K is a scale factor corresponding to the frequency modulation of the range transmitter.

2. Signal characteristics (Block B).- This description pertains to Block B of figure 39; the calculations are in regard to the signal spectrum characteristics, the bandwidth, the power level, the proportion of received power in the tracker step low pass filter (SLPF), and the power level required by the threshold circuitry (as determined by the tracker output).

a. Incidence angle: The incidence angle of each beam is calculated in the following manner:

$$\overline{\mu}_{Ij} = \underline{A}^T\ \underline{B}_j\ \overline{\mu}_{Bj}, \quad \text{where} \quad j = 1,\ 2,\ 3,\ 4,\ 5 \tag{80}$$

$$\cos \theta_j = \overline{\mu}_{Ij} \cdot \overline{\mu}_N \tag{81}$$

where the subscripts refer to the calculation being made for each of the radar antenna beams.

b. Radar cross section: The radar cross-section as seen by each beam in illuminating the terrain σ_o is calculated for use in the radar range equation. The reflectivity model used is based on the Muhleman equation (see ref. 11), which is

$$\sigma_o(\theta) = \frac{\eta\ \kappa\ \cos \theta}{(\sin \theta + \alpha \cos \theta)^3} \tag{82}$$

where α and κ depend on the wavelength, η is the ratio of the surface reflectivity and that of a perfectly-reflecting sphere; and θ is the incidence angle of a beam.

144

Three reflectivity models from reference 11 are shown in figure 41. Curve 2 was used for all the MOD6MV simulation runs described in this report (i.e., $\alpha = 0.035$, $\kappa = 0.037$, and $\eta = 0.063$). Radar evaluation is extremely dependent on the reflectivity model that is used. This is brought out in Chapters IV and **VI**. **It is very desirable to further investigate this area.**

c. Radar range equation: The radar range equation that is used in this simulation to calculate the power received at the antenna P_R is

$$P_R = \frac{\sigma_o \, K \, P_t \, G_o \, \lambda^2}{(4\pi)^2 \, R^2 \, \cos \theta} \tag{83}$$

where P_t is the transmitter power and G_o is the two-way antenna gain.
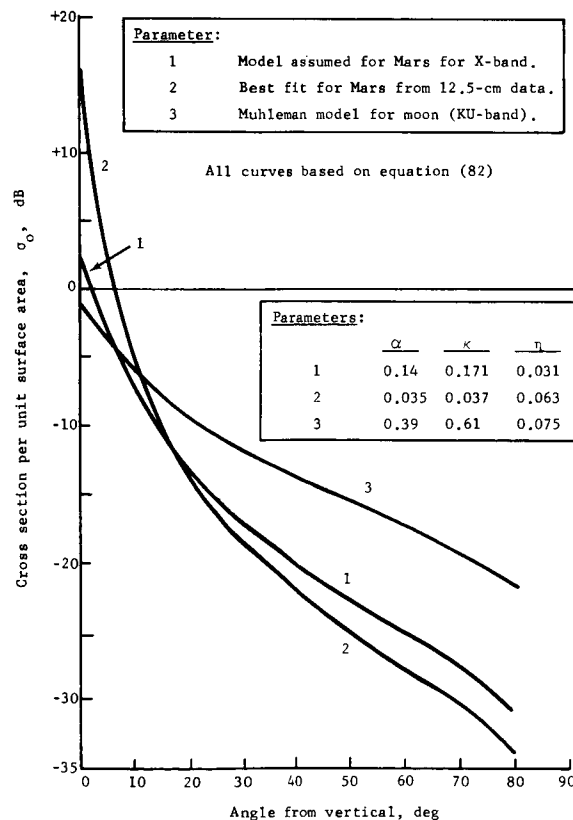
Figure 41.- Reflectivity Models Proposed for the
Modified LM Radar Simulation

The parameters used in the simulation representing the MOD-LM radar are given in table 16. These parameters were supplied by Robert Harrington of the Ryan Aeronautical Co., San Diego, California.

TABLE 16.- PARAMETERS USED IN SIMULATION
REPRESENTING THE MOD-LM RADAR

Parameters	Range	Velocity
Transmitter power	-14.1 dBw	-13.0 dBw
Waveguide loss	-1.8	-1.8
Pattern parameters	-6.0	-6.0
Antenna gain	27.2	28.2
Wavelength	-19.8	-20.6

d. Signal power: We need to determine the signal power that is seen by the tracker so that we can compare it to the tracker threshold. The spectrum seen by the tracker may be modified somewhat, due to lag of the tracker output (due to high tracking rates, the SLPFs may straddle the incoming Doppler spectrum as shown in figure 42).
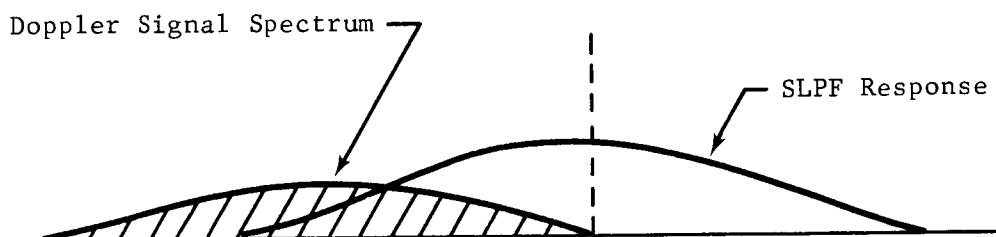
Figure 42.- Spectrum Overlap in the SLPFs Due to
High Tracking Rates

When this situation is detected in the simulation, the received power calculated from equation (83) is modified as follows:

$$P_{RT} = P_R + 10 \log \frac{\triangle BW}{BW_S} \qquad (84)$$

where $\triangle BW$ is the portion of the signal spectrum that appears in the tracker SLPF bandwidth when both bandwidths are idealized as shown in figure 43, and BW_S is the Doppler signal spectrum 3-dB bandwidth.
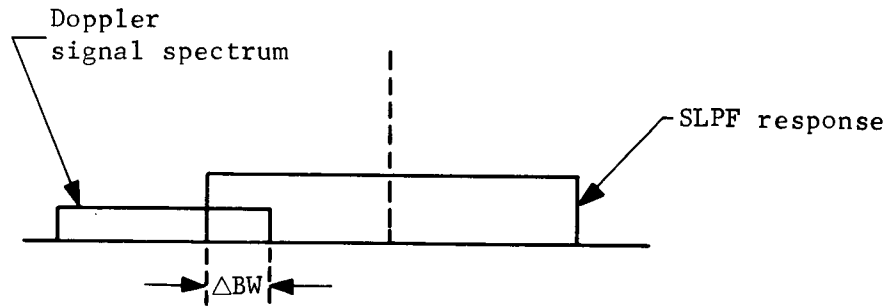
Figure 43.- Idealized Spectrums for the SLPF Bandwidth

e. Signal bandwidth: The Doppler signal spectrum bandwidth (see fig. 43) is calculated as follows:

$$\triangle f_d = \frac{2\triangle\gamma}{\lambda} \left| \overline{V}_B \right| \sin \gamma \tag{85}$$

where $\triangle\gamma$ is the average 3-dB beamwidth of the antenna, $\left| \overline{V}_B \right|$ is the total velocity of the vehicle, and γ is the angle between the centerline of the beam and the velocity vector, and the range signal spectrum bandwidth is defined by:

$$\triangle f_r = (SF) \; R \; \triangle\gamma \; \tan \; \theta + \frac{2V_{cp} \; \triangle\gamma}{\lambda} \tag{86}$$

(The derivation is found in Appendix F.)

The spectrum bandwidth is assumed to be proportional to the component of velocity perpendicular to the beam-pointing direction, as modified by the 3-dB beamwidth of the antenna. The spectrum is assumed to have a Gaussian distribution.

f. Tracker threshold level: The simulation made use of the receiver sensitivity curves supplied by Robert Harrington of the Ryan Aeronautical Co. These curves are shown in figures 44a thru 44d to determine the adequacy of the ratio required for tracking (referred to the antenna). Figure 44a shows the sensitivity of the velocity receiver when the LM radar operates in the wideband mode. This curve can be described as having a Doppler spectrum centered at 5000 Hz with a bandwidth of 390 Hz and power level (as calculated by the radar range equation and modified by the amount of spectrum overlap in the SLPF) exceeding -139 dBw -- and satisfies the track criterion. Figure 44b shows the sensitivity of the velocity receiver when the LM and Modified LM radars operate in the low mode. Figure 44c shows the sensitivity of the range receiver. The curves shown in figures 44a thru 44c were originally derived to satisfy the LM radar test requirement. Figure 44d shows the sensitivity of the velocity receiver for wide-band operation when the bandwidth of the SLPFs in the Mod-LM is changed from 2800 to 600 Hz. The curves shown in figures 44a thru 44d were curve-fit with straight line segments for use in the digital simulation. Each of the curves is then represented by equations of the form:

$$P_{TH} = g\left(f_{dt}, \ f_{Rt}\right) \tag{87}$$

where P_{TH} is the threshold tracking criterion referenced to the antenna, in dBw, and f_{dt} and f_{Rt} are the tracker output frequencies in the Doppler and range channels, respectively.

3. Mode switch (Block C).- Mode switching is based on range and velocity tracker outputs, and affects the SLPF bandwidths, tracker search limits, search rates, range scale factor, and receiver sensitivity. Table 17 describes the mode switching criteria. The criteria numbered 1, 2, 3, and 4 in table 17 apply for the LM-radar mode switching criteria established by Robert Harrington of Ryan Aeronautical Co. (ref. A13), and the criteria numbered 1-a, 2-a, 3-a, and 4-a apply for the suggested mode criteria change from 2500 to 1250 ft. The latter are presently being used in the simulation.
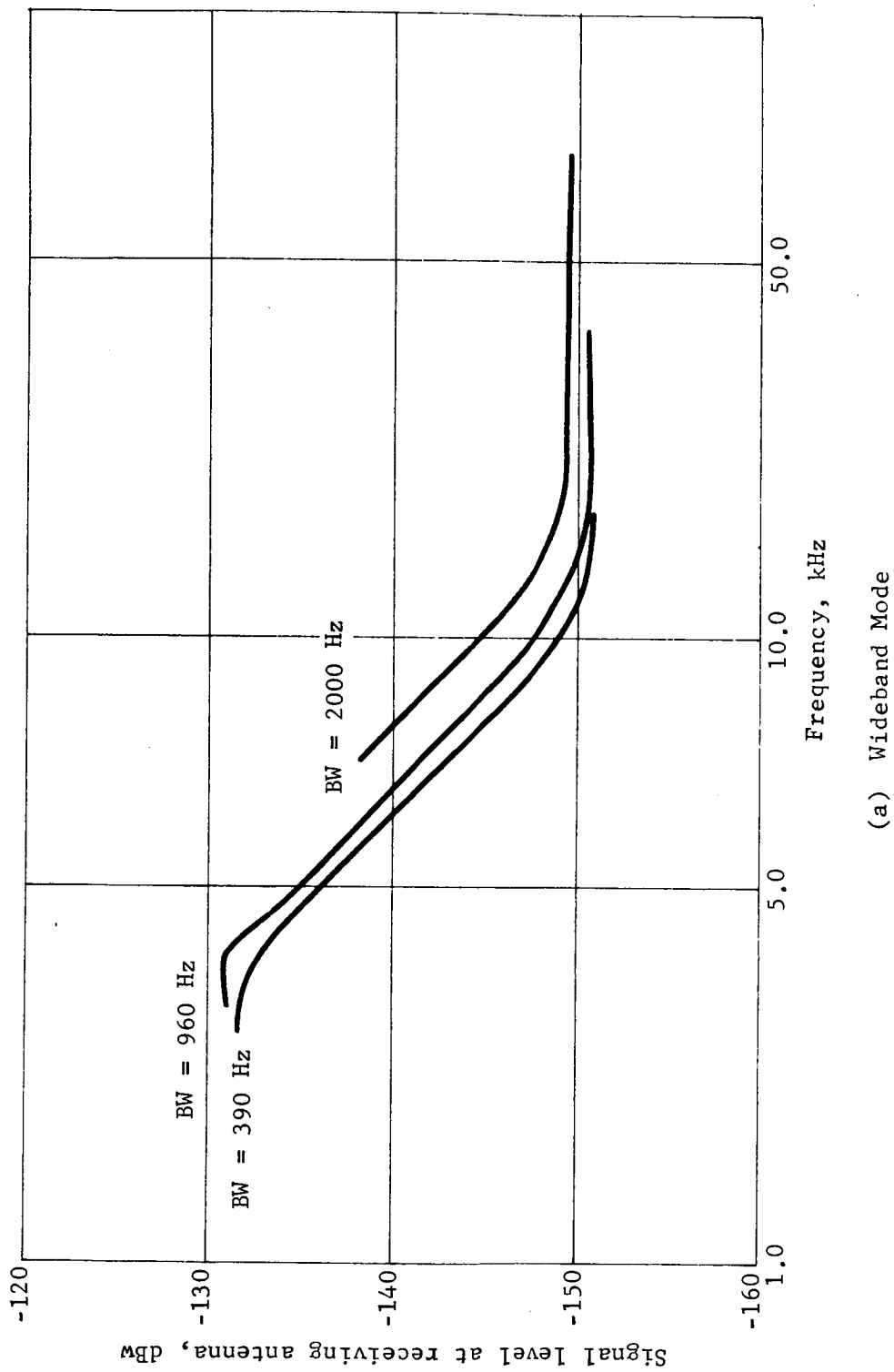
Figure 44.- Sensitivity of the Velocity Receiver in the Modified LM Radar System

(a) Wideband Mode

Frequency, Hz
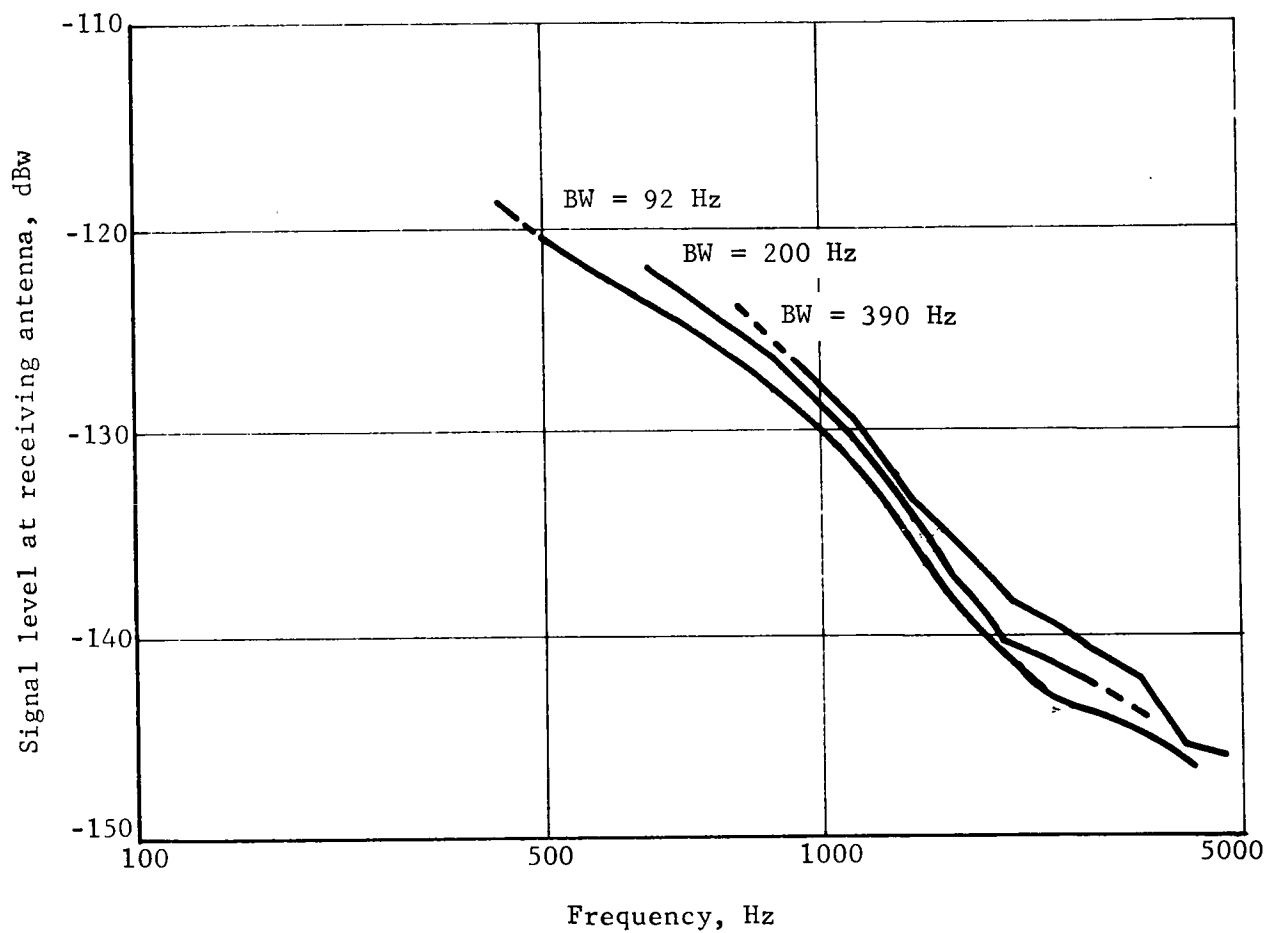
(b) Narrowband Mode

Figure 44.- Continued

Frequency, Hz

Signal level at receiving antenna, dBw
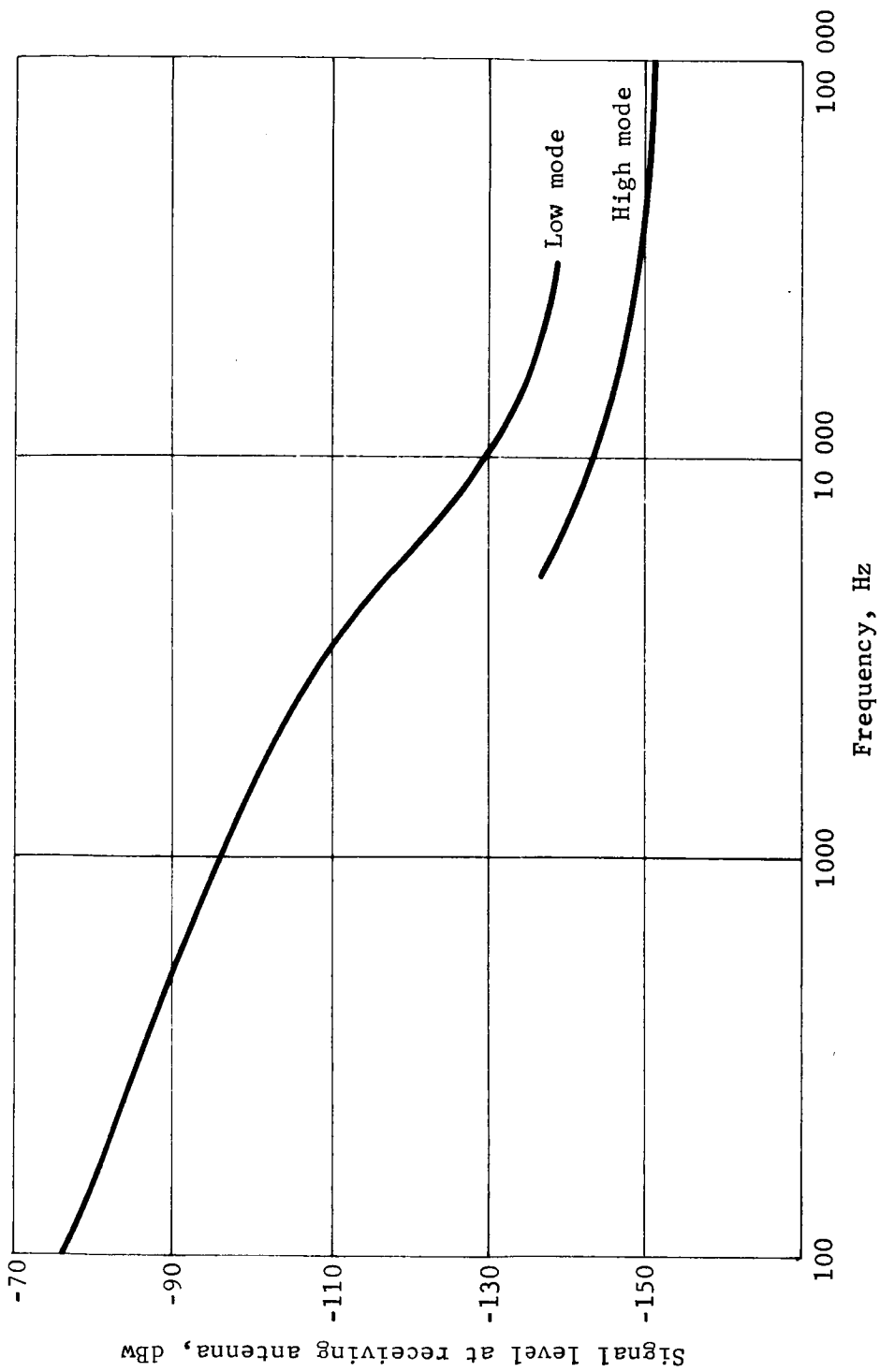
(c) Range Channel Acquisition Sensitivity

Figure 44.- Continued
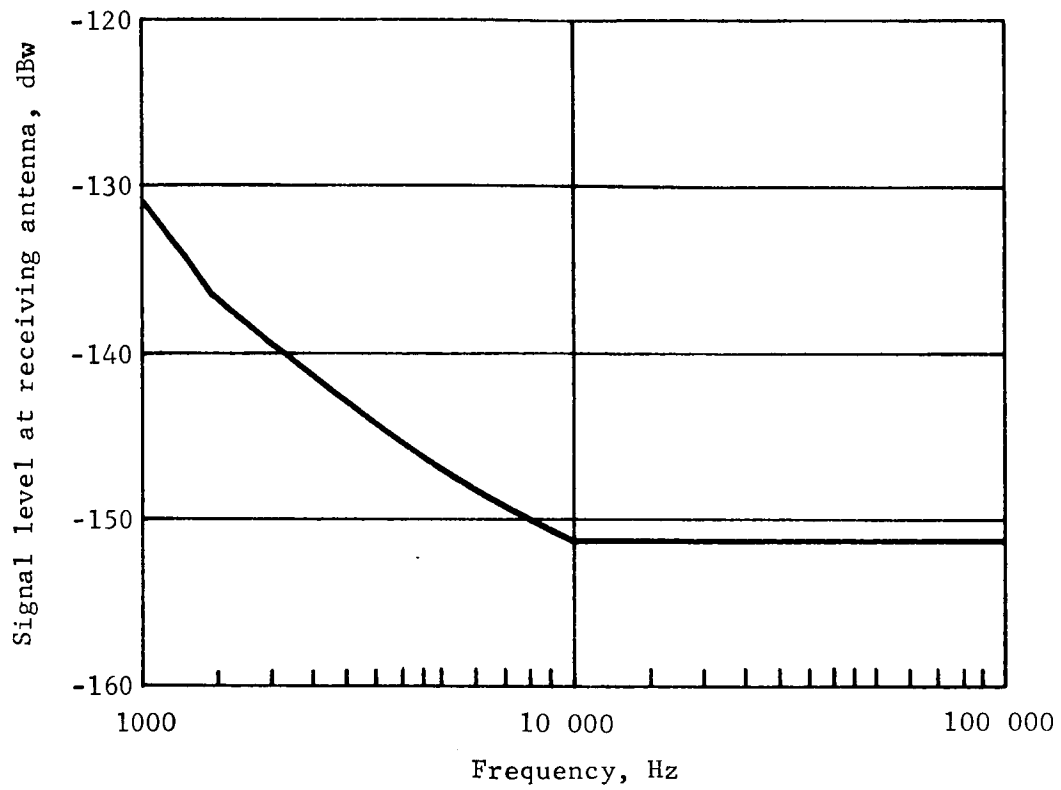
(d) Wideband Mode, Modified SLPF Bandwidth = 600 Hz

Figure 44.- Concluded

TABLE 17.- MODE SWITCHING CRITERIA

Criteria	Mode
1. Range < the frequency equivalent of 2500 ft 1-a. Range < the frequency equivalent of 1250 ft	Low mode throughout the system
2. Range > the frequency equivalent of 2500 ft 2-a. Range > the frequency equivalent of 1250 ft	High mode except the velocity in any individual velocity tracker between the equivalent frequency limits of ±65.5 fps will switch the SLPF bandwidths to the low mode equivalent to that channel
3. If low mode has been achieved, then: Range > the frequency equivalent of 3100 ft 3-a. If low mode has been achieved, then: Range > the frequency equivalent of 1850 ft	High mode applies as described above
4. Mode inhibit if the range beam or either of its compensating beams are in search mode 4-a. Same as 4.	Status quo

4. Noise generator (Block D).- The statistical characteristics of the tracker output are obtained by adding the appropriate jitter or noise to the Doppler frequency f_d and the range frequency f_R. The rms of the frequency jitter c and the time constant of the noise τ are functions of the Doppler spectrum bandwidth (ref. 12). Therefore

$$\sigma = \frac{BW_S}{2} \qquad (88)$$

$$\tau = \frac{1}{\pi\, BW_S} \qquad (89)$$

It was assumed that the noise followed a Gaussian distribution. Each velocity channel as well as the range channel has its own noise generator, which produces variations on the respective signals according to the parameters defined by equations (88) and (89).

5. Bias (Block E).- Although the simulation has the capability to add biases to the signals (see fig. 39), no runs were made with biases, because the outcome is predictable and is not a problem in any sense.

6. Tracker (Block F).- The closed-loop transfer function of the tracker is represented by a first-order lag, i.e.,

$$F(S)_{CL} = 1/(1 + \tau S) \tag{90}$$

where $0.05 < \tau < 0.07$. The closed-loop time constant τ of the tracker is specified to be within these limits. The value used in the simulations to date is $\tau = 0.06$.

7. Threshold and search control (Block G).- The threshold circuit indicated in this block merely takes the threshold-power-level criterion indicated from the sensitivity curves [see eq. (87)] and compares it with the received power indicated in the tracker, [see eq. (84)]. Then, the functions described in table 17 are carried out depending on the results of the comparison just described and the current state of the tracker.

Additional logic is provided to detect the presence of cross-coupling between the velocity beams. This logic operates by checking for cross-coupled energy for the three possible cases for each beam. If any cross-coupled signal is above the threshold, the signal is processed through the tracker bandwidth, the level of each signal in the bandwidth is compared, and the tracker is biased to follow the strongest signal present.

Cross-locking may occur for various combinations of surface conditions and vehicle attitudes, or may be forced to occur by selectively depressing the signal level in a beam for a fixed time and allowing the cross-coupling logic to operate.

The 0.5-sec lockout time mentioned in Tracker State 2 of table 17 refers to the time allowed the tracker to observe a signal below the threshold power level before it begins the search mode. The 0.1 sec mentioned in Tracker State 4 of table 18 is the time that the received signal must remain above the threshold (during the search mode) before normal tracking begins.

154

TABLE 18.- FUNCTIONS TRIGGERED AS A RESULT OF THRESHOLD CRITERIA

Tracker state	Threshold criteria	Function
1. Tracking	$P_{RT} > P_{TH}$ [a]	Continue tracking
2. Tracking	$P_{RT} < P_{TH}$	Commence 0.5 sec lockout. If $P_{RT} > P_{TH}$ - 3 dBw, the tracker is held at the last value it had during the lockout time. If $P_{RT} < P_{TH}$ - 3 dBw, the tracker continues tracking during the lockout time.
3. Search	$P_{RT} < P_{TH}$	Continue search
4. Search	$P_{RT} > P_{TH}$	Commence 0.1 sec proof time.

[a] P_{RT} = received power seen by the tracker as referred to the antenna;

P_{TH} = receiver threshold sensitivity as referred to the antenna.

a. Search control: The search mode occurs in the simulation on an individual-channel basis, according to the radar mode. The search limits and rates described in table 19 are for the existing LM radar; those in table 20 are for the Modified LM radar. It takes 0.2 sec for all beams, regardless of radar mode, to drive the tracker VCO from the low limit to the high limit of the search range.

b. Channel status: The status of output data is flagged in the following manner: if all velocity channels are tracking, a discrete is initiated to indicate this; if the range beam and its velocity-compensating beams are tracking, a discrete is also available to indicate this. These two discretes now serve as LM radar data flags. A suggested change, which was incorporated in the simulation, is to use a discrete for each individual channel, to indicate tracker locks and searches.

TABLE 19.- LM RADAR EXISTING SEARCH RATES AND LIMITS

Beam	Radar mode	Search limits	Search rates
1 and 2	High	-41.5 kHz $< f < 52.4$ kHz	27.4 kHz/sec for 1.44 kHz $< f < 52.4$ kHz 2.3 kHz/sec for -1.44 kHz $< f < 1.44$ kHz 27.4 kHz/sec for -41.5 kHz $< f < -1.44$ kHz
3	High	-20.3 kHz $< f < 77$ kHz	26.4 kHz/sec for 1.44 kHz $< f < 77$ kHz 2.3 kHz/sec for -1.44 kHz $< f < 1.44$ kHz 26.4 kHz/sec for -20.3 kHz $- f < -1.44$ kHz
1, 2, and 3	Low	-5.24 kHz $< f < 7.4$ kHz	2.3 kHz/sec
4	High	830 Hz $< f < 141.6$ kHz	25.3 kHz/sec
4	Low	830 Hz $< f < 38.5$ kHz	6.85 kHz/sec

TABLE 20.- SEARCH RATES AND LIMITS PROPOSED FOR THE MODIFIED LM RADAR

Beam	Radar mode	Search limits	Search rates
1, 2, and 3	High	$0 < f < 12.$ kHz	2.3 kHz/sec for $f < 1.44$ kHz 6.6 kHz/sec for 1.44 kHz $< f < 12.$ kHz
1, 2, and 3	Low	$0 < f < 6.$ kHz	2.14 kHz/sec
4	High	1 kHz $< f < 66.$ kHz	23.2 kHz/sec
4	Low	1 kHz $< f < 19.$ kHz	6.4 kHz/sec

8. Data output (Block H).- The velocity tracker outputs are con-
verted to body-axis velocities by the following relationships:

$$V_u = \frac{\lambda}{4 \cos \Lambda \cos \zeta} (D_1 + D_3) \qquad (91)$$

$$V_v = \frac{\lambda}{4 \sin \Lambda} (D_1 - D_2) \qquad (92)$$

$$V_w = \frac{\lambda}{4 \cos \Lambda \sin \zeta} (D_2 - D_3) \qquad (93)$$

where Λ and ζ are the beam configuration angles defined in
figure 40, D_1, D_2, and D_3 are the Doppler frequencies of
Beams 1, 2, and 3, respectively, and V_u, V_v, and V_w are the
body-axis velocities described in figure 40.

As shown in equation (94), the velocity trackers of Beams 1
and 3 are used to correct the velocity component of the Beam 4
range-tracker output.

$$R = \frac{f_R - \frac{\lambda_1}{2 \lambda_2} (D_1 + D_2)}{M_K} \qquad (94)$$

where f_R is the range tracker output, M_K is the range scale
factor (2.32 for high mode, 11.6 for low mode), R is the range
along the u axis (see fig. 40), λ_1 is the wavelength of the
range transmitter, and λ_2 is the wavelength of the velocity
transmitter.

For radar-prime-mode simulations, the radar outputs are fil-
tered by analog filters with first-order time constants. For
radar-aided, inertial-navigator simulations, a digitized output
is used, which has a specified count time. A quantization error
of ±1 Doppler cycle is added by using a uniform, random-number
generator.

C. Propulsion System Model

The model of the propulsion system consists of equations that describe the throttle valve dynamics, the engine thrust, the specific impulse, the flow rate, and the propellant-tank pressure blowdown effect.

Figure 45 shows a block diagram of this portion of the system, beginning with the mixing matrix inputs, ϵ_θ, ϵ_ψ, and T_e. Each input is filtered by a lead-lag network for inner-loop control compensation. It is difficult to simulate the pole frequency, P, because it is about 300 rad/sec, so in the digital model it is neglected. Since the mixing matrix is a linear operation, the zero (S+Z) is included in the linear portion of the valve model. The valve is essentially a second-order dynamic device, which, with the zero from the lead-lag network, is described by

$$\frac{X_1(S)}{B_1(S)} = \frac{\frac{P_2}{Z}(S + Z)}{S^2 + P_1 S + P_2} \tag{95}$$

The digital simulation of this transfer function is obtained by integrating equations (96) and (97).

$$\dot{A}_1 = P_2 \left(B_1\right) - P_2 \left(X_1\right) \tag{96}$$

$$\dot{X}_1 = A_1 + B_1 \left(\frac{P_2}{Z}\right) - P_1 \left(X_1\right) \tag{97}$$

In the simulation, X_1 and $\dot{X}_1$ are limited as follows:

$$X_{min} \leq X_1 \leq X_{max} \tag{98}$$

$$-\dot{X}_{max} \leq \dot{X}_1 \leq \dot{X}_{max} \tag{99}$$

Furthermore, when X_1 is on either the upper or lower limit and is trying to drive harder into the limit, $\dot{X}_1$ is set to zero. Valves 2 and 3 are described by the same equations, with the obvious change of subscript.
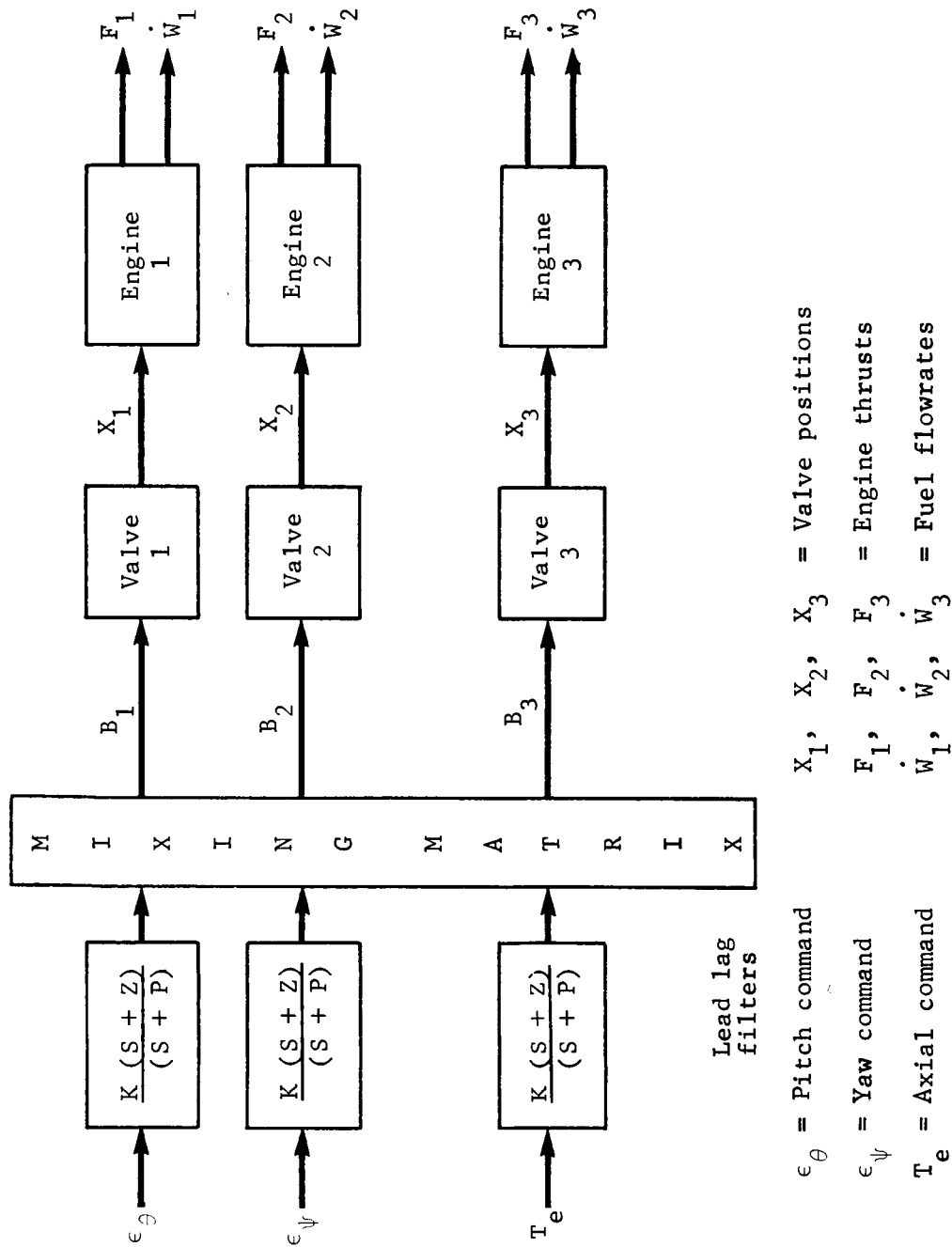
Figure 45.— Flow Block Diagram of the MOD6MV Calculations for the Propulsion System

ϵ_θ = Pitch command

ϵ_ψ = Yaw command

T_e = Axial command

X_1, X_2, X_3 = Valve positions

F_1, F_2, F_3 = Engine thrusts

$\dot{W}_1$, $\dot{W}_2$, $\dot{W}_3$ = Fuel flowrates

The propellant tank pressure blowdown is assumed to occur adiabatically, i.e., without the addition of heat, which is a conservative assumption. The initial pressurant gas volume is calculated from equation (100) to give the right blowdown pressure ratio when the input fuel is 100% used.

$$P_T = P_o \left(1.0 + \frac{Fuel}{Fuel_T} \cdot C_{PT1}\right)^{-\delta} \tag{100}$$

where

$$C_{PT1} = (BLD)^{1/\delta} - 1 \tag{101}$$

and BLD is the blowdown ratio, $Fuel_T$ is the initial fuel load in lb, δ is the ratio of the specific heats, and P_o is the initial tank pressure in psia.

The feed system is represented by steady-state pressure drop equations that seek to linearize the actual flowrate as closely as possible to the actual position of the valve. This is done by calculating a valve flow resistance which, with the other pressure drops in the feed system, gives the desired flow for the average pressure in the tank. The actual flowrate, however, is a linear function of valve postion only at this pressure and deviates somewhat at either higher or lower tank pressures.

In the simulation, we only approximated the steady-state, fluid-flow performance of the feed system because we did not account for the small changes in the thrust coefficient that occur at low flowrates. The equations used in the simulation are:

a. Desired flowrate:

$$\dot{W}_1 = \dot{W}_B \cdot X_1 \tag{102}$$

b. Flow resistance:

$$R = \left[\frac{\left(P_{BD} \cdot P_0\right) + \left(\dot{W}_1 \cdot \dot{W}_{C1}\right) - \dot{W}_{C2} \left(\frac{\dot{W}_{C3} \cdot \dot{W}_1^2}{2}\right)}{\dot{W}_{C3} \left(\frac{\dot{W}_1^2}{2}\right)}\right]^{\frac{1}{2}} \tag{103}$$

160

where:

$$\dot{W}_{C1} = -\frac{P_{CM}}{\dot{W}_{max}} \tag{104}$$

$$\dot{W}_{C2} = \frac{1}{\left(CD \cdot A_{INJ}\right)^2} \tag{105}$$

$$\dot{W}_{C3} = \frac{144}{\rho_F \cdot 32.2} \tag{106}$$

$$A_{INJ} = \left[\frac{72 \cdot C_{INJ}}{CD^2 \left(\rho_F \cdot 32.2\right)}\right]^{\frac{1}{2}} \tag{107}$$

$$C_{INJ} = \frac{\dot{W}_B^2}{P_{BD} \cdot P_0 + \dot{W}_B \left(\dot{W}_{C1}\right) - D_{PVM} \left(\dfrac{\dot{W}_B}{\dot{W}_{max}}\right)^2} \tag{108}$$

where $\dot{W}_B$ is the design flowrate in lb/sec, P_{BD} is the blow-down tank pressure in psia about which to linearize the flow resistance, D_{PVM} is the valve pressure drop in psi that occurs at the maximum flowrate, $\dot{W}_{max}$ is the maximum flowrate in lb/sec, P_{CM} is the maximum chamber pressure in psia, CD is the injector discharge coefficient, and ρ_F is the fuel density in slug/ft^3.

c. Actual flowrate:

$$\dot{W}_1 = \frac{\dot{W}_{C1} + \sqrt{\dot{W}_{C1}^2 + 2\left[\dot{W}_{C2}\left(\dot{W}_{C3}\right) + \dot{W}_{C3}\left(R^2\right)\right](PT)}}{\dot{W}_{C3}\left(\dot{W}_{C2} + R^2\right)} \tag{109}$$

d. Percent flowrate:

$$P_{CW} = \frac{\dot{W}_1}{\dot{W}_{max}} \tag{110}$$

e. Specific impulse:

$$I_{SP} = \text{Table lookup for } I_{SP} \text{ as a function of } P_{CW}$$

(This table lookup is based on test data that cover the range of flowrates at which the engine can operate.)

f. Engine thrust:

$$F1 = \dot{W}_1 \left(I_{SP} \right) \tag{111}$$

If desired, a constant thrust or regulated propulsion system can be used in the simulation by setting the blowdown ratio, BLD, less than one.

162

VIII. PARACHUTE DYNAMICS

A. General Discussion

The 6DOF equations of motion for a parachute-Lander combination in the presence of winds and gusts are described below. In this chapter, the results obtained with this simulation are compared with those from an earlier two-dimensional program (ref. 13). The simulation of the parachute descent begins with the parachute open and descending under trim conditions. When the Lander reaches vernier ignition altitude, the vernier engines are allowed to warm up for a few sec before the parachute is released. When the parachute is released, the parachute equations cease being computed, and the simulation focuses on the performance of the Lander capsule and its radar system.

The six basic assumptions inherent in this simulation are listed below:

1) The canopy and shroud lines act as a rigid body;

2) The canopy is symmetrical and hemispherical;

3) The elongation of the riser is proportional to the load;

4) The riser is massless and transmits tension and torsion only;

5) The capsule attachment harness acts like a rigid truss as long as the riser pull angle, λ_c, is less than half the apex angle of the truss (see fig. 46);

6) The body-axis system corresponds to the principal axes.
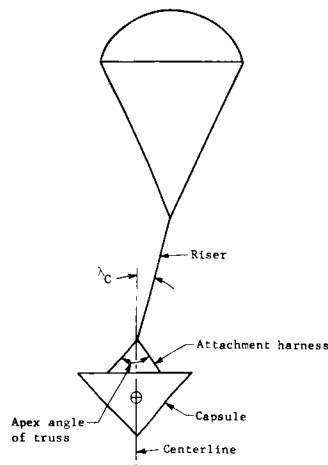
Figure 46.- Configuration of the Capsule
Attachment Harness

Some of the main features of the simulation are:

1) Both the parachute and the capsule have full 6DOF;

2) The aerodynamic forces and moments on the parachute and capsule can be expressed as functions of the angle-of-attack and/or the Mach number;

3) Horizontal and vertical wind profiles can be expressed as functions of the altitude and/or random wind gusts;

4) The apparent and enclosed masses of the parachute are included;

5) The simulation can be run with or without a parachute;

6) Coriolis terms are available;

7) The size of the parachute can be expressed as a function of time in order to simulate the reefing of the canopy;

8) The gravity is expressed as a function of the altitude;

9) The atmospheric density and the speed of sound are functions of the altitude;

10) Spherical- or flat-planet options are incorporated.

B.   Development of Model

1. Coordinate system.- A planet-fixed, tangent-plane coordinate system (X_{TP}, Y_{TP}, Z_{TP}) is initially oriented with respect to the rotating planet, as shown in figure 47. Note that the longitude of the planet is not defined.
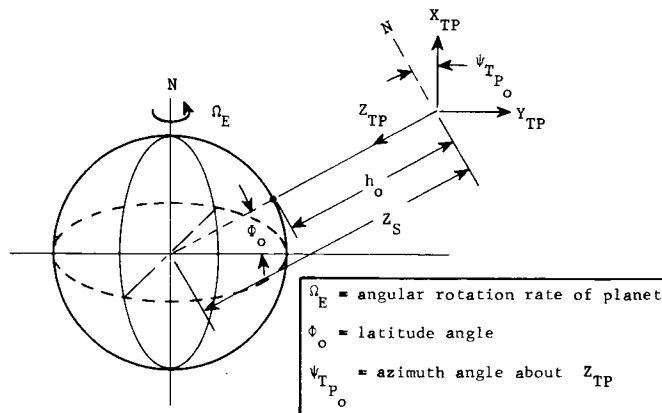
Figure 47.- Orientation of the Tangent-Plane Coordinate System

Figure 48 shows that an Euler angle transformation is required to express the tangent-plane coordinates of each body as body-axis coordinates $\left(X_B, \ Y_B, \ Z_B\right)$, where ψ is the first rotation $\left(\text{about the} \ Z_{TP} \ \text{axis}\right)$, θ is the second rotation (about the Y^1 axis), and φ is the third rotation (about the X^{11} axis).
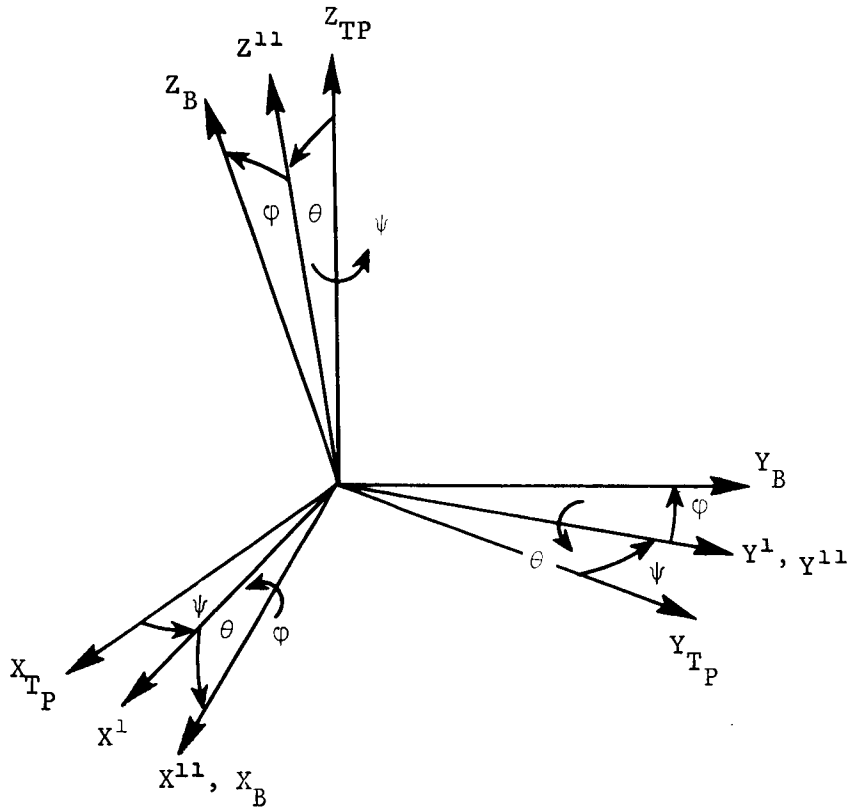
Figure 48.- Euler Angle Transformations Needed to Express Tangent-Plane Coordinates as Body-Axis Coordinates

2. Equations of motion.- The forces on each body are computed in the body-axis coordinate system of each body. A set of body-axis acceleration equations [eq. (112) thru (114)] is then re-solved into a set of planet-fixed, tangent-plane equations, which can then be integrated to obtain the velocities and positions for each body.

$$\ddot{X} = \left(F_{X_{BA}} + T_{X_{BA}} + F_X\right)\Big/ \text{Mass} + G_X \qquad (112)$$

$$\ddot{Y} = \left(F_{Y_{BA}} + T_{Y_{BA}} + F_Y\right)\Big/ \text{Mass} + G_Y \qquad (113)$$

$$\ddot{Z} = \left(F_{Z_{BA}} + T_{Z_{BA}} + F_Z\right)\Big/ \text{Mass} + G_Z \qquad (114)$$

$$\dot{P} = \frac{1}{A}\left[L_{BA} + L_T + L_X + (B - C)\,(Q \cdot R)\right] \qquad (115)$$

$$\dot{Q} = \frac{1}{B}\left[M_{BA} + M_T + M_Y + (C - A)\,(R \cdot P)\right] \qquad (116)$$

$$\dot{R} = \frac{1}{C}\left[N_{BA} + N_T + N_Z + (A - B)\,(P \cdot Q)\right] \qquad (117)$$

where: $F_{X_{BA}}$, $F_{Y_{BA}}$, and $F_{Z_{BA}}$ are the aerodynamic forces; $T_{X_{BA}}$, $T_{Y_{BA}}$, and $T_{Z_{BA}}$ are the thrust forces; F_X, F_Y, and F_Z are the coupling forces transmitted to the capsule or chute by the riser (expressed in the body-axis system); L_{BA}, M_{BA}, and N_{BA} are the aerodynamic moments; L_T, M_T, and N_T are the thrust moments; L_X, M_Y, and N_Z are the coupling moments produced by the riser force about the roll, pitch, and yaw axes; and A, B, and C are the principal moments of inertia about the roll, pitch, and yaw axes.

3. Determination of coupling force.- After determining the center-of-gravity positions and the Euler angles for the capsule and the parachute, the body-axis locations (denoted by the subscript B) of the riser attach point for the parachute (P) and the riser attach point for the capsule (C) are computed. These locations are then transposed to the tangent-plane coordinate system (see fig. 49) in order to determine the stretched riser length, SXZI.
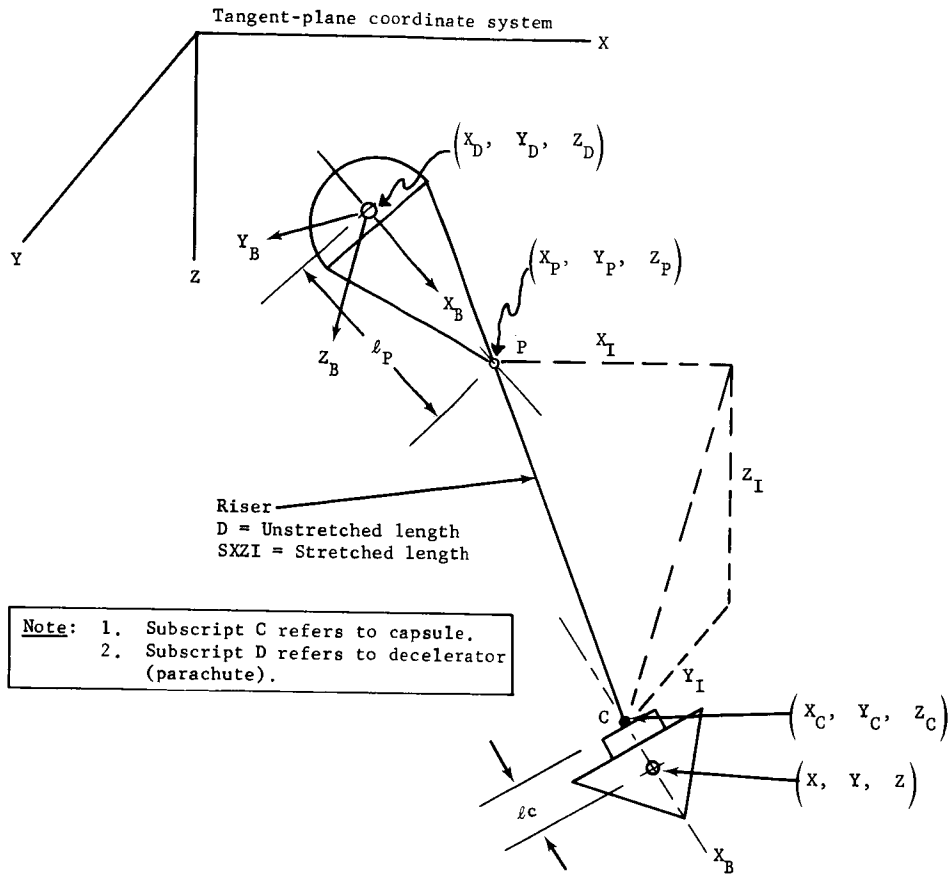
Figure 49.- Determination of the Stretched Riser Length

where

$$SXZI = \left(X_I^{\,2} + Y_I^{\,2} + Z_I^{\,2} \right)^{\frac{1}{2}} \tag{118}$$

$$X_I = X_C - X_P \tag{119}$$

$$Y_I = Y_C - Y_P \tag{120}$$

$$Z_I = Z_C - Z_P \tag{121}$$

$$\text{Coupling force} = T_R = (SXZI - D) \cdot K \tag{122}$$

and K is the spring constant of the riser. $T_R = 0$ when $(SXZI - D) < 0$.

4. Forces and moments transmitted to parachute.- Figure 50 shows the forces and moments that are transmitted to the parachute. Before attempting to solve equations (123) thru (132), point X_{CP}, Y_{CP}, Z_{CP} must be expressed in the chute-body coordinate system. K_S, the torsional spring constant of the riser, [eq. (129)] is equal to zero if a swivel is used.
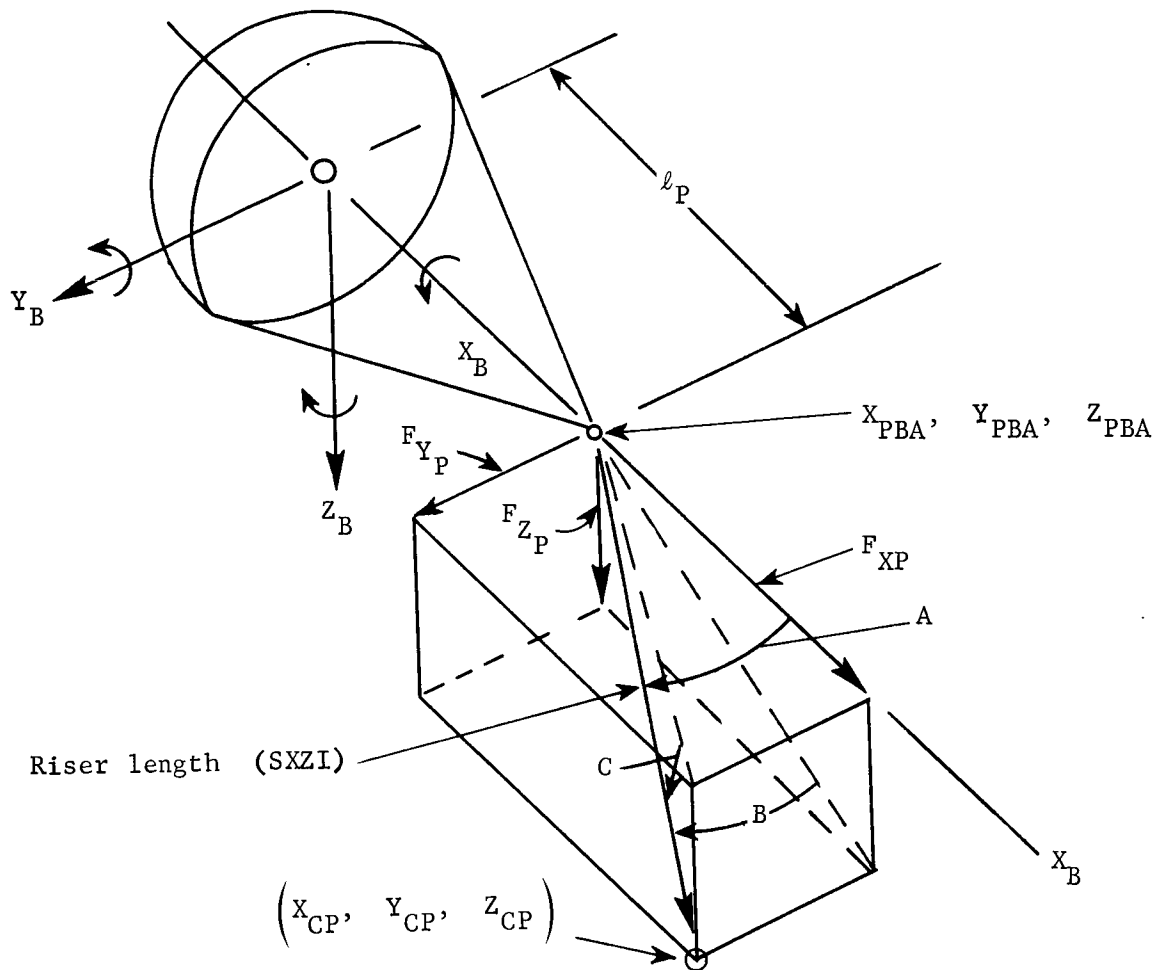
Figure 50.- Diagram Showing the Forces and Moments Transmitted to the Parachute

$$\cos A = \left(X_{CP} - X_{PBA} \right) \Big/ SXZI \tag{123}$$

$$\sin B = \left(Y_{CP} - Y_{PBA} \right) \Big/ SXZI \tag{124}$$

$$\sin C = \left(Z_{CP} - Z_{PBA} \right) \Big/ SXZI \tag{125}$$

a. Force components:

$$F_{XP} = T_R \left(X_{CP} - X_{PBA} \right) \Big/ SXZI \tag{126}$$

$$F_{YP} = T_R \left(Y_{CP} - Y_{PBA} \right) \Big/ SXZI \tag{127}$$

$$F_{ZP} = T_R \left(Z_{CP} - Z_{PBA} \right) \Big/ SXZI \tag{128}$$

b. Moments in body axis:

$$L_{XP} = K_S \left(\varphi_D \right) \tag{129}$$

$$M_{YP} = -F_{ZP} \left(1_P \right) \tag{130}$$

$$N_{ZP} = F_{YP} \left(1_P \right) \tag{131}$$

$$\varphi_D = \int \left(P - P_D \right) dt \tag{132}$$

5. Forces and moments transmitted to capsule.- Figure 51 shows the forces and moments that are transmitted to the capsule. Here Points $\left(X_{CBA}, \; Y_{CBA}, \; Z_{CBA} \right)$ and $\left(X_{CP}, \; Y_{CP}, \; Z_{CP} \right)$ must be expressed in the capsule-body coordinate system before attempting to solve equations (133) thru (142).
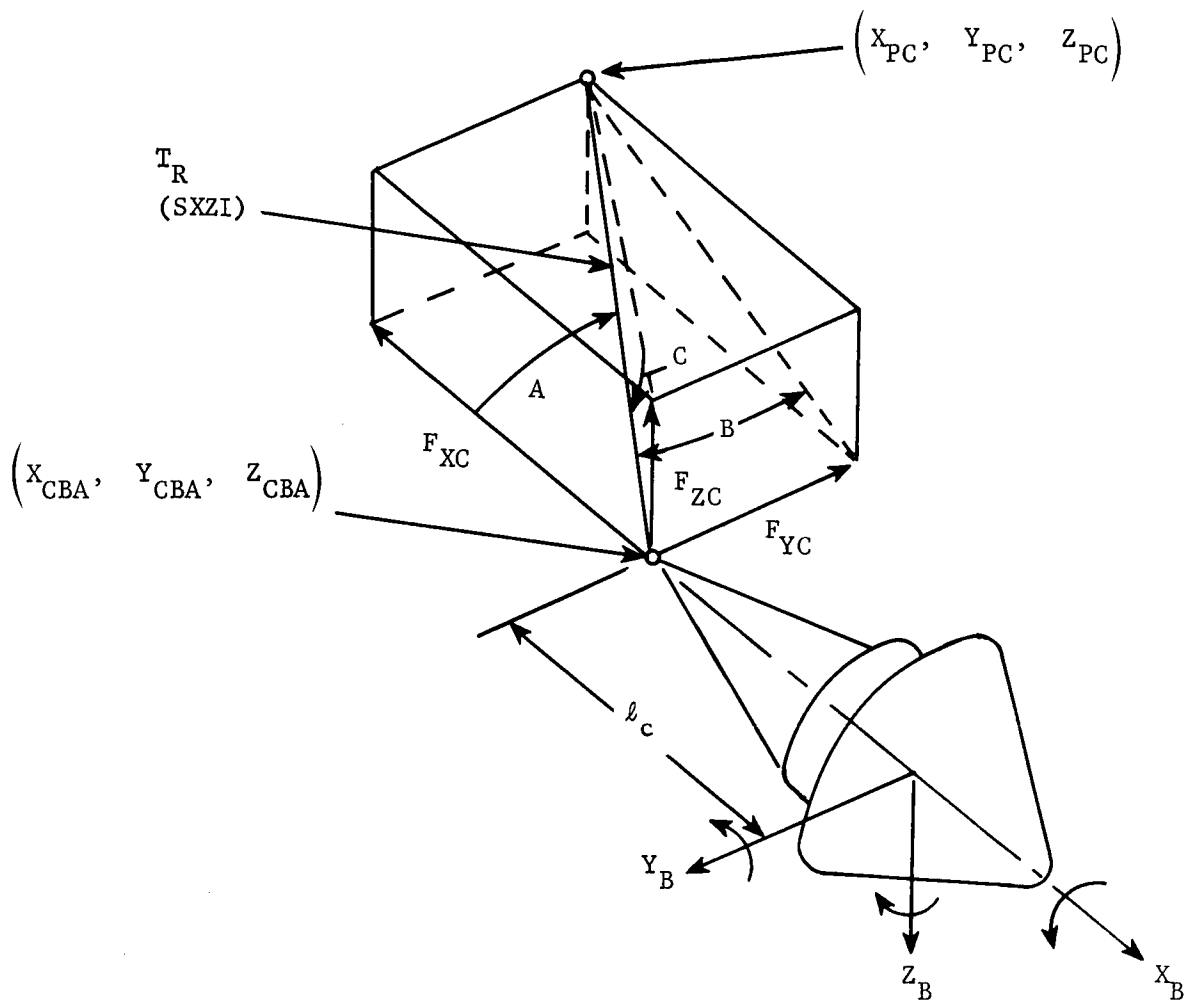
Figure 51.- Diagram Showing Forces and Moments Transmitted to Capsule

$$\cos A = \frac{X_{CBA} - X_{PC}}{SXZI} \tag{133}$$

$$\sin B = \frac{Y_{CBA} - Y_{PC}}{SXZI} \tag{134}$$

$$\sin C = \frac{Z_{CBA} - Z_{PC}}{SXZI} \tag{135}$$

a. Force components of T_R:

$$F_{XC} = -T_R \left(X_{C_{BA}} - Y_{PC} \right) \Big/ SXZI \qquad (136)$$

$$F_{YC} = -T_R \left(Y_{C_{BA}} - Y_{PC} \right) \Big/ SXZI \qquad (137)$$

$$F_{ZC} = -T_R \left(Z_{C_{BA}} - Z_{PC} \right) \Big/ SXZI \qquad (138)$$

b. Moments in body axis due to coupling force:

$$\text{Roll} = L_{XC} = -K_S \left(\varphi_D \right) \qquad (139)$$

$$\text{Pitch} = M_{YC} = F_{ZC} \left(1_c \right) \qquad (140)$$

$$\text{Yaw} = N_{ZC} = -F_{YC} \left(1_c \right) \qquad (141)$$

where

$$\varphi_D = \int \left(P - P_D \right) dt \qquad (142)$$

6. **Wind and gusts.**- Wind may be input into the problem either with a steady wind profile that has horizontal $\left(W_S \right)$ and vertical $\left(W_V \right)$ components, or with random gusts, using the probabilistic capability described in reference 2.

$$W_S = f(h) \qquad (143)$$

$$W_V = f(h) \qquad (144)$$

$$W_{SX} = W_S \left[\cos \left(\psi_W - \psi_{T_{PO}} \right) \right] + W_v \left(\frac{X}{Z_S} \right) \qquad (145)$$

$$W_{SY} = W_S \left[\sin \left(\psi_W - \psi_{T_{PO}} \right) \right] + W_v \left(\frac{Y}{Z_S} \right) \qquad (146)$$

$$W_{SZ} = W_{SX} \left(\frac{X}{Z_S} \right) + W_{SY} \left(\frac{Y}{Z_S} \right) + W_V \qquad (147)$$

If θ_{DR}, the downrange angle in the XZ plane, is small, then

$$\sin \theta_{DR} = \frac{X}{Z_S} \tag{148}$$

$$\cos \theta_{DR} = 1.0 \tag{149}$$
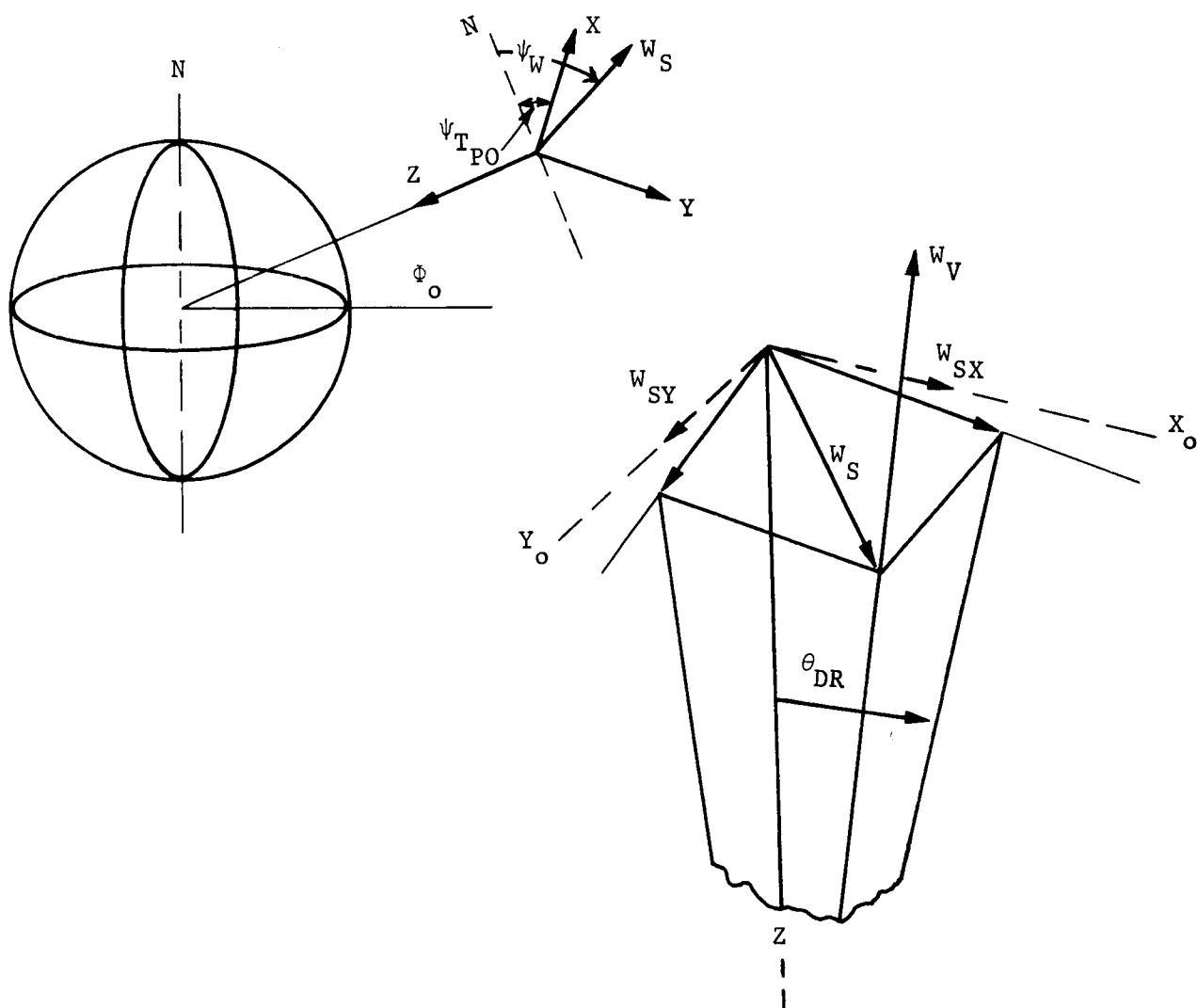
Figure 52.- Orientation of the Steady-Wind-Velocity Components

a. Total wind: Random wind gust components are added to W_{SX}, W_{SY}, and W_{SZ} if called for.

$$W_{TX} = W_{SX} + W_{GX} \tag{150}$$

$$W_{TY} = W_{SY} + W_{GY} \tag{151}$$

$$W_{TZ} = W_{SZ} + W_{GZ} \tag{152}$$

b. Velocity relative to air mass:
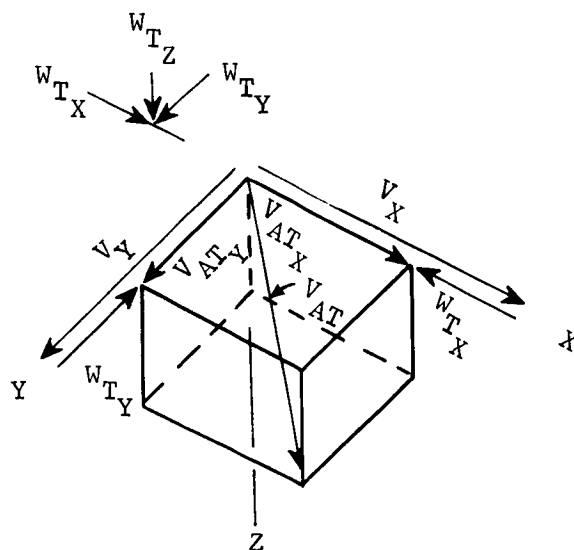
Figure 53.- Orientation of Wind-Velocity Components with Respect to the Air Mass

$$V_{AT_X} = V_X - W_{T_X} \tag{153}$$

$$V_{AT_Y} = V_Y - W_{T_Y} \tag{154}$$

$$V_{AT_Z} = V_Z - W_{T_Z} \tag{155}$$

$$V_{AT} = \left[V_{AT_X}{}^2 + V_{AT_Y}{}^2 + V_{AT_Z}{}^2 \right]^{\frac{1}{2}} \tag{156}$$

7. Aerodynamic forces and moments on parachute.- The aerodynamic forces and moments on the parachute are shown in figure 54. In this figure, C_X is the axial force coefficient, C_Y is the normal force coefficient, C_M is the pitch or yaw moment coefficient, C_L is the roll moment coefficient, C_{MQ} is the pitch or yaw damping coefficient, and C_{LP} is the roll damping coefficient.
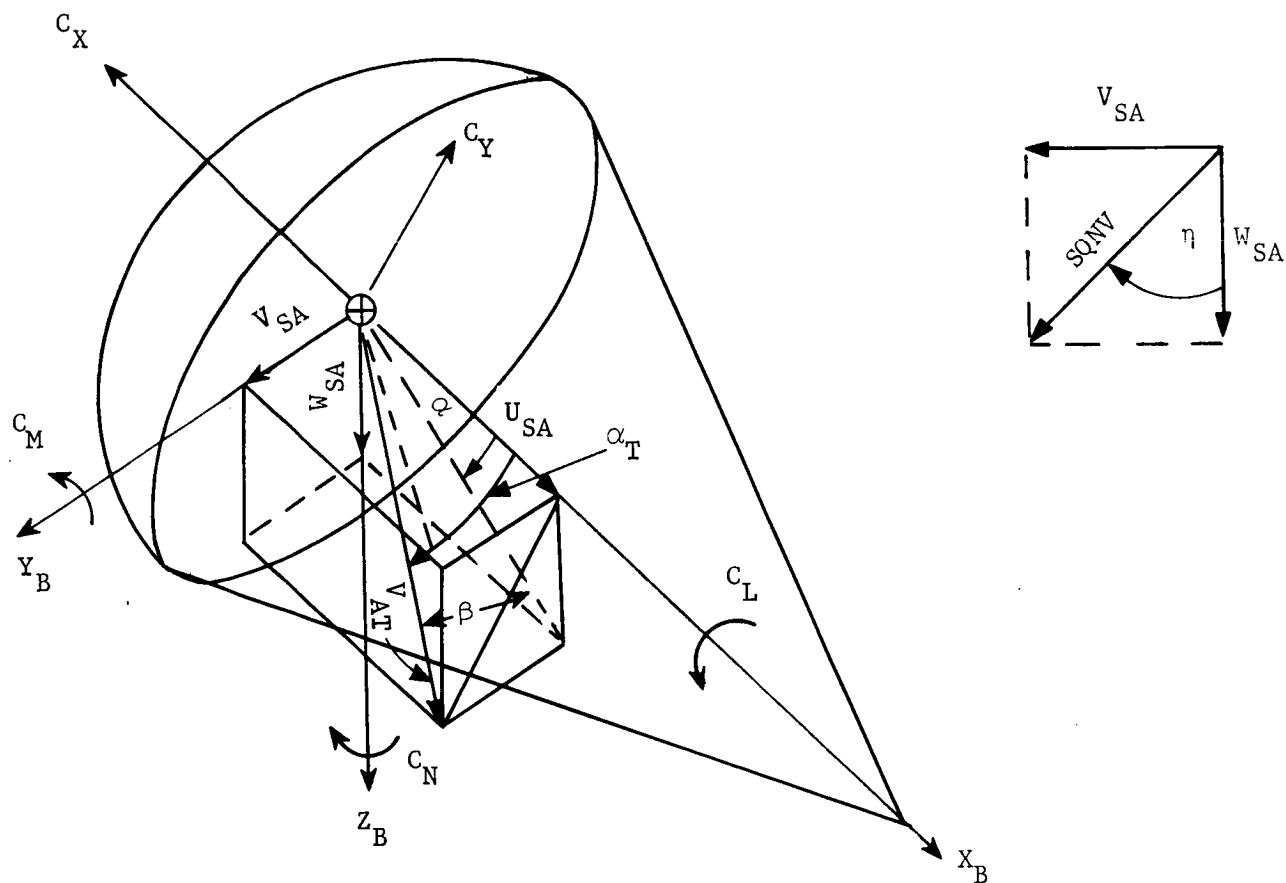
Figure 54.- Diagram Showing the Aerodynamic Forces and Moments on the Parachute

$$\alpha = \tan^{-1} \frac{W_{SA}}{U_{SA}} \tag{157}$$

$$\beta = \sin^{-1} \frac{V_{SA}}{V_{AT}} \tag{158}$$

$$SQNV = \left(V_{SA}^{\,2} + W_{SA}^{\,2}\right)^{\frac{1}{2}} \tag{159}$$

$$\alpha_T = \sin^{-1}\left(\frac{SQNV}{V_{AT}}\right) \tag{160}$$

Note that if SQNV = 0, then

$$\sin \eta = \cos \eta = 0 \tag{161}$$

but if SQNV $\neq$ 0; then

$$\sin \eta = \frac{V_{SA}}{SQNV} \tag{162}$$

$$\cos \eta = \frac{W_{SA}}{SQNV} \tag{163}$$

C. Typical Module Calling Sequence

The modules are typically called in the order shown in figure 55. The symbols shown in parentheses are the parameters which are calculated in the modules.
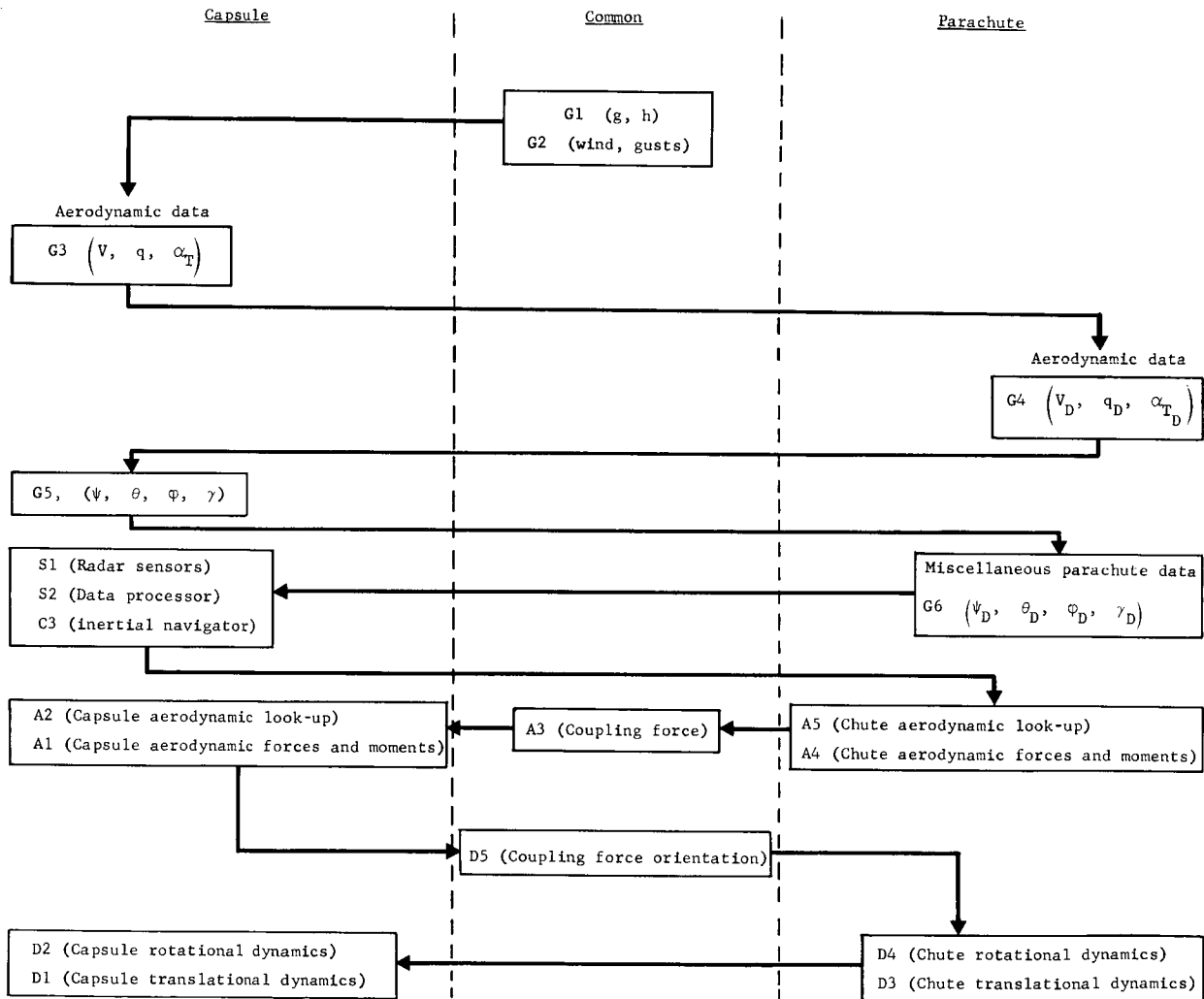
Figure 55.- Flow Block Diagram of the Order of Computations in a Typical Module Calling Sequence

D. Simulation Results

The equations of motion and their programing were verified by comparing the results of this simulation with the results from a two-dimensional parachute simulation in which a high level of confidence exists (ref. 13). The available integration routines were exercised to determine whether they could be used and to evaluate their effectiveness. Various computing intervals and riser spring constants were examined to demonstrate that realistic values of these parameters were executable. Each of the major program options was checked for proper operation, and before terminating the run, the parachute-release logic was verified.

The example used in the simulation was that of a 48-ft-diameter parachute decelerating a 900-lb capsule in the minimum $H_{\rho,S}$ Mars atmosphere. The program began at an altitude of 16 000 ft, shortly after the aeroshell was jettisoned. The wind profile used in this simulation is shown in figure 56.
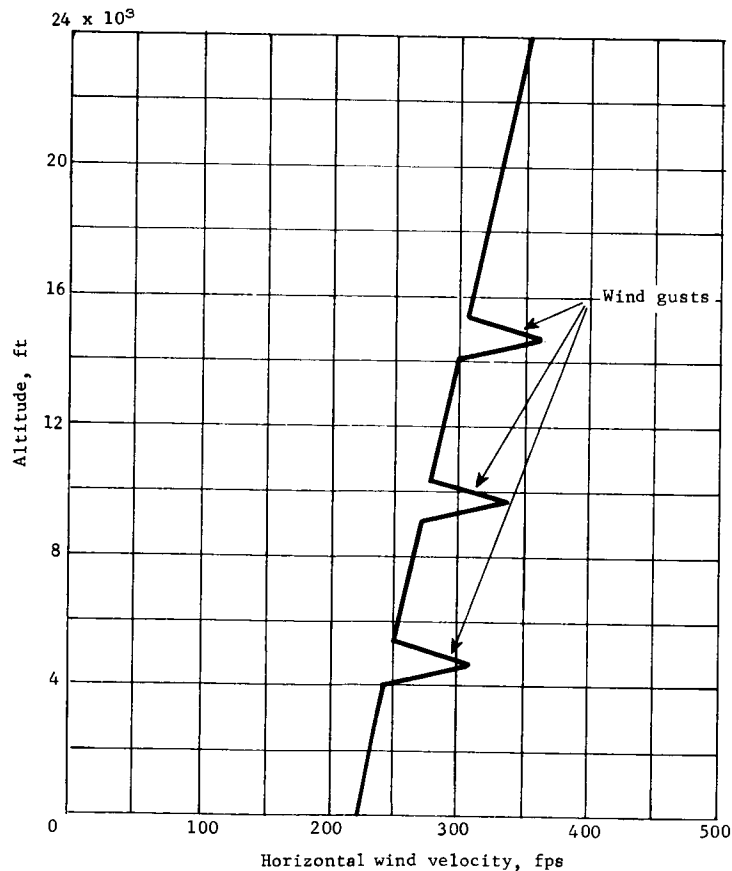
Figure 56.- Mars Minimum $H_{\rho,S}$ Atmosphere Wind Profile Used in the Parachute-Lander 6DOF Simulations

177

Although the wind profile shown in figure 56 does not agree exactly with the latest wind specification given in reference 8, it was used in order to make the simulation compatible with the single-plane program, which had been executed before the latest specification was issued. However, before the wind profile was used in later combined parachute-capsule terminal descent simulations, it was updated to reflect the minimum $H_{\rho,S}$ atmosphere defined in reference 8.

1. Comparison with two-dimensional program.- The results from the MOD6MV program are compared to those from the single plane program of reference 13 in table 21.

TABLE 21.- COMPARISON OF THE RESULTS OBTAINED FROM THE

MOD6MV AND SINGLE-PLANE COMPUTER PROGRAMS[a]

Parameter	MOD6MV program	Single-plane program
Relative velocity, fps	165.2	164.17
Inertial velocity, V_X, fps	-285.4	-285.8
Inertial velocity, V_Z, fps	164.6	163.75
Altitude, ft	9000	9021.6
Flight path angle, deg	-29.9	-29.8
Chute riser force, lb	351.7	349.5

[a]The parachute check runs were terminated arbitrarily at 9000 ft, after passing through two wind-sheer spikes. The data shown in tables 21 thru 23 simply summarize the conditions at the end of each run.

The response of the system is shown in figure 57a. Note that there is good agreement with the data obtained from the single-plane program. The curves in figure 57b show that the capsule attitude rates are very nearly equal in magnitude and have similar frequency patterns.
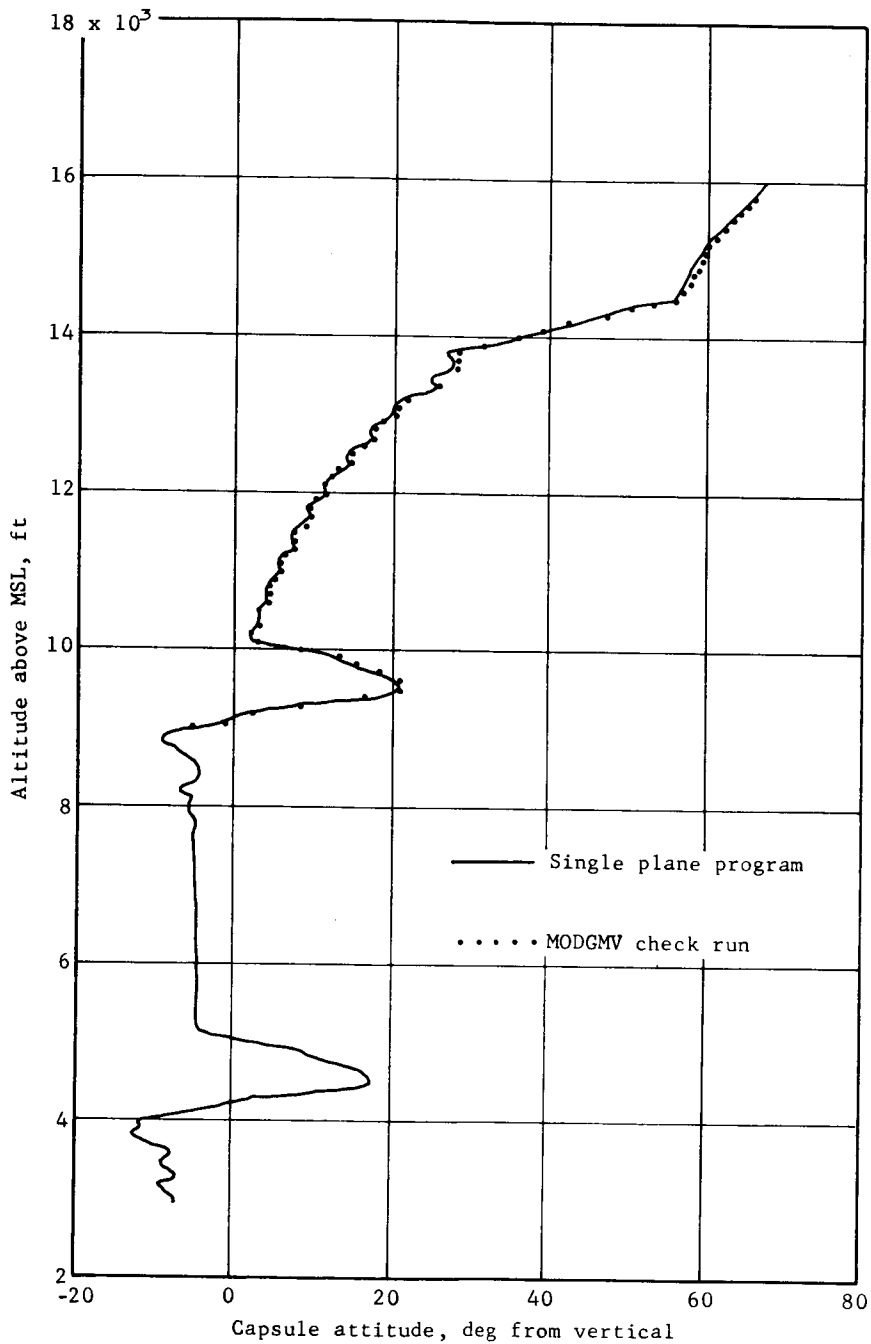
(a) Altitude vs capsule attitude

Figure 57.- Parachute-Lander 6DOF Simulation Results: Wind
Gust Response Comparison of the Wind Gust Res-
ponse Obtained from the Single-Plane and the
MOD6MV Parachute-Lander Simulations
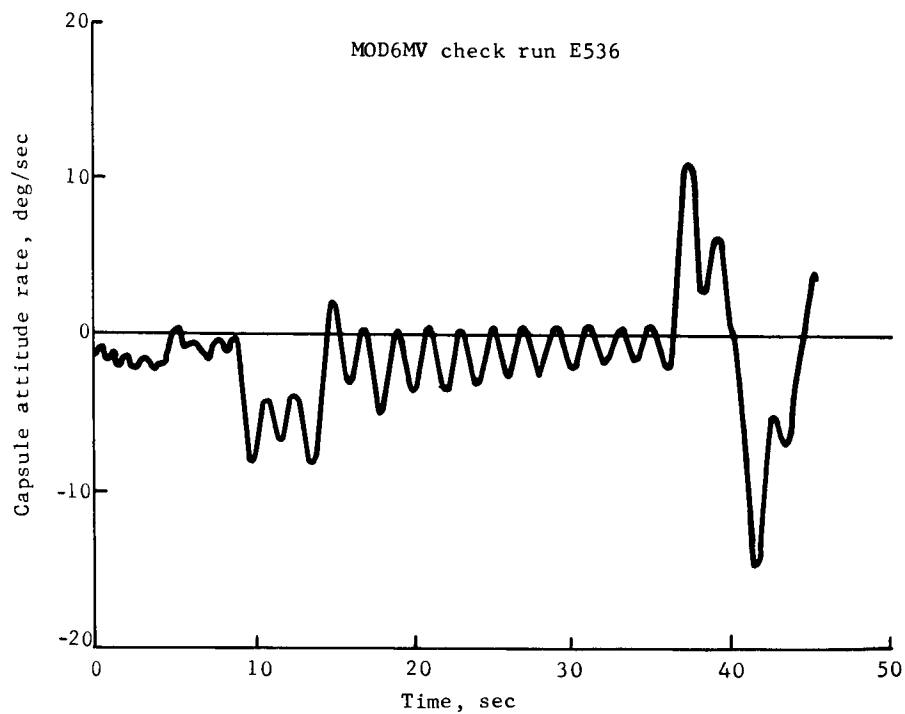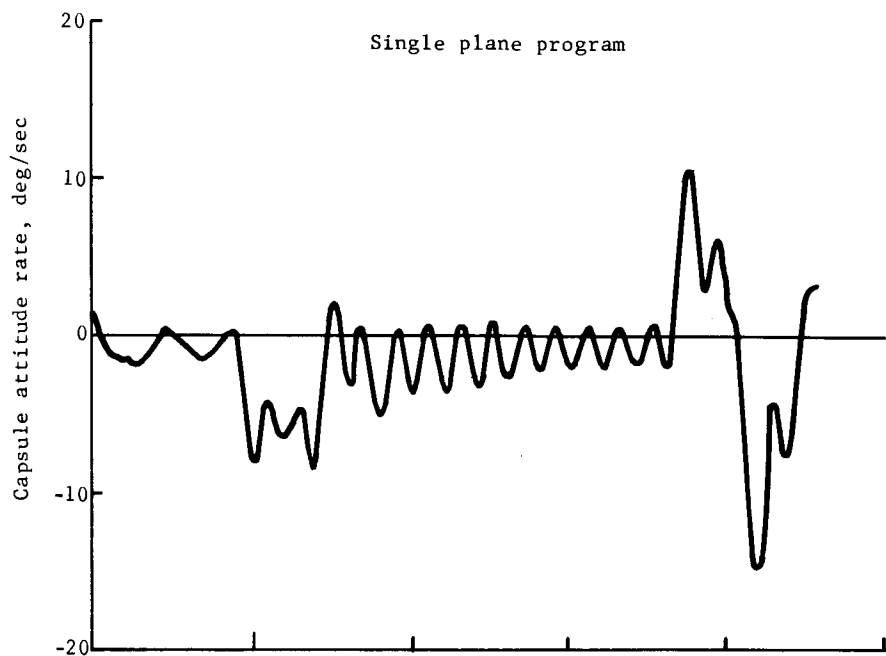
(b) Capsule attitude rate vs time

Figure 57.- Concluded

2. Integration routines.- Two integration routines were evaluated in terms of their accuracy and the computing time required. Table 22 compares the results obtained using simple, step-wise integration (FOMS) and fourth-order, Runge-Kutta integration for 43.6 sec of real time.

TABLE 22.- COMPARISON OF THE RESULTS OBTAINED USING
DIFFERENT INTEGRATION TECHNIQUES

Parameter	Integration	technique
	Runge-Kutta	FOMS
Fixed computing interval, sec	0.005	0.005
Computing time, sec	569	179
Relative velocity, fps	165.11	165.13
V_X, fps	-285.3	-285.38
V_Z, fps	164.51	164.54
Altitude, ft	8999	9001
Flight path angle, deg	-29.9	-29.9
Riser load, lb	351.6	351.3

This table shows that the use of the more-sophisticated Runge-Kutta integration routine is not justified, in view of the much longer computing time that it required.

3. Computing interval.- The parachute simulation described in reference 13 used variable computing intervals, with a lower limit of 0.00312 sec. To achieve good agreement with the results of that simulation, a fixed computing interval of 0.005 sec was used in the parachute-lander simulation. Although a 0.005-sec computing interval may be required for other phases of the terminal descent and landing system, table 23 shows that a computing interval of 0.01 sec is adequate for the parachute phase.

TABLE 23.- COMPARISON OF THE RESULTS OBTAINED USING
DIFFERENT COMPUTING INTERVALS

Parameter	Computing interval	
	0.01 sec	0.005 sec
Computing time, sec	119	179
Relative velocity, fps	165.217	165.13
V_X, fps	-285.48	-285.38
V_Z, fps	164.61	164.54
Altitude, ft	9001	9001
Flight path angle, deg	-29.9	-29.9
Riser load, lb	351.55	351.3

In general, the computing interval should be small enough to
follow the frequency response of the system. For this particular
problem, the period of the longitudinal oscillations in 0.33 sec
(based on a spring constant of 1000 lb/ft) and the period of the
angular capsule oscillations is 2.05 sec.. If 20 computations are
to be performed per cycle, the maximum computing interval will be
0.0165 sec.

4. Spring constant.- The stiffness of the equivalent spring con-
stant of the riser has a bearing on the computing interval re-
quired. The stiffer the spring, the higher the longitudinal fre-
quency, and therefore, the smaller the computing interval required.
The checkout runs included herein were made using a spring con-
stant of 200 lb/ft, since little difficulty is experienced with a
soft spring. Subsequent runs used a more realistic value of 1000
lb/ft to verify that the program can handle the higher frequency
involved.

5. Pitch and yaw case.- The motion of the system, which involves
all the equations of motion, was evaluated by moving the wind di-
rection 45 deg out of the pitch plane. (All the previous compari-
son runs, however, were run with the wind in the pitch plane.)
The wind profile and altitude time-histories in figure 58 were used
to correlate the gust response with altitude and time.

The capsule pitch- and yaw-rate responses to wind gusts are
shown in figures 59a and 59b. The responses begin at four sec and
again at 36 sec. The magnitude and frequency of these curves are
nearly equal -- as they should be. The pitching-over of the tra-
jectory appears as a negative bias in figure 59a.
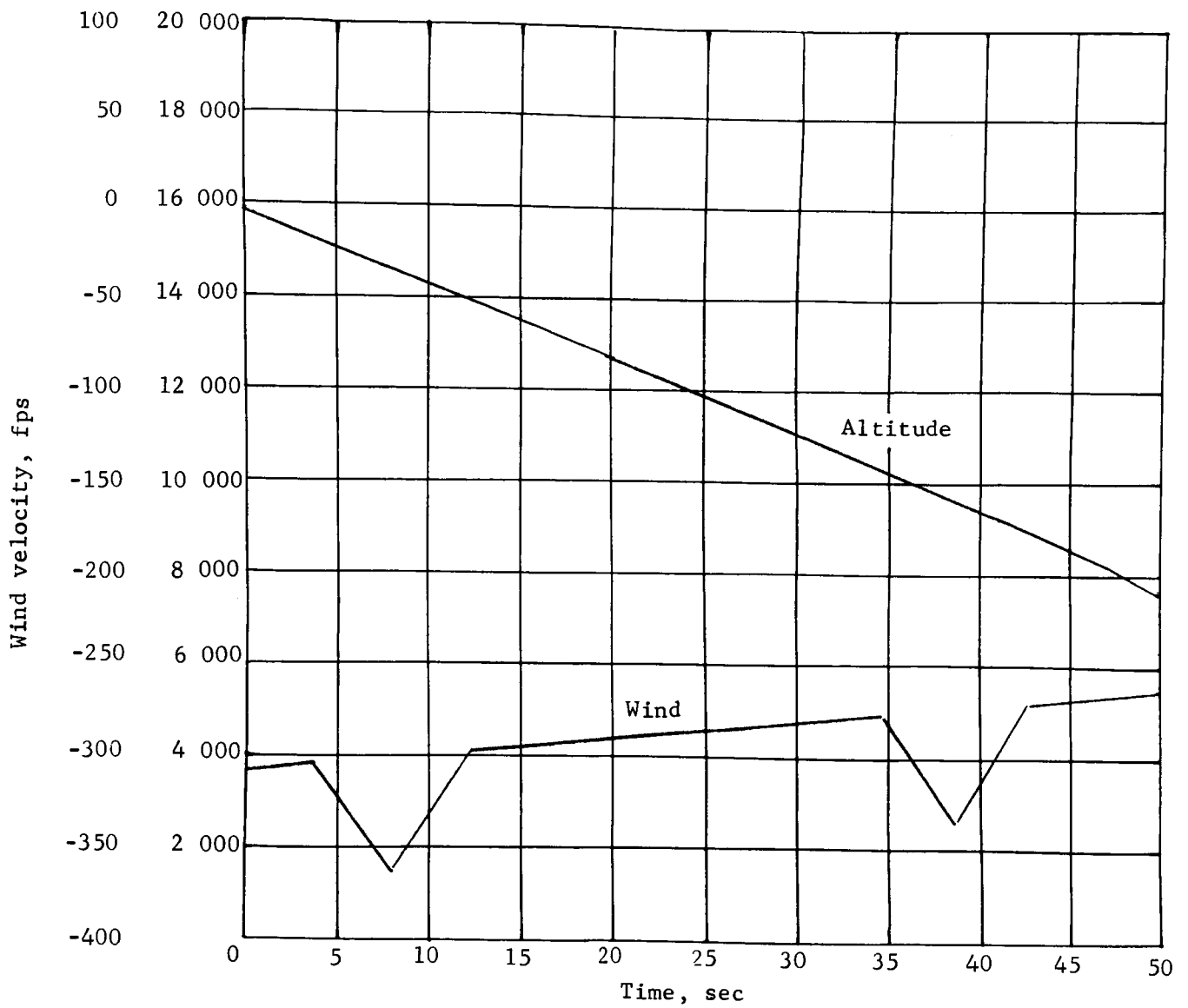
Figure 58.- Parachute-Lander 6DOF Simulation Results:
Wind Velocity and Altitude vs Time

The pitch Euler angle time-history is shown in figure 60a. Except for wind spikes (which produce bumps on the curve beginning at four and 36 sec) the curve reflects the trajectory pitchover from -0.44 rad (-26.5 deg) to -1.57 radians (-90 deg). The yaw Euler angle plot (fig. 60b) has large swing after 36 sec. This results because the yaw Euler angle switches quardants after having pitched over 90 deg. To fully understand this result it is necessary to use figure 60c to trace out the ordered Euler angle rotations.

6. Roll response.- To check out the roll coupling between the parachute and the capsule, we gave the capsule an initial roll rate of 1 rad/sec and used torsional spring constant of 10 ft-lb/rad and a chute roll-damping coefficient of -0.1 rad/sec. The resulting capsule and parachute roll response shown in figure 61 indicates that the chute will ultimately reduce the roll rate of the capsule without picking up much roll of its own. Although the response shown here may not be typical of parachute behavior, the system is responding correctly, in accordance with the equations of motion.

7. Combined parachute-terminal descent simulation results.- As a final checkout of the parachute program, a second run was made. This run began with the capsule at an altitude of 16 000 ft. After it descended through three wind gusts, the vernier engines were started and the parachute was staged. Then the capsule completed the terminal descent.

Some of the plots obtained from this run are shown in figures 62 thru 67. The radar was initialized in the unlocked condition. It locked and unlocked several times due to wind gusts during the parachute descent, but locked and remained locked during the terminal descent. This can be seen in the plot of U-axis velocity shown in figure 63. The effect of the 25-deg surface slope can be seen in the altimeter data of figure 62. Figure 64 shows how the pitch rate and pitch attitude varied with time. Notice that the maximum rate response to the wind gusts was 22 deg/sec. The thrust history for Engine 1 is shown in figure 65. During the parachute-descent phase, this engine if off; but at T = 50 sec, the engines are started, warmed up for two sec with the control loops open, the control loops are closed, and then the parachute is released. The thrust spikes that occur during the terminal descent phase result from attitude maneuvering and radar noise.

The altitude velocity curve, figure 66, shows the effect of the wind and gusts that are plotted in figure 67. During this run, the lander aerodynamics were not omitted after the parachute was released. Thus, after the engine started the velocity decreased significantly, due to the additional drag force. This effect is normal, if we assume that the engine thrust does not change the lander aerodynamic coefficients.

Martin Marietta Corporation,
    Denver, Colorado, August 25, 1969.
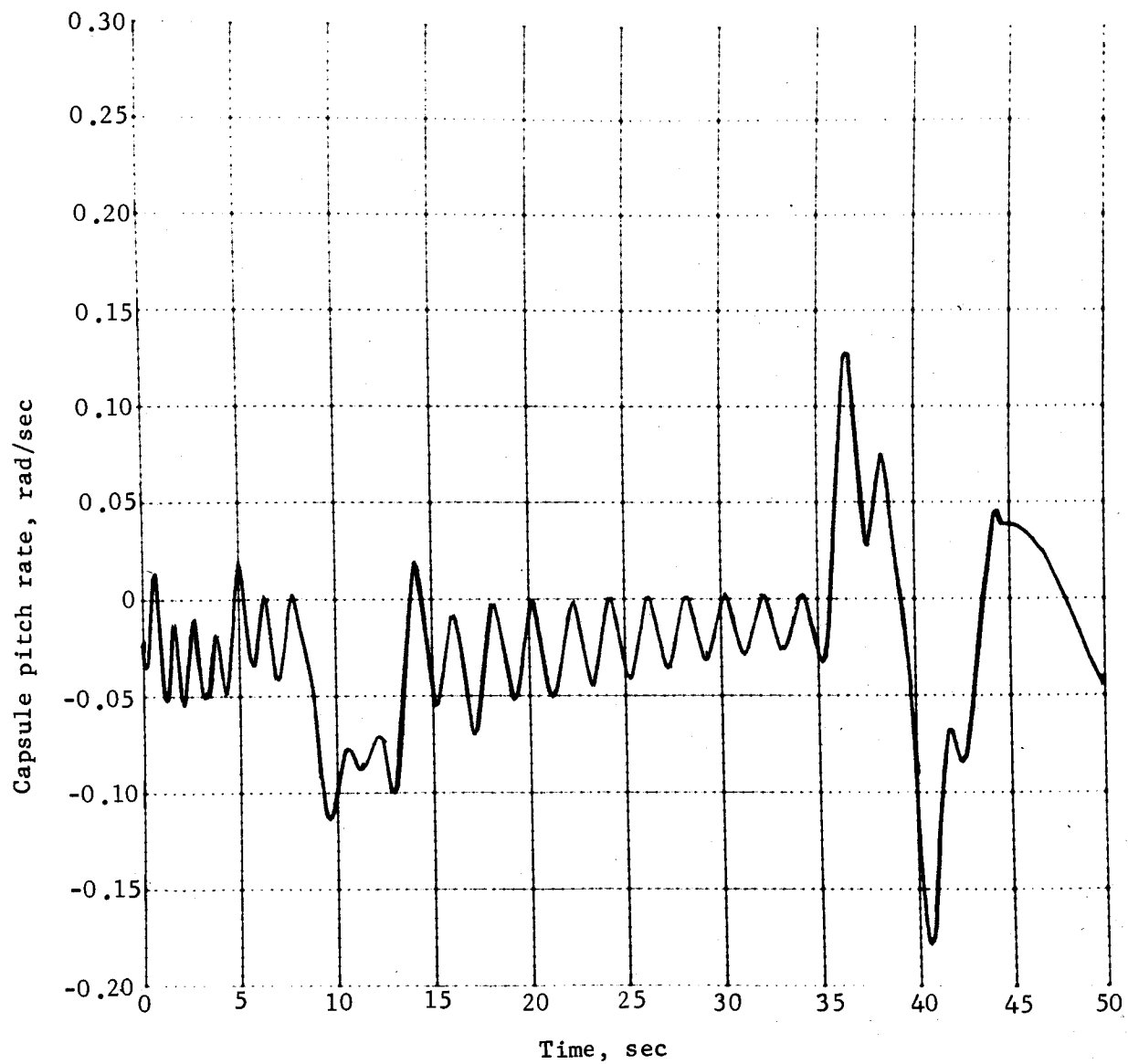
(a) Pitch rate response

Figure 59.- Parachute-Lander 6DOF Simulation Results: Capsule
Pitch- and Yaw-Rate Responses to Wind Gusts

Time, sec
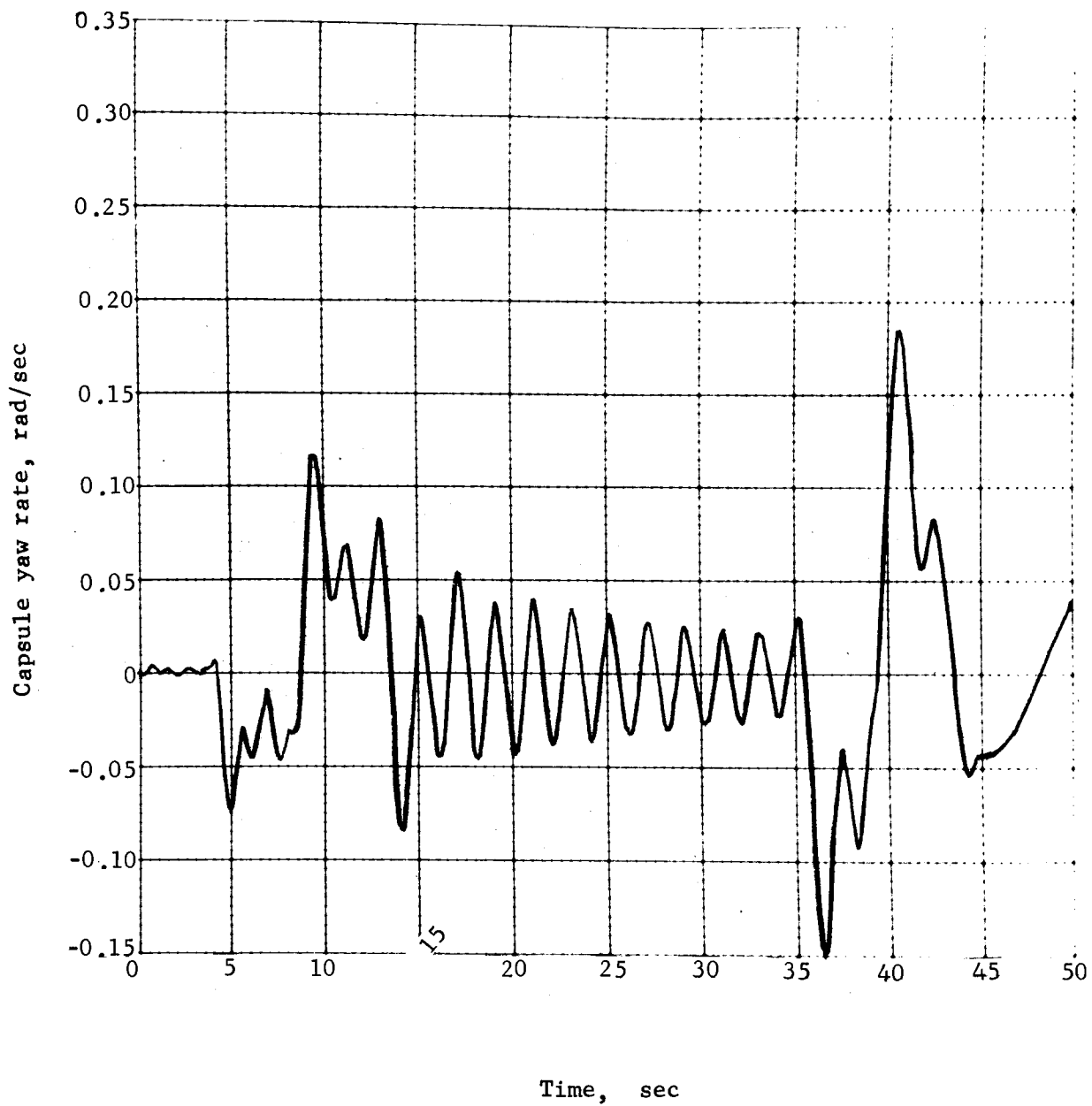
(b) Yaw Rate Response

Figure 59.- Concluded

Time, sec
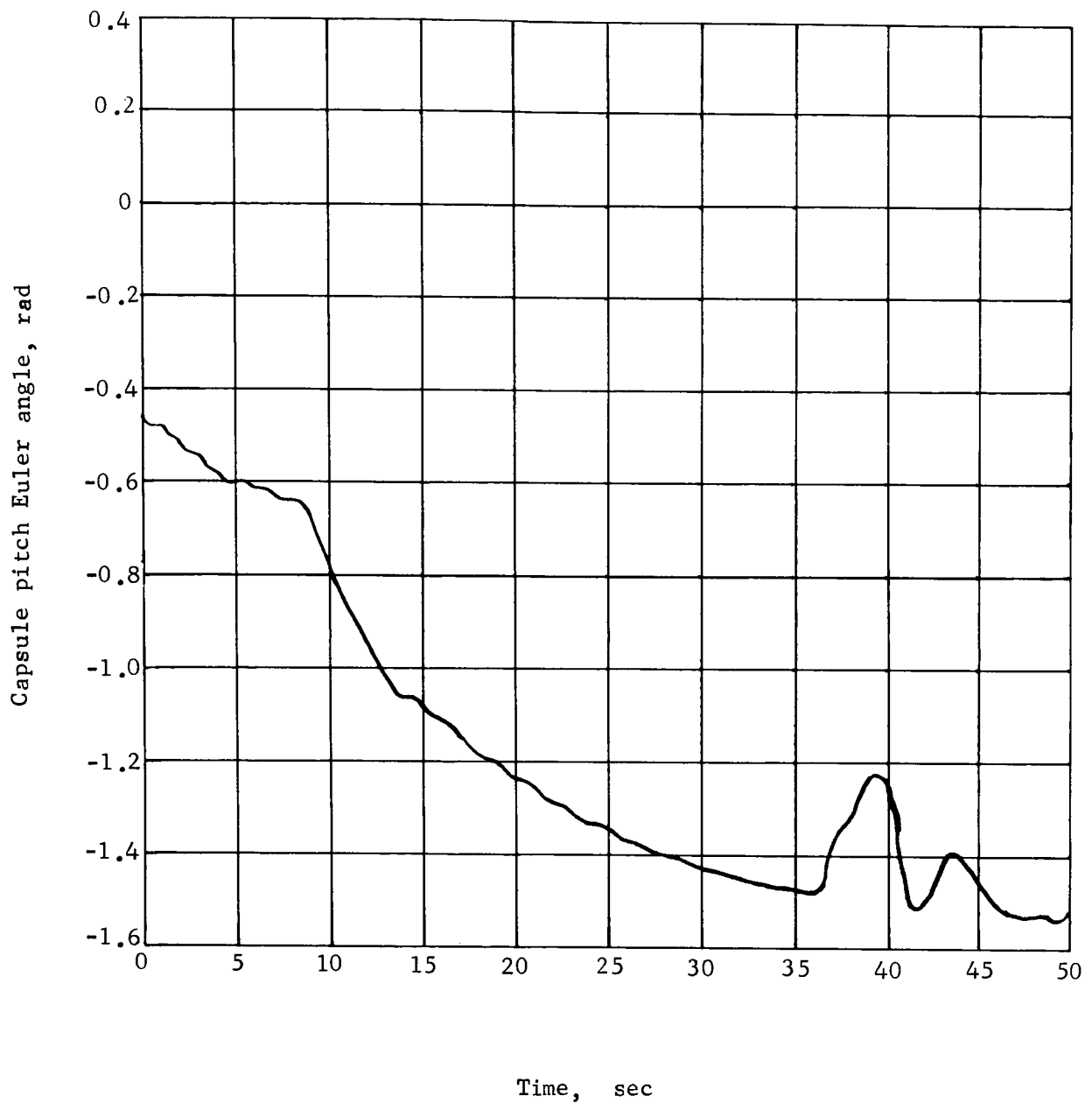
(a) Pitch-Euler-Angle Response

Figure 60.- Parachute-Lander 6DOF Simulation Results:
Capsule Pitch- and Yaw-Euler-Angle
Responses to Wind Gusts

Time, sec
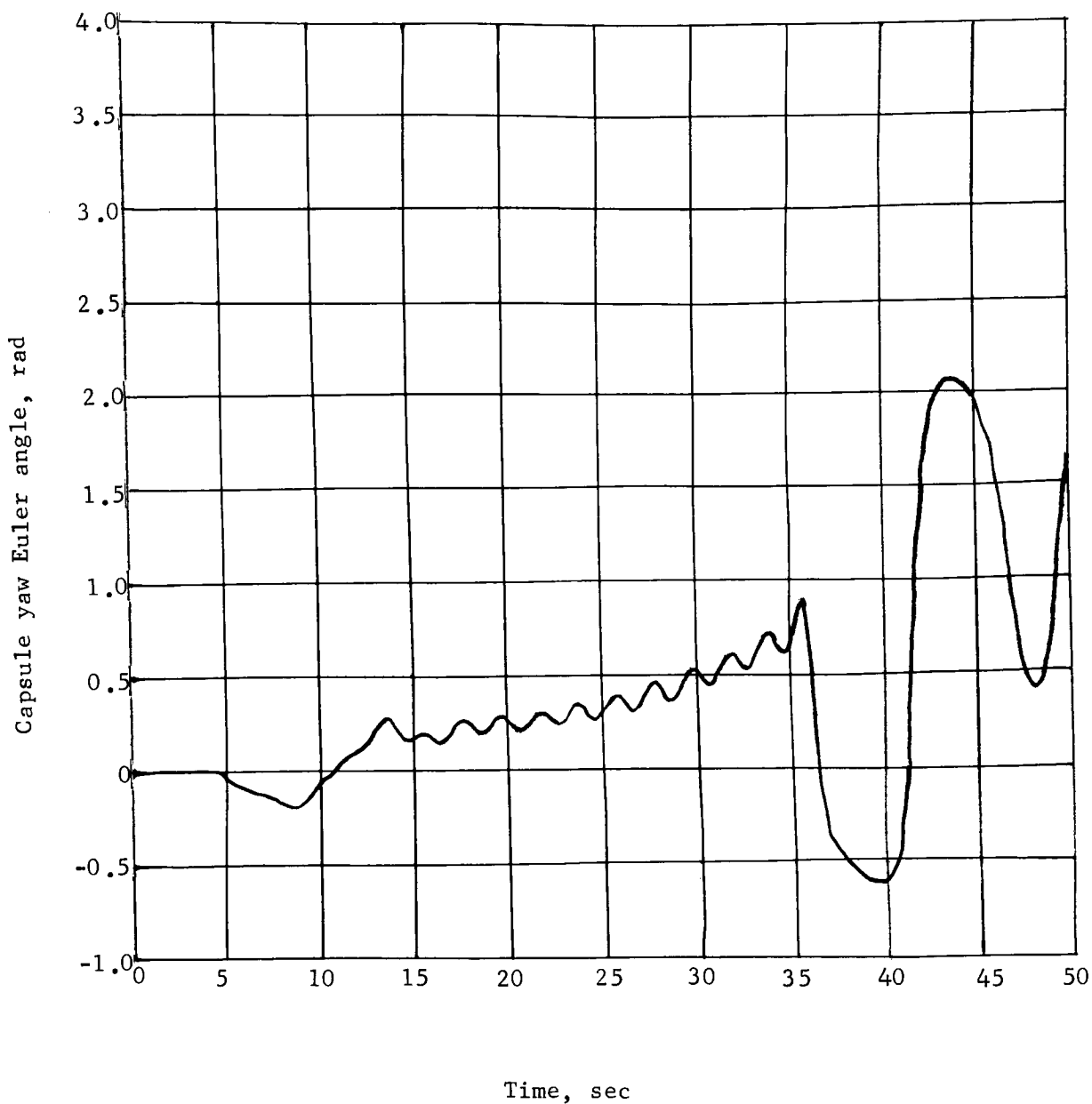
(b) Yaw-Euler-Angle Response

Figure 60.- Continued
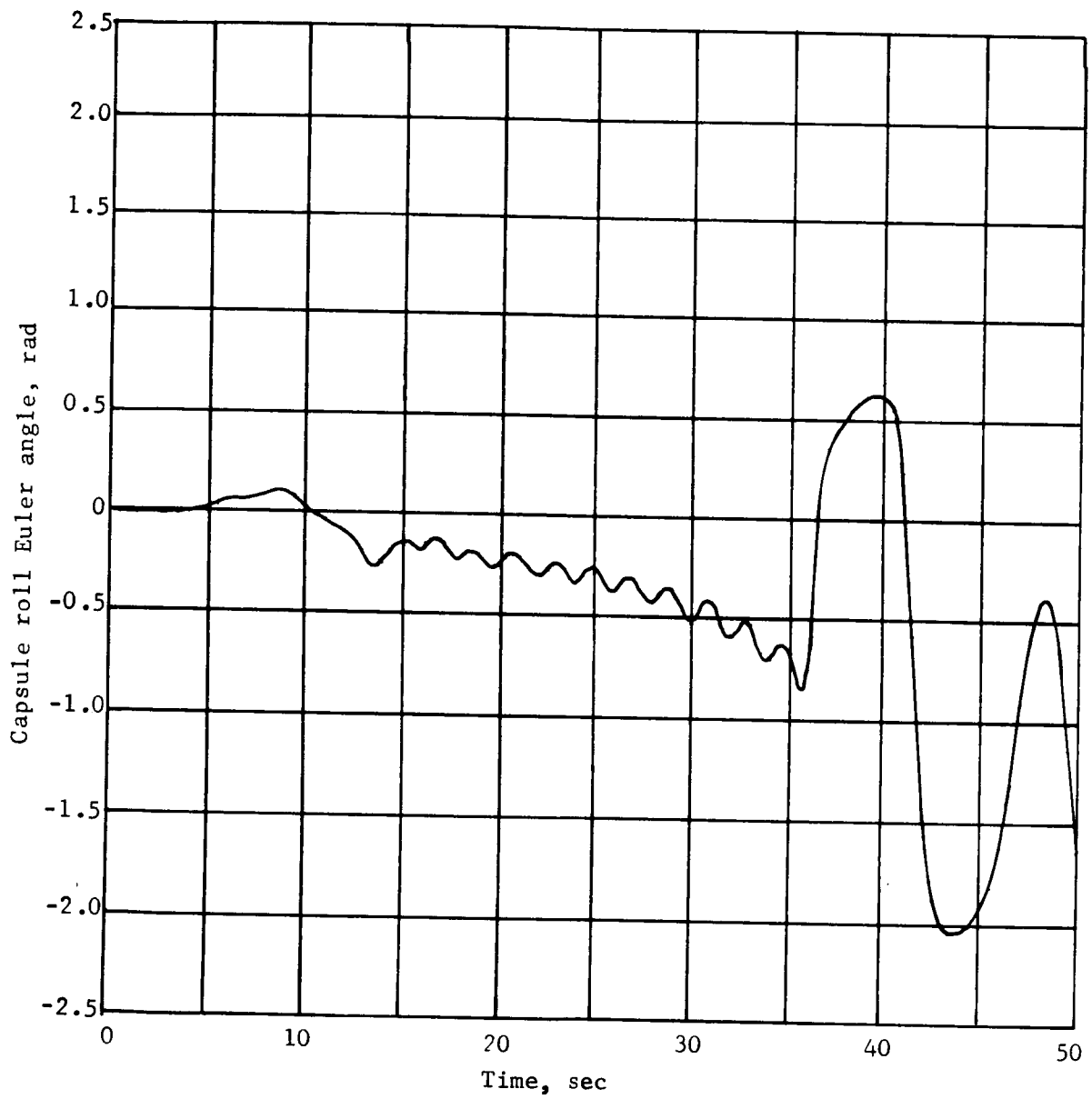
(c) Roll-Euler-Angle Response

Figure 60.-Concluded
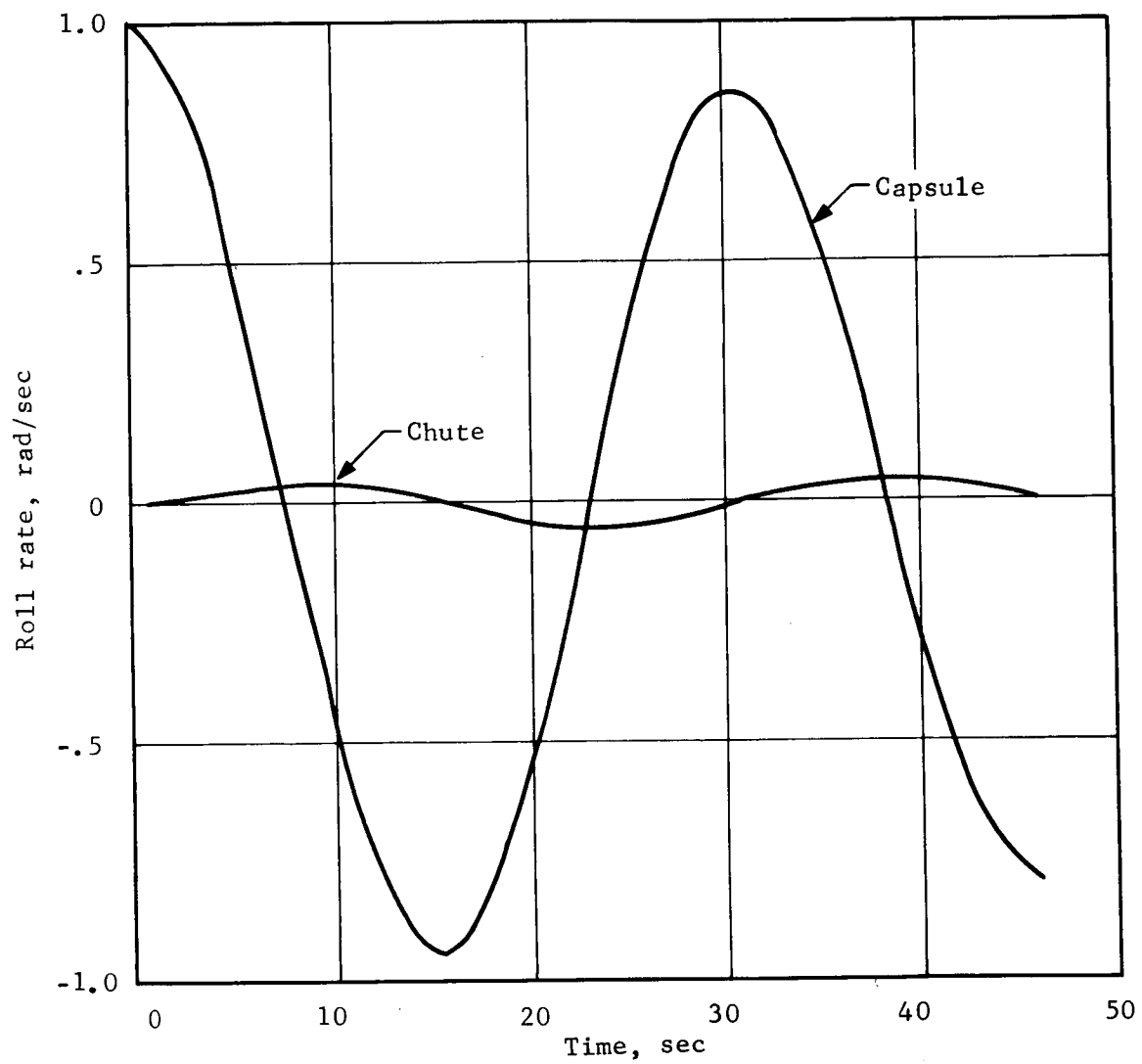
Figure 61.- Parachute-Lander 6DOF Simulation Results:
Roll-Coupling Response
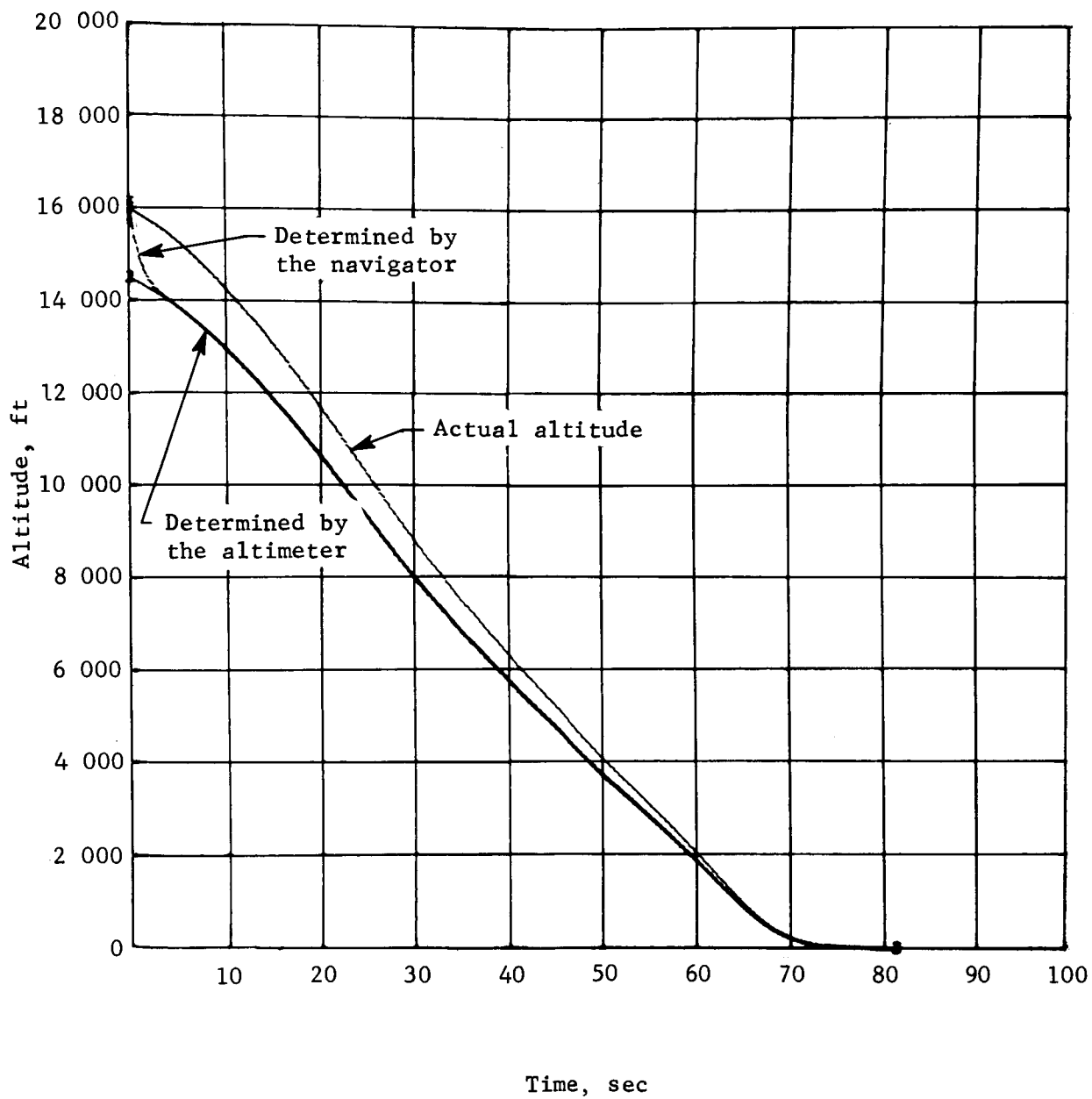
Figure 62.- Second Parachute-Lander Simulation Results:
Altitude vs Time
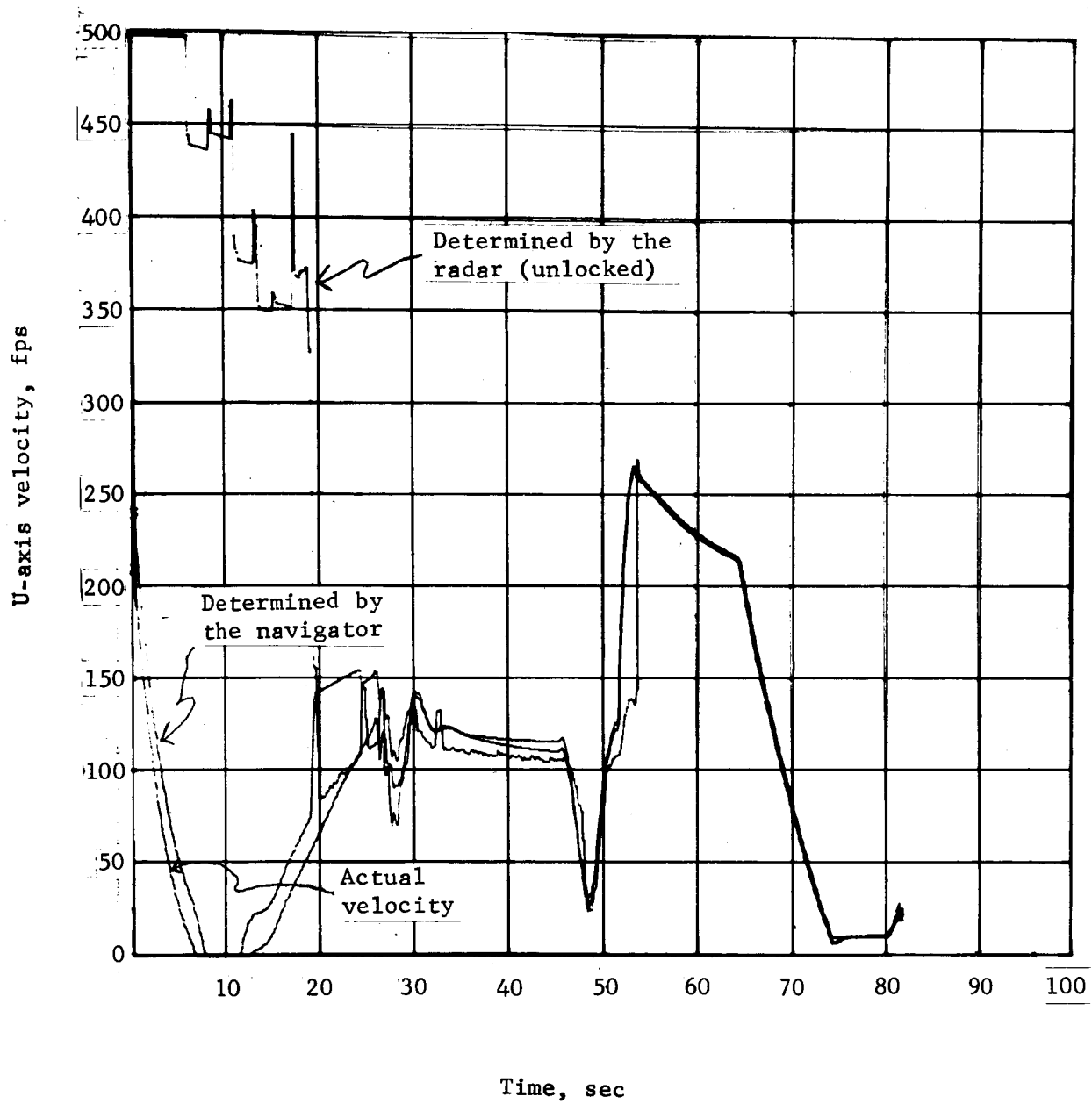
Figure 63.- Second Parachute-Lander Simulation Results:
U-Axis Velocity vs Time
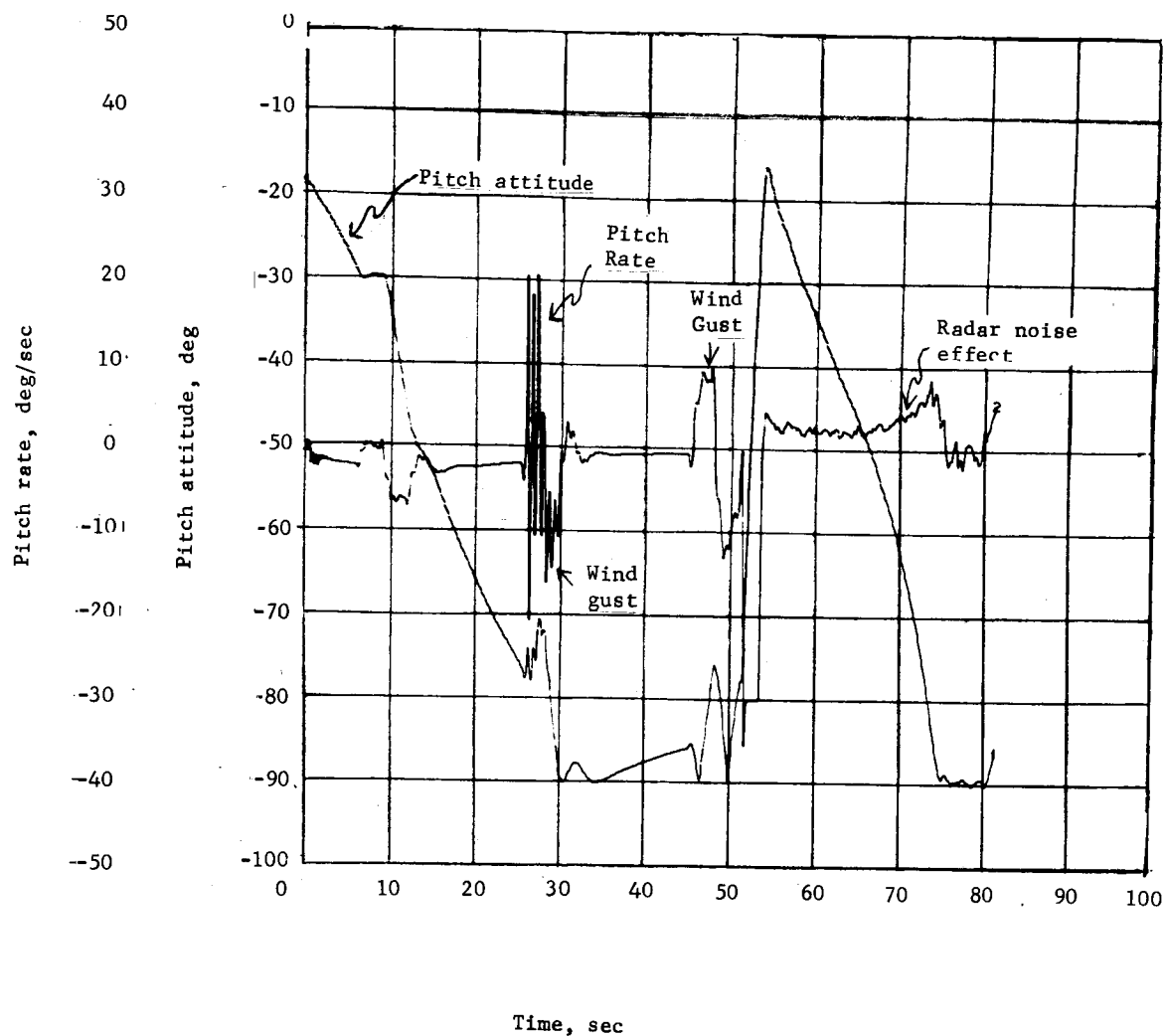
Figure 64.- Second Parachute-Lander 6DOF Simulation Results:
Pitch Rate and Pitch Attitude vs Time
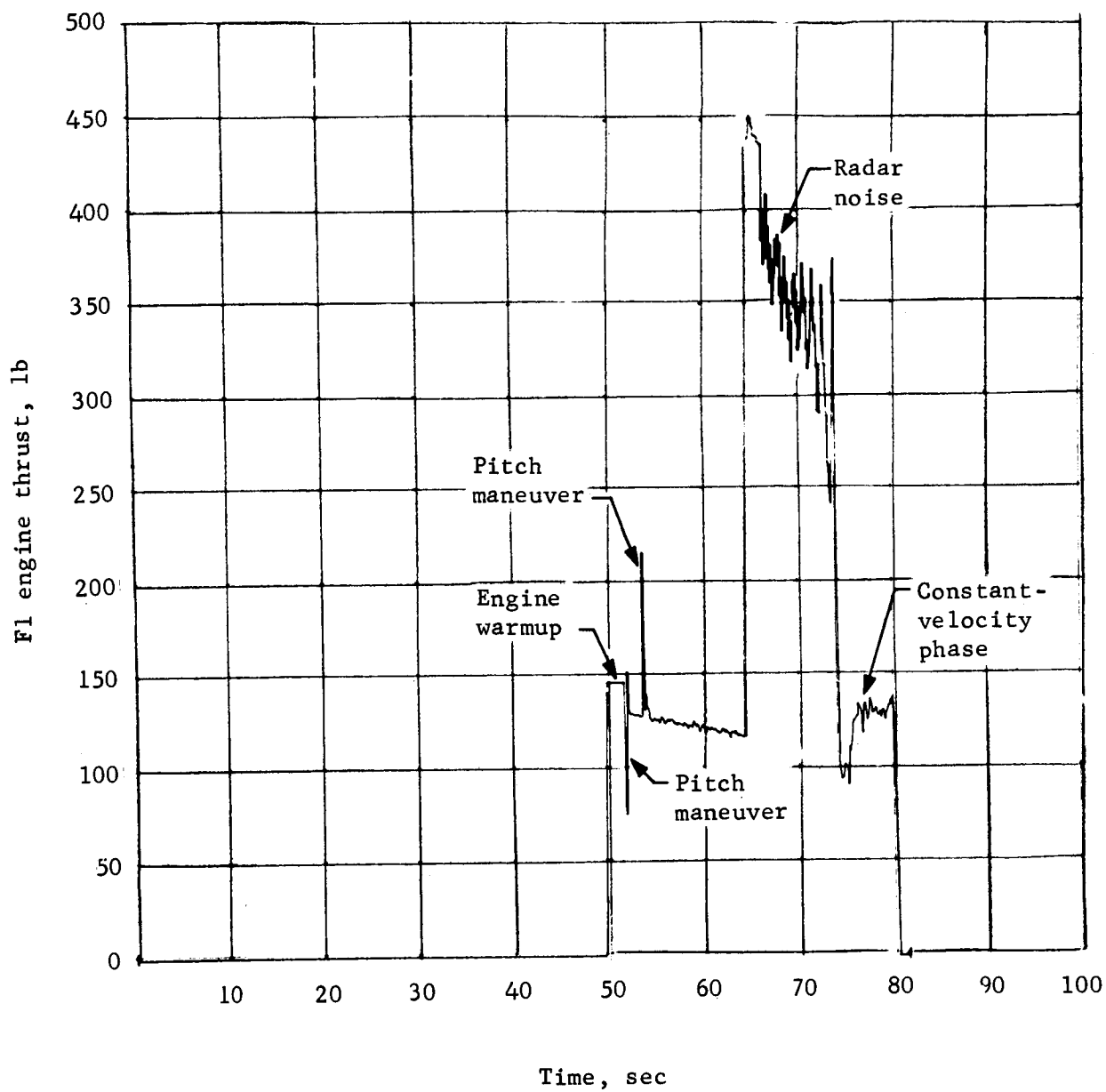
Figure 65.- Second Parachute-Lander Simulation Results:
F1 Engine Thrust vs Time
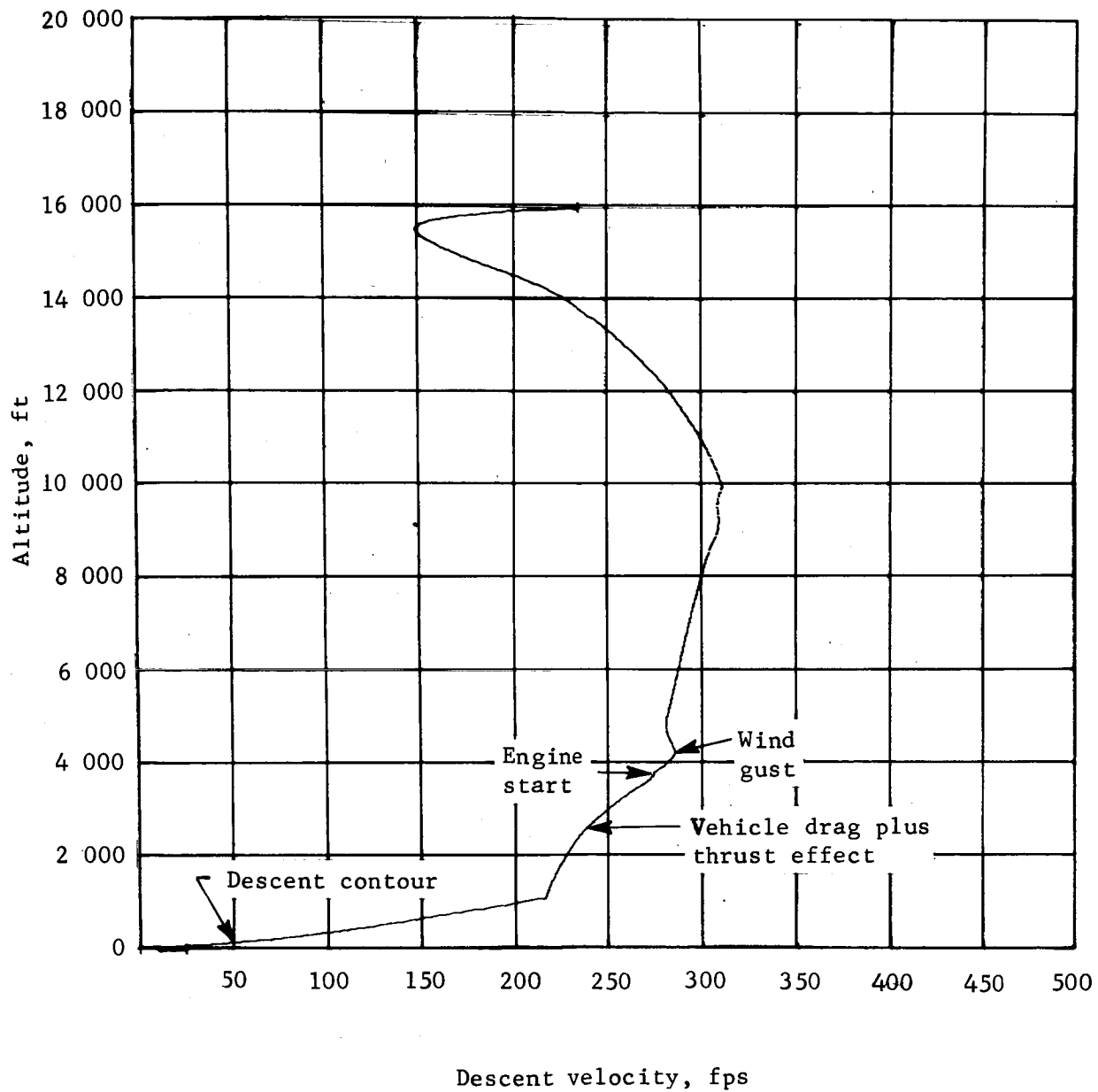
Figure 66.- Second Parachute-Lander 6DOF Simulation Results:
Descent Velocity vs Altitude
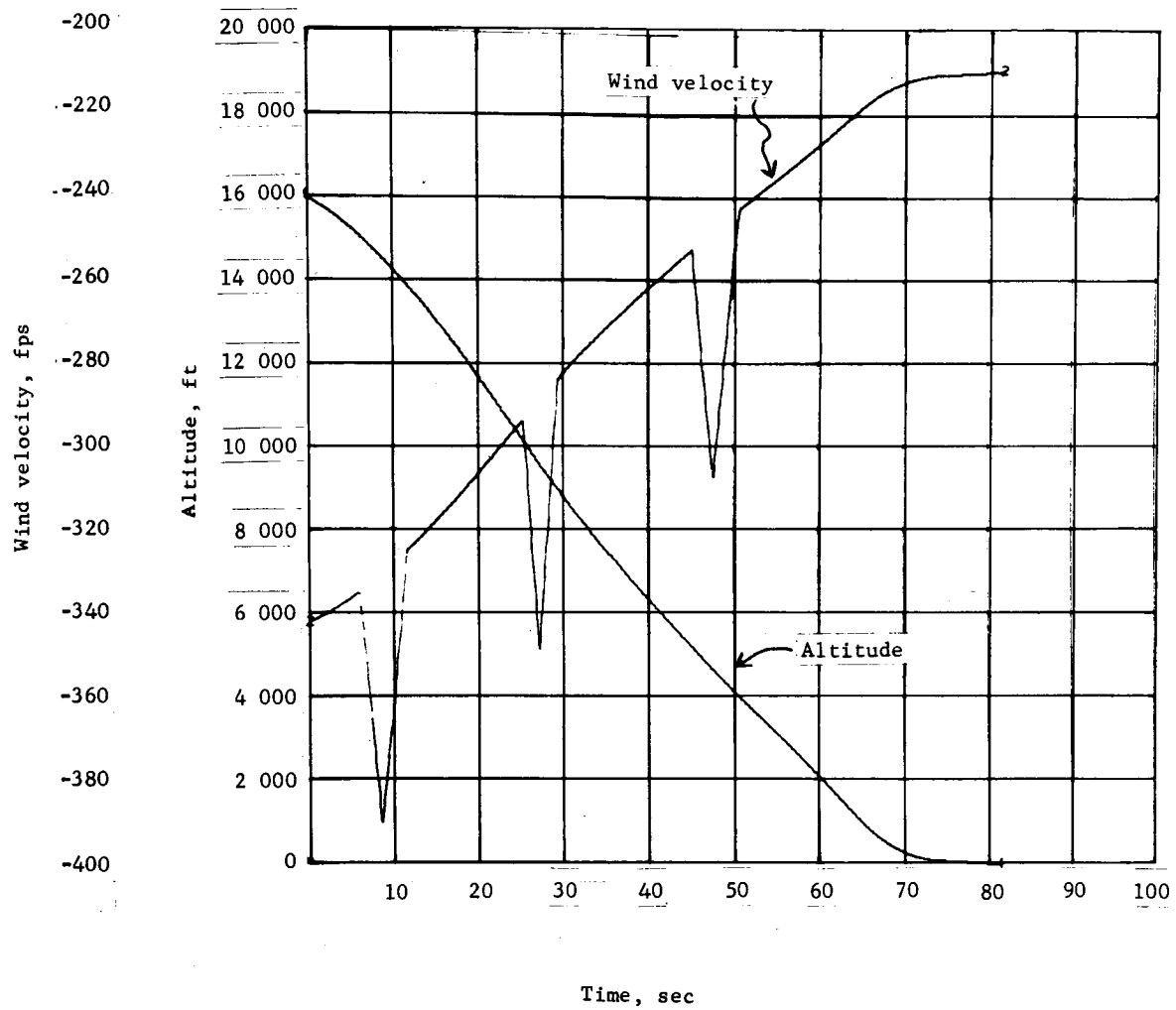
Figure 67.- Second Parachute-Lander 6DOF Simulation Results:
Wind Velocity and Altitude vs Time

APPENDIX A

RADAR-AIDED INERTIAL NAVIGATION
USING A KALMAN FILTER*

---

*The work presented in this appendix is based on notes
written by Robert N. Ingoldby, the principal investigator for
this portion of the study.

A Kalman filter is one method of formulating a statistical estimation process to extract information about the states of a dynamic system from measurements of signals related to the states. When applied to linear systems in which Gaussian white noise corrupts both the system and the measurements, the theory is well developed and has been applied, in concept at least, to many problems involving guidance, control, and information processing. In these cases, the filter gives a minimum-variance estimate.

If the system is nonlinear, as is the usual case, then the linear theory can still be applied if perturbation techniques are used to obtain linear approximations of the nonlinearities in the system.

If we make these assumptions, the dynamic equation for state propagation is

$$X_{k+1} = \Phi_{k+1,k}\left(X_k\right) + W_k \tag{A1}$$

and that for the measurements is

$$Z_{k+1} = H_{k+1}X_k + \eta_{k+1} \tag{A2}$$

where X_k is a vector of N states at time $t = t_k$, $\Phi_{k+1,k}$ is the state transition matrix that propagates the states at t_k to states at t_{k+1}, W_k is the dynamic modeling noise, Z_{k+1} is a vector of M measurements that is related to the states by the matrix H_{k+1}, and η_{k+1} is the measurement noise.

The Kalman filter makes use of the measurements and the known dynamic equations to generate an estimated state, $\hat{X}$. The equations for the filter are represented in discrete form as:

$$\hat{X}_{k+1} = \Phi_{k+1,k}\hat{X}_k + K_{k+1}\left[Z_{k+1} - H_{k+1}\Phi_{k+1,k}\hat{X}_k\right] \tag{A3}$$

where

$$K_{k+1} = P^*_{k+1}H^T_{k+1}\left[H_{k+1}P^*_{k+1}H^T_{k+1} + R_{k+1}\right]^{-1} \tag{A4}$$

$$P^*_{k+1} = \Phi_{k+1,k}P_k\Phi^T_{k+1,k} + Q_{k+1} \tag{A5}$$

$$P_{k+1} = P^*_{k+1} - K_{k+1} H_{k+1} P^*_{k+1} \qquad (A6)$$

Let us examine these equations. In equation (A3) we see that the new state, $\hat{X}_{k+1}$, is generated from the old state, $\hat{X}_k$, using the dynamic model, $\Phi_{k+1,k}$, and a term that includes the new measurement, Z_{k+1}. Because $H_{k+1} \Phi_{k+1,k} \hat{X}_k$ is what the filter thinks the new measurement will be, the bracketed term in equation (A3) is an error term, usually called the measurement residual. This error is multiplied by the optimum gain matrix K_{k+1}, to determine the correction term that must be applied to the estimated state.

Equations (A4) thru (A6) define how the gain matrix is computed. This matrix is based on the statistics of the measurement noise, the dynamic modeling error, and the initial estimates of the state. R_k is the covariance matrix of measurement error,

$$R_k = \text{Cov} \left[\eta_k \ \eta_k^T \right] \qquad (A7)$$

Q_k is the covariance matrix of the dynamic modeling error

$$Q_k = \text{Cov} \left[W_k \ W_k^T \right] \qquad (A8)$$

and P_k is the covariance matrix of the errors in the state estimate

$$P_k = \text{Cov} \left[\left(\hat{X}_k - X_k \right) \left(\hat{X}_k - X_k \right)^T \right] \qquad (A9)$$

Matrices R_k and Q_k and the initial conditions of P_k can not be defined without a knowledge of the particular system involved.

For the radar-aided inertial navigation problem, the states of interest are: the three body axis velocity components, the altitude, and the direction cosines relating the gravity vector to the body-axis coordinates. These states are described by the navigator equations:

$$\dot{u} = A_x - q \cdot w + r \cdot v + g \cdot A_{13} \tag{A10}$$

$$\dot{v} = A_y + p \cdot w - r \cdot u + g \cdot A_{23} \tag{A11}$$

$$\dot{w} = A_z - p \cdot v + g \cdot u + g \cdot A_{33} \tag{A12}$$

$$\dot{H} = -A_{13} \cdot u - A_{23} \cdot v - A_{33} \cdot w \tag{A13}$$

$$\dot{A}_{13} = A_{23} \cdot r - A_{33} \cdot q \tag{A14}$$

$$\dot{A}_{23} = A_{33} \cdot p - A_{13} \cdot r \tag{A15}$$

$$\dot{A}_{33} = A_{13} \cdot q - A_{23} \cdot p \tag{A16}$$

where u, v, and w are the body-axis velocity components along the X_b, Y_b, and Z_b axes, respectively, A_x, A_y, and A_z are the measured accelerations in these directions, p, q, and r are the attitude rates about these axes, g is the gravitational constant assumed for the planet, H is the altitude of the vehicle with respect to the planet, and A_{13}, A_{23}, A_{33} are direction cosines.

If equations (A10) thru (A16) are mechanized in the flight computer, they can replace the state propagation matirx, ϕ, in calculations made to update the states with time.

If the Kalman filter is to be mechanized to estimate only the four states (u, v, w, and H), then the measurement matrix, H, is the identity matrix, because the radar measurements are u_R, v_R, and w_R from the velocity radar and H_A from the altimeter. Thus, equation (A3) can be computed from the navigator outputs and the measurements if we are given the gain matrix, K.

For conventional Doppler inertial systems, the elements of K are selected as constants, usually in diagonal form. Alternatively, the Kalman filter can be used to compute an optimal time-varying gain matrix; in this computation, the assumptions of linearity and Gaussian statistics are required.

If in equations (A10) thru (A16) only u, v, w, and H are to be estimated, then all the other parameters (p, q, r, etc) can be considered as time-varying coefficients in equations (A10) thru (A13). Then the equations are linear and Φ can be computed using standard techniques. In this analysis, we assumed that Φ would be computed by the flight computer using rectangular integration, which yields

$$\Phi_{k+1,k} = dt \begin{bmatrix} 1/dt & r_k & -q_k & 0 \\ -r_k & 1/dt & p_k & 0 \\ q_k & -p_k & 1/dt & 0 \\ -A_{13_k} & -A_{23_k} & -A_{33_k} & 1/dt \end{bmatrix} \tag{A17}$$

The covariance matrix of measurement errors, R, is nondiagonal because u_R, v_R, and w_R are computed from the same radar beam velocities. R has the form

$$R = \begin{bmatrix} C_{uu} & C_{uv} & C_{uw} & 0 \\ C_{uv} & C_{vv} & C_{vw} & 0 \\ C_{uw} & C_{vw} & C_{ww} & 0 \\ 0 & 0 & 0 & C_{hh} \end{bmatrix} \tag{A18}$$

R is generally time-varying, since the radar errors are a function of velocity and altitude. The numerical values used in equation (A18) can be obtained from error analysis of the radar.

The covariance matrix of dynamic modeling errors, Q, contains all the errors that could significantly affect those states which have not been modeled in propagating the state estimates from one point in time to the next. These errors include:

1) Accelerometer errors;

2) Gyro errors;

3) Errors in the unestimated states of A_{13}, A_{23}, and A_{33};

4) Errors due to the variation of gravity; and

5) Errors due to the effect of surface slope on altitude (referenced to the landing site).

APPENDIX A

Over the short trajectory times for which the filter will be operating, the accelerometer, gyro, and gravity errors have negligible effect. However, the effect of errors in the unmodeled states A_{13}, A_{23}, and A_{33} can be significant. In equations (A10) thru (A16), we see that if we perturbate the direction cosines as

$$A_{13} = A_{13_t} + \Delta A_{13} \tag{A19}$$

$$A_{23} = A_{23_t} + \Delta A_{23} \tag{A20}$$

$$A_{33} = A_{33_t} + \Delta A_{33} \tag{A21}$$

then after rectangular integration of the equations, error terms exist as follows:

$$\Delta u = g \cdot \Delta A_{13} \cdot dt \tag{A22}$$

$$\Delta v = g \cdot \Delta A_{23} \cdot dt \tag{A23}$$

$$\Delta w = g \cdot \Delta A_{33} \cdot dt \tag{A24}$$

$$\Delta H = -(\Delta A_{13} \cdot u + \Delta A_{23} \cdot v + \Delta A_{33} \cdot w) \, dt \tag{A25}$$

then Q becomes

$$Q = Cov \ Y \ Y^T \tag{A26}$$

$$Y^T = [\Delta u, \ \Delta v, \ \Delta w, \ \Delta H] \tag{A27}$$

To account for the surface slope effect on the altitude estimate, a term representing its mean square error can be added to the (4, 4) element of Q.

Two special modules were included in the MOD6MV computer program to evaluate the operation of the Kalman filter. These modules solved equations (A10) thru (A16) and the Kalman filter equations during the parachute- and terminal-descent phases of the Mars Lander mission. The following discussion summarizes the results of the computer runs.

Q was computed using u = 300 fps, v = 20 fps, w = 20 fps, 3σ attitude errors (10 deg) in pitch and yaw, a nominal pitch angle of -60 deg, and a nominal yaw angle of 0 deg. Then R was computed using 1σ errors of 1.5% along each Modified-LM radar beam and a 1σ altimeter error of 32 ft. The numerical result was

$$R = \begin{bmatrix} 12.2 & 23.0 & 16.4 & 0 \\ 23.0 & 174.0 & 62.0 & 0 \\ 16.4 & 62.0 & 89.0 & 0 \\ 0 & 0 & 0 & 1024.0 \end{bmatrix}$$

If a radar beam unlocks, the filter should be set to ignore the data associated with that beam. In the simulation, this was accomplished by increasing the appropriate elements in R until the radar beam relocked. This caused the corresponding elements in K to go to very small values, thus effectively ignoring the affected measurement.

Initially, P was loaded with large values. A 1σ velocity error of 300 fps and a 1σ altitude error of 150 ft were used. However, in all runs, the first valid radar measurement reduced the values in P close to those in R.

Five computer runs were made to evaluate the operation of the Kalman filter. During the parachute phase, the filter was merely updating the state estimates every 200 msec; but during the terminal descent, the estimated states (still being up-dated) were used for vehicle guidance in the radar-aided inertial navigation mode.

Run B265

Q and R were as defined for the simulation and were con-stant matrices through the entire run. As the vehicle descended and the velocity decreased, the filter began ignoring the radar data. This is because after some time the terms in P and K become small since the filter thought it knew what the trajectory was; since R was computed at high values of velocity, it gave an unnecessarily-conservative estimate of the measurement errors at low velocities. Thus, the filter ignored the data after it had reduced the values in P below those in R.

APPENDIX A

Run G439

In this run, appropriate terms in R were made proportional
to velocity squared and altitude squared (this assumption is
consistent with a percentage error specification for the radars)
and Q was held constant. This filter became unstable because
when the side velocities went to zero, the filter thought it was
getting perfect data.

Run B631

In this run, Q was increased by a factor of 20. R was
computed as in the previous run, except that no term was allowed
to decrease below 0.5. In this run, the filter relied upon the
radar data to an excessive degree, which caused the vehicle steer-
ing to be very sensitive to radar noise.

Run B521

This run is the same as Run B631, except that Q was only
four times as large as the Q of Run B265. This run produced
fairly good results. Although there was some lateral velocity
(5 fps) at landing, this could probably have been eliminated
with further juggling of the computer gains.

In conclusion, it appears that a Kalman filter can be used
for radar-aided inertial navigation, even though its benefits
are of questionable value when compared to the simpler naviga-
tion approach described in Section III-A.

The following specific conclusions can be made:

1) The filter will not work satisfactorily unless R
   is computed as a function of the vehicle velocities.

2) Q must be chosen carefully and must be verified
   by simulation.

3) When filter outputs are used for closed-loop steer-
   ing during terminal descent, they can give rise to
   stability problems that result because of difficulty
   in predicting the nature of K, which is actually
   a gain incorporated into the control loops.

4) The results obtained here show that the simpler
   navigation approach is difficult to improve on,
   particularly, if the initial radar data is used
   directly to initialize the navigator outputs.

APPENDIX B

DESCRIPTION OF THE TIME-CORRELATED
MONTE CARLO RADAR LOCK PROGRAM

APPENDIX B

This Monte Carlo program evaluates the lock status of the radar beam on a time-correlated basis. The program is able to simulate various parachute trajectories or terminal-descent trajectories (500 flights provides a reasonable computer cost) to study the effect of atmospheric densities, wind velocities, wind gusts, and terrain slope. In this manner, the program provides a measure (in a probabilistic sense) of success in meeting guidance and control requirements. The program will provide the following data:

1) The probability of having at least three radar beams locked T sec before the capsule descends to engine-ignition altitude (4000 ft), or engine-cutoff altitude (10 ft).

2) The probability of having three radar beams locked for at least T sec before the capsule descends to engine-ignition altitude or engine-cutoff altitude.

3) The probability of having beam cross-lock T sec before the capsule descends to engine-ignition altitude or engine-cutoff altitude.

4) The probability of having beam cross-lock for T sec before the capsule descends to engine-ignition altitude or engine-cutoff altitude.

For the parachute-descent time-correlated Monte Carlo program, tables have been compiled that list altitude, velocity, and flight path angle as functions of time for three specific atmospheric densities. At the start of each trajectory or case, the atmospheric density will be sampled using a probability histogram as defined in reference 8. An interpolation subroutine is used to determine the proper values of velocity, altitude, and flight path angle. In a similar manner, wind velocity, gusts, and gust altitude are determined with the aid of histograms defined in reference 8. Then, using the tables, a trajectory is generated at specified time intervals and the beam velocities, incidence angles, etc, are computed (see Appendix C). The radar lock status will be computed, but this time the radar search function is included. As time is incremented down a trajectory, the time during which each beam is locked or cross-locked is also computed. As this process is repeated, say 500 times, an overall time-of-lock probability histogram can be constructed, which includes the random nature of the trajectory as well as time-dependent effects such as gust response and radar sweep time.

APPENDIX B

The geometry computations at each time point are handled in the same manner as those in the static Monte Carlo program described in Appendix C.

Statistics are tracked for 3-, 4-, and 5-beam radars using modified LM radar parameters. A flow diagram is shown in figure B1.

Figure B1.- Flow Block Diagram of the Parachute Descent
Time-Correlated Monte Carlo Radar Lock Com-
puter Program

211

C

A   B

```
┌─────────────────────────┐
│ Compute incidence angles │
│   and beam velocities    │
└─────────────────────────┘
```

```
┌──────────────────────────────────────────┐
│ Radar signal computation: given altitude,  │
│   incidence angles, and beam velocities,   │
│   compute:                                  │
│     Received power per beam based on speci- │
│       fied reflectivity model               │
│     Receiver Threshold                      │
│     Sidelobe power in each beam from each of│
│       the other beams                       │
│     Doppler frequency of beams              │
└──────────────────────────────────────────┘
```

```
┌──────────────────────────────────────────┐
│ Conditional radar lock:                     │
│     Compare power received to receiver      │
│       thresholds, and set conditional lock  │
│       matrix                                │
│     Determine if radar has broken lock or   │
│       cross-locked                          │
│     Set search mode flags                   │
└──────────────────────────────────────────┘
```

```
┌──────────────────────────────────────────┐
│ Radar lock computation:                     │
│     First time point:  initialize tracker   │
│       frequencies                           │
│     Search for main-beam and side-lobe signals│
│     Determine if main beam signal exceeds threshold.│
│       If not, determine if a side-lobe signal ex-│
│       ceeds the threshold                   │
│     Set lock matrix                         │
└──────────────────────────────────────────┘
```

```
┌──────────────────────────────────────────┐
│ Lock logic computations:                    │
│     Set cross-lock matrix                   │
│     Set cross-locks matrix with sufficient main signal│
│     Set counters each time point for 3-, 4-, and 5-beam│
│       radars                                │
│     Increment length of time that each beam is cross-│
│       locked for the first, second, and total time in-│
│       crement and the length of time that three beams│
│       are locked for 3-, 4-, and 5-beam radars for the│
│       first, second, third, and total time │
└──────────────────────────────────────────┘
```

Repeat at ΔT sec intervals until
capsule descends below 4000 ft

E   D

Figure B1.- Continued

212

E   D

Pass through logic to determine mean, minimum,
  and maximum trajectory times
Increment for averaging:
    Time that each beam is cross-locked for the
      first, second, and total time
    Time that three beams are locked for 3-, 4-,
      and 5-beam radars for the first, second,
      third, and total time

Increment:
    Probability distribution bins for the time
      three beams are locked for 3-, 4-, and 5-
      beam radars
    Probability distribution bins for the time
      beams 1, 2, 3, 4, and 5 are cross-locked
    The following and reference them to 4000 ft:
      Lock and conditional-lock matrices
      Number of trajectories with at least one
        cross lock
      Joint probability of cross-lock on each beam
      Joint probability of cross-lock conditioning
        for each beam
      Number of cross-locks on a beam having a main-
        beam lock condition
      Probability of one, two, three, four, and five
        beams locked for 3-, 4-, and 5-beam radars
      Number of 1-, 2-, 3-, 4-, and 5-beam lock
        conditions

Repeat ITOT times
(usually 500)

Output results

Figure B1.- Concluded

APPENDIX C

DESCRIPTION OF THE STATIC
MONTE CARLO RADAR LOCK PROGRAM

This Monte Carlo program works on the premise that the results of a large number of specific cases, each case being randomly computed, will yield the probability that a certain outcome will occur. For instance, the result may be that 47 out of 1000 times a radar beam will be unlocked at altitude of 4000 ft. Figure C1 shows a flow chart of the program. In general, the technique used is to obtain random samples for surface slope, wind velocity, etc, and then, for that specific set of random numbers, go through the geometry to compute beam incidence angles and the velocity along each beam. Next, the radar threshold (required received power referred to the antenna) is computed for each beam. For the LM radar, this threshold is a function of the velocity of the beam or the doppler frequency in the beam. Then, using the incidence angle, the altitude, and a reflectivity curve (in this case, the one shown in fig. 23), the radar range equation is used to compute the received power in each beam.

If this power is above the threshold the beam is locked; if the power is below the threshold, the beam is unlocked. We assume that the condition has existed long enough for the radar proof time to be satisfied. The equations for these calculations are the same as those given in reference 4 for the LM radar.

Furthermore, for each beam, a side-lobe power level is computed by subtracting 28.9 dB from the main-lobe power. Then these side lobe power levels are checked against the thresholds of the other appropriate beams to determine whether a side-lobe lock potentiality exists. For instance, assume that the threshold in Beam 2 is -150 dB and that the received power in Beam 1 is -100 dB. Then, the side-lobe power from the Beam 1 direction that is seen by Beam 2 would be -128.9 dB, and a potential cross-lock situation would exist. Further assume that the main-lobe power in Beam 2 is -160 dB, so that an unlock in Beam 2 is declared. The Monte Carlo program would then increment a counter to record that Beam 2 was unlocked at the same time that a potential cross-lock condition existed. Taking many cases, this would produce the joint probability function $P(c,u)$ discussed in reference 14. Counters are included to record all combinations of beam unlock and cross-lock, including cross-lock with the transmitted fourth beam of the LM radar.

Notice that the existence of a potential cross-lock condition does not mean that the radar will definitely cross-lock. The probability of cross-lock depends on the time required for the tracker to move to the side-lobe frequency, the proof time, and whether the geometrical conditions creating the side lobe-power remain there that long. This probability can be assessed by the time-correlated Monte Carlo program.
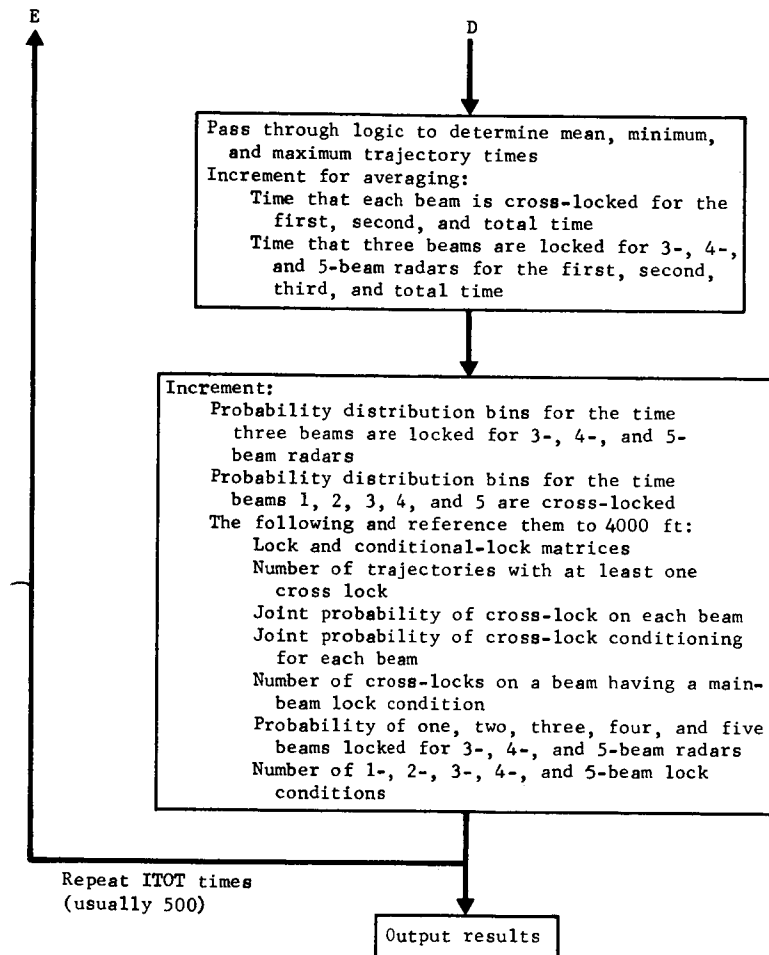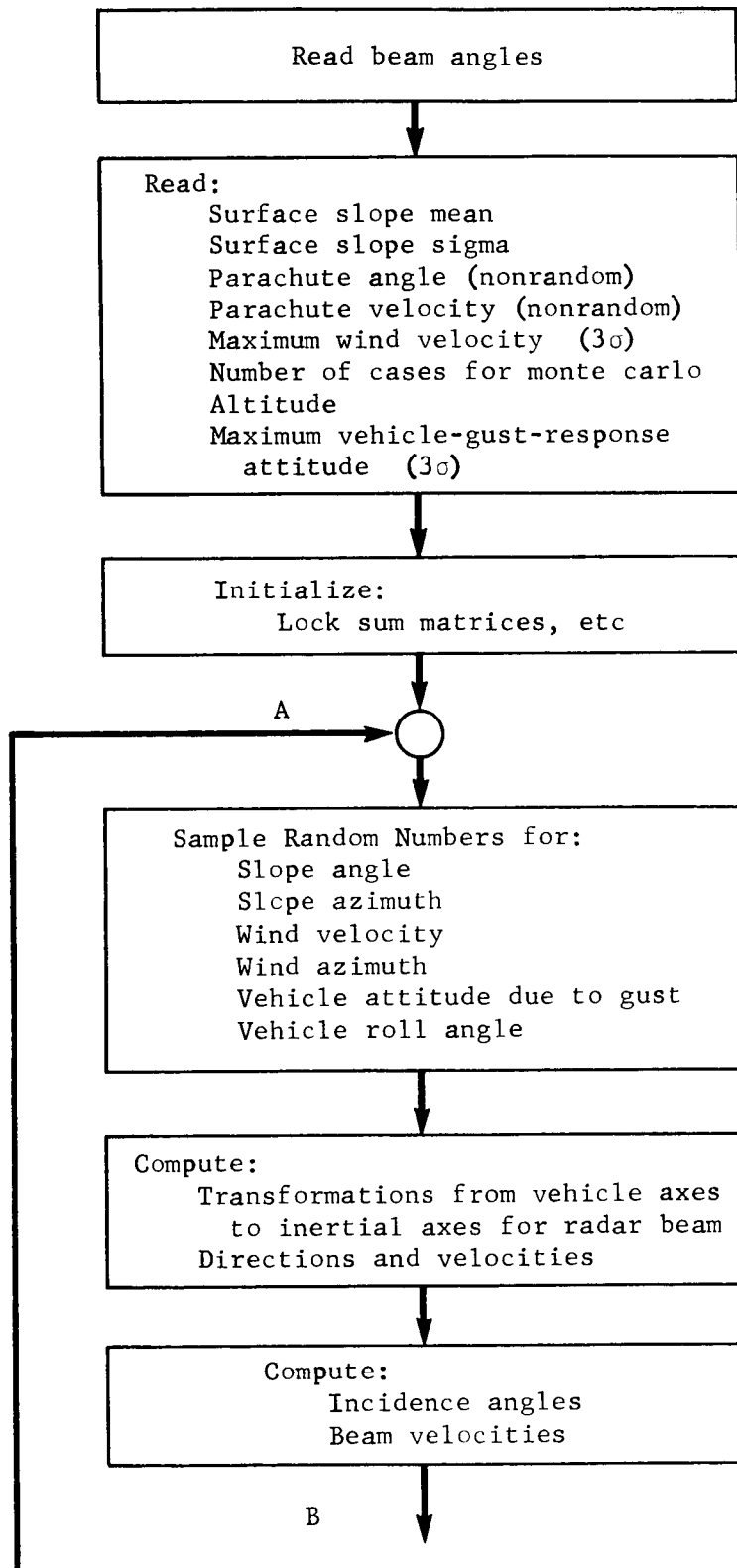
Figure C1.- Flow Block Diagram of the Parachute-Descent Static Monte
        Carlo Radar Lock Program

TO A

B

Radar lock computations:
    Increment counters for
        Beams 1 - 4 unlocked
        Beams 1 - 4 unlocked and cross-locked
        Beams i + j unlocked (all combinations)
        Beams i + j + k unlocked (all combinations)
        Beams 1 + 2 + 3 + 4 unlocked

Radar lock computation: given altitude, incidence
    angles, and beam velocities, compute:
        Received power per beam based on specified
            reflectivity model
        Receiver threshold
        Sidelobe power in each beam from each of the
            other beams

Repeat
ITOT times
(usually 1000)

Output Results

APPENDIX C

A. Monte Carlo Program Geometry

Figure C2 shows the geometry used in the program to calculate beam incidence angles and velocities. First assume the following coordinate system on the surface:
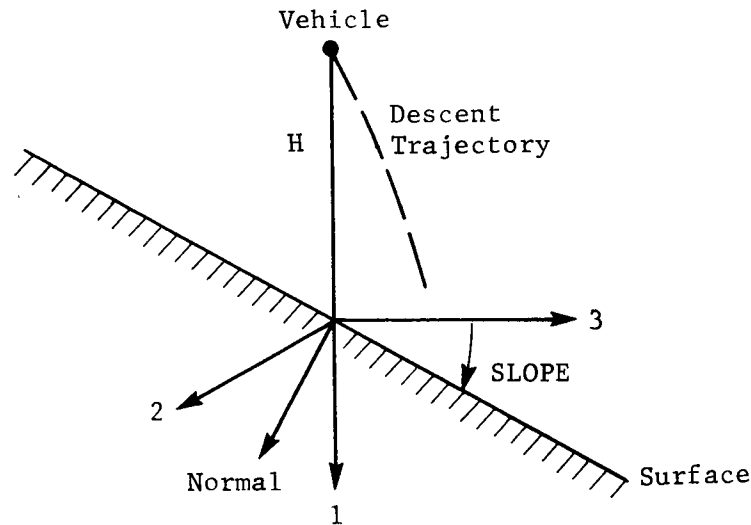
Figure C2.- Geometry Used in the Parachute-
Descent Static Monte Carlo Radar-
Lock Program to Calculate Beam
Incidence Angles and Velocities

The coordinates of the unit vector normal to the slope in the 1,2,3 system are:

$$YSLOP(1) = COS(SLOPE) \tag{C1}$$

$$YSLOP(2) = 0. \tag{C2}$$

$$YSLOP(3) = -SIN(SLOPE) \tag{C3}$$

The vehicle trajectory may be going up or down or across the slope. Define a $1'$ $2'$ $3'$ system rotated about the 1 axis by an arbitrary angle AZ. This is the slope azimuth. The transformation between these coordinate systems is:

$$\begin{bmatrix} X1' \\ X2' \\ X3' \end{bmatrix} = \begin{bmatrix} 1 & 0 & 0 \\ 0 & CA & SA \\ 0 & -SA & CA \end{bmatrix} \begin{bmatrix} X1 \\ X2 \\ X3 \end{bmatrix} \qquad (C4)$$

where

$$CA = COS(AZ) \qquad (C5)$$

$$SA = SIN(AZ) \qquad (C6)$$

In the primed system, the vehicle has some velocity vector $\overline{V}$ at an angle from the vertical THAVG. Think of this as the velocity of the vehicle with respect to the atmosphere. (The atmosphere may be moving with some steady wind velocity which will be added later.)

This velocity vector is expressed in the primed system as:

$$V(1') = V_V = VTERM \cdot COS(THAVG) \qquad (C7)$$

$$V(2') = 0. \qquad (C8)$$

$$V(3') = VHO = -VTERM \cdot SIN(THAVG) \qquad (C9)$$

The atmosphere (or wind) may be moving at any arbitrary azimuth direction with respect to these velocities. We assume that the wind is blowing horizontally, rather than up or down the slope. Thus, we have a vector diagram as shown in figure C3.
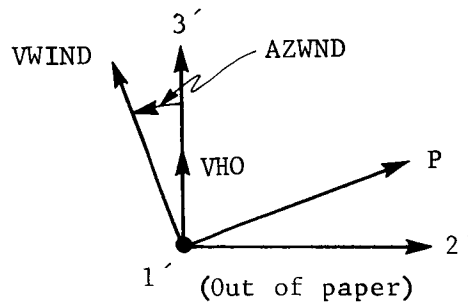
Figure C3.- Wind Velocity with Respect
to Vehicle Velocities in
the Primed Coordinate System

Vectorially adding the wind velocity to the velocity components above, we have

$$V(1') = V_V \tag{C10}$$

$$V(2') = -VWIND \cdot SIN(AZWND) \tag{C11}$$

$$V(3') = VHO + VWIND \cdot COS(AZWND) \tag{C12}$$

These are then the components of the total velocity of the vehicle with respect to the surface expressed in the $1', 2', 3'$ coordinate system.

Now we must derive a relationship between these coordinate systems and the vehicle body axes. The vehicle will have a pitch angle defined by the initial angle, THAVG, combined suitably with a pitch angle produced by a wind gust. Because the wind gust is assumed to be in the same direction as VWIND, the vehicle will pitch about an axis normal to VWIND (namely the P axis shown in fig. C3). To simplify combining the gust pitch angle with THAVG, we will assume that both angles can be treated as vectors. This assumption is valid for angles up to about 20°. THAVG is an angle about the $2'$ axis. Figure C4 illustrates the geometry.
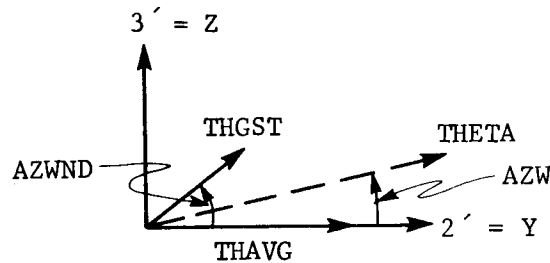
Figure C4.- Orientation of the Primed Coordinate System with Respect to the Vehicle Body Axes

Vector addition yields

$$TY = THAVG + THGST \cdot COS(AZWND) \tag{C13}$$

$$TZ = THGST \cdot SIN(AZWND) \tag{C14}$$

$$THETA = (TY \cdot TY + TZ \cdot TZ)^{\frac{1}{2}} \tag{C15}$$

THETA is the total vehicle pitch angle. Sign is not a prob-
lem here since AZWND can vary arbitrarily from 0 to 2π radians.
THETA will be an angle about an axis rotated AZW from the 2´
axis, where

$$SIN(AXW) = SAW = TY/THETA \tag{C16}$$

$$COS(AZW) = CAW = TZ/THETA \tag{C17}$$

Let us define the 1´´,2´´,3´´ system with respect to the
1´,2´,3´ system as shown in figure C5:

1´, 1´´ (Out of paper)
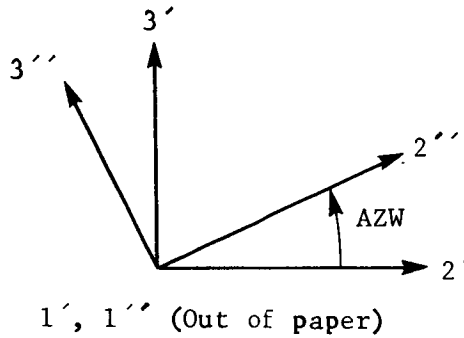
Figure C5.- Orientation of the Double-
Prime Coordinate System
with Respect to the Prime
Coordinate System

Then the transformation becomes

$$
\begin{bmatrix} X1´´ \\ X2´´ \\ X3´´ \end{bmatrix}
=
\begin{bmatrix} 1 & 0 & 0 \\ 0 & CAW & SAW \\ 0 & -SAW & CAW \end{bmatrix}
\begin{bmatrix} X1´ \\ X2´ \\ X3´ \end{bmatrix}
=
\begin{bmatrix} C \end{bmatrix}
\begin{bmatrix} X1 \\ X2 \\ X3 \end{bmatrix}
\tag{C18}
$$

where

$$
\begin{bmatrix} C \end{bmatrix}
=
\begin{bmatrix}
1 & 0 & 0 \\
0 & (CA \cdot CAW - SA \cdot SAW) & (SA \cdot CAW + CA \cdot SAW) \\
0 & (-CA \cdot SAW - CA \cdot SAW) & (CA \cdot CAW - SA \cdot SAW)
\end{bmatrix}
\tag{C19}
$$

APPENDIX C

As stated on the previous page, the vehicle is pitched an angle THETA about the $2''$ or P axis. Then, the vehicle may be at an arbitrary roll angle PHI about the roll axis. The transformation matrix relating the vehicle-body-axis system to the $1'', 2'', 3''$ system is

$$
\begin{bmatrix} X_b \\ Y_b \\ Z_b \end{bmatrix} = |B| \begin{bmatrix} X1'' \\ X2'' \\ X3'' \end{bmatrix} = \begin{bmatrix} CTH & 0 & -STH \\ STH \cdot SPH & CPH & SPH \cdot CTH \\ STH \cdot CPH & -SPH & CTH \cdot CPH \end{bmatrix} \begin{bmatrix} X1'' \\ X2'' \\ X3'' \end{bmatrix} \quad (C20)
$$

where

$$CTH = COS(THETA) \quad (C21)$$
$$STH = SIN(THETA) \quad (C22)$$
$$CPH = COS(PHI) \quad (C23)$$
$$SPH = SIN(PHI) \quad (C24)$$

The beam directions can be expressed as unit vectors in body coordinates. For instance, if ALF is the angle about the X_b axis to the beam $-X_b$ plane, and if GAM is the beam splay angle from the centerline, then the beam direction is

$$\overline{1}_{beam} = COS(GAM) \overline{1}_{X_b} + SIN(GAM) \cdot SIN(ALF) \overline{1}_{Y_b}$$
$$- COS(ALF) \cdot SIN(GAM) \overline{1}_{Z_b} \quad (C25)$$

where $\overline{1}_{beam}, \overline{1}_{X_b}, \overline{1}_{Y_b},$ and $\overline{1}_{Z_b}$ are unit vectors.

We can obtain the beam direction in the original inertial coordinate system $(1,2,3)$ by using the transformations derived above. That is, if

$$[A] = [B][C] \quad (C26)$$

then

$$\overline{1}_{beam}\Big|_{(1,2,3)} = [A]^T \overline{1}_{beam}\Big|_{(X_b,Y_b,X_b)} \quad (C27)$$

where the superscript T denotes matrix transposition. Since there are four beams, the Monte Carlo program uses the following operation:

224

$$[YBM]_{4 \times 3} = [XBM]_{4 \times 3} \ [A]_{3 \times 3} \qquad (C28)$$

where YBM has rows which are the beam-direction components along
the 1,2, and 3 axes, respectively, and XBM has rows which
are the beam-direction components along the X_b, Y_b, Z_b axes,
respectively.

Now that we have the beam directions in the 1,2,3 system
and the normal to the surface slope in the same system, we can
compute the incidence angle for each beam by:

$$TAN(AINC \ 1) = \frac{[YBM(I)] \ X \ [YSLOP]}{[YBM(I)] \cdot [YSLOP]} \qquad (C29)$$

where X denotes the vector cross-product, the dot denotes the
vector dot-product, and I denotes the appropriate row of the
matrix. This method assumes that the same surface slope is seen
by each beam.

We must know the velocity along each beam to determine the
doppler frequency and the receiver sensitivity threshold.

First, the velocity in the $1'', 2'', 3''$ system is found by
solving:

$$\begin{bmatrix} V(1'') \\ V(2'') \\ V(3'') \end{bmatrix} = \begin{bmatrix} 1 & 0 & 0 \\ 0 & CAW & SAW \\ 0 & -SAW & CAW \end{bmatrix} \begin{bmatrix} V(1') \\ V(2') \\ V(3') \end{bmatrix} \qquad (C30)$$

Then,

$$\begin{bmatrix} V_{X_b} \\ V_{Y_b} \\ V_{Z_b} \end{bmatrix} = [B] \begin{bmatrix} V(1'') \\ V(2'') \\ V(3'') \end{bmatrix} \qquad (C31)$$

The velocity along each beam component in the system is found
by combining the dot product of each velocity component in the
body-axis system with appropriate rows of the XBM matrix.

The preceeding equations are solved to obtain beam velocities
and incidence angles for each pass of 1000 passes in the Monte
Carlo program. For each pass different values for SLOPE,

VWIND, THGST, AZWND, AZ, and PHI are chosen from random-number-generator subroutines. The values for THAVG, VTERM, H, and radar beam angles are parameters which do not change in a given set of 1000 cases. Thus, each pass can be interpreted as one possible trajectory point. By making 1000 passes, we obtain the statistical information for that trajectory point for 1000 random geometrical conditions.

B. Radar Lock Equations

The Monte Carlo program uses a subroutine that, for a given beam velocity, incidence angle, and altitude, will define whether the beam is locked or not. Using the beam velocity, the program computes the doppler frequency and then computes the receiver threshold using curve-fitted equations for the sensitivity curves given in reference 4 (for simulation of cw radars). Then using the altitude H and the incidence angle, the program computes the range to the surface along the beam direction as

$$R = H/COS(AINC1) \tag{C32}$$

This method of computing range is based on the assumption that the surface is a plane that slopes at the angle SLOPE used in the preceeding geometry equations. This plane is assumed to have the same slope at all the points where the beam intersect with the surface. Figure C6 below shows the geometry for a single direction. α is the slope in the direction of the beam direction.
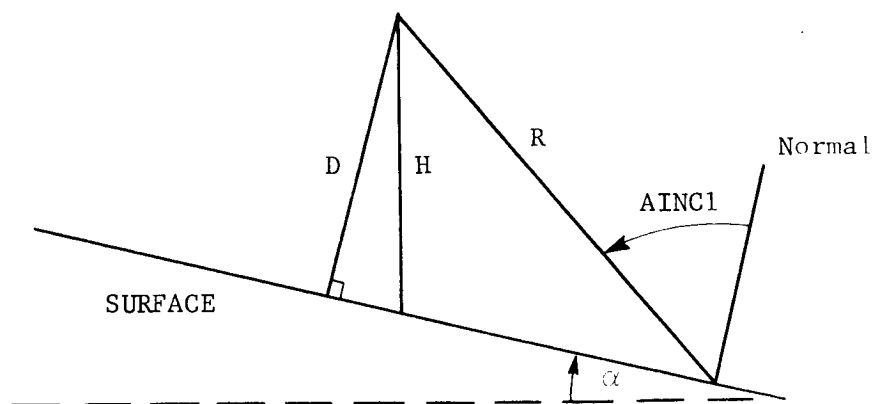
Figure C6.- Geometry Used in the Parachute-Descent Static Monte Carlo Radar-Lock Program to Compute Range

APPENDIX C

Actually

$$R = D/COS(AINC1) \tag{C33}$$

for this geometry. However, using H instead of D causes less
than 1.5 dB of conservative error in the radar range equation and
simplifies the computation for range. The radar range equation
used is

$$PR = C + 4.343 \, Log_e \, (1/COS \, \theta \cdot R^2) + CSEO \tag{C34}$$

where P is the power received, CSEO is the sigma zero from
the reflectivity model, C is a constant depending on trans-
mitted power, antenna gain, carrier frequency, microwave losses,
etc, R is the range, and θ is the incident angle.

For the ICW radar, an efficiency factor is added to equa-
tion (C34), but for a Bessel sideband radar, the range-dependent
Bessel coefficient must be included. The cross-lobe powers are
computed as previously described.

If the power received is less than the threshold, the beam
is interpreted as being unlocked. If the side-lobe power is
above the threshold, a potential cross-lobe lock is said to exist.
The dynamics of the tracker, bandwidth, etc, cannot be included
in a static point evaluation of this type.

APPENDIX D

INTERLEAVED VERSUS SIDE-BY-SIDE APERTURE ANTENNAS

The side-by-side aperture antenna system offers the advantages of lower beam coupling, better side-lobe control, greater beam-positioning flexibility, greater beam-shaping flexibility, and higher redundant reliability. Its disadvantages are increased weight and size.

In the radar performance study, the probabilities of cross-lobe and side-lobe lockup were defined in terms of selected reflectivity curves and arbitrarily-assumed side-lobe levels. Because increasing the aperture size improves the performance of an interleaved antenna system, one of the considerations for all modulations was the variation in side-lobe level. The other important consideration was the increase in coupling for the respective channels to the interleaved antenna system. For all cases considered, we assumed that the planar array systems would be comprised of rectangular slots which are not space-tapered.

In most analyses of the coupling of the rectangular slot, Babinet's theorem is invoked to prescribe the analysis in terms of a dipole antenna in free space (no ground plane). Using the electric and magnetic vector potentials, the electric and magnetic fields are given by

$$
\begin{bmatrix} \hat{E} \\ \\ \hat{H} \end{bmatrix} = \begin{bmatrix} - jw\hat{A} - \dfrac{jw}{k^2} \nabla(\nabla \cdot \hat{A}) - \dfrac{1}{\epsilon}\nabla X \hat{F} \\ \\ - jw\hat{F} - \dfrac{jw}{K^2} \nabla(\nabla \cdot \hat{F}) + \dfrac{1}{\mu}\nabla X \hat{A} \end{bmatrix} \tag{D1}
$$

For the rectangular slot shown in figure D1, the electric field is given by

$$
E = -\frac{1}{\epsilon}\nabla X \tilde{F} = - \frac{1}{\epsilon r^2 \sin \theta} \begin{bmatrix} \hat{a}_r & r\hat{a}_\theta & r(\sin \theta)\hat{a}_\varphi \\ \\ \dfrac{\partial}{\partial r} & \dfrac{\partial}{\partial \theta} & 0 \\ \\ F_r & rF_\theta & 0 \end{bmatrix} \tag{D2}
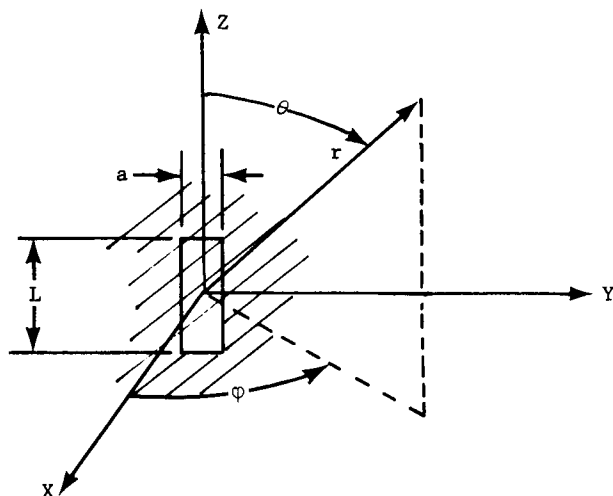$$

Figure D1.- Geometry for a Rectangular Slot in a Planar-Array Antenna
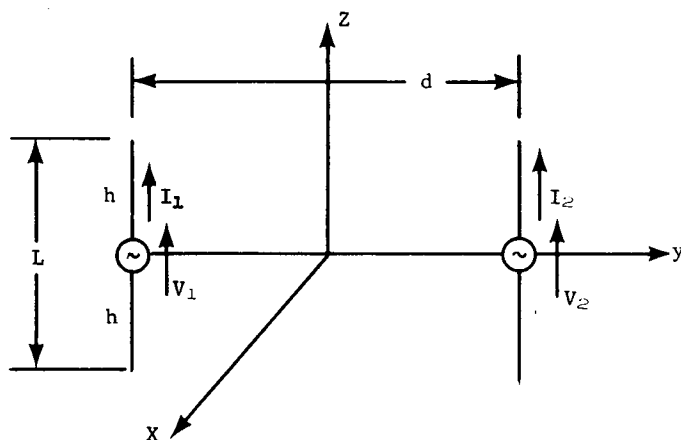

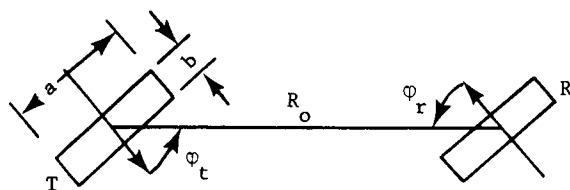Figure D2.- Arrangement of Two Dipoles in a Planar-Array Antenna

Figure D3.- Reduction of Coupling by Orienting the Inclination Angle of a
Rectangular Slot in a Planar-Array Antenna

or

$$\hat{E} = -\hat{a}_{\varphi} \frac{1}{\epsilon r} \left[\frac{\partial}{\partial r}\left(rF_{\theta}\right) - \frac{\partial}{\partial \theta}(Fr) \right] \tag{D3}$$

where

$$\begin{bmatrix} F_r \\ F_{\theta} \end{bmatrix} = \begin{bmatrix} F_z \cos \theta = \left(\dfrac{VmL \exp^{-jkr}}{4\pi r}\right) \; (\cos \theta) \\ F_z \sin \theta = \left(\dfrac{-VmL \exp^{-jkr}}{4\pi r}\right) \; (\sin \theta) \end{bmatrix} \tag{D4}$$

or

$$E_{\varphi} = \left(\frac{VmL \exp^{-jkr}}{4\pi\epsilon}\right) \; \left(\frac{jk}{r} + \frac{1}{r^2}\right) \tag{D5}$$

and for

$$\hat{H} = -jw\hat{F} - \frac{jw}{k^2}\left[\nabla\left(\nabla \cdot \hat{F}\right)\right] \tag{D6}$$

where in spherical coordinates

$$\nabla \cdot \hat{F} = \frac{1}{r^2}\left[\frac{\partial}{\partial r}\left(r^2 \, F_r\right)\right] + \frac{1}{r \sin \theta}\left[\frac{\partial}{\partial \theta}\left(F_{\theta} \sin \theta\right)\right] \tag{D7}$$

$$\nabla\left(\nabla \cdot \hat{F}\right) = \frac{\partial}{\partial r}\left[\left(\nabla \cdot \hat{F}\right) \hat{a}_r\right] + \frac{1}{r}\left\{\frac{\partial}{\partial \theta}\left[\left(\nabla \cdot \hat{F}\right) \hat{a}_{\theta}\right]\right\} \tag{D8}$$

then

$$\begin{bmatrix} H_r \\ H_{\theta} \end{bmatrix} = \begin{bmatrix} \left(\dfrac{VmL \exp^{-jkr}}{2\pi}\right) \; (\cos \theta) \; \left(\dfrac{2}{Z_o r^2} + \dfrac{2}{jw\mu r^3}\right) \\ \left(\dfrac{VmL \exp^{-jkr}}{2\pi}\right) \; (\sin \theta) \; \left(\dfrac{jk}{Z_o r} + \dfrac{1}{Z_o r^2} + \dfrac{1}{jw\mu r^3}\right) \end{bmatrix} \tag{D9}$$

Utilizing Babinet's principle,

$$\hat{H}_o^* = \hat{E}_o \tag{D10}$$

$$\hat{E}_o^* = -Z_o^2 \hat{H}_o \tag{D11}$$

Then, the fields of the slot $\left(E_{\varphi s}, H_{\theta s}\right)$ can be represented by the fields of the wire $\left(E_{\theta w}, H_{\varphi w}\right)$ as

$$\begin{bmatrix} E_{\varphi s} \\ \\ H_{\theta s} \end{bmatrix} = \begin{bmatrix} H_{\varphi w} \\ \\ \dfrac{-E_{\theta w}}{Z_o^2} \end{bmatrix} \tag{D12}$$

For the two dipoles shown in figure D2, the basic array expression can be utilized:

$$\hat{E}_n(\theta,\varphi) = \left(\frac{\exp^{-jkr}}{r}\right)\left(\hat{E}_{(\theta,\varphi)}\right)\sum_{n=0}^{N-1} A_n \exp^{jn\psi} = \Big[E(\theta,\varphi)\Big]\Big[\mathcal{F}(\psi)\Big] \tag{D13}$$

where

$$\mathcal{F}(\psi) = \sum_{n=0}^{N-1} A_n \exp^{jn\psi} \tag{D14}$$

and for a uniform array

$$\mathcal{F}(\psi) = 2\sum_{n=0}^{(N-1)/2} A_n \cos\left(n\psi + \varphi_n\right) \tag{D15}$$

or for the 2-dipole array

$$E(\theta,\varphi) = 2\, Ed(\theta,\varphi)\cos\left(\frac{kd\cos\theta - \psi_o}{2}\right) \tag{D16}$$

where

$$Ed(\theta,\varphi) = Id \frac{\cos\left(\pi\frac{\cos\theta}{2}\right)}{\sin\theta} \tag{D17}$$

The coupling is normally defined in terms of the mutual impedance. Considering identical antennas $\left(Z_{11} = Z_{22}\right)$

$$\begin{bmatrix} V_1 \\ V_2 \end{bmatrix} = \begin{bmatrix} Z_{11} & Z_{12} \\ Z_{22} & Z_{12} \end{bmatrix} \begin{bmatrix} I_1 \\ I_2 \end{bmatrix} \tag{D18}$$

and for

$$Z_{12} = |Z_{12}| \, e^{j\alpha} \tag{D19}$$

we have

$$\begin{bmatrix} W_1 \\ W_2 \end{bmatrix} = \begin{bmatrix} |I_1^2| \, \left[R_{11} + |Z_{12}| \cos\left(\alpha + \psi_o\right)\right] \\ |I_2^2| \, \left[R_{22} + |Z_{12}| \cos\left(\alpha - \psi_o\right)\right] \end{bmatrix} \tag{D20}$$

Then, the total power W of the antennas is

$$W = W_1 + W_2 = 2 \, |I_1|^2 \left[R_{11} + (R_{12}) \cos\psi_o\right] \tag{D21}$$

and

$E(\theta,\varphi) =$

$$2 \left\{ \frac{W}{2 \left[R_{11} + (R_{12}) \left(\cos\psi_o\right)\right]} \right\}^{\frac{1}{2}} \left[\frac{\cos\left(\frac{\pi\cos\theta}{2}\right)}{\sin\theta} \right] \left[\cos\left(\frac{kd\cos\varphi-\psi_o}{2}\right)\right] \tag{D22}$$

and the gain of the two dipoles compared to a single dipole is

$$\frac{G_a}{G_d} = \frac{E_a^2}{E_d^2} = \frac{2(R_{11})\left[\cos^2\left(\frac{kd\cos\varphi_o - \psi_o}{2}\right)\right]}{R_{11} + (R_{12})\left(\cos\psi_o\right)} \tag{D23}$$

Now, since the power transmitted is

$$W_t = I_1^2 \left[\text{Re}(Z_{11}) \right] \tag{D24}$$

and the received power in a matched load is

$$W_r = I_2^2 \left[\text{Re}(Z_{22}) \right] = \frac{I_1^2 |Z_{12}|^2}{4 \left[\text{Re}(Z_{22}) \right]} \tag{D25}$$

then the field coupling C is

$$C = \frac{W_r}{W_t} = \frac{|Z_{12}|^2}{4(R_{11})(R_{22})} \tag{D26}$$

where

$$\left| \begin{matrix} R_{11} \\ \\ R_{22} \end{matrix} \right| = \left| \begin{matrix} \text{Re}(Z_{11}) \\ \\ \text{Re}(Z_{22}) \end{matrix} \right| \tag{D27}$$

Because the coupling may be reduced by orientation of the inclination angle (see fig. D3), the coupling C can be expressed (see ref. 15) in terms of the directivities $D_t \left(\varphi_t \right)$ $D_r \left(\varphi_r \right)$ as

$$C = \left[C_o(R_o) \right] \left[D_t(\varphi_t) \right] \left[D_r(\varphi_r) \right] \left(N_{qt,qr} \right) \tag{D28}$$

for a rectangular aperture with dimensions (a,b)

where

$$D(\varphi) = \frac{3}{2F} \left(\cos^2 \varphi \right) \left(\frac{\sin V}{V} \right)^2 \left(\frac{\cos U}{1 - \frac{4U^2}{\pi 2}} \right)^2 \tag{D29}$$

and

$$U = \pi \left(\frac{a}{\lambda} \right) \sin \varphi \tag{D30}$$

$$V = \pi \left(\frac{b}{\lambda} \right) \cos \varphi \qquad\qquad (D31)$$

$$F \approx 1 \text{ when } \frac{a}{\lambda} \text{ and } \frac{b}{\lambda} < 1 \qquad\qquad (D32)$$

Curves illustrating the relative magnitude of the coupling co-efficient $C(R_o)$ and the directional constants $D_t(\varphi_t)$ and D_r (φ_r) are shown in figures D4 and D5. Figure D4 shows that $C(R_o)$ decreases at the rate of 6dB/octave. In figure D5, Curve I shows the case where both φ_t and $\varphi_r = 0°$, and Curve II shows the case where both φ_t and $\varphi_r = \pi/2$. As shown in figure D4, for case I $\left(\text{when } \varphi_r \text{ and } \varphi_t = 0°\right)$, the isolation between inter-leaved antennas would be about 16 dB for $R_o/\lambda = 0.5$ and 22dB for $R_o/\lambda = 1.0$. For the side-by-side aperture antennas, the curves can be extrapolated (using 6dB/octave) to greater than 60dB for separate 18x18-in. apertures, if we make the assumption that the effective array $R_o > 18$ in.

From equation (D13), we can see that if the number of ele-ments N of the interleaved array equals the number of elements of an equivalent array without interleaved elements, then the array field $E_n(\theta,\varphi)$ is unaltered if $E(\theta,\varphi)$ is unaltered.

From equation (D22), the effects of coupling or mutual impedance are shown to decrease the gain of the individual element $E(\theta,\varphi)$ by the R_{12} term. From these equations, it would appear that the basic side-lobe structure is not altered with respect to the main beam if the above conditions are retained. The additional elements of the interleaved array appear as an equivalent yagi antenna (fig. D6); and the excitation in the reference array elements produces a traveling wave in the corresponding elements of the interleaved array. The current driving the nth element is

$$I_n (Z`) = I (Z`) \left(\exp^{-jk_x ns} \right) \qquad\qquad (D33)$$

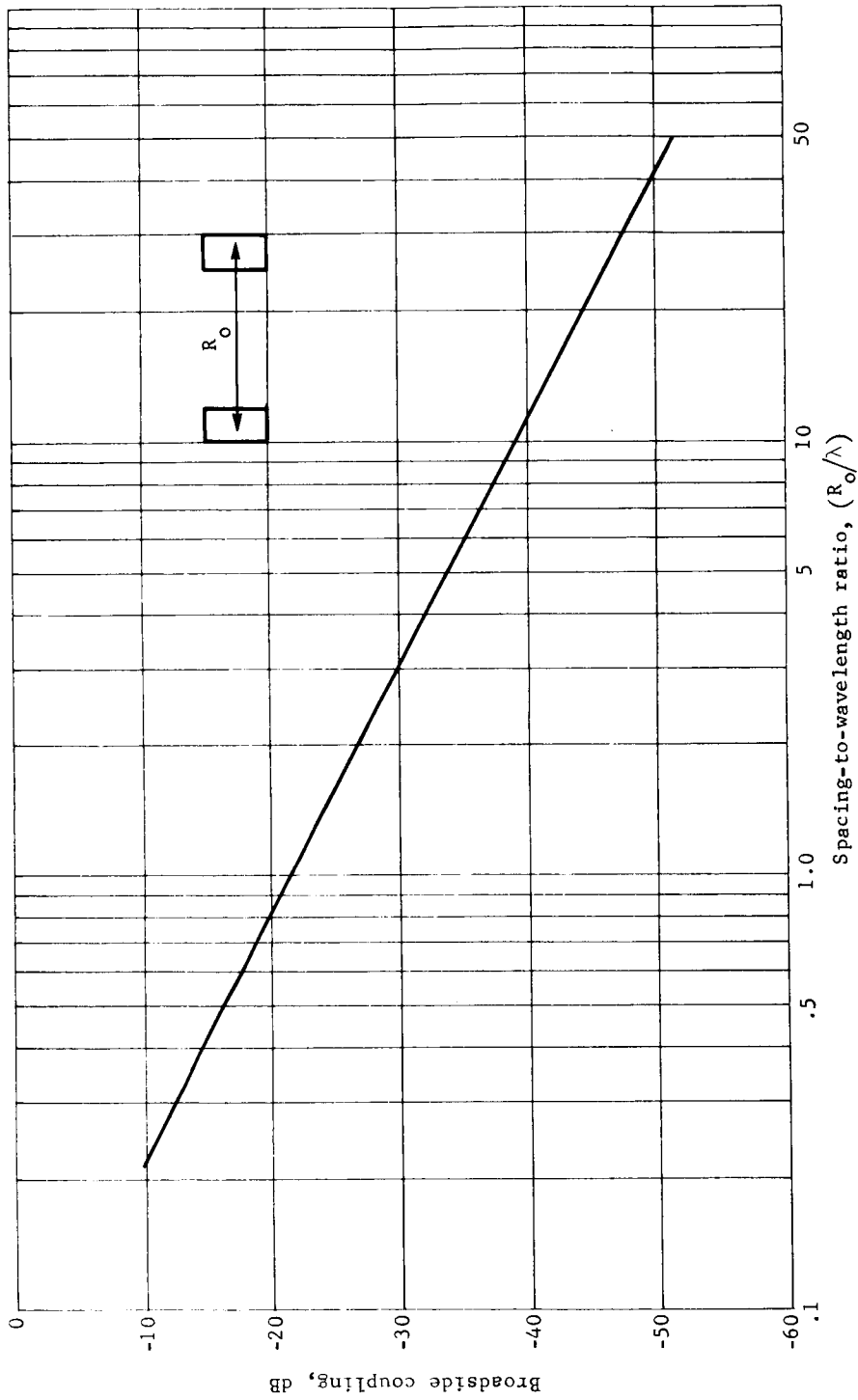and the magnetic vector potential in the far field is

Figure D4.- Broadside Coupling of Open-Ended Slots as a Function of the Center-to-Center Spacing in a Planar-Array Antenna
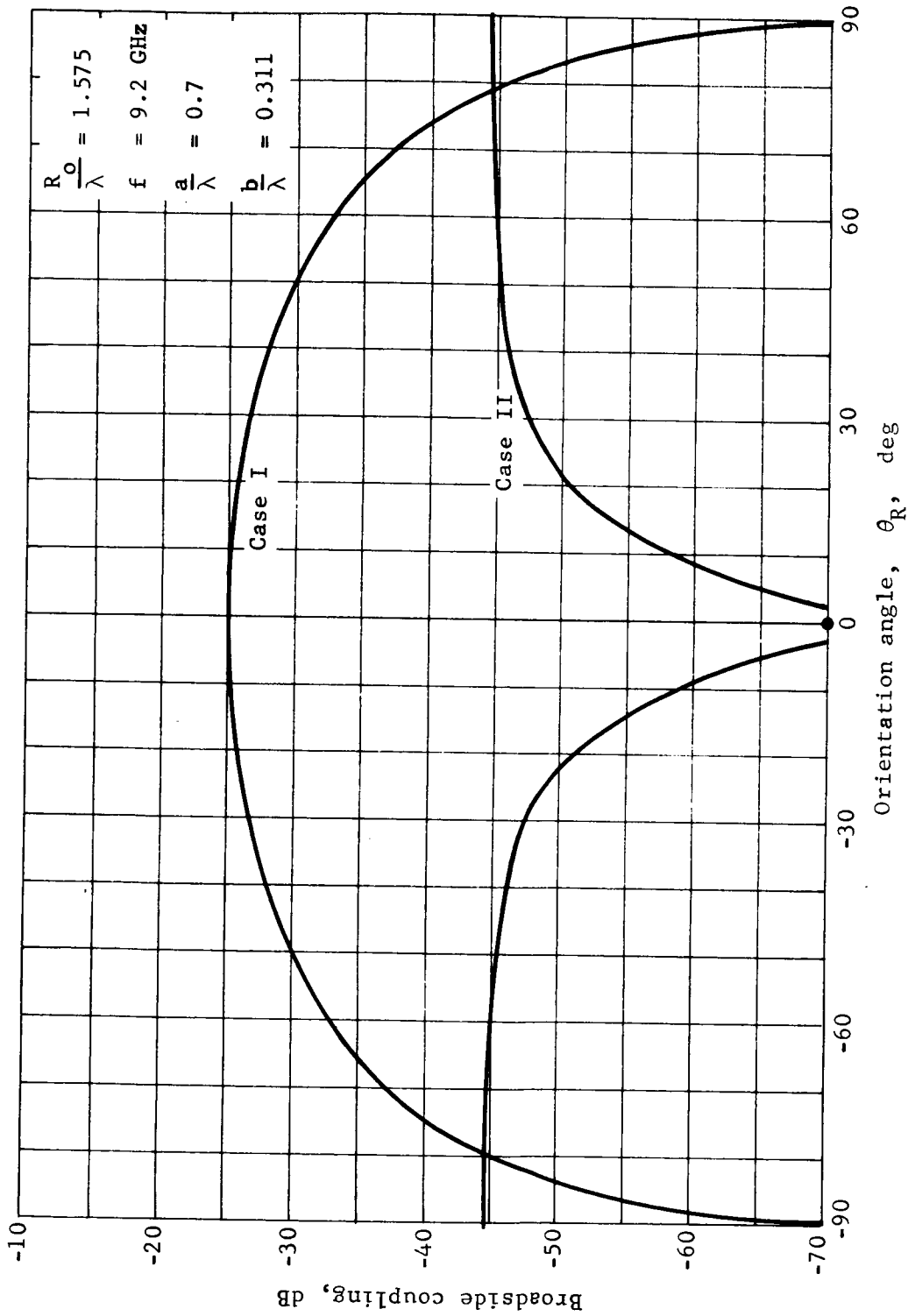
Figure D5.- Broadside Coupling of Open-Ended Slots as a Function of the Orientation of Two Slots in a Planar-Array Antenna
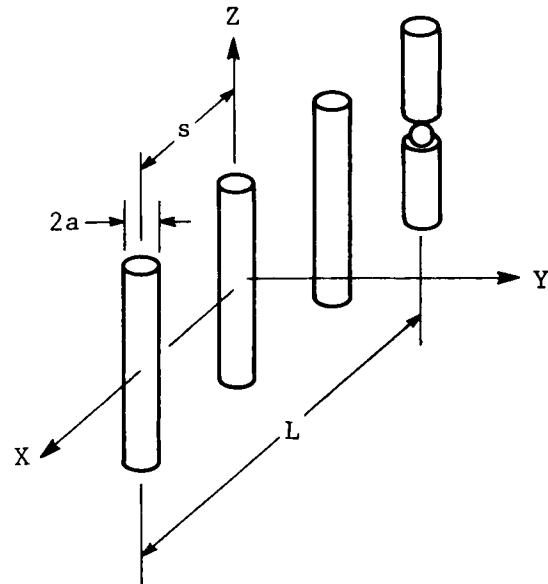
Figure D6.- Elements of an Interleaved-Dipole-Array Antenna

$$A_z = \sum_{n=-\infty}^{\infty} A_{zn} = \frac{\mu}{4\pi} \sum_{n=\infty}^{\infty} \int_{-h}^{h} \frac{I(Z^`)\left(\exp^{-jkxs}\right)\left(\exp^{-jkrn}\right)}{r_n} dz^` \tag{D34}$$

If we recognize the effect of the interleaved array to be the $\exp\left(-jk_x s\right)$, where

$$\cos k_x s = (\cos ks) - \tfrac{1}{2}\exp\left\{ks f\left[(h,a)\right]\right\} \tag{D35}$$

and

$$(h,a) = \left[\frac{(\cos kn)\left(\frac{\sin kh}{kh}\right) - kh (\cos kh)\left(\frac{\cos ka}{ka}\right)}{\sin kh - kh (\cos kh)}\right] \tag{D36}$$

then we can see that the change in the far field pattern depends on: the equivalent slot dimensions (a,b) related to the dipole dimensions (h,a); the slot spacing (ks) or phase relationship; and the excited element with respect to its location on the array. If we note that the exponential term, $\exp\left(-jk_x s\right)$, can be expressed in an alternating power series that can be maximized by selecting the spacing S in multiples of $\lambda/2$, then we see that the maximum contribution from the other elements would occur at the center of the array, with a taper at the ends of the array. For a multiple-beam array, the main beams would not occur at the center, and the side-lobe structure would be increased on the sides of the main beams near the center of the array.

APPENDIX E

MARTIAN SURFACE REFLECTIVITY

APPENDIX E

Two sets of reflectivity curves were used in the simulation. One set consisted of two upper and lower bound curves with the corresponding mean curve as described in reference 8. The other set of reflectivity curves that was used is based on the following assumptions: a certain portion of the local terrain will have a specular return similar to that measured on earth (ref 16); the greater portion of the return will be from the diffuse surface, which means that this return will be dependent on the local terrain roughness and electrical characteristics; and the beamwidth-illuminated area will tend to average these variations into an effective mean curve at higher altitudes.

For the diffuse surface components, the normalized radar cross-section per unit area σ_0 can be expressed in terms of the Fresnel reflection coefficients.

$$R^+ = \frac{(Y^2 \cos \theta) - (Y^2 - \sin^2 \theta)^{\frac{1}{2}}}{(Y^2 \cos \theta) + (Y^2 - \sin^2 \theta)^{\frac{1}{2}}} \tag{E1}$$

where

$$Y = \left(\epsilon_{rc}/\mu_{rc}\right)^{\frac{1}{2}} \approx \left(\epsilon/\epsilon_0\right)^{\frac{1}{2}} \tag{E2}$$

Then, if a curve-fitting model such as Beckmann's model is used for the microscopic roughness from reference 17 (fig. E1)

$$P(\theta) = \frac{1}{(\cos^4 \theta + R \sin^4 \theta)^{3/2}} \left(\exp \left\{-\frac{1}{4} \tan \theta \left[\text{erfc } (K \cot \theta)\right]\right\}\right) \tag{E3}$$

The effect of surface slope and beamwidth averaging can be incorporated into the sigma zero expression

$$\left(\sigma_0\right)_R = \sigma_0 \left\{\exp \left[-\tan^2 \varphi_0 \pm \left(S_I^2 \pm S_R^2\right)\left(\frac{4}{ab}\right)\right]\right\} \tag{E4}$$

where it can be seen from figure E2 that

$$\tan \varphi_0 = \frac{2h}{T} \cos \theta = 2 \tan \alpha \cos \theta \tag{E5}$$

where $\tan \alpha$ is the surface height divided by the surface decorrelation distance, ϵ is the incidence angle to a flat surface, and the integration intervals are
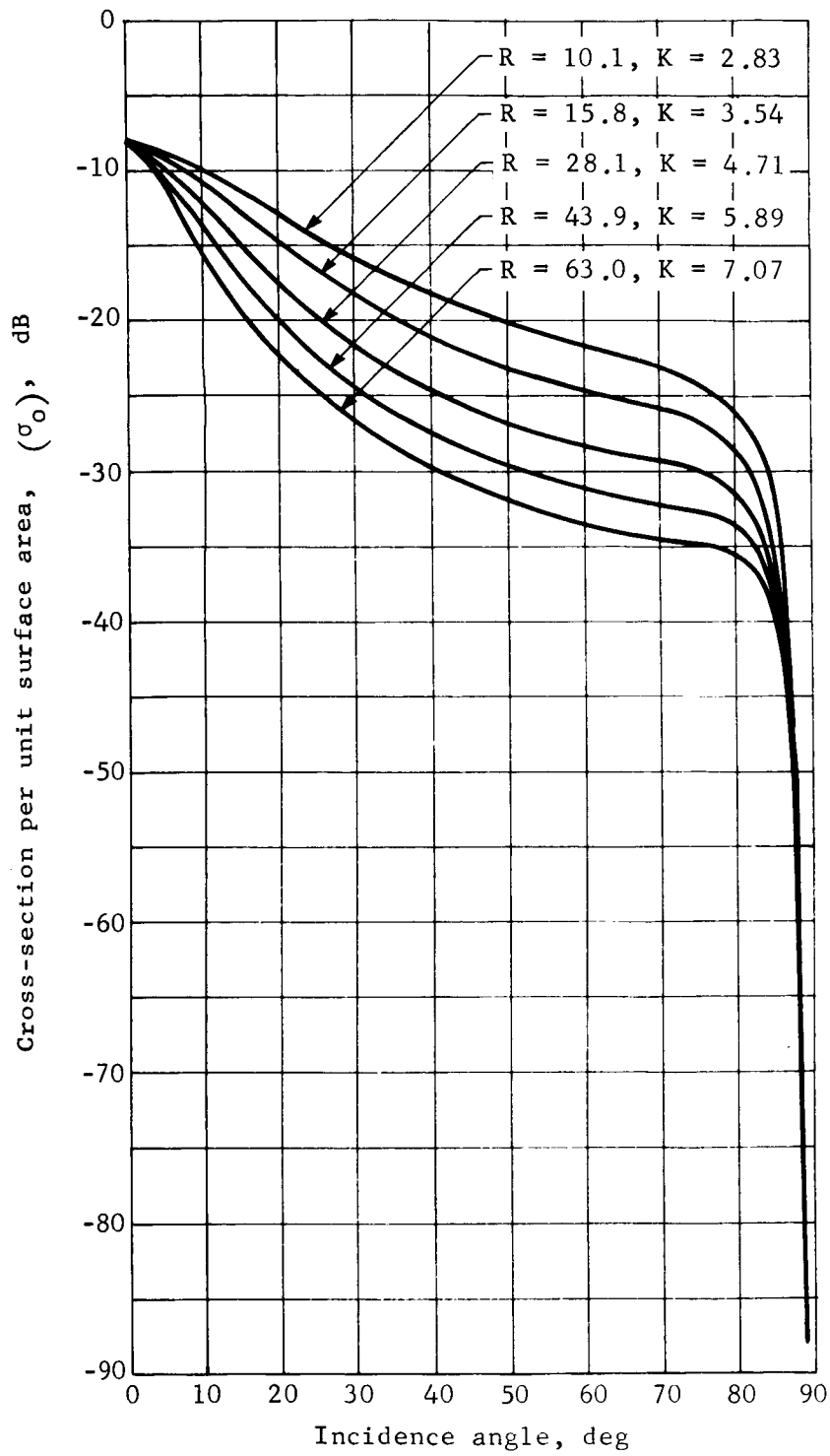
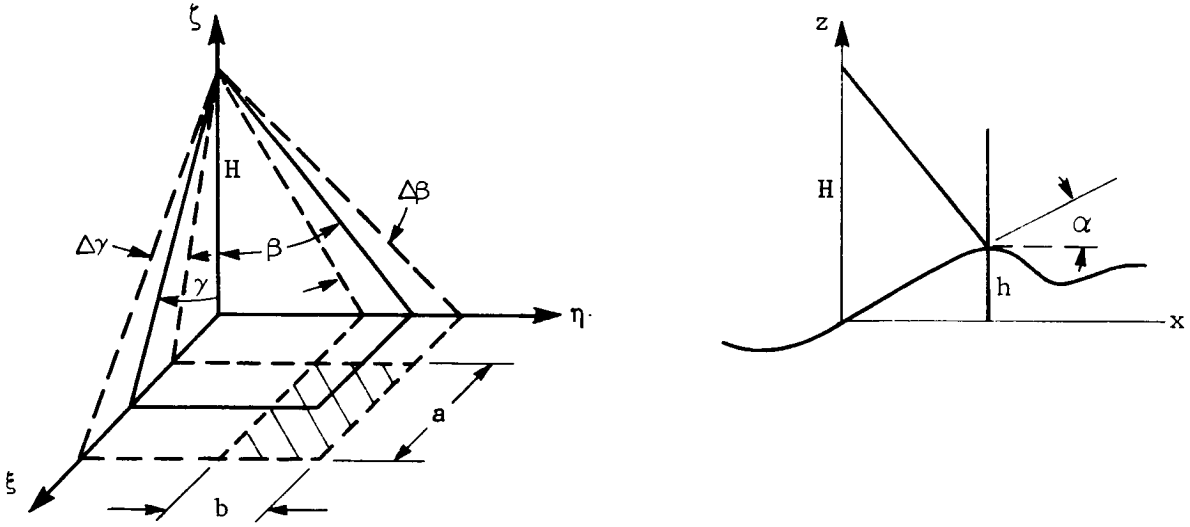Figure E1.- Beckmann Reflectivity Curves

Figure E2.- Effect of Surface Slope and Beamwidth Averaging
on Mars Surface Reflectivity

$$a = H \left[\tan \left(\gamma + \frac{\Delta \gamma}{2} \right) - \tan \left(\gamma - \frac{\Delta \gamma}{2} \right) \right] \tag{E6}$$

$$b = H \left[\tan \left(\beta + \frac{\Delta \beta}{2} \right) - \tan \left(\beta - \frac{\Delta \beta}{2} \right) \right] \tag{E7}$$

If we consider the microscopic roughness $(\sigma < \lambda)$ to be super-imposed on a microscopic rough surface $(\sigma > \lambda)$, the effects of the beamwidth smoothing can be seen from figure E3. In calculating the effects of beamwidth averaging, the surface roughness was considered to be normally distributed

$$R_h(\xi,\eta) = \left(\sigma_h \right)^2 \left[\exp \left(- \frac{\xi^2}{\xi_o^2} - \frac{\eta^2}{\eta_o^2} \right) \right] \tag{E8}$$

with slopes

$$R_{\tan \varphi}(\xi,\eta) = \tan^2 \varphi_o \left[\exp \left(- \frac{\xi^2}{\xi_o^2} - \frac{\eta^2}{\eta_o^2} \right) \right] \tag{E9}$$
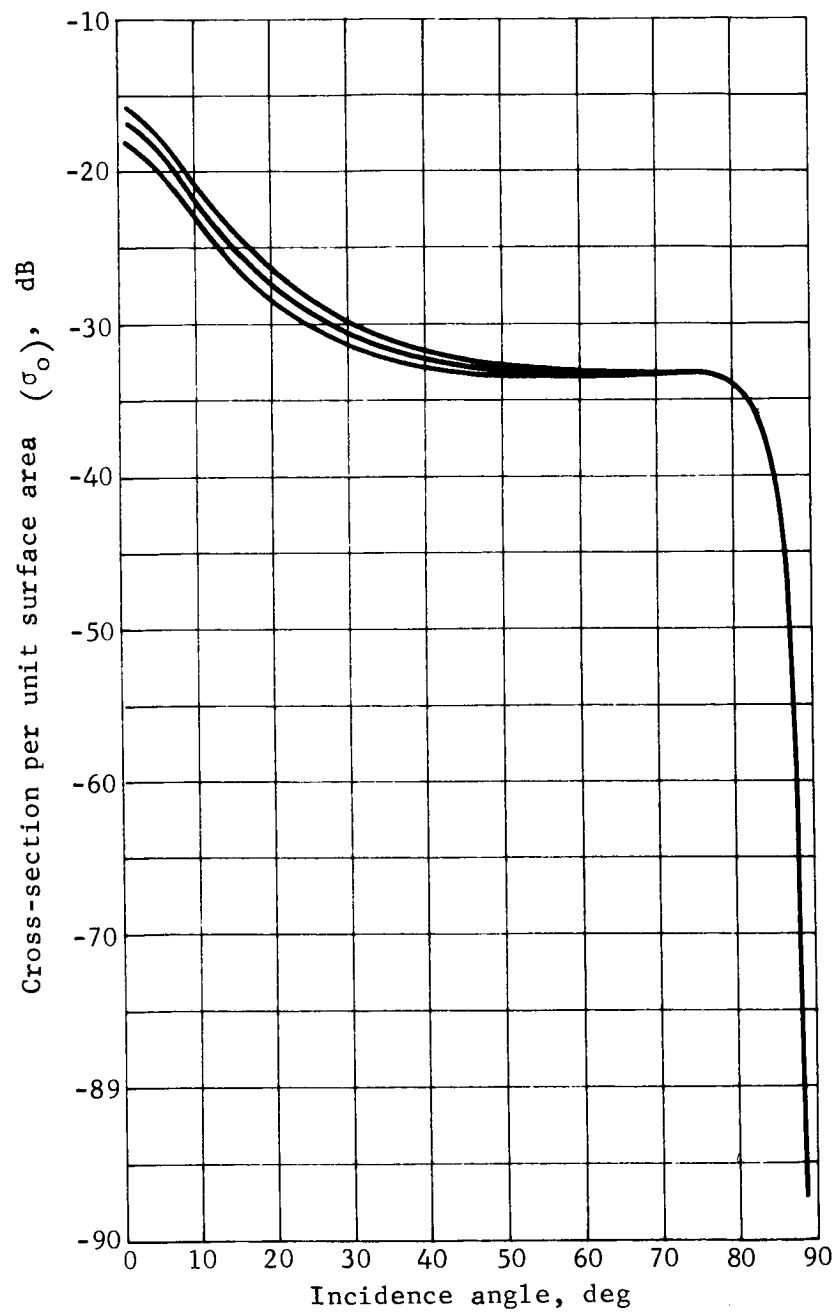
Figure E3.- Mean and Variance Curves for Mars Surface
Reflectivity at an Altitude of 4000 ft

$$p(\tan \varphi_1, \tan \varphi_2) = \frac{1}{2\pi \left(\tan^2 \varphi_o\right) \left\{1 - [\rho(\xi,\eta)]^2\right\}^{\frac{1}{2}}}$$

$$\left\{\exp\left[-\left(\frac{\tan^2 \varphi_1 + \tan^2 \varphi_2 - 2(\tan \varphi_1)(\tan \varphi_2)[\rho(\xi,\eta)]}{2 \tan^2 \varphi_o \left\{1 - [\rho(\xi,\eta)]^2\right\}}\right)\right]\right\} \quad (E10)$$

Now we can define the exponential autocovariance function

$$R_\varphi(\xi,\eta) = \tan^2 \varphi_o \left[\exp\left(-\frac{\xi}{\xi_o} - \frac{\eta}{\eta_o}\right)\right] \quad (E11)$$

and the sample average

$$S_o^2 = \frac{4}{ab} \int_0^a \int_0^b \left(1 - \frac{\xi}{a}\right)\left(1 - \frac{\eta}{b}\right)\left[R_f(\xi,\eta)\right] d\xi \, d\eta \quad (E12)$$

Now we evaluate the variance terms $\left(S_I^2, S_R^2\right)$ of the imaginary and real components (vertical and horizontal) of the surface slopes at φ_1 and $\varphi_2 \leq \pi/4$ radians.

$$S_R^2 \approx \frac{6}{ab}\left[\exp^{\left(-\tan^2\varphi_o\right)}\right]\left[\sum_{k=1}^{4} \frac{\left(\tan^2 \varphi_o\right)}{(2k)!} I_1 I_2\right] + \frac{2}{ab}\left[\exp^{\left(-\tan^2\varphi_o\right)}\right](I_3 I_4) \ldots$$

$$\ldots - \frac{2}{ab}\left[\exp^{\left(-5 \tan^2 \varphi_o\right)}\right](I_5 I_6) - \frac{2}{ab}\left[\exp^{\left(-5 \tan^2 \varphi_o\right)}\right]\left[\sum_{k=1}^{4} \frac{\left(3 \tan^2 \varphi_o\right)^{2k}}{(2k)!} I_7 I_8\right] \quad (E13)$$

$$S_I^2 \approx \frac{10}{ab}\left[\exp^{\left(-\tan^2 \varphi_o\right)}\right]\left(\tan^2 \varphi_o\right)\left(I_9 I_{10}\right) + \frac{10}{ab}\left[\exp^{\left(-\tan^2 \varphi_o\right)}\right]\left[\sum_{k=1}^{3} \frac{\left(\tan^2 \varphi_o\right)}{(2k+1)!} I_{11} I_{12}\right] \ldots$$

$$\ldots - \frac{2}{ab}\left[\exp^{\left(-5 \tan^2 \varphi_o\right)}\right]\left[\sum_{k=1}^{3} \frac{\left(3 \tan^2 \varphi_o\right)}{(2k+1)!} I_{15} I_{16}\right] - \frac{6}{ab}\left[\exp^{\left(-5 \tan^2 \varphi_o\right)}\right]\left(\tan^2 \varphi_o\right)(I_{13} I_{14}) \quad (E14)$$

where

$$I_1 I_2 = \left[\left(\frac{\xi_o}{2k}\right) \; 1 - \left[\exp^{\left(-2ka/\xi_o\right)}\right] \; - \left(\frac{\xi_o}{2k}\right)^2 \left\{ 1 - \left[\exp^{\left(-2ka/\xi_o\right)}\right] \left(1 + \frac{2ka}{\xi_o}\right)\right\}\right] \cdots$$

$$\cdots \left[\left(\frac{\eta_o}{2k}\right)\left[1 - \exp^{\left(-2kb/\eta_o\right)}\right] \; - \left(\frac{\eta_o}{2k}\right)^2 \left\{ 1 - \left[\exp^{\left(-2kb/\eta_o\right)}\right] \left(1 + \frac{2kb}{\eta_o}\right)\right\}\right] \qquad \text{(E15)}$$

$$I_3 I_4 = \frac{ab}{4} \qquad \text{(E16)}$$

$$I_5 I_6 = \frac{ab}{4} \qquad \text{(E17)}$$

$$I_7 I_8 = I_1 I_2 \qquad \text{(E18)}$$

$$I_9 I_{10} = \left[\xi_o \left[1 - \exp^{\left(-a/\xi_o\right)}\right] \; - \xi_o^2 \left\{ 1 - \left[\exp^{\left(-a/\xi_o\right)}\right] \left(1 + \frac{a}{\xi_o}\right)\right\}\right] \cdots$$

$$\cdots \left[\eta_o \left[1 - \exp^{\left(-b/\eta_o\right)}\right] \; - \eta_o^2 \left\{ 1 - \left[\exp^{\left(-b/\eta_o\right)}\right] \left(1 + \frac{b}{\eta_o}\right)\right\}\right] \qquad \text{(E19)}$$

$$I_{11}I_{12} = \left[\left(\frac{\xi_o}{2k+1}\right) \left\{ 1 - \exp^{\left[-(2k+1)a/\xi_o\right]}\right\} - \left(\frac{\xi_o}{2k+1}\right)^2 \left(1 - \left\{\exp^{\left[-(2k+1)a/\xi_o\right]}\right\} \left[1 + \frac{(2k+1)a}{\xi_o}\right]\right)\right] \cdots$$

$$\cdots \left[\left(\frac{\eta_o}{2k+1}\right) \left\{ 1 - \exp^{\left[-(2k+1)b/\eta_o\right]}\right\} - \left(\frac{\eta_o}{2k+1}\right)^2 \left(1 - \left\{\exp^{\left[-(2k+1)b/\eta_o\right]}\right\} \left[1 + \frac{(2k+1)b}{\eta_o}\right]\right)\right] \qquad \text{E20)}$$

$$I_9 I_{10} = I_{13} I_{14} \qquad \text{(E21)}$$

$$I_{15} I_{16} = I_7 I_8 \qquad \text{(E22)}$$

APPENDIX F

RANGE SIGNAL BANDWIDTH
FOR THE MODIFIED LM RADAR SYSTEM

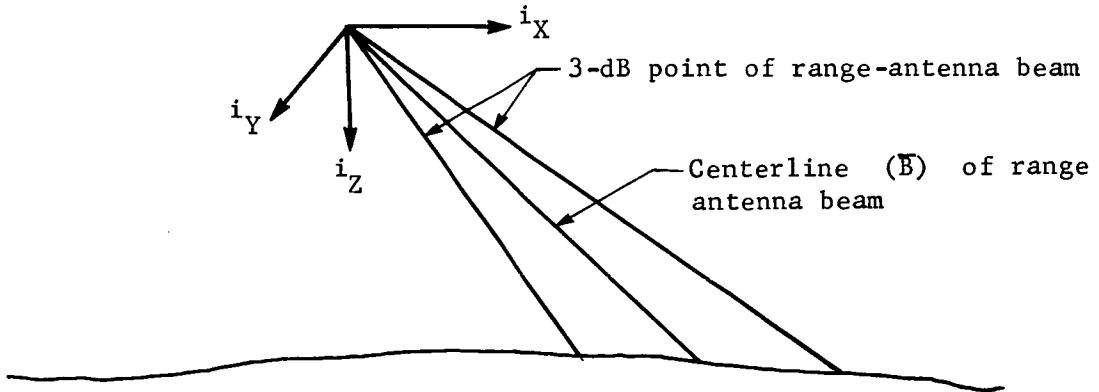The geometry used in the derivation of the range signal bandwidth is shown in figure Fl.

Figure Fl.- Frequencies at the 3-dB Points of the
Range-Antenna Beam in the i_Z - $\overline{B}$
Plan

The figure indicates the frequencies at the 3-dB points of the range antenna beam in the plane defined by the vectors $\overline{i}_Z$ and $\overline{B}$. These frequencies are proportional to the range and velocity of the beam. Equation (Fl) is used to compute the bandwidth in this plane:

$$EW = f_{RZ} + f_{D2} - f_{R1} + f_{D1} \tag{F1}$$

where BW is the range signal bandwidth, f_R is the frequency proportional to the range, f_D is the frequency proportional to the velocity, and where f_{R2} is always greater than f_{R1}.

Note that is the Doppler BW in the i_Z - $\overline{B}$ plane is

$$BW_D = f_{D2} - f_{D1} \tag{F2}$$

and if the BW proportional to the range is

253

$$BW_R = f_{R2} - f_{R1} \qquad (F3)$$

then equation (F1) can be written as

$$BW = BW_R \pm BW_D \qquad (F4)$$

The Doppler BW will be additive when the velocity vector is above the conic generated by swinging the beam-pointing vector about the vertical, and subtractive when the velocity vector is within the cone.
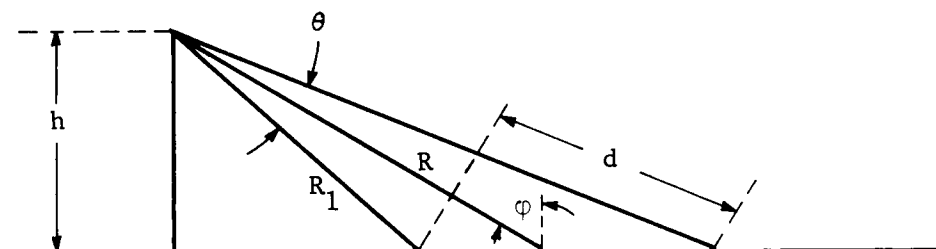

Figure F2.- Geometry for Calculating the Doppler
Bandwidth BW_R

From figure F2 we can see that d is proportional to BW_R. d can be found from

$$d = R_2 - R_1 = \frac{h}{\cos\left(\varphi + \frac{\theta}{2}\right)} - \frac{h}{\cos\left(\varphi - \frac{\theta}{2}\right)} \qquad (F5)$$

Then,

$$BW_R \approx (SF) \, R\theta \, \tan \varphi \qquad (F6)$$

where SF, the range scale factor, is in units of Hz/ft.

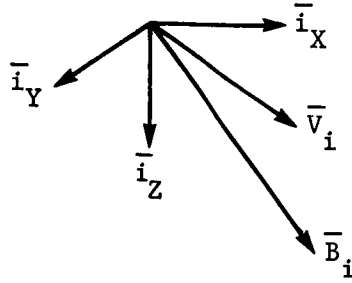Figure F3 shows the geometry used to obtain the Doppler bandwidth, BW_D, in the plane described in figure F1.

Figure F3.- Geometry for Calculating the Doppler
Bandwidth BW_D

In this figure, $\overline{B}_i$ is the range-beam pointing vector, $\overline{V}_i$ is the velocity vector, and $\overline{i}_X$, $\overline{i}_Y$, $\overline{i}_Z$ are the unit vectors along the inertial axes.

The problem is to determine the component of $\overline{V}_i$ perpendicular to $\overline{B}_i$ and the component in the plane defined by $\overline{i}_Z$ and $\overline{B}_i$. Since the range beam points along the $\overline{U}$ body axis

$$\overline{B}_i = [\overline{\overline{A}}]^T [B] = \begin{bmatrix} A_{11}{}^i X \\ A_{12}{}^i Y \\ A_{13}{}^i Z \end{bmatrix} \tag{F7}$$

where $\overline{\overline{A}}$ is the inertial-to body-axis transformation and $\overline{B}$ is the range-beam pointing vector in the body-coordinate system.

A unit vector perpendicular to $\overline{i}_Z$ and $\overline{B}_i$ is given by

$$\overline{P} = \overline{i}_Z \times \overline{B}_i = \begin{bmatrix} 0 \\ 0 \\ \overline{i}_Z \end{bmatrix} \times \begin{bmatrix} A_{11} \ \overline{i}_X \\ A_{12} \ \overline{i}_X \\ A_{13} \ \overline{i}_X \end{bmatrix} = \begin{bmatrix} -A_{12} \ \overline{i}_X \\ A_{11} \ \overline{i}_Y \\ 0 \quad 0 \end{bmatrix} \tag{F8}$$

We want to find the unit velocity perpendicular to $\overline{B}_i$ in the plane defined by $\overline{i}_Z$ and $\overline{B}_i$. This is

$$\overline{CP} = \overline{P} \times \overline{B}_i = \begin{bmatrix} -A_{12}\,\overline{i}_X \\ A_{11}\,\overline{i}_Y \\ 0 \quad 0 \end{bmatrix} \times \begin{bmatrix} A_{11}\,\overline{i}_X \\ A_{12}\,\overline{i}_Y \\ A_{13}\,\overline{i}_Z \end{bmatrix} = \begin{bmatrix} (A_{11}\,A_{13}) & \overline{i}_X \\ (A_{12}\,A_{13}) & \overline{i}_Y \\ \left(-A_{12}{}^2 - A_{11}{}^2\right) & \overline{i}_Z \end{bmatrix} \tag{F9}$$

and so the component of the velocity lying along $\overline{CP}$ is

$$\overline{CP} \cdot \overline{V}_i = V_{CP} \tag{F10}$$

Then:

$$BW_D = \frac{2\,V_{CP}(\theta)}{\lambda} \tag{F11}$$

If V_{CP} is positive, then BW_D is additive; and if V_{CP} is negative, then BW_D is subtracted from BW_R.

$$BW = (SF)\,R\theta\,\tan\varphi + \frac{2\,V_{CP}(\theta)}{\lambda} \tag{F12}$$

Equation (F12) will be used in the simulation as long as BW is greater than the Doppler spectrum defined by

$$DS = \frac{2\,[V(\theta)]}{\lambda}\,(\sin\gamma) \tag{F13}$$

where γ is the angle between the range-beam pointing vector and the velocity vector. Otherwise, the bandwidth defined by equation (F13) is used.

REFERENCES

1. Preston, Billie W.; et al: MOD6MV Simulator Program Terminal Descent User's Guide. CR-22-69-16, Martin Marietta Corporation Denver, Colo., July 1969.

2. Diesel, John W.; et al: Modularized Six-Degree-of-Freedom (MOD6DF) Computer Program. Litton Systems, Inc, Woodland Hills, Cal. (USAF AF33(615)-3204).

3. Ingoldby, Robert N.; and Seibel, Richard P.: Terminal Descent Control System Analysis. PR 22-10-94-21, Martin Marietta Corporation, Denver, Colo., Jan. 1968.

4. Mann, Michael K.; Preston, Billie W.; and Stafford, Parker S.: Final Summary Report, Study of a Soft Lander Module for Mars Missions; Vol. III, LM Radar Evaluation and Vernier Phase Simulation. NASA CR-66728-3, Jan. 1969.

5. Stafford, Parker S.: Landing Radar Application Considerations. TN-37-69-11, Martin Marietta Corporation, Denver, Colo., Mar. 1969.

6. Anon: Viking Lander System and Project Integration, Technical Proposal. P-69-27, Martin Marietta Corporation, Denver, Colo., Apr. 1969.

7. Hull, Keith L.: Terminal Descent Navigation for a Planetary Lander. Paper presented at 5th Space Congress, Cocoa Beach, Fla., Mar. 1968.

8. Michael, William H., Jr.; Wood, George P.; and Young, A. Thomas: Mars Engineering Model. M73-106-0, Langley Research Center, Langley Station, Hampton, Va.

9. Anon.: IBM 1130 Scientific Subroutine Package, Programmer's Manual. H20-0252-0, International Business Machines Corp., White Pines, N. Y., 1966.

10. Broderick, Richard F.; and Hayre, H. S.: Doppler Return from a Random Rough Surface. IEEE Transactions on Aerospace and Electronic Systems, Vol. AES-5, No. 3, May 1969, pp. 441-449.

11. Muhleman, D. O.: Radar Scattering from Venus and the Moon. Astron. J., Vol. 69, No. 1, Feb. 1964.

12. Berger, F. B.: The Nature of Doppler Velocity Measurements. IRE Transactions of Aeronautical and Navigational Electronics, 1957.

13. Moog, Richard D.: Mars Lander Parachute Dynamics. TN-37-69-20, Martin Marietta Corporation, Denver, Colo., Jan. 1969.

14. Broderick, Richard F.; Mann, Michael K.; and Stafford, Parker S.: Interim Report, Development of a Martian Soft Lander Terminal Descent Program. Martin Marietta Corporation, Denver, Colo., Apr. 1969. (NAS1-8913)

15. Lyon, J. A.; et al.: Derivation of Aerospace Antenna Coupling-Factor Interference Prediction Techniques. Technical Report AFAL-TR-66-57, University of Michigan, Ann Arbor, Michigan, Apr. 1966, p. 31.

16. Grant, C. R.; and Yaplee, B. S.: Backscattering from Water and Land at Centimeter and Millimeter Wavelengths. Proc. IRE, Vol. 45, July 1957.

17. Beckmann, Peter; and Klemperer, W. K.: Interpretation of the Angular Dependence of Backscattering from the Moon and Venus. Radio Science, Vol. 69D, No. 12, Dec. 1965, pp. 1669-1673.